****

University of L'Aquila

DEPARTMENT OF PHYSICAL AND CHEMICAL SCIENCES
Ph.D. degree in Physical and Chemical Sciences
XXXIII cycle

On the use of micro-Raman and photoluminescence spectroscopy for the study of doping concentration in classic and two-dimensional semiconductors: the case of p-type Si and molybdenite

SSD FIS/01

Candidate:
Stefano Palleschi

Ph.D. Coordinator:
Prof M. Aschi

Supervisor:
Prof L. Ottaviano

Intenship Supervisor
at Lfoundry:
Dr O. A. Cacioppo

Thesis submitted in 2021

On the use of micro-Raman and photoluminescence spectroscopy for the study of doping concentration in classic and two-dimensional semiconductors: the case of p-type silicon and molybdenite

Stefano Palleschi

19 aprile 2022

ACKNOWLEDGEMENTS

I would like to express my great gratitude to my PhD supervisor, Prof. Luca Ottaviano, for guiding my research with dedication, making valuable and constructive suggestions and supporting me in the most critical moments. I would like to offer my special thanks to Dr. Onofrio Antonino Cacioppo, Dr. Giuseppe Moccia and Dr. Marco Renzelli, who hosted me during my 18-month internship at Lfoundry Srl. and provided me with continuous support and useful information. I would like to acknowledge the contribution of my colleagues at Lfoundry: Dr. Silvia Tosti, Dr. Valerio Latini, Dr. Vito La Tona, Dr. Vanda Granato, Dr. Tiziana Del Buono, Dr. Albert Antonacci and Mr. Venico Zuffranieri for their help in collecting the experimental data. I would also like to thank the technicians of the Failure Analysis Laboratory at Lfoundry for their diligent support. I am especially grateful to my fellow PhD students: Dr. Gianluca D'Olimpio, Dr. Ilaria Iacoboni and Dr. Dario Mastrippolito, who shared with me the hard and stimulating work of research and elaboration of scientific results.
A special thanks goes to my family.

CONTENTS

Acknowledgements 1

Abstract 9

Citation to published journals 11

1 Introduction 12
1.1 General motivations 12
1.2 Objectives of this thesis 16
1.3 Organization of this thesis 17

2 Relevant properties of silicon and two-dimensional MoS_2 19
2.1 Silicon crystal structure, electronic energy bands, phonon dispersion curves 19
2.2 MoS_2: a transition metal dichalcogenide 23
2.2.1 MoS_2 lattice structure 25
2.2.2 electronic band structure and excitons in MoS_2 27
2.2.3 Phonon properties in MoS_2 31
2.3 Doping in homogeneous semiconductors 35
2.3.1 free charge carrier densities in thermal equilibrium 35
2.3.2 extrinsic semiconductors 37
2.3.3 quasi-Fermi levels 41
2.3.4 degenerate semiconductors 41

3 Basics of important optical phenomena in semiconductors 43
3.1 Basics of Raman Scattering 43
3.2 Macroscopic description 44
3.3 Microscopic Description 48
3.4 Resonant Raman scattering 50
3.5 Photoluminescence 52
3.5.1 Band-to-band transitions 55
3.5.2 Free-to-bound transition 56
3.5.3 Donor-acceptor pair transition 56
3.5.4 Exciton emission 57
3.5.5 Free-exciton PL in terms of exciton polariton emission 58
3.6 Fano interference effect in Raman scattering of doped Si 59
3.6.1 p-type Si case 60
3.6.2 n-type Si case 61
3.6.3 General considerations 63

4 Experimental Methodology 68
4.1 Experimental setup 69
4.1.1 Basic setup of a Raman and PL spectroscopy system 69
4.1.2 Raman and PL instruments. 72
4.1.3 Additional instruments. 73
4.1.4 Ancillary techniques 74
4.2 Silicon analysis: materials and methods 74
4.2.1 Si samples 75
4.2.2 Si crystal orientation and scattering configuration . . 76
4.2.3 Considerations on the spectral effects of laser power 77
4.2.4 Fitting method for Raman analysis of Fano effect . . . 78
4.3 MoS_2 analysis: materials and methods 81
4.3.1 Samples of MoS_2 monolayer 81
4.3.2 Resonant Raman spectrum of MoS_2 monolayer 82
4.3.3 PL spectrum of MoS_2 monolayer 83
4.3.4 Setting for Raman measurements of MoS_2 samples . 84
4.3.5 Annealing procedures 84
4.3.6 Free electron density by three level model and mass-action law 84

5 Doping characterization of p-type Si wafers via multi-wavelength micro-Raman spectroscopy 88
5.1 Introduction 89
5.2 Results and discussion 92
5.2.1 Raman analysis of Czochralski silicon wafers 92
5.2.2 Raman analysis of implanted silicon wafers 100
5.2.3 Raman analysis of beveled Si wafers 103
5.3 Conclusions to Chapter 5 109

6 Raman and photoluminescence analyses of single-layer MoS_2 via thermally controlled sulphur vacancy doping 111
6.1 Introduction 112
6.2 Results and discussion 115
6.2.1 Morphological evidences of thermal annealing on 2D MoS_2 115
6.2.2 Non-resonant Raman and PL analyses before and after annealing 120
6.2.3 Bottom-up layer engineering and PL evidences: a rationale 126
6.2.4 Power dependent PL analysis and electron density estimation. 128
6.2.5 Resonant Raman analysis 131
6.3 Conclusions to Chapter 6 134

7 Conclusions and Outlook 136
7.1 Conclusions 136
7.2 Outlook 138

Bibliography 141

173

LIST OF TABLES

2.1 Specifications of high-symmetry points and directions of the first Brillouin Zone of fcc, diamond, and zinc-blende lattices. From [55]. 20

5.1 Fano fitting parameters of the Raman spectra at different excitation of CZ-Si samples doped at different B concentrations. 95

5.2 Fano fitting parameters of Raman spectra acquired with near-UV excitation of ${BF_2}^+$-implanted & LTA silicon samples doped with different B concentrations. 104

6.1 Spectral feature specifications of non-resonant Raman spectra of single-layer MoS_2 before and after annealing. 122

6.2 Quantitative analysis of PL spectra using a constrained fit in terms of neutral and charged excitons A^0 and A^-. 124

LIST OF FIGURES

1 (a) Crystallographic unit cell of diamond structure. (b) first Brillouin Zone of face-centered cubic crystal lattice 20
2 (a) Electronic band structures of Si. (b) Detail of the central direct transition at Γ. 21
3 Phonon dispersion curves for silicon. 22
4 Molly Hill Molybdenite [96]. 24
5 Crystal structures of MoS_2 polytypes. 26
6 Primitive Unit Cell of 2H-MoS_2. 27
7 (a) Band structure of MoS_2 from bulk to monolayer. (b) First Brillouin zone of MoS_2. (c) Absorption spectrum of the monolayer of MoS_2. 29
8 Schematic representation of the excitonic radiative transition at K point in the Brillouin zone of MoS_2 30
9 (a) Atomic displacements of Raman-active and IR-active MoS_2 phonon modes. (b) Phonon dispersion branches of the monolayer and bulk of MoS_2. (c) Raman spectra of the monolayer (1L), bilayer (2L), and bulk of MoS_2 for 532 nm excitation wavelength.. 33
10 Classification and properties of long-wavelength lattice vibration of 2H:MoS_2. Table taken from [122].. 34
11 Schematic representation of the energy levels in an extrinsic semiconductor 38
12 Schematic diagrams of Stokes and anti-Stokes Raman scattering. 45
13 Feynman diagrams contributing to one-phonon Stokes Raman process and explanation of their usage. 49
14 Exciton-polariton dispersion curves 58
15 Schematic illustration of the optically induced electronic transitions in highly doped p-type Si leading to the typical Fano line shape in Raman scattering. 61
16 Schematic representation of the conduction bands in Si along the <100> direction near the edge of the Brillouin zone X_1. . . 62
17 Schematic representation of a Fano resonance. 63
18 Schematic optical diagram of a micro-Raman and PL spectrometer. 70
19 Schematic line-shape of a Fano function 79
20 Schematic of spectral fit with calculated parameters and Chi-square. 81
21 Energy level diagram of the three-level model for excitonic states in 2D MoS_2.. 85

22 In (a), (b) and (c) Raman spectra of CZ-Si samples at different B doping concentration acquired at different excitation. In (d), (e) and (f) Raman spectra of the highest doped sample with fitting analysis.. 93
23 Raw data of Raman spectra of CZ-Si samples with different B doping recorded at different excitation conditions.. 94
24 Dependence of Fano fitting parameters on B-doping concentration from analysis of Raman spectra of CZ-Si samples. 96
25 Fano fitting parameters as a function of doping concentration plotted against data available in the literature for direct comparison. 97
26 Raman Si peak broadening and frequency softening, result of Fano matching analysis, averaged over excitation wavelengths, plotted as a function of doping concentration of CZ-Si samples. 98
27 (a) Fano asymmetry parameter q versus excitation energy from Raman analysis of the B-doped CZ-Si samples. (b) Slope values (m) of the trends in panel (a) plotted as a function of doping concentration. 99
28 (a) TEM image of $BF_2{}^+$-implanted & LTA Si crystal. (b) Boron (B) and fluorine (F) SIMS depth concentration profiles. 101
29 Raman Si peak Fano total width (FWHM) ($2\Gamma_F$) (a) and peak position (ω_0) (b) of $BF_2{}^+$-implanted <A silicon samples acquired with visible and near-UV excitations, plotted as functions of doping concentration. 102
30 Near-UV Raman analysis of $BF_2{}^+$-implanted & LTA silicon samples at different doping concentrations. (a,b and c) Spectral analysis, (d,e and f) Fano fitting parameters as a function of doping concentration. 103
31 Fano fitting parameters as functions of doping concentration of $BF_2{}^+$-implanted & LTA-Si samples together with CZ-Si samples and literature derived data. 105
32 Boron SIMS profiles (panels (a), (b)), boron SIMS and SRP profiles (c) and corresponding Raman spectra using near-UV excitation (panels (d), (e) and (f)) of B-doped Si wafers with different doping concentrations. 106
33 Fano broadening parameters as a function of surface doping concentrations estimated by boron SIMS and SRP of p-type Si samples, plotted in overlap with the linear model derived from B-doped CZ-Si wafers. 107
34 Raman-based doping concentration profile obtained on the beveled surface of a p-type B-doped Si wafer. 108

35 AFM images of MoS_2 flakes on SiO_2/Si substrate. 116

36 (a) AFM image of a MoS_2 flake on SiO_2/Si(100) after an ageing of 48 months in dry air, in (b) the same flake after a bath in de-ionised water for 1 hour. 118
37 Optical microscope images of few-layer MoS_2 flakes (a) before and (b) after annealing at 400 °C for 40 min in air showing heat-induced degradation.. 118
38 Optical and AFM images of MoS_2 flakes before and after annealing in air. The disappearance of a single-layer flake of MoS_2 after annealing is clearly visible.. 119
39 Non-resonant Raman spectra of monolayer MoS_2 acquired with excitation wavelength 532 nm before and after annealing. 121
40 PL spectra of monolayer MoS_2 before and after annealing in air (a) and in UHV (b). 123
41 Normalised spectral PL intensity (left axis) and percentage of sulphur vacancies (right axis) determined as a function of annealing temperature.. 125
42 Log-log plot of mean normalized PL intensity yields as functions of excitation laser power measured before and after the annealing.. 128
43 Power dependent PL intensity analysis of total PL signal and fitted peaks spectral weight (A^0 and A^-).. 129
44 RT resonant Raman spectra of single-layer MoS_2 on SiO_2/Si(100) substrate as-exfoliated (bottom panel) and annealed (top panel) in air at 275 °C for 40 min.. 131
45 Raman spectral yield and PL spectral yield plotted as a function of annealing temperature. An inset shows the plot of the PL yield as a function of Raman yield. 132
46 Intensity ratio of E^1_{2g} and A_{1g} Raman fitted peaks measured before and after the annealing plotted as functions of PL Intensity Ratio.. 133

ABSTRACT

In this work, we develop characterization techniques based on Raman and PL spectroscopy for the study of doping effects in p-type Si and MoS_2. Doping monitoring is a critical factor in the proper fabrication of Si-based electronics, which inherently requires the fabrication of targeted doped regions at the nanoscale. We show that it is possible to measure the dopant concentration in p-type Si over a wide range ($10^{15} \div 10^{20}$ cm^{-3}) using laser excitation in the visible and near UV regions. We exploit the effect of doping-dependent Fano interference in the first-order Raman spectrum of Si. The Raman spectra of differently doped Si samples are analysed with unprecedented accuracy using an improved fitting method that employs a convolution of Fano and Gaussian functions to distinguish the physical and instrumental contributions of emission. Regardless of the excitation wavelength, the one-phonon Si peak exhibits broadening, frequency-softening, and intensity decay as a function of doping concentration, which are accurately determined for reliable doping characterization. The experimental data are directly compared with the relevant literature data of highly doped Si, showing that the proposed analysis is consistent with the previous studies at high doping concentrations and complementary in the intermediate concentration range ($10^{15} \div 10^{18}$ cm^{-3}). The fitted peak broadening and frequency shift parameters show linear trends as a function of doping concentration, which are used to construct calibration curves for doping monitoring applications. Differential penetration of light of different wavelengths into Si is used to probe the subsurface of Si wafers at different depths, allowing nondestructive characterization of doping. The application of near-UV Raman analysis to small-angle beveled samples enables doping profiling. The doping profile of p-type Si is reproduced down to 100 nm with good doping sensitivity (10 ppm) in the ($10^{18} \div 10^{20}$) cm^{-3} concentration range. Excellent vertical (10 nm) and lateral (1 μm) resolutions demonstrate that Raman profiling is an efficient alternative to the more onerous SIMS and SRP techniques.
This work also reports on the study of the effects of thermal annealing of mechanically exfoliated single and multilayer samples of MoS_2 deposited on a SiO_2/Si substrate. The changes in Raman and PL responses due to annealing of the samples in the temperature range of (200 $\div$ 300 °C) are analysed. Optical microscopy and AFM analyses of samples annealed up to 400 °C are also reported. We demonstrate the presence of a nano-confined water film at the interface between MoS_2 and the substrate. The thickness of this water film can be reduced by annealing and restored by water baths. Then we directly demonstrate the sublimation of the bottom layer of MoS_2 at the interface with SiO_2 by annealing at the highest temperatures. Annealing processes in the temperature range of (200 $\div$ 300) °C lead to an increase in the sulphur

vacancy concentration at the basal planes of the flakes. Passivation of sulphur vacancies by H_2O and O_2 adsorption after air exposure leads to the deplation of free electrons in MoS_2, which is reflected in PL and Raman responses. PL emission, due to radiative recombination of neutral excitons (A^o) and charged excitons (A^-), show an increase in integrated intensity after annealing, demonstrating the direct correlation between the population of type A excitons and sulphur vacancy concentration. The relative weight of the A^o and A^- components of the PL spectrum can be tuned by annealing in the temperature range (200 ÷ 300) °C, with A^- dominating at the lower temperatures and A^o dominating at the higher temperatures. Mathematical models using A^o and A^- intensities allow us to quantitatively estimate the variation in sulphur concentration and the change in free electron density in annealed MoS_2 compared to pristine exfoliated MoS_2 as a function of annealing temperature. Considering the typical vacancy concentrations of mechanically exfoliated MoS_2, we estimate sulphur vacancy concentration values close to 10^{14} cm^{-2} after annealing at $\sim$ 300 °C. For the mean density of free electrons, we find values of the order of 10^{13} cm^{-2} for freshly exfoliated MoS_2 with a decrease by several integer factors after annealing at 300 °C. We then demonstrate the direct correlation of the integrated intensity yield of the resonant-Raman spectra with the corresponding PL spectral yield as a function of annealing temperature, providing experimental evidence for exciton-phonon coupling in 2D MoS_2. The in-plane E^1_{2g} phonon mode shows strong coupling with type A excitons, while the out-of-plane A_{1g} mode does not. This indicates an in-plane orientation of the type A excitonic wave functions within the 2D plane of the single-layer MoS_2.

CITATION TO PUBLISHED JOURNALS

Majority of Chapter 5 appears as:

Palleschi S., Mastrippolito D., Benassi P., Nardone M., and Ottaviano L. (2021). Micro-Raman investigation of p-type B doped Si(100) revisited. In: *Applied Surface Science* 561, *p.* 149691. [1],

Mastrippolito D., **Palleschi S.**, Tosti S., and Ottaviano L. (2021). Doping profiling of beveled Si wafers via UV-micro Raman spectroscopy. In: *Applied Surface Science* 567, *p.* 150824 [2].

Majority of Chapter 6 appears as:

Palleschi S., D'Olimpio G., Benassi P., Nardone M., Alfonsetti M., Moccia G., Renzelli M., Cacioppo O. A., Hichri A., Jaziri S., Politano A., Ottaviano L. (2020). On the role of nano-confined water at the 2D/SiO_2 interface in layer number engineering of exfoliated MoS_2 via thermal annealing. In: *2D Materials* 7.2, *p.* 025001 [3],

Mastrippolito D., **Palleschi S.**, D'Olimpio G., Politano A., Nardone M., Benassi P., and Ottaviano L. (2020). Exciton–phonon coupling and power dependent room temperature photoluminescence of sulphur vacancy doped MoS_2 via controlled thermal annealing.
In: *Nanoscale* 12 *(36), pp.* 18899–18907 [4].

INTRODUCTION

1

1.1 GENERAL MOTIVATIONS

Silicon (Si) is the most commonly used semiconductor for solid-state electronics. Semiconductors are fundamental because they allow switching between on and off states at room temperature, an operation achieved by diodes and transistors. The silicon-based metal-oxide-semiconductor field-effect transistor (MOSFET) is the ubiquitous active element in the standard fabrication technology called complementary MOS (CMOS) for the very large scale integration (VLSI) microchips used in computers, smartphones, digital cameras, and in the majority of current electronic devices [5]. Si is the most important semiconductor material for electronics, despite it cannot be considered the optimal semiconductor for the better electronic properties. There are several reasons for the predominance of Si. Si is one of the most abundant elements on Earth, where it is found in natural quartzite and elsewhere. The efficiency of the extraction, purification and crystallization processes make Si a frontrunner from an economic point of view. Although Si does not have very high carrier mobility, it was preferred over germanium at the beginning of electronics development in the 1950s and 1960s because it has a larger energy band gap, which allows better operation at higher temperatures, and because it has a higher melting point (1412 °C versus 937 °C) to withstand higher processing temperatures [6]. The moderate band gap of Si leads to a relatively low intrinsic concentration of free charge carriers, which has the advantage of low leakage current for better electronic device performance. There are not only physical advantages that have led to the widespread use of Si in recent decades, but also technological advantages. Si can be produced in high purity and in very large size. Doping of pure Si can be done with high accuracy and in a very wide concentration range, allowing different electrical properties for optimal device operation. Another technical aspect that has favored Si in the past is the fact that it is very easy to grow a very stable, high quality insulator on the Si surface, namely SiO_2, which has historically been the dielectric element in MOSFETs and is also used as an insulator and passivation layer for integrated circuits (ICs). Moreover, the enormous efforts made in the last decades to achieve ever better performance of the devices and the production process, as well as the high level of knowledge to optimize the various aspects of design and manufacturing, make it very difficult for other materials or technologies to compete with Si electronics today. In addition, continuous improvement in electronic products and emergence of new technologies such as Artificial Intelligence (AI) and Internet of Things (IoT) are leading to steady growth of the semiconductor market. The Covid-19 pandemic also seems to be playing an

unexpected role in the recent growth of Si chips demand [7].
According to the Semiconductor Application Forecaster (SAF) from International Data Corporation (IDC), global semiconductor revenue grew to USD 464 billion in 2020, 10.8% higher than 2019 revenue, and is expected to grow 17.3% in 2021 compared to 2020 [8, 9].
For these reasons, semiconductors research remains attractive and improvements in the physical and technological aspects of Si technology can be very enticing.
Especially for the fabrication of advanced ICs, which require extremely shallow regions with very high carrier concentration in the subsurface of the Si wafer, it is of utmost importance that doping is obtained with accurate knowledge and reliable control. Therefore, it is desirable for semiconductor manufacturing facilities (Fabs or factories) where the doping processes are performed to rely on an analytical method for characterising the doping concentration below the wafer surface that provides rapid feedback and is effective at the nanoscale.
Currently, there are a number of techniques that can be used to study the doping concentration of Si-based materials, but they have different drawbacks. Electrochemical capacitance voltage (ECV) [10] and four-point probe resistivity measurement [11] have very low spatial resolution. Spreading resistance profiling (SRP) [12] and secondary ion mass spectrometry (SIMS) [13] are effective at the nanoscale, but both are destructive. In particular, SRP and SIMS are capable of obtaining a depth profile of the doping concentration and are currently the standard techniques for this purpose. However, they require special sample preparation, precise control of environmental conditions, and equipment that is generally only accessible with a significant budget [14, 15]. SRP can probe a very large concentration range ($10^{12} \div 10^{21}$ cm^{-3}), but has limited lateral resolution (not less than 20 μm) [16–18]. SIMS provides an elemental dopant profile, whether or not the atoms of the dopant species are electrically active, and with high spatial resolution, but requires rather complex and expensive instrumentation as high-vacuum equipment [19–21].
On the other hand, the doping concentration in Si can be determined by a Raman spectroscopy technique, which we aim to develop in this study. Micro-Raman spectroscopy allows to study the material with a high lateral resolution in the order of micrometers and to probe the subsurface of the material at selected depths by using different excitation wavelengths due to their different optical penetration in the opaque Si. Laser excitations in the visible range can achieve depth resolutions in the micrometer range, while laser excitations in the near UV range can achieve depth resolutions in the nanometer range. This is ideal for very shallow doped regions used for the source/drain and source/drain-extension regions in MOSFETs within CMOS technology.
The technique we wish to investigate makes use of the analysis of the Fano interference effect in the Raman spectrum of doped Si, which, as

Cardona and co-workers showed in the 1970s, is known to be quantitatively related to the free carrier concentration in the semiconductor [22–24]. After the pioneering studies of Cardona and co-workers who investigated highly doped material (doping concentration $> 5 \times 10^{18}$ cm^{-3}), several works have focused on the study of a Raman analysis to characterise the doping concentration in Si-based material [14, 25–28]. However, no study has extended this approach to the study of intermediate and low doping concentrations and has verified the validity of the underlying physical concept in the case of UV excitation wavelengths to take advantage of the lower penetration depth of this light for a better spatial resolution of the analysis. With the advantages of modern spectral fitting analysis, it is now possible to evaluate the effects of doping on the Raman spectrum with unprecedented accuracy, not only at high doping concentrations, but also at intermediate concentrations ($10^{16} \div 10^{18}$ cm^{-3}), which require higher sensitivity. The high vertical resolution in the nanometer range and the high sensitivity to the doping concentration favor the use of a Raman-based technique not only to characterize the sub-surface doping content, but also to produce a doping depth profile. We believe this can be done using spectroscopic analysis in conjunction with the bevel method borrowed from the SRP technique, where a sample beveled at a small angle is used to probe the interior of the material by surface (on the bevel) measurements [29].

On the other hand, despite the continued increase in demand for microchips for electronics, some of the current research is focused on new technological solutions and strategies in the prospect of a feared standstill in performance improvement. Indeed, the potential progress in performance improvement predicted by Moore's Law appears to be close to the finish line. Moore's Law states that the number of transistors that can be packed into a given unit of an integrated circuit doubles about every 18 months [30, 31]. However, the race to shrink transistors, which has so far made it possible to keep up with Moore's law, seems to be reaching its physical limits (lateral dimensions < 10 nm) and also leads to further complications in device modeling [32].
Studies on 2D materials aim to continue this law and extend this limit of miniaturization to the atomic level [33]. Moreover, 2D crystals with atomic thickness represent a perfect playground for the exploration of physics at low dimensions, with the prospect of realizing novel devices based on entirely new physics and technology. With this perspective, the Institute of Electrical and Electronics Engineers (IEEE), one of the world's leading professional organizations for technological advancement, is supporting the creation of roadmaps for key players in the global microelectronics industry. In these International Roadmaps for Devices and Systems (IRDS), several International Focus Teams (IFTs) assess the current state and future evolution of the ecosystem, with each team focusing on a specific research area and creating 15-year action plans. The IFTs' 2017 reports, titled Emerging Research Material and

Beyond CMOS, identify in MoS_2 one of the most promising materials for technology development in the near future [33].
MoS_2 is a transition metal dichalcogenide that occurs naturally. It is an exfoliable material that can be obtained two-dimensionally down to a single layer less than one nanometer thick. There are several methods to obtain MoS_2 in the 2D phase. Top-down techniques start from layered bulk material to obtain progressively thinner samples. Examples of these techniques include mechanical exfoliation [34] and chemical liquid exfoliation [35]. Then there are bottom-up techniques such as chemical vapor deposition (CVD), where starting from the basic constituents of the material, molecular recognition leads to self-assembly of the elements to form structures of higher dimensions [36] . MoS_2 is a semiconductor and therefore complementary to the semimetal graphene [37]. It raises many expectations both in the context of the More Moore strategy, for which an extension of the functionalities of CMOS technology is envisaged through the hybrid integration of new technologies and materials, and in the context of the Beyond CMOS strategy, which proposes the creation of completely new information processing paradigms [33]. In this latter perspective, the special excitonic properties of MoS_2 attract for the development of novel excitonic devices that use excitonic states as a new computational state variable [38–40].
The electronic properties of MoS_2 are strongly dependent on the thickness of the material. Its peculiar electronic semiconductor structure, which depends on the number of layers and undergoes an indirect-direct band gap transition from the bulk to the monolayer phase, makes MoS_2 particularly interesting for optoelectronic applications [41–43]. In the ultrathin 2D phase, the enhancement of quantum confinement and the reduction of dielectric screening within the material lead to enhanced interactions between charged particles in the material and strong interaction with electric fields [44, 45]. For this reason surface modifications that introduce doping become particularly effective, leading to new optoelectronic effects and opening the prospect of powerful optoelectronic devices [46–50].
However, due to the novelty of this field, there is still much to be done for 2D materials such as MoS_2 and their experimental applications to be effectively used in electronic applications on a global scale. Further investigation of many physical and technological aspects is needed. In particular, the study of optical and electronic properties is useful for potential applications in optoelectronics. Therefore, it is crucial to search for efficient and reliable methods to study these properties and to control changes caused by structural defects, such as atomic vacancies, that often occur on the surfaces of 2D materials.
For this reason, in this work, besides the studies on Si, we also develop a technique based on Raman and PL spectroscopy together with annealing processes to study MoS_2 and to investigate some particular

optical and electronic properties of this material. We study the changes in the Raman and PL responses of MoS_2 and in the associated optoelectronic properties in dependence of a variation of the doping level in the material. We find that the doping level depends on the formation of structural defects such as sulphur vacancies on the surface of the 2D material. The concentration of sulphur vacancies can be altered by annealing processes. This mechanism can also be used to develop a method to reduce the number of layers of MoS_2 by thinning the sample flakes by partial sublimation.
The common feature of our research on Si and MoS_2 lies in the ability of using spectroscopic techniques to study the change effects in certain optical observables of materials that are ultimately caused by changes in the electronic density, i.e. the doping level, in the materials themselves. In the case of Si, this experimental evidence will be used to study the doping concentration in wafers for electronics, and in the case of MoS_2, to obtain information on optoelectronic properties and on structural, topological and morphological aspects of the material in order to increase the knowledge of this emerging material.

1.2 OBJECTIVES OF THIS THESIS

The objectives of this work can be outlined as follows:

To obtain a quantitative characterization of the doping state of crystalline Si by a clean, simple and fast Raman analysis. The non-invasive nature of a spectroscopic technique could make this a useful tool in foundries for product control and process monitoring, and also provide an in-line diagnostic tool for investigating dopant activation after dopant introduction;

To develop an efficient method for doping profiling in Si that is effective in terms of nanoscale spatial depth resolution and can compete with the more onerous techniques currently in use;

To study the optical and electronic properties of 2D MoS_2 through doping variations by Raman and PL spectroscopy. A deep understanding of the correlation between the optical properties and doping through photon-electron and phonon-electron interactions can be useful to investigate new physics as well as advance new technologies;

To use the variations in optical properties by spectroscopic analysis to monitor the sulphur vacancy concentration and doping level in 2D MoS_2;

To evaluate the feasibility of selective sublimation of MoS_2 layers by thermal treatments in order to achieve a novel exfoliation method of the material;

To investigate the dynamics, interplay and spatial orientation of different types of excitonic states in the MoS_2 monolayer accessible by resonant Raman and PL spectroscopy and whose population is modifiable by thermal treatments.

1.3 ORGANIZATION OF THIS THESIS

This work is organized as follows:

Chapter 2 introduces the materials studied in this work, namely Si and MoS_2, and gives an overview of the crystal structure, electronic band structure and phonon dispersion curves for both. In the latter case, special attention is paid to the excitonic states that characterize the optical properties of MoS_2 in the single-layer phase. The last section of this chapter is devoted to the basic theory of doping in semiconductors.

Chapter 3 provides the necessary theoretical basis of Raman scattering and PL emission. As for Raman scattering, the macroscopic and microscopic approaches are treated separately and a section is devoted to Raman scattering under resonant conditions. Concerning PL emission, we give a brief discussion of luminescence concepts, highlighting the various recombination mechanisms that can occur in a semiconductor due to band-to-band recombination as well as recombination involving carriers trapped in impurities and annihilation of excitons. A description of PL by excitons in terms of exciton-polariton emission is also given. The chapter concludes with a basic description of Raman-specific Fano interference effects in highly doped Si.

Chapter 4 introduces experimental and analytical methods by presenting the technical aspects and developments necessary for conducting experiments and analysing the data obtained. A detailed description of the spectrometer setups used in this work for Raman and PL spectroscopy is given, highlighting the main parts and functions of a spectrometer. This is followed by an overview of the material and methods used to study the doping concentration in Si. Then there is a description of the samples of differentially doped Si, followed by a detailed explanation of the method used to fit the recorded Raman spectra to evaluate the Fano effect detectable in the spectra. This is followed by an explanation of the methods used to obtain and analyse the Raman and PL spectra of MoS_2 in single and few-layer phases. At this point, the annealing procedures that were performed on MoS_2 samples to produce changes in the sulphur vacancy concentration in this material are reported. The chapter concludes with the presentation of a statistical model, called the three-level model, for describing the population density of two different types of excitonic states in MoS_2, which is useful for estimating the density of free electrons in single-layer flakes of MoS_2.

Chapter 5 describes a Raman spectroscopy-based doping characterization technique for monitoring the dopant content in p-type Si-based material. First, the need for doping characterization in semiconductor technology is outlined, current solutions are reported, and the Raman spectroscopy approach is proposed to achieve an alternative method with significant advances. Then, the technique is developed using extensively the considerations from the chapters 3 and 4. The experimental

Raman scattering data of optimally arranged sets of differently doped Si samples are analyzed and discussed in the framework of the Fano interference effect model. The method for interpreting the doping concentration is presented and its validity for measurements with excitation laser lines in the visible to near-UV range is demonstrated. Subsurface doping monitoring and doping profiling are demonstrated, and application to state-of-the-art nanoelectronic configurations is reported.

Chapter 6 contains a detailed study of single and few-layer MoS_2 samples using PL and resonant Raman spectroscopy in combination with optical and atomic force microscopy and annealing processes. The study represents an attempt to improve the understanding of the influence of structural defects in MoS_2 on the very interesting optical properties of the material, taking into account the doping change induced by the variation of the sulphur vacancy concentration. The morphological effects of annealing on the material are rationalized and a bottom thinning procedure is proposed. It is shown that the PL response of the MoS_2 monolayer correlates directly with the change in sulphur vacancy concentration and can be interpreted as a consequence of a change in doping concentration within the material. The variation of sulphur vacancy concentration and doping concentration are quantitatively evaluated using mathematical models. Some fundamental properties of the excitonic states are investigated by studying the phonon-exciton interaction using PL and resonant Raman analyzes, which provide direct evidence for exciton-phonon coupling in 2D MoS_2 and give insight into the spatial orientation of the excitonic wave function with respect to the plane of the MoS_2 monolayer.

Chapter 7 summarizes the results from the previous chapters and gives an outlook on the improvements of the proposed techniques.

2 RELEVANT PROPERTIES OF SILICON AND TWO-DIMENSIONAL MoS_2

In this chapter, we describe some fundamental properties of silicon (Si) and molybdenum disulfide (MoS_2) that are useful for understanding the experimental results presented in this thesis. We give an overview of the crystal structures, electronic band structures and phonon dispersion curves of Si and MoS_2, in the latter case with special reference to the excitonic states. Subsequently, the basic concepts of doping in semiconductors are presented with their fundamental physical background.

2.1 SILICON CRYSTAL STRUCTURE, ELECTRONIC ENERGY BANDS, PHONON DISPERSION CURVES

Si is a nonmetallic chemical element from carbon group 14 in the periodic table (also group IVa), it has atomic number 14 and atomic weight 28.086. Si is one of the most abundant elements in the Earth's crust after oxygen, 27.7 % of the crust is silicon. An atom of Si has an empirical atomic radius of 110 pm and the electronic configuration $1s^2 2s^2 2p^6 3s^2 3p^6$.

As a single crystal, e.g., obtained by slowly pulling a seed crystal from molten silicon (Czochralski process [51]), Si has the cubic crystal structure of diamond, space group denoted by O_h^7 ($Fd3m$ in international notation). An sp^3 hybridization of the $3s^2 3p^2$ shells of the Si atom is responsible for the tetrahedral arrangement of chemical bonds between a Si atom and its four nearest neighbors in the crystal lattice. The Bravais lattice of Si is a face-centered cubic (fcc) with a basis of two atoms in $(0,0,0)$ and $(1/4,1/4,1/4)\,a$, where a is the lattice constant ($a = 5.431$ Å). In other words, the unit cell of Si consists of two interpenetrating identical fcc Bravais lattices shifted along the cubic body diagonal by 1/4 of the diagonal length [52]. The unit cell of diamond structure of Si is illustrated in Figure 1 (a). The unit cell contains a total of 8 Si atoms, 8 at the corners 1/8 each in the cell, 6 atoms in the faces 1/2 each in the cell, 4 atoms inside the cell.

Considering the Si element weight of 28 atomic mass units ($amu \simeq 1.66 \times 10^{-24}\,g$) and the lattice constant of 5.43 Å, the mass density of Si crystal results 2.33 g cm^{-3}. The inter-atomic spacing between atoms in a primitive cell is 2.34 Å, the number density of atoms is $5 \times 10^{22}\,cm^{-3}$ [53].

The reciprocal lattice of Si can be described by its primitive cell. It can be shown that the reciprocal lattice of a direct fcc lattice is a body-centered cubic (bcc) lattice with lattice constant $4\pi/a$, where a is the direct lattice constant. Constructed as a Wigner-Seitz cell, the truncated octahedron within the cube in Figure 1 (b) represents the primitive cell of the reciprocal lattice of diamond and zinc-blende structures, and

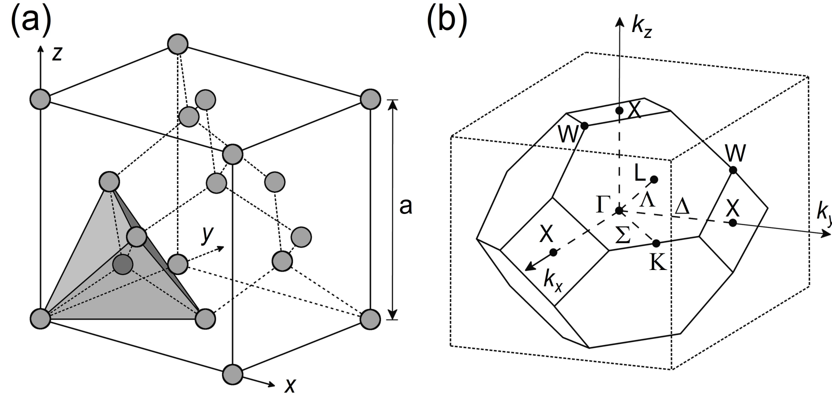

Figure 1. (a) Crystallographic unit cell of diamond structure, the shaded area shows a primitive cell. Adapted from [54]. (b) Wigner-Seitz cell of the reciprocal lattice of an fcc crystal as diamond and zinc-blende, known as the first Brillouin Zone. High-symmetry points and directions are given in the usual notations. Adapted from [55].

hence of Si, and is referred to as the first Brillouin Zone (BZ) [55]. The labels Γ, L, X, W, K denote the points of high symmetry of the BZ, while Δ, Λ, Σ denote the direction of high symmetry $\langle 100\rangle$, $\langle 111\rangle$, $\langle 110\rangle$ connecting the center Γ with the edge of the BZ. In table 2.1 we report some specifications of the BZ high-symmetry points and directions.

Table 2.1. Specifications of high-symmetry points and directions of the first Brillouin Zone of fcc, diamond, and zinc-blende lattices. From [55].

point	degeneracy	direction
Γ, $(0,0,0)$	1	
X, $2\pi/a(\pm1,0,0)$, $2\pi/a(0,\pm1,0)$, $2\pi/a(0,0,\pm1)$	6	Δ, $\langle 100\rangle$
L, $2\pi/a(\pm1/2,\pm1/2,\pm1/2)$	8	Λ, $\langle 111\rangle$
K, $2\pi/a(\pm3/4,\pm3/4,0)$, $2\pi/a(0,\pm3/4,\pm3/4)$, $2\pi/a(\pm3/4,0,\pm3/4)$	12	Σ, $\langle 110\rangle$

The band structure of Si can be determined by pseudopotential methods [56, 57], the results are shown in Figure 2 (a). The labels in Figure 2 (a) are derived from the group theory notation of the indirect representations of the space group of the crystal. The electronic states are affected by the crystal potential with its invariance properties, therefore the electronic wave functions reflect the crystal symmetries. Consequently, the electronic states and energy levels can be classified according to the irreducible representations of the point group of the wave vector [58, 59].

The upper valence bands and the lower conduction bands are generated by the bonding and anti-bonding combinations of s_x, p_x, p_y, p_z, atomic orbitals [60]. While the maximum of the valence band (VB) is located at $\boldsymbol{k} \simeq 0$ (point Γ), the minimum of the conduction band (CB) is located along the direction [100] (Δ) at a point very close to the edge X of the BZ, making Si a semiconductor with an indirect band gap. The indirect energy gap (E_g) is slightly temperature dependent and approaches 1.17 eV at $T = 0\,\mathrm{K}$ and 1.12 eV at room temperature [55, 60].

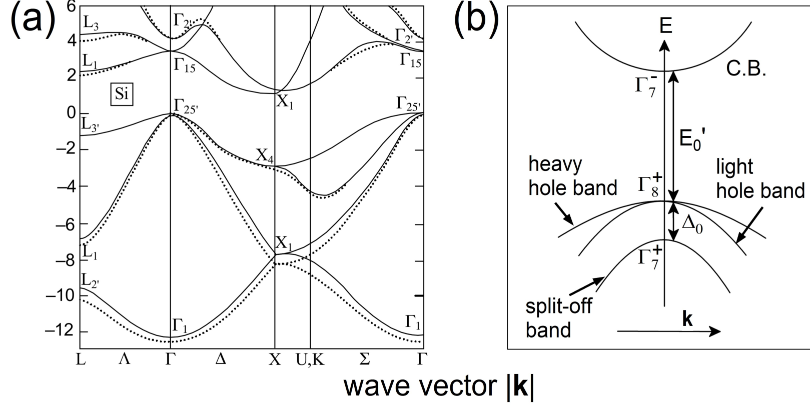

Figure 2. (a) Electronic band structures of Si obtained by a nonlocal pseudopotential method (solid line) and a local pseudopotential method (dotted line) [56]. Adapted from [61]. (b) Schematic representation of the electronic band structure of a cubic semiconductor, detailed at the central direct transition at $\boldsymbol{k} \simeq 0$ and including the spin-orbit splitting effect. Adapted from [60].

The top of the valence bands at $\Gamma_{25'}$ are very important because, under thermodynamic equilibrium, they host most of the free holes. In $\Gamma_{25'}$ the valence bands arise from the bonding combinations of the p_x, p_y, p_z, orbitals and are sixfold degenerate [60]. In reality, the degeneracy is broken by the spin-orbit interaction, leading to a splitting of the upper valence bands into $p_{3/2}$- and $p_{1/2}$-bands. In Figure 2 (b) we show a schematic representation of the electronic bands in which the splitting effect due to spin-orbit interaction has been taken into account. The $p_{3/2}$-bands form the heavy-hole band and the light-hole band, which are fourfold degenerate at $\boldsymbol{k} \simeq 0$ (Γ_8^+ in Figure 2 (b)). The $p_{1/2}$ bands, called split-off bands, are twofold degenerate (Γ_7^+ in Figure 2 (b)). The spin-orbit separation at $\boldsymbol{k} \simeq 0$ is $\Delta_0 = 0.044\,eV$ [23]. The values of the effective masses of heavy hole, light hole and split-off hole, averaged over all possible $\boldsymbol{k}$ directions, are 0.54, 0.15, 0.23 respectively in units of free electron mass [58].
Now we present some qualitative features of the phonon dispersion curves in the Si crystal. The dispersion curves of phonons in Si, which are experimentally measurable by neutron scattering spectroscopy [62–

64] or infrared absorption [65, 66], can be plotted as a function of phonon momentum along high symmetry directions in the first BZ (see Figure 3). As can be seen for any crystal with two atoms per primitive cell, the phonon dispersion curves consist of six branches, three for the acoustic modes and three for the optical modes. In Figure 3 the acoustic branches lie on the lower energy part of the plot.

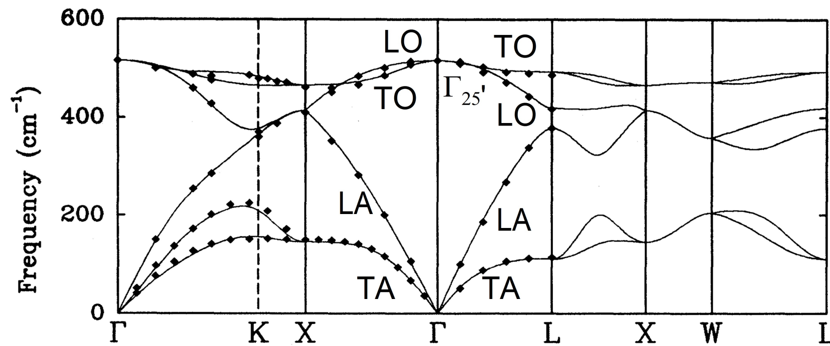

Figure 3. Phonon dispersion curves for silicon. The continuous curves are calculated from [67], the points are experimental data from [62]. Adapted from [67].

A complessive motion of atoms, as occurs in a phonon mode, is characterized by a displacement of atoms in real space and a wave vector $\boldsymbol{k}$ in reciprocal space. The displacement of atoms of a phonon mode with wave vector along a high symmetry direction of the first BZ can be either parallel or perpendicular to the wave vector direction and is consequently classified as transverse or longitudinal. It can be shown that both the displacement of the atoms and the wave vector of the mode depend on the symmetry properties of the crystal. It follows that phonons with wave vector $\boldsymbol{k}$ is indistinguishable to those with wave vector $\boldsymbol{q} + \boldsymbol{G}$, where $\boldsymbol{G}$ is a reciprocal lattice vector. The symmetry operations transforming $\boldsymbol{k}$ into equivalent vectors $\boldsymbol{q} + \boldsymbol{G}$ belong to the group of symmetry of $\boldsymbol{k}$ (group of the wave vector) [58]. The phonon modes at any point $\boldsymbol{k}$ in reciprocal space can be classified according to the irreducible representations of the symmetry group of $\boldsymbol{k}$ at that particular $\boldsymbol{k}$.
Phonons with $\boldsymbol{k}$ near the center of the BZ have a relatively long wavelength and involve atoms that are dislocated in various contiguous unit cells. Focusing on a primitive cell invested by a phonon mode, one can show that the two basis atoms move in phase in the case of an acoustic phonon or out of phase in the case of an optical phonon. Considering in particular the optical phonons of symmetry $\Gamma_{25'}$ at $\boldsymbol{k} \simeq 0$, which are of specific interest in first-order Raman spectroscopy of Si [68], the TO and LO branches are degenerate in diamond-type crystal [58]. Thus, it is possible to observe in the Raman spectra of Si the one-phonon Raman

scattering signal originating either from all three degenerate optical phonons or only from those of a particular symmetry (LO or TO), depending on the particular geometrical and polarization configurations adopted in the light scattering experiment.

2.2 MOS_2: A TRANSITION METAL DICHALCOGENIDE

The special electronic properties of graphene [34, 69, 70], such as its very high carrier mobility with a reported value of $\sim 15\,000\,\mathrm{cm^2V^{-1}\,sec^{-1}}$ at 300 K [71], have also attracted the interest of researchers in other two-dimensional inorganic materials (2D). Since the semimetal property of graphene limits its application in nanoelectronic devices [72], special efforts have been directed towards $2D$ materials with semiconductor properties.
Many $2D$ materials appear in the bulk as a structure of stucked layers (monolayer units) held together by relatively weak van der Waals (vdW) interactions. Each monolayer unit has a independent crystal structure in which the atoms are strongly bonded together by predominantly covalent bonds. A monolayer unit can be constituted by a single atomic layer (like in graphene), or several atomic layers strongly bonded together (like in MoS_2).
Due to the weak vdW interactions between the monolayers and the independent strongly bonded structure of the monolayer unit, single or few monolayers can be isolated from the bulk crystal using top-down techniques such as mechanical exfoliation [34], electrochemical exfoliation with lithium intercalation [73], chemical liquid exfoliation [35, 74]. Recently, a thorough review on the mechanical exfoliation with an accurate determination of the number of layers of 2D MoS_2 samples [75] was presented. In addition, 2D crystals can also be obtained by bottom-up methods such as hydrothermal synthesis [76, 77], wet chemical synthesis [78], molecular beam epitaxy [79], chemical vapour deposition (CVD) [36, 80], etc.
An example of this class of materials are transition metal dichalcogenides (TMDCs). TMDCs in the 2D phase have attracted considerable attention because of their diverse properties and natural occurrence. There are more than 40 layered compounds in the TMDC class of materials, all of which have the same chemical formula MX_2, where M is a transition metal from groups 4 to 10 (Ti, Zr, Hf, Mo, W, Rc, Pd, etc.) and X represents the chalcogen atoms (S, Se, or Te) [81, 82]. Bulk TMDs have different electronic properties, e.g. HfS_2 is an insulator, MoS_2 and WS_2 are semiconductors, WTe_2 and $TiSe_2$ are semimetals, NbS_2 and VSe_2 are real metals [82, 83]. Indeed, TMDCs have long been known in materials science and engineering and have led to important industrial applications as solid lubricants and surface protectants[81, 84–88]. An important reason for the considerable recent attention paid to TMDs in the $2D$ phase is their layer-dependent electronic properties and sizable

Figure 4. Molybdenite on quartz, from the Molly Hill mine, Quebec, Canada. (author: John Chapman. 🄯 CC BY-SA 3.0, from [96])

band gaps around $1-2$ eV [81, 84], which makes them particularly promising for the development of field-effect transistors (FETs) or as light-absorbing materials in new-generation alternative optoelectronic devices [89].

In particular, molybdenum disulfide (MoS_2) [90] has attracted much interest because of its unique physical, optical, and electronic properties [91–95].

Molybdenum is a transition metal from group 6 and period 5 of the periodic table, its atomic number is 42, its electronic configuration is $[Kr]4d^5 5s^1$, its Russell-Saunders term symbol is $^7S_3$, its ionisation potential is of 7.13 eV. Sulphur is a chemical element from group 16 (chalcogens) and period 3 of the periodic table, its atomic number is 16, its electronic configuration is $[Ne]3s^2 3p^4$, so it has six valence electrons, its Russell-Saunders term symbol is $^3P_2$, its ionisation potential is 10.36 eV. In MoS_2, the Mo atom has oxidation state $+4$, the S atom has oxidation state -2.

Molybdenum disulfide (MoS_2) is an inorganic compound found in nature in the form of the mineral *molybdenite* (see Figure 4). Its appearance and properties are very similar to those of graphite. It is easily cleaved basally, leaving a dark green mark [96], like graphite on paper.

With its layered structure, molybdenite has long been used as a lubricant. As an insubstantial powder, it is a dry lubricant, but can also be used as an additive in oil or grease [97, 98]. It is also widely used as a catalyst in the desulfurization process [99] and in various applications such as hydrogen storage [100], in electrical capacitors [101] and as a

cathode in lithium batteries [102].
In the bulk phase, Molybdenum Disulfide is a semiconductor with an indirect bandgap of ($\sim 1.3\,eV$) [103]. However, this property gradually changes as the number of layers decreases, so that the single layer of MoS_2 can be considered a semiconductor with a direct bandgap [94, 104]. The value of the direct bandgap remains controversial. Early work reported a value of $\sim 1.8\,eV$ [94] but more recent theoretical work reports higher values $(2.1 \div 2.8)\,eV$ [105–109]. In any case, these properties make MoS_2 particularly interesting because it is optically active in the visible spectrum [89].

2.2.1 *MoS_2 lattice structure*

In the bulk phase, MoS_2 consists of planar structures arranged one above the other to form a layered material. Each planar structure in turn consists of three layers, with one layer of Mo atoms sandwiched between two layers of S atoms [110–112]. Each three-layered structure forming a MoS_2 layer is connected to the others by relatively weak van der Waals interactions, with a binding energy of $\sim 20\,meV/\mathring{A}^2$ [113, 114]. Within each layer, the atoms of the metal Mo and those of the chalcogen S are bound together by strong covalent bonds [82].
Considering the fundamentals of sphere packing, the most usual structure of MoS_2 consists of two pairs of adjacent close-packed layers represented by the sphere packing sequence AbA BaB, the close-packed layers A and B consist of sulphur, the interstitial layers *b* or *a* are of molybdenum [115, p. 125].
In both sandwiches, AbA and BaB, the interstice Mo atom displays a trigonal prismatic coordination. This structure is known as 2H phase, where the numeral indicates the number of sandwiches per unit cell along an axis orthogonal to the layers, H stands for hexagonal and refers to the crystal symmetry (see Figure 5 (a)).
A less common polytype of MoS_2 known as the 3R phase is characterized by a rhombohedral crystal symmetry with a unit cell consisting of three stacked S-Mo-S sandwiches with an AbA BcB CaC stacking sequence in which the S atoms occupy the place of the close-packed atoms and the Mo atoms occupy the place of the interstices. In each sandwich, the metal atom displays a trigonal prismatic coordination, as in the previous case of 2H (see Figure 5 (b)).
Moreover, it was observed in [116] that the MoS_2 nanosheets prepared by chemical Li intercalation do not belong to the polytypes 2H or 3R, but to a different polytype 1T (see 5 (c)). This structure can be represented by the AcB sphere-packing sequence, in which the interstice Mo atom exhibits an octahedral coordination. In the 1T structure, there is only one S-Mo-S layer per unit cell and the overall crystal is characterized by trigonal symmetry.

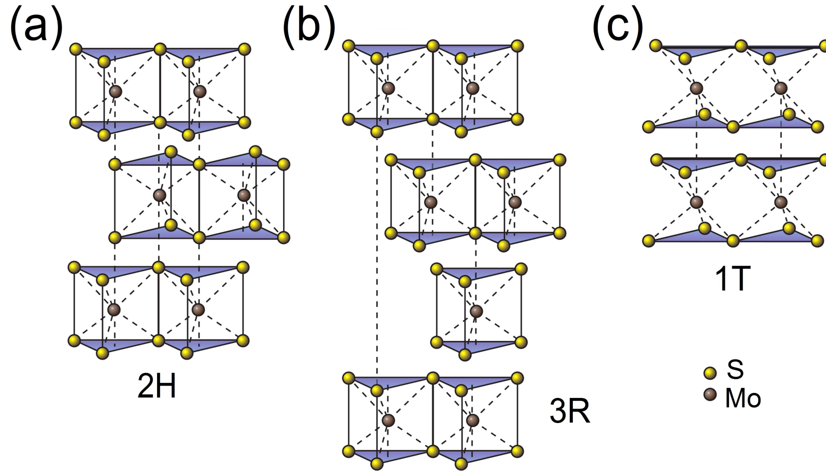

Figure 5. Crystal structures of MoS_2 polytypes. (a) Hexagonal crystal symmetry, two S-Mo-S layers per unit cell, trigonal prismatic Mo atom coordination. (b) rhombohedral crystal symmetry, three S-Mo-S layers per unit cell, trigonal prismatic Mo atom coordination. (c) trigonal crystal symmetry (1T-MoS_2), one S-Mo-S layer per unit cell, octahedral Mo atom coordination. Adapted from [89].

The trigonal 1T polytype is not stable, and it has been observed to revert to the original 2H phase apon both annealing at moderate temperature (≈200 °C) and aging at lower temperatures for several weeks. [117–119]. The more common 2H-MoS_2 structure is symbolized by the space group type $P6_3/m\,m\,c$ in the notation of Hermann-Mauguin (point group D6h), therefore MoS_2 is a centrosymmetric crystal [120–122].
The primitive unit cell of 2H-MoS_2 is shown in Figure 6, it contains 6 atoms, 4 atoms of S and 2 atoms of Mo. The lattice parameters of the primitive unit cell are $a = b = 3.15$ Å and $c = 12.3$ Å. [120].
The polytype 3R-MoS_2 has a crystal structure belonging to the trigonal space-group type $R3m$, with a rhombohedral unit cell with $a = b = 3.15$ Å and $c = 18.33$ Å [123]. The 1T-MoS_2 structure belongs to the trigonal space-group type $P3$ [124] with a primitive unit cell and a threefold rotational axis in the $\vec{c}$ direction.
As can be seen from the previous arguments, a single layer (monolayer) of MoS_2 has only two possible structures: from 2H and 3R bulk materials we can obtain a trigonal prismatic monolayer, symbolized as 1H-MoS_2, or else from a 1T bulk material we can obtain an octahedral monolayer, symbolized as 1T-MoS_2. These different phases can be identified by high-resolution scanning transmission electron microscopy (STEM), as shown in [125]. In the case of the monolayer, the symmetry of the inversion with respect to a centre is missing, so the monolayer is not centrosymmetric and the space group to which it belongs is $P6m2$ (point group D3h) [122].

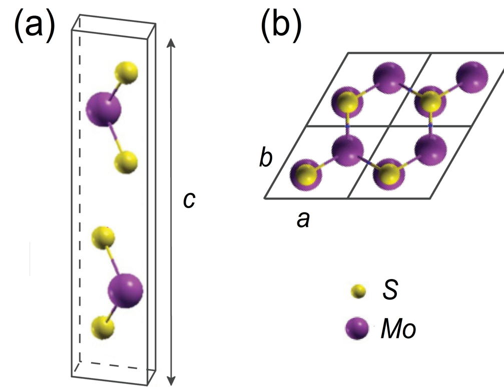

Figure 6. (a) Primitive Unit Cell $(P6_3/mmc)$ of 2H-MoS_2. The bulk unit cell contains 2 Mo atoms and 4 S atoms. Each of the Mo atoms is coordinated to 6 S atoms in a trigonal prismatic coordination. The primitive vectors are $\boldsymbol{a} = (a, 0, 0), \boldsymbol{b} = (a/2, \sqrt{3}a/2, 0), and \boldsymbol{c} = (0, 0, c)$. $a = b = 3.15$ Å, $c = 12.3$ Å. (b) Top view of 2×2 unit cells of MoS_2. Adapted from [122].

2.2.2 *electronic band structure and excitons in MoS_2*

Theoretical and experimental studies showed a strong dependence of the semiconducting electronic structures of MoS_2 nanosheets on their layer number [94, 104, 106, 126, 127]. A gradual transition from the indirect bandgap of the bulk crystal to a direct bandgap of the mono-layer sample has been demonstrated, which makes the single layer phase particularly interesting for optoelectronic applications [92, 94, 95, 104, 128, 129].
Figure 7 (a) shows the band structures of MoS_2 samples representative of bulk, four-layer, bilayer and monolayer flakes of MoS_2 in their evolution from indirect to direct bandgap semiconductors [104]. In Figure 7 (b) we show the first Brillouin zone of MoS_2, which highlights the high-symmetry points and directions of the reciprocal lattice of MoS_2 [130]. As can be seen from the Figure 7 (a), in case of bulk MoS_2, the top of the VB is located at Γ point (centre of BZ), the bottom of the CB is located in the middle of the high-symmetry direction connecting Γ and K; this point is sometimes referred to as Λ [94, 104]. Otherwise, in case of monolayer, both the top of the VB and the bottom of the CB are at K point.
Moving from bulk to thinner and thinner sheet of material up to the single layer of MoS_2, one observes a progressive increase in the indirect bandgap, with the bottom of the CB at Λ rising slightly and the top of the VB at Γ decreasing sharply (see Figure 7 (a)). The variation is such that in the extreme case of monolayer, the indirect bandgap is larger than the direct bandgap at K, which, on the other hand, shows no significant changes as the number of layers of the material varies

[94, 104, 131, 132].
The reason for the different behaviour of the K and Γ points as a function of the number of layers lies in the different nature of the electronic states that form the bands at these points. The top of the VB at K consists of electronic states formed by the *d* orbitals of the Mo atom. These orbitals are only slightly affected by the interlayer interactions because they are strongly localized in the midplane of the S-Mo-S layer, so that their energy level does not depend on the crystal thickness [104, 106, 127, 133]. On the other hand, the VB at the Γ point arises from the hybridization of *d* orbitals of the Mo atom and p_z orbitals of the S atom, which in this case are influenced by the interaction between the layers, hence the dependence on the layer number [104].
Two thin peaks labeled A and B at about 1.8 eV and 2.0 eV in the absorption spectrum of bulk MoS_2 reveal the presence of two excitonic transitions associated with direct optical transitions between band edges at the K point in the BZ [112, 134]. Similar observations have also been made for other TMDCs [105, 135, 136].
Excitonic states can be viewed as quasiparticles consisting of an excited electron and a hole bound by a Coulomb force, making the system resemble a hydrogen-like atom. For few-layer nanosheets of MoS_2, the absorption spectrum resembles that of bulk, except for small deviations in the energies of the A and B peaks [94]. For a monolayer undoped sample of MoS_2, the authors of [47] give 1.92 eV and 2.08 eV for A and B absorption peaks, respectively. The absorption spectrum of a monolayer sample of MoS_2 is shown in Figure 7 (c) [47].
The separation between peaks A and B is due to the spin-orbit splitting of the valence bands at the K point in Brillouin zone. The absorption peaks A and B correspond to the $K_4 \to K_5$ and $K_1 \to K_5$ transitions, respectively, where K_4 and K_1 denote the initial states at the top of the split valence bands and K_5 denotes the final state at the direct optical band gap at the K point [112] (see Figure 8).
The energy splitting of the valence band at K of about 0.30 eV is reflected in the different location of peaks A and B, although the distance between the peaks of about 160 meV does not exactly correspond to the valence band splitting because of the different binding energy of excitons A and B [112].

Photoluminescence (PL) and photocurrent experiments also reveal the presence of optical transitions that can be associated with excitons A and B in both bulk and thin films of MoS_2. [94, 104, 107, 112].
Normally, the binding energy of excitons in direct bandgap semiconductors has values on the order of a few units or a few tens of meV (see, e.g., Table 6.4 in [58, page 272]). The confinement effect and the concomitant reduction in the dielectric screening that occurs in very thin materials such as nanosheets of MoS_2 results in a much higher binding energy for the excitons that can be populated in these materials.

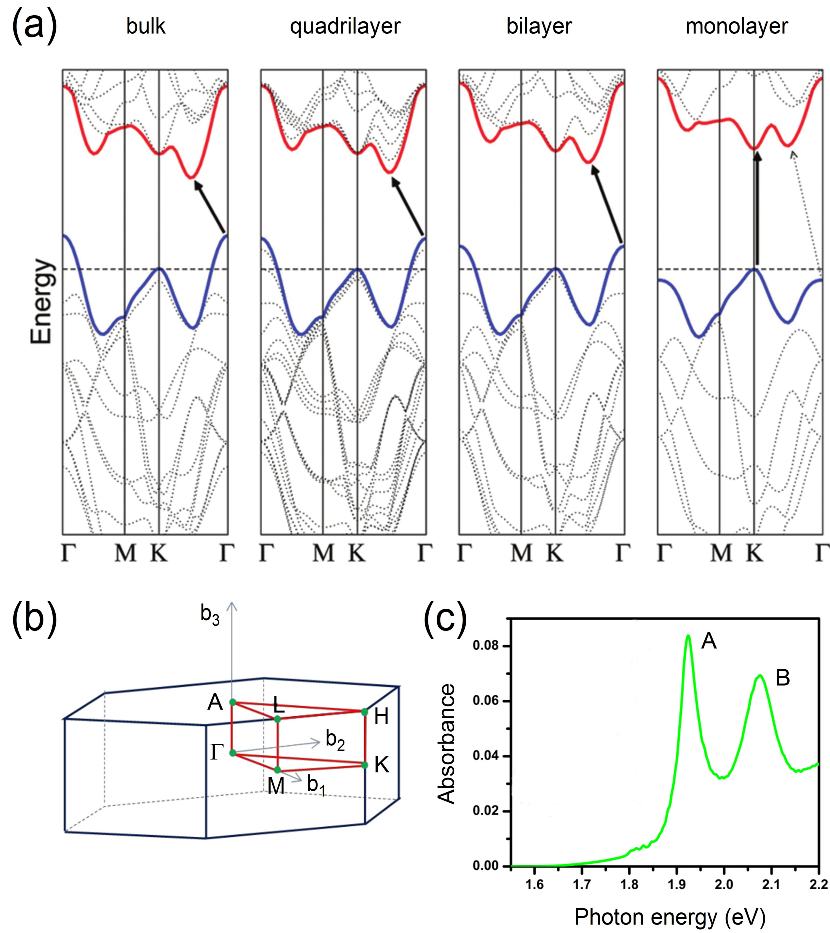

Figure 7. (a) Evolution of the electronic band structure of MoS_2, from left to right: bulk, quadrilayer, bilayer, monolayer. The solid arrows indicate an indirect-to-direct bandgap transition at monolayer. Adapted from [104]. (b) First Brillouin zone of MoS_2 highlighting the high-symmetry points and directions. (c) Absorption spectrum of a monolayer MoS_2, the two peaks A and B are assigned to exciton states at point K of the Brillouin zone. Adapted from [47].

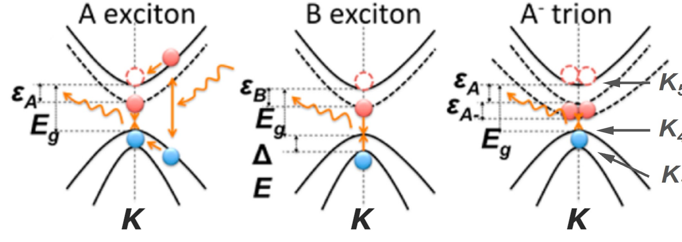

Figure 8. Schematic representation of the energy configuration at K point in the Brillouin zone of MoS_2 showing the radiative transitions of the exciton A^0 (A in the figure), the exciton B, and the charged exciton (trion) A^- . E_g denotes the band gap, Δ the spin-orbit splitting of the valence bands. ε_A, ε_B and ε_{Ameno} denote the binding energies of A^0 , B and A^- , respectively. K_1, K_4, K_5 denote the states at the top of the split valence bands and the bottom of the conduction band. Adapted from [45].

In [107], the authors obtain a binding energy of $\sim$ 570 meV for exciton A for a MoS_2 single layer suspended in air. In [137], considering a model where one surface of the single-layer MoS_2 is in vacuum and the other on a SiO_2 substrate, binding energies of 455 meV and 465 meV are calculated for excitons A and B, respectively. Monolayer MoS_2 grown on HOPG is shown to have a band gap of 2.15 or 2.35 eV depending on the experimental measurement conditions, and the measured PL peak corresponding to the A exciton is at 1.93 eV (obtained at temperature 79 K), which then gives binding energy values of 220 or 420 meV [138–140].

In [141], the authors calculated the Bohr radius of the A exciton (distance between electron and hole) for MoS_2 to be about 1 nm, which is three times the unit cell dimension ($a = 3.16$ Å).

Moreover, in [141] the authors theoretically predict the existence of other excitonic states besides A and B, found in absorption at energies between 2 and 2.8 eV, whose peaks merge into a much broader band due to electron-phonon interaction. Between these states, a series of excitonic states should form the excitonic C peak at about $2.5 - 2.6$ eV. The exciton C is expected to arise from direct transitions between the top of the valence band and the bottom of the first three conduction bands near the Γ point in the BZ [141].

In addition to bare excitons, which are electrically neutral (have no charge) because they consist of one electron and one hole, there can also be charged excitons, which are positive if they consist of two holes and one electron, and negative if they consist of two electrons and one hole [142–144].

In [47] Mak et al. demonstrate by absorption and photoluminescence spectroscopy the presence of negative excitons, so-called *trions*, in the MoS_2 single layer, which can be populated by optical excitation. The

trion is formed by an energetically favourable transition through the capture of an additional electron to an exciton (e.g. $e^{-} + A^{0} \rightarrow A^{-}$). Normally, trions can be observed in most common two-dimensional semiconductors, but at temperatures far below room temperature. In the case of the MoS_2 monolayer, however, the trions can be detected even at room temperature due to their relatively high binding energy ($\sim 20 - 30$ meV relative to the neutral exciton) [45, 47, 144, 145].
A schematic representation of the electronic configuration of the excitons and trions formed at the K point of the BZ in MoS2 can be derived from Figure 8 [45]. This formation mechanism shows us how a possible excess of negative charge can favour the formation of trions A^{-} at the expense of neutral excitons A^{0} [146, 147]. Thus, one element that indirectly affects the relative fraction of excitable trions and excitons in a monolayer MoS_2 sample is the electron charge density in the material (n_{el}).
In particular, the presence of the trions A^{-} has been demonstrated by the observation and analysis of the photoluminescence peak attributed to exciton A. In fact, the photoluminescence peak A is due to the overlap of two peaks, designated A^{-} and A^{0} , which are due to the radiative recombination of negative trions and neutral excitons, respectively [45, 47, 49, 148].
Another interesting aspect related to excitons in MoS_2 and other TMDCs is their unique valley polarisation properties. In the case of the single MoS_2 layer, the breaking of spatial inversion symmetry leads to important polarisation and selection rules for the spin and momentum of the electrons and holes forming excitons A and B, which can be used advantageously in valleytronics [149–152]. In valleytronics, the confinement of charge or spin carriers in selected extremes (*valleys*) of electronic bands, known as valley polarisation, is used to develop a new class of devices [149]. In the case of monolayer MoS_2, the two extremes of the K valence bands split by the spin-orbit effect are spin-polarised due to the noncentrosymmetry of the single layer. Moreover, the spin polarisation is reversed due to the time reversal symmetry in the K and K points (-K is usually denoted as K') of the Brillouin zone. Thus, the spin property is coupled with the crystalline moment K or K'. Appropriately polarised optical excitation allows a selective population of excitons, e.g. of type A at K or K'; de-excitation processes, which are governed by the same section rules as excitation processes, allow light emissions with the same polarisation as the incident light, thus enabling optical addressability of the excitonic valley properties [149, 153, 154].

2.2.3 *Phonon properties in MoS_2*

A complete treatment of lattice dynamics in TMDCs can be obtained from group theory [155–160]. In the case of 2H-MoS_2, the primitive

unit cell contains six atoms, four sulphur atoms, and two molybdenum atoms (see Figure 6 (a)). The presence of six atoms in the primitive unit cell would result in 18 vibrational normal modes, three of which are acoustic and the remaining 15 optical, but because of the lateral degeneracy of some of them there are only 12 distinct optical phonon branches plus three acoustic [161]. At the high-symmetry point Γ of the Brillouin zone shown in Figure 7 (b), the symmetries of the phonon modes in the case of bulk MoS_2 can be assigned to the irreducible representations of the group D6h [161]:

$$\Gamma_{bulk} \equiv A_{1g} \otimes 2A_{2u} \otimes 2B_{2g} \otimes B_{1u} \otimes E_{1g} \otimes 2E_{1u} \otimes 2E_{2g} \otimes E_{2u}.$$

Here we can distinguish three acoustic vibrations of symmetry A_{2u} and E_{1u}; then there are four Raman-active optical modes (E^1_{2g}, E^2_{2g}, E_{1g}, and A_{1g}); two infra red (IR) active optical modes (A_{2u} and E_{1u}); finally, there are four optically inactive (silent) modes (B_{1u}, E_{2u}, and $2B_{2g}$) [157, 161]. In the case of the single layer of MoS_2, the spatial inversion symmetry of the bulk is lost, the symmetry of the point group is reduced from D_{6h} to D_{3h}, there are three atoms in the primitive cell and thus nine phonon modes at the Γ point, six optical and three acoustic phonon branches. [122]. The nomenclature of the phonon branches at the point Γ changes according to the irreducible representations of the group D_{3h} [119]:

$$\Gamma_{monolayer} \equiv 2A''_2 \otimes A'_1 \otimes 2E' \otimes E''.$$

Here the acustic modes are of symmetry A''_2 and E', there is an IR-active mode of symmetry E', and three Raman-active modes (A'_1, E'' and E'). However, the two main Raman-active optical phonons observed in the most common experimental setups (back-scattering configuration) and belonging to the A'_1 and E' representations are often associated with the A_{1g} and E^1_{2g} bulk modes, respectively [119].

Figure 9 (b) [122] shows the phonon dispersion curves and densities of states (DOS) of MoS_2 in the single layer and bulk phases. In support, *TABLE II* in Figure 10, taken from the work of Molina-Sánchez et al. [122] provides a summary of the atomic displacement properties and frequencies of the phonon modes at Γ point in the BZ.

For the purposes of this thesis, it is useful to focus on the four Raman-active phonon modes that occur at the frequencies [158]:

$$\begin{aligned} \omega(E^2_{2g}) = 32cm^{-1}, \quad \omega(E_{1g}) = 287cm^{-1}, \\ \omega(E^1_{2g}) = 383cm^{-1}, \quad \omega(A_{1g}) = 409cm^{-1}. \end{aligned} \tag{2.1}$$

The modes E_{1g}, E^1_{2g} and A_{1g} are due to atomic vibrations within the single S-Mo-S layer of MoS_2. In contrast, the mode E^2_{2g} is due to rigid vibrations of the neighbouring layers in the stack forming the material.

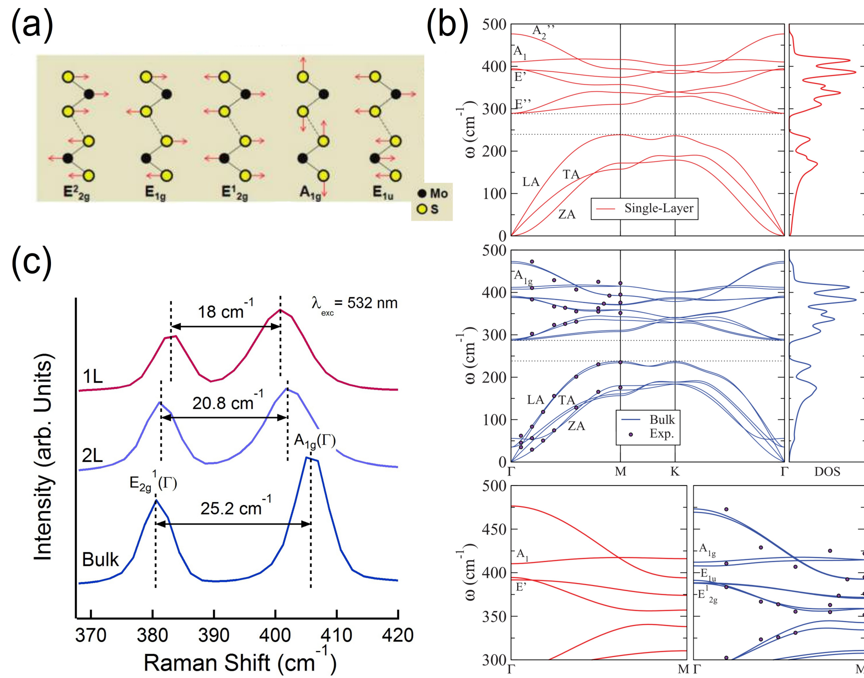

Figure 9. (a) Mo and S atoms displacements involved in the Raman-active (E^2_{2g}, E_{1g}, E^1_{2g}, A_{1g}) and IR -active (E_{1u}) phonon modes. Adapted from [46]. (b) Phonon dispersion branches of MoS_2 in single layer and bulk phases. The corresponding densities of states are indicated on the right side of the branches. The bottom panels show magnified branches near the E^1_{2g} and A_{1g} modes. (c) Stokes Raman spectra of the monolayer (1L), bilayer (2L), and bulk of MoS_2 recorded at an excitation wavelength of 532 nm. The frequency difference between the peaks is indicated, showing the dependence on thickness.

D_{3h}	D_{6h}	Character	Direction	Atoms	ω_{MoS_2} (cm^{-1})	
A_2	A_{2u}	Acoustic	Out of plane	Mo + S	0.0	0.0
	B_{2g}^2	Inactive	Out of plane	Mo + S	–	55.7
–	E_{2g}^2	Raman	In plane	Mo + S	–	35.2
A_1	A_{1g}	Raman	Out of plane	S	410.3	412.0
	B_{1u}	Inactive	Out of plane	S		407.8
A_2''	A_{2u}	Infrared ($\boldsymbol{E}\|\|\boldsymbol{c}$)	Out of plane	Mo + S	476.0	469.4
	B_{2g}^1	Inactive	Out of plane	Mo + S		473.2
E'	E_{2g}^1	Raman	In plane	Mo + S	391.7	387.8
	E_{1u}	Infrared ($\boldsymbol{E}\perp\boldsymbol{c}$)	In plane	Mo + S		391.2
E''	E_{1g}	Raman	In plane	S	289.2	288.7
	E_{2u}	Inactive	In plane	S		287.1

Figure 10. Lattice vibration of 2H:MoS_2 at Γ in the Brillouin zone. The long-wavelength phonon modes are classified according to the irreducible representation of the point groups D_{3h} and D_{6h} for monolayer and bulk MoS_2, respectively. The vibrational direction of the atoms is in-plane (out-of-plane) if it is perpendicular (parallel) to the primitive unit cell vector $\boldsymbol{c}$. Taken from [122].

Figure 9 (a) [46] shows a schematic representation of the atomic displacements and vibrational directions occurring in the Raman-active and IR -active (E_{1u}) phonon modes.
Theoretical calculations on TMDCs predict that phonon mode frequencies differ from bulk to monolayers [159]. Indeed, using Raman spectroscopy, it has been experimentally observed that the frequency of the phonons E_{2g}^1 and A_{1g} varies with the number of layers of MoS_2 nanosheets [46, 122, 162, 163]. In particular, it was observed that the Raman peaks A_{1g} and E_{2g}^1 obtained under non-resonant conditions (e.g., with laser excitation of 533 nm) exhibit a red shift and a blue shift, respectively, when the number of layers decreases from $4-5$ layers to a monolayer. Figure 9 (c) shows the thickness dependence of the frequencies of E_{2g}^1 and A_{1g} Raman peaks for MoS_2 samples in bulk, bilayer and single layer phases. This feature is commonly used in the characterization of thin nanosheets of MoS_2 material to identify monolayer samples and to estimate the number of layers of the samples, with sensitivity ranging from 1 to about 4-5 layers. [46, 161–163].
Based on the classical model for coupled harmonic oscillators, the frequencies of both A_{1g} and E_{2g}^1 would decrease with decreasing sample thickness, as the less intense van der Waals forces between the layers cause a decrease in the restoring forces on the atoms [46]. While the A_{1g} mode agrees with this prediction, the E_{2g}^1 mode exhibits an anomalous blue shift with decreasing layer number. This unexpected behavior is attributed to a decrease in dielectric screening with the thinning of the

material, which enhances the long-range Coulomb interactions between the effective charges and the restoring forces on the vibrating atoms [122].

2.3 DOPING IN HOMOGENEOUS SEMICONDUCTORS

2.3.1 *free charge carrier densities in thermal equilibrium*

Some of the most important aspects of a semiconductor are the concentration of free charge carriers within it and how this can be modulated by the intentional or unintentional introduction of impurities, known as doping. The number of electrons per unit volume in CB and the number of holes per unit volume in VB, denoted n_c and p_v, respectively, depends on the temperature (T) and the presence of impurities in the material. The general expression for the free carrier concentration in thermal equilibrium can be written as [52]:

$$n_c(T) = \int_{\varepsilon_c}^{\infty} d\varepsilon \, g_c(\varepsilon) \frac{1}{e^{(\varepsilon-\mu)/K_B T} + 1}, \tag{2.2}$$

$$\begin{aligned} p_v(T) &= \int_{-\infty}^{\varepsilon_v} d\varepsilon \, g_v(\varepsilon) \left(1 - \frac{1}{e^{(\varepsilon-\mu)/K_B T} + 1}\right) = \\ &= \int_{-\infty}^{\varepsilon_v} d\varepsilon \, g_v(\varepsilon) \frac{1}{e^{(\mu-\varepsilon)/K_B T} + 1}. \end{aligned} \tag{2.3}$$

Where $g_c(\varepsilon)$ and $g_v(\varepsilon)$ are the densities of states in BC and BV, respectively, μ is the chemical potential, also called the Fermi energy level, K_B is the Boltzmann constant, and ε_c and ε_v denote the bottom of CB and the top of VB, respectively. The statistical factors multiplying the densities of states in the integrals in (2.2) and (2.3) give the occupation probabilities of electrons and holes, respectively, at the energy level ε. At typical working temperature of semiconductor electronics and if the impurity concentration is not too high (nondegenerate case), the following conditions are satisfied:

$$\begin{aligned} \varepsilon_c - \mu \gg K_B T, \\ \mu - \varepsilon_v \gg K_B T. \end{aligned} \tag{2.4}$$

and justify the following approximations:

$$\begin{aligned} e^{(\varepsilon-\mu)/K_B T} + 1 \approx e^{(\varepsilon-\mu)/K_B T} \quad for \quad \varepsilon > \varepsilon_c, \\ e^{(\mu-\varepsilon)/K_B T} + 1 \approx e^{(\mu-\varepsilon)/K_B T} \quad for \quad \varepsilon < \varepsilon_v, \end{aligned} \tag{2.5}$$

which allow to write the free carrier densities as:

$$\begin{aligned} n_c(T) &= e^{-(\varepsilon_c-\mu)/K_BT} \int_{\varepsilon_c}^{\infty} d\varepsilon\, g_c(\varepsilon)\, e^{-(\varepsilon-\varepsilon_c)/K_BT} \\ &= e^{-(\varepsilon_c-\mu)/K_BT}\, N_c(T), \end{aligned} \tag{2.6}$$

$$\begin{aligned} p_v(T) &= e^{-(\mu-\varepsilon_v)/K_BT} \int_{-\infty}^{\varepsilon_v} d\varepsilon\, g_v(\varepsilon)\, e^{-(\varepsilon_v-\varepsilon)/K_BT} \\ &= e^{-(\mu-\varepsilon_v)/K_BT}\, P_v(T). \end{aligned} \tag{2.7}$$

The terms $N_c(T)$ and $P_v(T)$ are called the effective densities of states of CB and VB, respectively. Their change with T is much slower than the exponential factors by which they are multiplied. Exploiting the quadratic approximation of the energy $\varepsilon(\boldsymbol{k})$ in the neighborhood of the band extrema, it is possible to obtain for the effective densities:

$$N_c(T) = \frac{1}{4}\left(\frac{2m_cK_BT}{\pi\hbar^2}\right)^{3/2}, \tag{2.8}$$

$$P_v(T) = \frac{1}{4}\left(\frac{2m_vK_BT}{\pi\hbar^2}\right)^{3/2}. \tag{2.9}$$

Here the effective masses m_c and m_v result from the principal values of the mass tensors of the conduction band and the valence band, respectively [52]. Calculations of the effective densities for pure Si are reported in [164] and give $N_c(T) = 2.86 \times 10^{19}\, cm^{-3}$ and $P_v(T) = 3.10 \times 10^{19}\, cm^{-3}$ at $T = 300\,\mathrm{K}$ [164].
The product of the number carrier densities n_c and p_v does not depend explicitly on the Fermi level μ and leads to the so-called mass action law for semiconductors [52].

$$\begin{aligned} n_c(T)p_v(T) &= e^{-(\varepsilon_c-\varepsilon_v)/K_BT} N_c(T)P_v(T) \\ &= e^{-\varepsilon_{gap}/K_BT} N_c(T)P_v(T). \end{aligned} \tag{2.10}$$

In the intrinsic case, i.e. for pure material or very low impurity concentration, the number of electrons in CB is equal to the number of holes in VB ($n_c = p_v = n_i$) and using the law of mass action we simply obtain:

$$n_i = \sqrt{n_c\, p_v} = e^{-\varepsilon_{gap}/2K_BT}\sqrt{N_c\, P_v}. \tag{2.11}$$

The value of $n_i = 1.07 \times 10^{10}\, cm^{-3}$ is obtained for pure Si at $T = 300\,\mathrm{K}$ [164].
The above equations (2.6) and (2.7) for n_c and p_v allow us to obtain an expression for the Fermi level in the intrinsic case by simply equating the two densities and forming the logarithm of the two terms:

$$\mu_i = \varepsilon_v + \frac{\varepsilon_{gap}}{2} + \frac{K_BT}{2}\log\left(\frac{P_v}{N_c}\right), \tag{2.12}$$

from which it can be seen that μ_i lies approximately in the middle of the energy gap of the semiconductor.

2.3.2 *extrinsic semiconductors*

In extrinsic semiconductors, which are fundamental to electronics, the presence of impurities in the material creates extra electrons in CB and/or holes in VB. The process of providing additional charge carriers is called doping. The impurities that provide electrons in CB are called donors, those that provide holes in VB are called acceptors. A semiconductor doped with donors is called an n-type semiconductor; if it is doped with acceptors, it is called a p-type semiconductor. Effective doping is achieved only when some original atoms in the lattice sites are replaced by impurities, which are then called substitutional impurities. In semiconductors of the group IV, such as Si, doping is achieved by adding elements of the group V or of the group III, e.g. As or B, respectively.
An element of the V group has five valence electrons and forms a tetrahedral bond with four surrounding Si atoms in the substitutional position, the remaining fifth electron does not form a bond. [52]. The substitutional impurities of the V group can be represented by the addition of a fixed positive charge (+e) to a host atom in its site together with an additional weakly bonded electron, which can be easily promoted to CB. For this reason impurities of V group are donors. For this reason, impurities of the V group are donors. In other words, doping by donors introduces additional electronic levels in the band gap of the semiconductor, very close to the bottom of the CB at an energy level ε_d, so that the relation $\varepsilon_c - \varepsilon_d \ll \varepsilon_{gap}$ holds.
Group III elements may represent acceptor impurities in group IV semiconductors. An acceptor impurity can be represented by the addition of a fixed negative charge (-e) on the host atom along with a weakly bound hole that can be easily promoted to VB. Again, we can say that acceptors introduce additional electronic levels ε_a in the band gap, very close to the top of VB with $\varepsilon_a - \varepsilon_v \ll \varepsilon_{gap}$. The acceptor levels are empty when the holes are bound to the impurities, electrons can easily be excited, e.g. by thermal energy, from the top VB to ε_a, which neutralize the bound holes, as a consequence the same number of free holes is created in VB.
To fully characterize the doping state of a semiconductor, it is important to calculate the number of free charge carriers at a given temperature and Fermi level. For this purpose, it is convenient to start from an ideal situation at $T = 0\,\mathrm{K}$ and consider a semiconductor with N_d donors and N_a acceptors per unit volume with $N_d > N_a$ (this condition does not lead to a loss of generality, the reverse condition would lead to the same results). At $T = 0\,\mathrm{K}$ we can imagine the ground state situation in which the VB is completely filled (zero free holes), the acceptor levels are also completely filled with electrons supplied by the donors, the donor levels are partially filled with $N_d - N_a$ electrons per unit volume, and the CB is completely empty. At $T \neq 0$ we can assume

that a number of electrons have left the VB and the acceptor levels to redistribute between the donor levels and the CB, leaving the total number of electrons unchanged.
Clearly, the number of electrons in the CB and donor levels ($n_c + n_d$) at $T \neq 0$ must be given by their value at $T = 0\,\text{K}$, ($N_d - N_a$), plus a number of electrons originating from the VB and acceptor levels, which can be determined by the number of holes in the VB and acceptor levels ($p_v + p_a$) [52]:

$$n_c + n_d \; = \; N_d - N_a + p_v + p_a \tag{2.13}$$

A schematic representation of the energy bands and impurity levels with the respective electron densities at $T = 0\,K$ and $T \neq 0$ is shown in Figure 11.

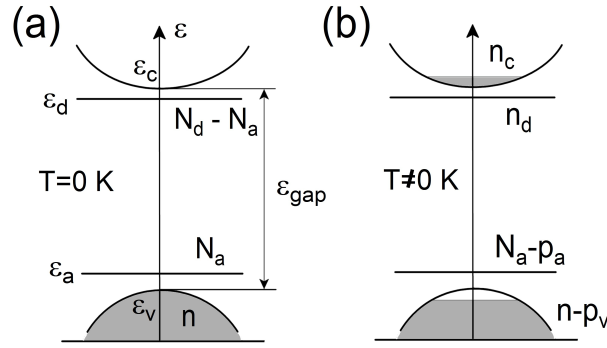

Figure 11. Schematic representation of the energy bands and impurity levels in an extrinsic semiconductor with the respective densities of electrons at $T = 0\,K$ (a) and $T \neq 0$ (b)

To determine n_c and p_v, we need to find the Fermi level $\mu(T)$ in the case of an extrinsic semiconductor. This can be found by developing the equation (2.13) together with the mass action law in its equivalent form ($n_c p_v = n_i^2$).
Before proceeding, it is convenient to find explicit relations for n_d and p_a, which can be obtained by statistical mechanics arguments. n_d, the density number of electrons bound to the donors, can be determined by the product $\langle n \rangle N_d$, where $\langle n \rangle$ is the mean number of electron in a single donor impurity. Similarly, p_a, the density number of holes bound to the acceptors, can be determined by multiplying the mean number of holes in a single acceptor impurity $\langle p \rangle$ by the total density number of acceptors ($p_a = \langle p \rangle N_a$).
In the context of statistical mechanics of the grand canonical ensemble, it is possible to obtain the very general expressions of $\langle n \rangle$ for a system in thermal equilibrium [165],

$$\langle n \rangle \; = \; \frac{\sum N_j e^{-\beta(E_j - \mu N_j)}}{\sum e^{-\beta(E_j - \mu N_j)}}, \tag{2.14}$$

where the system has a number of states with N_j electrons and E_j energy, and $\beta = 1/K_B T$. More specific considerations about the accessible states of the system corresponding to donor impurity or acceptor impurity, and the number of electrons and energies of these states, lead to the expressions [52]:

$$\langle n \rangle = \frac{1}{\frac{1}{2}e^{\beta(\varepsilon_d - \mu)} + 1}, \tag{2.15}$$

$$\langle p \rangle = \frac{1}{\frac{1}{2}e^{\beta(\mu - \varepsilon_a)} + 1}. \tag{2.16}$$

Consequently, the number densities of electrons and holes bound to donor and acceptor levels are given by:

$$n_d = \frac{N_d}{\frac{1}{2}e^{\beta(\varepsilon_d - \mu)} + 1}, \tag{2.17}$$

$$p_a = \frac{N_a}{\frac{1}{2}e^{\beta(\mu - \varepsilon_a)} + 1}. \tag{2.18}$$

Now, considering that the energy levels ε_d and ε_a are very close to the band edges and remembering the assumptions under nondegenerate conditions (2.4), we can assume:

$$\begin{aligned} \varepsilon_d - \mu \gg K_B T, \\ \mu - \varepsilon_a \gg K_B T, \end{aligned} \tag{2.19}$$

which together with (2.17) and (2.18) guarantee that the impurities are fully ionized by thermal excitation and $n_d \ll N_d$ and $p_a \ll N_a$. The equation (2.13) can therefore be simplified and the system of equations:

$$\begin{cases} n_c - p_v \simeq N_d - N_a = \Delta n \\ n_v p_v = n_i^2 \end{cases} \tag{2.20}$$

after simple algebraic calculations yields:

$$\begin{aligned} n_c &= \frac{1}{2}\Delta n + \frac{1}{2}\sqrt{\Delta n^2 + 4n_i^2}, \\ p_v &= -\frac{1}{2}\Delta n + \frac{1}{2}\sqrt{\Delta n^2 + 4n_i^2} \end{aligned} \tag{2.21}$$

where $\Delta n = N_d - N_a$ gives a measure of the deviation of the extrinsic case from the intrinsic behavior.
Using (2.6) and (2.7) and using $n_i = exp(-\beta(\varepsilon_c - \mu_i))N_c$ and $p_i = exp(-\beta(\mu_i - \varepsilon_v))P_v$ with μ_i the Fermi level for the intrinsic case, we can write:

$$\begin{aligned} n_c = e^{-\beta(\varepsilon_c - \mu)} N_c = n_i e^{-\beta(\mu_i - \mu)} \\ p_v = e^{-\beta(\mu - \varepsilon_v)} P_v = p_i e^{-\beta(\mu - \mu_i)} \end{aligned} \tag{2.22}$$

and substituting these last results into (2.21), and then subtracting the second equation of (2.21) from the first, we obtain after simple passes:

$$e^{\beta(\mu-\mu_i)} - e^{-\beta(\mu-\mu_i)} = \frac{\Delta n}{n_i}$$

or equivalently

$$2senh[\beta(\mu-\mu_i)] = \frac{\Delta n}{n_i}. \tag{2.23}$$

From the above relation, the Fermi level for the case of an extrinsic semiconductor can be derived:

$$\mu = \mu_i + \frac{1}{2\beta} senh^{-1}\Big(\frac{\Delta n}{n_i}\Big). \tag{2.24}$$

Using the equations (2.20), useful information can be obtained about the density of free charge carriers in the extreme cases of low and high doping. In the case of low doping, where there is intrinsic behavior, we can assume that $n_i >> |N_d - N_a|$ and thus expand the square root in (2.21) to obtain:

$$\begin{aligned} n_c &\simeq \frac{1}{2}\Delta n + n_i = \frac{1}{2}(N_d - N_a) + n_i, \\ p_v &\simeq -\frac{1}{2}\Delta n + n_i = -\frac{1}{2}(N_d - N_a) + n_i. \end{aligned} \tag{2.25}$$

Otherwise, in the case of high doping ($|N_d - N_a| >> n_i$), we have the n-type and p-type extrinsic regimes:

$$\left.\begin{aligned} n_c &\simeq \Delta n = N_d - N_a \\ p_v &\simeq \frac{n_i^2}{\Delta n} = \frac{n_i^2}{N_d - N_a} \end{aligned}\right\} \quad \text{for } N_d > N_a \tag{2.26}$$

$$\left.\begin{aligned} n_c &\simeq -\frac{n_i^2}{\Delta n} = \frac{n_i^2}{N_a - N_d} \\ p_v &\simeq -\Delta n = N_a - N_d \end{aligned}\right\} \quad \text{for } N_a > N_d \tag{2.27}$$

From the above relations it is seen that the excess of charge carriers due to impurities is found almost entirely in the CB in the case of the n-type and in the VB in the case of the p-type, leaving the opposite band almost undoped.

Analogously, from the equation (2.24), exploiting the relation

$$senh^{-1}\Big(\frac{\Delta n}{n_i}\Big) = ln\Big(\frac{\Delta n}{n_i} + \sqrt{\Big(\frac{\Delta n}{n_i}\Big)^2 + 1}\Big),$$

we can expand the square root in the case of $|N_d - N_a| >> n_i$ to obtain the Fermi levels in the extrinsic regimes:

$$\mu = \mu_i + \frac{K_B T}{2} ln\Big(\frac{2N_d}{n_i}\Big) \quad n - type \tag{2.28}$$

$$\mu = \mu_i - \frac{K_B T}{2} ln\Big(\frac{2N_a}{n_i}\Big) \quad p - type \tag{2.29}$$

2.3.3 *quasi-Fermi levels*

Under the condition of thermodynamic equilibrium, the Fermi level is unique for both electrons and holes. Otherwise, there may be situations that deviate from thermal equilibrium, for example, when current injection or optical excitation continuously produces electrons and holes in the respective bands. In this case, the semiconductor can reach a quasi-equilibrium state by very fast intraband relaxations of electrons and holes in the respective bands, since these transitions are much faster than those of electron-hole recombination processes.
Electrons and holes are then characterized by two different Fermi levels, which are called quasi-Fermi levels. Under quasi-equilibrium conditions, the equations (2.6) and (2.7) must be modified by:

$$\begin{aligned} n_c(T) &= e^{-\beta(\varepsilon_c-\mu_c)} \int_{\varepsilon_c}^{\infty} d\varepsilon\, g_c(\varepsilon)\, e^{-(\varepsilon-\varepsilon_c)/K_BT} \\ &= e^{-\beta(\varepsilon_c-\mu_c)}\, N_c(T), \end{aligned} \tag{2.30}$$

$$\begin{aligned} p_v(T) &= e^{-\beta(\mu_v-\varepsilon_v)} \int_{-\infty}^{\varepsilon_v} d\varepsilon\, g_v(\varepsilon)\, e^{-(\varepsilon_v-\varepsilon)/K_BT} \\ &= e^{-\beta(\mu_v-\varepsilon_v)}\, P_v(T). \end{aligned} \tag{2.31}$$

Here μ_c and μ_v are the quasi-Fermi levels of electron and hole. The product of n_c and p_v gives:

$$n_c p_v \;=\; e^{-\beta(\varepsilon_c-\varepsilon_v-\mu_c+\mu_v)} N_c P_v \;=\; n_i^2 e^{\beta(\mu_c-\mu_v)}. \tag{2.32}$$

This relation replaces the mass action law of thermodynamic equilibrium ($n_c p_v = n_i^2$).
The above considerations are valid only if the differences $\varepsilon_c - \mu_c$ and $\mu_v - \varepsilon_v$ are greater than some K_BT. If these conditions are not satisfied, e.g., if one of the quasi-Fermi levels is very close to the respective band edge or beyond within the bands, the above relations for the free carrier densities (2.30) and (2.31) cannot be applied, and the semiconductor is in a state very similar to the so-called degenerate state that occurs at very high doping.

2.3.4 *degenerate semiconductors*

Very high doping of donors or acceptors, say N_d or N_a above $10^{20}\ cm^{-3}$, causes the impurity level, ε_d or ε_a, to spread out and degenerate into a band that overlaps with the CB or VB [166]. In these cases, the semiconductor is called degenerate. In degenerate semiconductors, the law of mass action is invalid, and the electrical properties of the material resemble those of a metal rather than a semiconductor.
Joyce and Dixton gave a useful analytical approximate expression for

the Fermi level in the degenerate cases [167]:

$$\frac{\mu_c - \varepsilon_c}{K_B T} \simeq ln\left(\frac{n_c}{N_c}\right) + \frac{1}{\sqrt{8}}\frac{n_c}{N_c} - \left(\frac{3}{16} - \frac{\sqrt{3}}{9}\right)\left(\frac{n_c}{N_c}\right)^2 + ... \quad n - type \tag{2.33}$$

$$\frac{\varepsilon_v - \mu_v}{K_B T} \simeq ln\left(\frac{p_v}{P_v}\right) + \frac{1}{\sqrt{8}}\frac{p_v}{N_v} - \left(\frac{3}{16} - \frac{\sqrt{3}}{9}\right)\left(\frac{p_v}{P_v}\right)^2 + ... \quad p - type \tag{2.34}$$

BASICS OF IMPORTANT OPTICAL PHENOMENA IN SEMICONDUCTORS

3

This chapter is devoted to a brief introduction to the theories of Raman scattering, photoluminescence emission, and Fano interference effects in Raman spectroscopy, as they are essential for understanding the experimental results presented in this thesis. More detailed discussions can be found in [23, 58, 168–171].

3.1 BASICS OF RAMAN SCATTERING

Raman scattering is named after Chandrasekhara V. Raman, who discovered the effect in 1928 while studying how light interacts with liquids and vapours [172]. Raman spectroscopy, that is the optical technique based on the Raman effect, has been used for several decades in solid-state science to study various material properties, such as molecular and lattice dynamics, chemical and structural identification, orientation of crystals, phase changes, phonon dispersion, phonon density of states, electronic states, and the response of the material to external influences, such as deformation, doping, functionalization, and the amount and type of defects [173–180] etc. When a monochromatic beam of light, such as a laser source, impinges on a sample, it can be elastically or inelastically scattered. Of the scattered photons, most have undergone elastic scattering, their energy is conserved after interaction with matter, and this phenomenon is known as Rayleigh scattering. On the other hand, a minority of the scattered photons have undergone inelastic scattering, their energy can be smaller or larger than the incident energy, and this phenomenon is called Raman scattering, Stokes when the energy of the outgoing light is smaller than that of the incident light, anti-Stokes when the energy is larger. Rayleigh radiation has an intensity about 1-2 orders of magnitude less than the incident light, while Raman radiation is about 5-6 orders of magnitude less intense than Rayleigh radiation. Raman scattering in solids is due to the indirect interaction between the incident photons and the vibrational modes in the material (called phonons), the electrons mediate the scattering, although they remain unchanged after the process [58]. Schematically, the process of Raman scattering can be described as follows: An incoming photon, characterized by its momentum, energy, and polarization $(\boldsymbol{k}_i, \omega_i, \boldsymbol{e}_i)$, is absorbed by the material and excites the system from an initial state $|i\rangle$ to an intermediate (virtual) state $|n\rangle$, where this transition does not have to conserve energy but must conserve momentum. From $|n\rangle$, the system emits a photon characterized by $(\boldsymbol{k}_s, \omega_s, \boldsymbol{e}_s)$ and relaxes to the final state $|f\rangle$. If the energy of the photon happens to closely match the energy of an allowed electronic transition, the process is a special case of Raman scattering called resonant Raman scatter-

ing, which will be discussed later. In the case of Rayleigh scattering, $\hbar\omega_s = \hbar\omega_i$ and the final state is identical to the initial state. In the case of Raman scattering, on the other hand, the final state differs from the initial state due to the creation (in the case of Stokes scattering) or annihilation (anti-Stokes scattering) of an excited state of the system. The difference in energy between the final state and the initial state is balanced by the difference in energy between the incident and emitted photons. The conservation laws for energy and momentum for the whole process can be written as:

$$\pm\hbar\omega_0 = \hbar\omega_i - \hbar\omega_s, \tag{3.1}$$

$$\pm\hbar\boldsymbol{q} = \hbar\boldsymbol{k}_i - \hbar\boldsymbol{k}_s. \tag{3.2}$$

The sign + (-) applies to the anti-Stokes (Stokes) process, $\hbar\omega_0$ is the energy of the phonon and is equal to the difference in energy between the final and initial states ($\hbar\omega_0 = E_f - E_i$), $\hbar\boldsymbol{q}$ is the momentum of the phonon and represents the change in the momentum of the system.
A schematic representation of the Raman Stokes and anti-Stokes processes is shown in Figure 12, energetic diagrams are shown in Figure 12 (a), an illustrative picture of a spectrum is shown in Figure 12 (b), the insets illustrate the scattering processes. At a given temperature (T), the initial state of the Stokes process is more populated than that of the anti-Stokes process due to the difference in the occupation probability of the different energy levels (see Figure 12 (a)). As a result, the Stokes scattering has a larger probability than the anti-Stokes scattering, and for a given vibrational mode, the Stokes spectral line is more intense than the anti-Stokes line (see Figure 12 (b)).

In the following section 3.2 we consider a simple classical description of Raman scattering by phonons in solids, which provides a qualitative understanding of the phenomenon. However, to gain a more detailed understanding, we need a quantum mechanical approach, which is the subject of section 3.3.

3.2 MACROSCOPIC DESCRIPTION

Light traveling through a medium can be transmitted or absorbed, and a very small fraction can be scattered by inhomogeneities in the medium. Fluctuations in the density of the medium due to collective atomic vibrations (phonons in crystals) constitute dynamic inhomogeneities and can lead to inelastic scattering of light, called Raman scattering. Consider an infinite medium characterized by an electric susceptibility χ, and for simplicity assume at this stage that the medium is isotropic and χ is a scalar. The presence of an electromagnetic field in the medium due to an incident radiation will induce polarization in the material with the same frequency and wave vector of the incident radiation. We can consider the form of sinusoidal plane waves for the electromagnetic

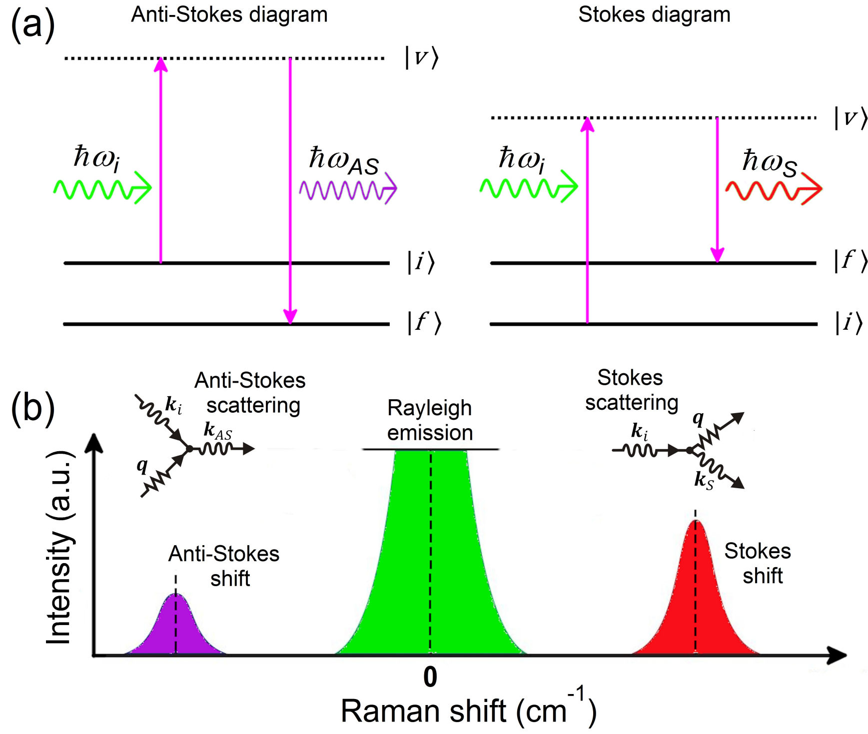

Figure 12. (a) Schematic energy diagrams illustrating the transitions involved in anti-Stokes and Stokes Raman scattering. (b) Illustration of a Raman spectrum showing the anti-Stokes and Stokes lines as a function of the frequency difference between the incident and scattered light, conventionally called Raman shift. The central peak (cut) represents the Rayleigh emission. The insets represent the scattering processes, in anti-Stokes scattering the absorption of a photon plus a phonon leads to the emission of a photon, while in Stokes scattering the absorption of a photon leads to the emission of a phonon plus a photon.

field and the induced polarization, so we have:

$$\boldsymbol{E}(\boldsymbol{r},t) = \boldsymbol{E}(\boldsymbol{k}_i,\omega_i)\,cos(\boldsymbol{k}_i \cdot \boldsymbol{r} - \omega_i t), \quad (3.3)$$

$$\boldsymbol{P}(\boldsymbol{r},t) = \boldsymbol{P}(\boldsymbol{k}_i,\omega_i)\,cos(\boldsymbol{k}_i \cdot \boldsymbol{r} - \omega_i t). \quad (3.4)$$

The amplitude of the induced polarization is given by [58]:

$$\boldsymbol{P}(\boldsymbol{k}_i,\omega_i) = \chi(\boldsymbol{k}_i,\omega_i)\,\boldsymbol{E}(\boldsymbol{k}_i,\omega_i). \quad (3.5)$$

At finite T, there are fluctuations in χ generated by thermally excited phonons. A phonon is characterized by atomic displacements $\boldsymbol{Q}(\boldsymbol{r},t)$ which can be described by:

$$\boldsymbol{Q}(\boldsymbol{r},t) = \boldsymbol{Q}(\boldsymbol{q},\omega_0)\,cos(\boldsymbol{q} \cdot \boldsymbol{r} - \omega_0 t), \quad (3.6)$$

Assuming the adiabatic approximation for which $\omega_i \gg \omega_0$, the electric susceptibility χ, which depends on frequencies of order ω_i, can be

regarded as a function of $\boldsymbol{Q}(\boldsymbol{r},t)$. Under the ordinary condition that the amplitudes of the atomic displacements are small with respect to the lattice parameter, we can adopt the harmonic approximation and use the Taylor series expansion in $\boldsymbol{Q}$ of χ:

$$\chi(\boldsymbol{k}_i,\omega_i,\boldsymbol{Q}) = \chi_0(\boldsymbol{k}_i,\omega_i) + (\partial\chi/\partial\boldsymbol{Q})_0\,\boldsymbol{Q}(\boldsymbol{r},t) + \cdots . \quad (3.7)$$

The first term χ_0 represents the susceptibility at equilibrium without fluctuations, the second term represents a fluctuating susceptibility induced by $\boldsymbol{Q}(\boldsymbol{r},t)$. Using (3.7), the polarization amplitude (3.5) can be rewritten as:

$$P(\boldsymbol{k}_i,\omega_i) = \chi_0(\boldsymbol{k}_i,\omega_i)\,\boldsymbol{E}(\boldsymbol{k}_i,\omega_i) + (\partial\chi/\partial\boldsymbol{Q})_0\,\boldsymbol{Q}(\boldsymbol{r},t)\,\boldsymbol{E}(\boldsymbol{k}_i,\omega_i), \quad (3.8)$$

and substituting (3.8) into (3.4) we have:

$$\boldsymbol{P}(\boldsymbol{r},t,\boldsymbol{Q}) = \boldsymbol{P}_0(\boldsymbol{r},t) + \boldsymbol{P}_{ind}(\boldsymbol{r},t,\boldsymbol{Q}), \quad (3.9)$$

where the first term

$$\boldsymbol{P}_0(\boldsymbol{r},t) = \chi_0(\boldsymbol{k}_i,\omega_i)\,\boldsymbol{E}(\boldsymbol{k}_i,\omega_i)\,cos(\boldsymbol{k}_i\cdot\boldsymbol{r} - \omega_i t) \quad (3.10)$$

oscillates in phase with $\boldsymbol{E}(\boldsymbol{r},t)$, and the second term, using Werner's relation $cos(\alpha)cos(\beta) = 1/2[cos(\alpha+\beta) + cos(\alpha-\beta)]$, results to be constituted of two terms oscillating with different frequencies:

$$\begin{aligned}\boldsymbol{P}_{ind}(\boldsymbol{r},t,\boldsymbol{Q}) = &\frac{1}{2}\,(\partial\chi/\partial\boldsymbol{Q})_0\,\boldsymbol{Q}(\boldsymbol{q},\omega_0)\,\boldsymbol{E}(\boldsymbol{k}_i,\omega_i)\\ &\times\{cos[(\boldsymbol{k}_i+\boldsymbol{q})\cdot\boldsymbol{r} - (\omega_i+\omega_0)]\\ &+ cos[(\boldsymbol{k}_i-\boldsymbol{q})\cdot\boldsymbol{r} - (\omega_i-\omega_0)]\}.\end{aligned} \quad (3.11)$$

The term with wave vector $\boldsymbol{k}_S = (\boldsymbol{k}_i - \boldsymbol{q})$ and frequency $\omega_S = (\omega_i - \omega_0)$ is responsible for Stokes radiation, the term with wave vector $\boldsymbol{k}_{AS} = (\boldsymbol{k}_i + \boldsymbol{q})$ and frequency $\omega_{AS} = (\omega_i + \omega_0)$ produces anti-Stokes radiation. While $\boldsymbol{P}_0(\boldsymbol{r},t)$ produces Rayleigh radiation. The plot of the intensity of Stokes and anti-Stokes radiations as a function of the frequency difference of the incident and scattered radiations forms the Raman spectrum, and the frequency difference is called the Raman shift.
As a consequence of conservation of momentum, the value of $\boldsymbol{q}$ involved in a one-phonon Raman process must be less than twice the photon wave vector. Considering visible light as the excitation source, it results that the value of $|\boldsymbol{q}|$ is of the order of 10^6 cm^{-1}, which is much smaller than the size of the first Brillouin zone (BZ) ($\sim 10^8 cm^{-1}$ in a semiconductor). Therefore, in single-phonon Raman spectroscopy, only the phonons belonging to the center of the BZ can be studied. Nevertheless, it is possible to consider Raman scattering processes involving more than one phonon. Theoretically, this can be achieved by extending the Taylor series of susceptibility (3.7) to second or higher order terms

in $\boldsymbol{Q}(\boldsymbol{r}, t)$. The second-order terms lead to an additional induced polarization, which results in the so-called second-order Raman emissions. Considering two phonons with frequencies ω_a and ω_b and wave vectors $\boldsymbol{q}_a$ and $\boldsymbol{q}_b$, we have Raman scattering processes, whose emissions can have frequencies $(\omega_i \pm \omega_a \pm \omega_b)$ and wave vectors $(\boldsymbol{k}_i \pm \boldsymbol{q}_a \pm \boldsymbol{q}_b)$. Wave vector conservation in two-phonon Raman processes leads to $\boldsymbol{q}_a \pm \boldsymbol{q}_b \approx 0$, so in this case we can have wave vectors with sufficiently high magnitudes to study the whole BZ.
The intensity of the scattered radiation (I_s) collected in a chosen direction in unit solid angle can be obtained from the energy power radiated by the induced polarizations $\boldsymbol{P}_{ind}$. I_s will be proportional to the projection of $\boldsymbol{P}_{ind}$ onto the polarization direction of the scattered radiation ($\hat{\boldsymbol{e}}_s$), as $I_s \propto |\boldsymbol{P}_{ind} \cdot \hat{\boldsymbol{e}}_s|^2$. Considering (3.11), we can write:

$$I_s \propto |\hat{\boldsymbol{e}}_i \cdot (\partial\chi/\partial\boldsymbol{Q})_0 \, \boldsymbol{Q}(\boldsymbol{q}, \omega_0) \cdot \hat{\boldsymbol{e}}_s|^2. \tag{3.12}$$

More generally, χ is a second-rank tensor, so $(\partial\chi/\partial\boldsymbol{Q})_0$ is a third-rank tensor, and given the unit vector $\hat{\boldsymbol{Q}} = \boldsymbol{Q}/|\boldsymbol{Q}|$, we can define a second-rank tensor ($\boldsymbol{R} = (\partial\chi/\partial\boldsymbol{Q})_0 \, \hat{\boldsymbol{Q}}$) known as Raman tensor. In this way, a proportionality relation can be written as:

$$I_s \propto |\hat{\boldsymbol{e}}_i \cdot \boldsymbol{R} \cdot \hat{\boldsymbol{e}}_s|^2. \tag{3.13}$$

The symmetry properties of the crystal are reflected in the symmetry properties of χ and $\boldsymbol{R}$. Thus, by controlling the scattering geometries and polarization directions $\hat{\boldsymbol{e}}_i$ and $\hat{\boldsymbol{e}}_s$, it is possible to study the symmetry of the Raman tensor. The scattered radiation can vanish for certain choice of the geometrical configuration of the scattering, leading to the so-called Raman selection rules. These are often used to study the symmetry of Raman active phonons.
From an experimental point of view, a quantity of considerable interest is the scattering efficiency η, which is the ratio between the energy of the scattered electromagnetic radiation per unit time per unit frequency interval in unit solid angle and the energy of the incident radiation crossing the incident surface in unit time [58],

$$\eta = \left(\frac{\omega_s}{c}\right)^4 VL \left| \hat{\boldsymbol{e}}_i \cdot \left(\frac{\partial\chi}{\partial\boldsymbol{Q}}\right)_0 \cdot \boldsymbol{Q}(\boldsymbol{q}, \omega_0) \cdot \hat{\boldsymbol{e}}_s \right|^2. \tag{3.14}$$

In 3.14, ω_s is the scattering frequency, V is the scattering volume, L is the scattering length (V= AL with A the incident area). $L \simeq 1/\alpha$, where α is the absorption coefficient. Note the four-power dependence of η on ω_s.
Considering a quantum mechanical treatment of light in photons, it is convenient to define η in terms of the differential scattering cross section ($d^2\sigma/d\Omega d\omega_s$):

$$\eta = \left(\frac{\omega_i}{\omega_s A}\right)\left(\frac{d^2\sigma}{d\Omega d\omega_s}\right), \tag{3.15}$$

where the differential scattering cross section can be defined as the ratio of the number of photons scattered into a cone with solid angle $\delta\Omega$ pointing in a specific direction and with frequency ω_s with tolerance $\delta\omega_s$, divided by the number of incident photons per unit area (incident flux).

3.3 MICROSCOPIC DESCRIPTION

We have previously described Raman scattering as an inelastic process in which the absorption of an incident photon by a medium leads to the excitation of the system to an intermediate state, from which the system relaxes and emits a photon with a different energy. The final state differs from the initial state by the creation (in the case of Stokes scattering) or annihilation (in the case of anti-Stokes scattering) of a phonon. Due to conservation of energy, the emitted photon has lost or gained energy by the amount required to create or annihilate the phonon.
A more complete description of inelastic scattering of light, appropriate to a microscopic scale and a quantum mechanical perspective, can be achieved by focusing on the role that electrons have in the material as mediators of the interaction [58]. Considering that the subjects involved in the scattering process are photons, electrons and phonons, the initial state $|i\rangle$ of the system before scattering is characterized by a number of photons, $N(\omega_i)$ with frequency ω_i and $N(\omega_s)$ with frequency ω_s. Assuming that the temperature is $T \neq 0$, there are also N_q phonons in the system. The electrons in the material can all be considered in their ground states. After a Raman scattering process, the system is in a final state $|f\rangle$ in which $N(\omega_i)$ is decreased by one, $N(\omega_s)$ is increased by one, N_q is increased (decreased) by one in the case of Stokes (anti-Stokes) scattering. We can distinguish three steps in the progression of scattering. In the first step, the incident photon entering inside the medium couples to an electron, the interaction being described by an electron-radiation Hamiltonian H_{eR}, the system is excited to an intermediate state $|a\rangle$ by creating an electron-hole (e-h) pair (or an exciton). In the second step, the e-h pair interacts with the lattice via an electron-phonon interaction Hamiltonian H_{e-ion} and is scattered to another intermediate state $|b\rangle$ with the creation or annihilation of a phonon in the case of Stokes or anti-Stokes scattering. In the third step leading to the final state $|f\rangle$, the e-h pair recombines radiatively emitting a scattering photon. The probability for photons to enter Raman scattering can be calculated with third-order perturbation theory using Feynman diagrams [181–183]. A Feynman diagram consists of lines, called propagators, and intersections of lines, called vertices. A sequence of propagators and vertices is assumed to progress from left to right as a function of time. Progressive excitations, such as photons, phonons, e-h pairs, are represented by propagators drawn with arrows.

An arrow pointing to a vertex indicates annihilation of an excitation, while an arrow coming out of a vertex indicates the creation of an excitation. Different processes contribute to the one-phonon Raman scattering. Once a particular process has been depicted by a diagram, the other can be obtained by swapping the time order in which the vertices occur in the diagram [58].

We will focus here on the one-phonon Stokes Raman scattering, it

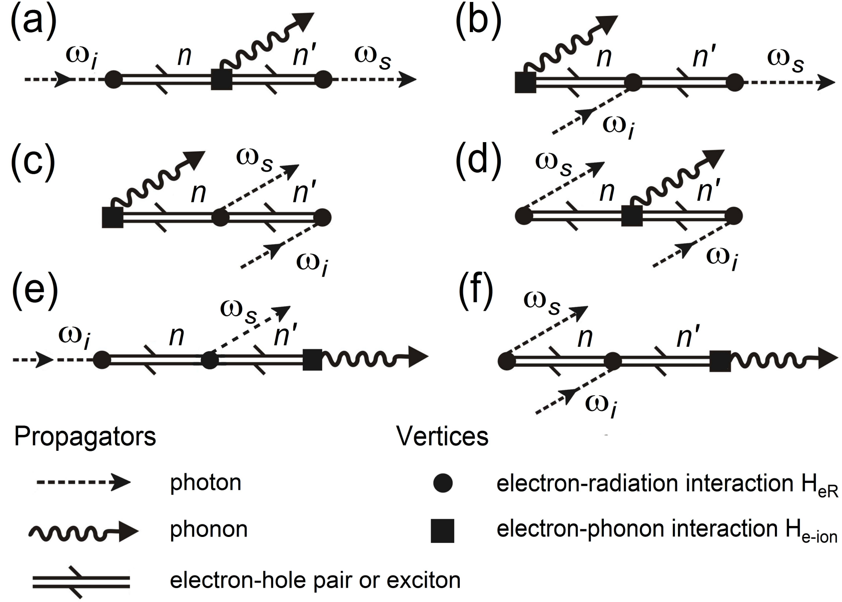

Figure 13. (a)-(f) Feynman diagrams depicting the six scattering processes that constitute the one-phonon Stokes Raman scattering. (b)-(f) are obtained from (a) by permuting the occurrence of the vertices. Below is a legend of the symbols used in the diagrams. Adapted from [58].

will then be easy to extend the derivation to the anti-Stokes scattering. The Stokes scattering process described earlier is depicted by the first Feynman diagram in Figure 13 (a). The other five diagrams are obtained from the first diagram by permuting the time order in which the vertices occur. The probability of scattering from the state $|i\rangle$ to $|f\rangle$ is obtained from the Fermi Golden Rule, where each diagram contributes one term to the probability amplitude. Looking at the first diagram, the first vertex in it represents the interaction between the incident photon (of frequency ω_i) and an electron in a ground state within the material, leading to the excitation of an e-h pair. This interaction introduces a term of the form:

$$\sum_n \frac{\langle n| H_{eR}(\omega_i) |i\rangle}{[\hbar\omega_i - (E_n - E_i)]} \tag{3.16}$$

where $|i\rangle$ and E_i denote the initial state and its energy, $|n\rangle$ and E_n denote the intermediate states and their energy, with summation running over

all intermediate states. The second and third vertices of the diagram introduce similar terms that multiply the first term (3.16) to give:

$$\sum_n \left(\frac{\langle f| H_{eR}(\omega_s) |n'\rangle \langle n'| H_{e-ion}(\omega_0) |n\rangle}{[\hbar\omega_i - (E_n - E_i)] [\hbar\omega_i - \hbar\omega_0 - (E_{n'} - E_i)]} \times \frac{\langle n| H_{eR}(\omega_i) |i\rangle}{[\hbar\omega_i - \hbar\omega_0 - \hbar\omega_s - (E_f - E_i)]} \right). \tag{3.17}$$

As mentioned earlier, the scattering leaves the electrons unchanged, so we can identify the final electronic state with the initial state and put $|f\rangle = |i\rangle$ and $E_f = E_i$ into the above expression. Thus the last term in the denominator becomes $[\hbar\omega_i - \hbar\omega_0 - \hbar\omega_s]$ and due to the conservation of energy in the whole scattering process it is approximately zero, thus giving a divergent factor which can be replaced by a delta function ($\delta(\hbar\omega_i - \hbar\omega_0 - \hbar\omega_s)$). Thus, if we consider only the first Feynman diagram, the scattering probability resulting from the Fermi golden rule will be given by:

$$P_{ph}(\omega_s) = \left(\frac{2\pi}{\hbar}\right) \left| \sum_{n',n} \frac{\langle i| H_{eR}(\omega_s) |n'\rangle \langle n'| H_{e-ion}(\omega_0) |n\rangle \langle n| H_{eR}(\omega_i) |i\rangle}{[\hbar\omega_i - (E_n - E_i)] [\hbar\omega_i - \hbar\omega_0 - (E_{n'} - E_i)]} \right|^2 \times \delta(\hbar\omega_i - \hbar\omega_0 - \hbar\omega_s). \tag{3.18}$$

The total scattering probability is obtained by exploiting all Feynman diagrams in Figure 13, where each diagram gives an additional term in the squared modulus in (3.18). A complete expression can be found in [58]. The scattering probability contains information on electron-radiation and electron-phonon couplings via the matrix elements of the interaction Hamiltonian H_{eR} and H_{e-ion}, respectively. However, the full expression of the scattering probability, despite its generality, is not easy to use because of the difficulty in determining the unknown electron-phonon matrix elements [58]. The scattering probability is simpler under certain conditions that allow studies of electronic states, electron-phonon interactions, and electronic band structure and exciton states in semiconductors, as we will discuss in the following section.

3.4 RESONANT RAMAN SCATTERING

Resonant Raman scattering occurs when the energy of the incoming photon involved in the scattering process is close to the energy of an electronic transition [184–186]. In a semiconductor, for example, resonant Raman scattering can be achieved by tuning the incident light to resonate with a strong interband transition [58]. In this resonant condition, some of the intermediate states involved in the Raman scattering process are not virtual, but real, accessible, states. The corresponding terms in the probability amplitude of the scattering become predominant over the others as their denominator tends to zero. Moreover,

among the scattering processes involving a real resonant state described by the Feynman diagrams of Figure 13, the one corresponding to the first Feynman diagram provides the strongest contribution to resonant Raman scattering. To understand this, we consider a Raman scattering process in a semiconductor and assume that the initial state $|i\rangle$ is the ground state $|0\rangle$ with energy $E_i = 0$ and no excited e-h pairs. If we denote by $|a\rangle$ the real intermediate state, by E_a its energy, the scattering probability (after integration over ω_s) can be written as:

$$P_{ph}(\omega_i) = \left(\frac{2\pi}{\hbar}\right) \left| \frac{\langle 0| H_{eR}(\omega_s) |a\rangle \langle a| H_{e-ion} |a\rangle \langle a| H_{eR}(\omega_i) |0\rangle}{[\hbar\omega_i - E_a] [\hbar\omega_s - E_a]} + C \right|^2, \tag{3.19}$$

Here only the term related to the resonant first Feynman diagram is explicit, the other terms of the Raman scattering process, i.e. the non-resonant terms and the resonant terms related to the other Faynman diagrams, are included in the constant C. Only the term of the first diagram contains the factor $(\hbar\omega_i - E_a)(\hbar\omega_s - E_a)$ in the denominator. In resonant condition, $\hbar\omega_i$ is very close to E_a and $(\hbar\omega_i - E_a)(\hbar\omega_s - E_a)$ can be considered as a second-order vanishing factor, since $\hbar\omega_s$ is very similar to $\hbar\omega_i$ differing only by the small phonon energy (on the order of meV versus the energy of the electronic transitions on the order of eV). The other resonant terms related to the rest of the Feynman diagrams contain either $(\hbar\omega_i - E_a)$ or $(\hbar\omega_s - E_a)$ in their denominator and show amplification in resonant condition, but less strongly than the first term.
In Eq. (3.19) it is implicitly assumed that the state $|a\rangle$ has infinite lifetime, this is not correct, the excited e-h pairs have finite lifetime due to radiative or non-radiative recombination. This can be accounted for in (3.19) by replacing E_a by $E_a - i\Gamma_a$, where $\Gamma_a = \hbar/\tau_a$ is the damping constant and τ_a is the finite lifetime of the intermediate state $|a\rangle$. Thus, when the exciting source is in resonance with a real excitable state $|a\rangle$, the Raman scattering probability can be written as:

$$P_{ph}(\omega_i) \approx \left(\frac{2\pi}{\hbar}\right) \left| \frac{\langle 0| H_{eR}(\omega_s) |a\rangle \langle a| H_{e-ion} |a\rangle \langle a| H_{eR}(\omega_i) |0\rangle}{[\hbar\omega_i - E_a + i\Gamma_a] [\hbar\omega_s - E_a + i\Gamma_a]} \right|^2. \tag{3.20}$$

The enhancement of the Raman cross section at resonance with an interband transition in a semiconductor is generally two orders of magnitude relative to the non-resonant background [187]. In contrast, an increase of several orders of magnitude has been reported when the resonant state is an exciton state [188].
The effective enhancement of Raman scattering in resonance condition can be used advantageously in the study of small samples such as 2D materials, nanoparticles, nanotubes, etc., where Raman signals are very

weak [189–193]. Similarly, higher order multiphonon Raman signals, which are much weaker than first order Raman signals, become more easily detectable in resonant condition. Thus, resonant Raman scattering facilitates the study of phonons from the entire BZ.
Rich information on electron-radiation and electron-phonon interactions, electronic band and phononic branch structures has been extensively obtained with resonant Raman scattering in the study of sp^2 carbon systems (graphene, carbon nanotubes) as well as Transition metal dichalcogenides such as MoS_2, WSe_2, WS_2, and in II-VI and III-V semiconductors such as CdS, GaP, GaSe, ...etc. [161, 194–200]. In this work, resonant Raman scattering was used to study p-type doped Si and MoS_2 in the monolayer phase in sections 5 and 6, respectively.

3.5 PHOTOLUMINESCENCE

Atoms can emit light by spontaneous emission when electrons in excited states fall to lower levels through radiative transitions. In semiconductors, light emission is commonly referred to as luminescence. There are several mechanisms that can produce luminescence in a semiconductor, each involving different external excitations. When the excitation is due to the injection of electrons and holes, the luminescence is called electroluminescence, thermoluminescence is due to thermal heating, photoluminescence (PL) is stimulated by the absorption of external photons [58, 201, 202]. In PL experiments, the energy of the absorbed photons is higher than the band gap of the semiconductor, and the emitted photons have lower energy than that of the exciting radiation. The absorption of a photon can cause the excitation of an e-h pair in the semiconductor, i.e., the transition of an electron from the valence band (VB) to the conduction band (CB) with the creation of a hole in VB. The de-excitation of an e-h pair can occur radiatively with the emission of a photon and this process is commonly referred to as radiative recombination. In a semiclassical approach, emission can occur only if an external electromagnetic wave is present in the emitting medium, and the probability of the radiative process is proportional to the intensity of the electromagnetic field, this is known as stimulated emission. However, radiation by a medium can also be produced without the presence of an external field, this is called spontaneous emission and can occur in an excited semiconductor containing e-h pairs regardless of how the e-h pairs were promoted.
An accurate description of the microscopic interaction that occurs in absorption, stimulated emission, and spontaneous emission can be achieved by a quantum mechanical treatment (see [203]), but for a basic understanding we can resort to the interpretation first proposed by Einstein without the use of quantum mechanics [58, 204–206].
Considering a medium with two nondegenerate energy levels n and m exposed to an external electromagnetic wave, we can define the Einstein

coefficients B_{nm}, B_{mn}, and A_{mn}, which denote the rates of absorption, stimulated emission, and spontaneous emission, respectively. B_{nm} is the rate for absorption of electromagnetic radiation with frequency ν, between ν and $\nu + \Delta\nu$, due to the transition of an electron from level n to level m, per unit of electromagnetic energy density. B_{mn} denotes the rate for stimulated emission due to the inverse transition. Also B_{mn} is defined per unit of electromagnetic energy density and within the frequency interval (ν,$\nu + \Delta\nu$). A_{mn} denotes the rate for spontaneous emission due to the transition from m to n. Unlike B_{nm} and B_{mn}, A_{mn} is not defined per unit of energy density. Based on the principle of detailed balance [207], it is possible to derive the following relation for the Einstein coefficients [58]:

$$B_{nm} = B_{mn}, \tag{3.21}$$

$$A_{mn} = \frac{8\pi h\nu^3 n_r^3}{c^3} B_{mn}, \tag{3.22}$$

where n_r is the refractive index of the medium, h is Planck's constant, ν is the photon frequency, c is the vacuum light velocity. The term multiplying B_{mn} in (3.22) is the density of electromagnetic modes with frequency ν (between ν and $\nu + \Delta\nu$) multiplied by the photon energy $h\nu$. For a medium in thermal equilibrium, we can now define the total emission rate R_{mn} as the radiation due to electron transitions from level m to level n:

$$R_{mn} = A_{mn} + B_{mn}\,\rho_e(\nu), \tag{3.23}$$

where $\rho_e(\nu)$ is the photon energy density $(8\pi h\nu^3 n_r^3/c^3)N_p$ with N_p the photon occupation number. Considering (3.22), (3.23) and the expression of $\rho_e(\nu)$, we can simply rewrite the total emission rate as:

$$R_{mn} = A_{mn}\,(1 + N_p). \tag{3.24}$$

In (3.24), the term proportional to N_p is due to stimulated emission. We restrict the considerations here only to spontaneous emission under the assumption that in the PL phenomena usually considered the photon density $\rho(\nu)$ $(= \rho_e(\nu)/h\nu \propto N_p)$ is small, so that the second term in (3.24) can be neglected. Under this approximation, we obtain $R_{mn} \simeq A_{mn}$, and extending the above consideration from discrete levels to valence and conduction bands in a semiconductor, one can write the total emission rate for the radiative recombination transitions from CB to VB as:

$$R_{cv} = A_{cv}\,f_c(1 - f_v), \tag{3.25}$$

where f_c and f_v are the occupation probabilities of the conduction band and the valence band, respectively.

In order to satisfy the detailed balance principle, we can relate the total emission from CB to VB with the corresponding absorption of photons in the inverse transition from VB to CB. Thus, if we define the

absorption rate per unit of photon density $P_{vc}(\nu)$, we can derive the relation:

$$R_{cv} = \rho(\nu)\, P_{vc}. \tag{3.26}$$

Then, using the empirical relationship between the absorption rate P_{vc} and the absorption coefficient α [58]:

$$P_{vc} = \frac{\alpha c}{n_r}, \tag{3.27}$$

and making explicit $\rho(\nu)$ as $(8\pi\nu^2 n_r^3/c^3)N_p$ with, according to Bose-Einstein statistic, $N_p = 1/(exp(h\nu/K_B T) - 1)$, where K_B is Boltzmann's constant, we can simply obtain from (3.26) and (3.27) the relation:

$$R_{cv}(\nu) = \frac{8\pi\nu^2 n_r^2}{c^2(e^{\frac{h\nu}{K_B T}} - 1)}\, \alpha(\nu). \tag{3.28}$$

This equation was obtained by considering generations and recombinations of charge carriers between the valence and conduction bands in a semiconductor considered in thermal equilibrium.

Since the emission from a semiconductor at room temperature in thermal equilibrium is very low, luminescence experiments are performed under a different condition known as quasi-thermal equilibrium, in which the emission is sufficiently strong. This condition is reached after an initial excitation of a non-equilibrium distribution of e-h pairs and a subsequent very fast thermalization of the e-h pairs. The relaxation time from the non-equilibrium distribution to the quasi-equilibrium distribution is very short compared to the recombination time of the e-h pairs. Although the quasi-equilibrium condition is achieved by an external excitation, the emission of luminescence must be regarded as spontaneous emission [58]. To summarize, a PL experiment can be considered to proceed in three sequential steps: First, an external energy source, such as an incident light, excites e-h pairs; the e-h pairs thermalize among themselves and reach a distribution of quasi-thermal equilibrium; finally, the e-h pairs recombine radiatively and emit photons.

In a semiconductor in quasi-equilibrium after thermalization, the free electrons and free holes are accumulated at the extremes of the CB and VB, respectively. In the case of direct band gap, the recombination of an e-h pair can occur directly with the emission of a photon, while in the case of indirect band gap, in order to satisfy the conservation of momentum in the lattice, the radiative recombination can only occur with the participation of a phonon. In indirect bandgap semiconductors such as Si, the probability of radiative recombination is lower than that of other competing nonradiative recombination processes, so the resulting emission is very small. It should be noted that in non-radiative recombination processes the excited e-h pairs annihilate due to the excitation of phonons in the system.

3.5.1 *Band-to-band transitions*

In general, transitions involving recombination of e-h pairs consisting of free electrons in CB and free holes in VB are called band-to-band transitions. In this case, the emission rate of photons can be defined by [58]:

$$R_{ph} = \frac{n_e n_h}{\langle \tau_r \rangle}, \tag{3.29}$$

n_e and n_h are the concentration of excited electrons and holes, respectively, and $\langle \tau_r \rangle$ is the averaged radiative recombination time. Note that it is necessary to take the average $\langle \tau_r \rangle$ of the radiative recombination time τ_r because it depends on the energy of the e-h pairs, which changes in the thermalized quasi-equilibrium distribution. In PL experiments, the concentrations n_e and n_h are equal and far exceed the intrinsic carrier concentrations of the semiconductor n_i, p_i ($n_e = n_h >> n_i = p_i$). In this case, it is common to define a free carrier radiative lifetime τ_{rad} as the time required for the excited carrier (electron or equivalently hole) to be radiatively annihilated in an e-h pair recombination. The radiative recombination rate for each charge carrier can thus be written as:

$$\frac{1}{\tau_{rad}} = \frac{n_e}{\langle \tau_r \rangle} = \frac{n_h}{\langle \tau_r \rangle}. \tag{3.30}$$

If we also consider non-radiative recombination processes and denote by τ_{nonrad} the non-radiative recombination lifetime, we can define the total recombination rate ($1/\tau_{tot}$) of e-h pairs as:

$$\frac{1}{\tau_{tot}} = \frac{1}{\tau_{rad}} + \frac{1}{\tau_{nonrad}}. \tag{3.31}$$

From the ratio of the radiative recombination rate to the total recombination rate, the luminescence efficiency can be derived:

$$\eta_R = \frac{1/\tau_{rad}}{1/\tau_{rad} + \tau_{nonrad}} = \frac{1}{1 + \tau_{rad}/\tau_{nonrad}}. \tag{3.32}$$

If $\tau_{rad} << \tau_{nonrad}$ it follows that $\eta_R \approx 1$ and the maximum possible emission is obtained. If $\tau_{rad} >> \tau_{nonrad}$ we have $\eta_R \approx 0$ and the processes of light emission are very inefficient. Thus, the shorter the radiative lifetime with respect to the non-radiative lifetime, the higher the luminescence efficiency of a PL experiment.

Considering the special case of a semiconductor with a direct bandgap, one can show (see [58]) that the intensity of a band-to-band spectrum of PL follows the proportionality relation:

$$I_{PL} \propto \begin{cases} (\hbar\omega - E_g)^{1/2} \, exp[-\hbar\omega/(K_B T)] & for \, \hbar\omega > E_g, \\ 0 & oterwhise. \end{cases} \tag{3.33}$$

where $\hbar\omega$ is the energy of the emitted photons [58]. From (3.33), the PL intensity increases due to the term $(\hbar\omega - E_g)^{1/2}$ but decreases exponentially due to the term $exp[-\hbar\omega/(K_B T)]$.

3.5.2 *Free-to-bound transition*

The basic description of PL emission in a semiconductor arises considering band-to-band transitions. In fact, however, other processes of e-h radiative recombination can occur that involve transitions between different energy levels. In the so-called free-to-bound transition, the recombination of a free charge carrier with a bound opposite charge takes place. The bound charge are trapped in acceptor or donor impurities. Thus, a free electron can recombine with a hole trapped at an acceptor, or a free hole can recombine with an electron trapped at a donor.
The energy levels of the acceptor or donor impurities are very close to the band extremes in the band gap and are therefore called shallow levels, analogously the acceptor or donor impurities are said shallow impurities. At a relatively high temperature, all the shallow impurities are ionized and no free-to-bound transitions occur. Conversely, at a sufficiently low temperature, the thermal energy is less than the ionization energy and the charge on the impurities is frozen, so that free-to-bound recombinations can occur. Examples of the emission of free-to-bound transitions are observed for Zn-doped GaAs at 4.2 K for various acceptor concentrations [208]. The emitted photon energy is given by:

$$\hbar\omega = E_g - E_{imp}, \quad (3.34)$$

where E_{imp} is the binding energy of the impurity. As can be seen from (3.34), the emission due to free-to-bound transitions can be exploited to measure the binding energy of impurities [58].

3.5.3 *Donor-acceptor pair transition*

Another process of e-h radiative recombination can involve the transition between two sites with opposite bound charges. This occurs in the so-called compensated semiconductors, in which both donor and acceptor impurities are present in similar concentrations. In a compensated semiconductor, we can consider an equilibrium situation in which there are ionized donors (D^+) and ionized acceptors (A^-), for example, due to the transitions of electrons from donors to acceptors. Free electrons from CB and free holes from VB can be trapped by ionized D^+ and A^-, respectively, leading to D^0 and A^0 neutral sites. Radiative recombination can occur via a transition of the electron in D^0 to the hole in A^0 and this process is called donor-acceptor pair transition. The energy of the emitted photon is given by:

$$\hbar\omega = E_g - E_D - E_A + \frac{e^2}{\epsilon R}, \quad (3.35)$$

where E_D and E_A are the donor and acceptor binding energies, respectively. The last term in (3.35) represents the increase in photon energy

corresponding to the lowering in the energy of the emitting pair of D^0 and A^0 due to the Coulomb attraction of the final state of the (D^+, A^-) pair. In the Coulomb term, ϵ is the static dielectric constant and R is the distance between the sites of the (D^+, A^-) pair.

3.5.4 *Exciton emission*

Another process of radiative recombination can occur via annihilation of the special state of the e-h pair known as exciton.
The Coulomb interaction between a photoexcited electron and the electrons remaining in the incompletely filled VB can be regarded as an e-h attractive interaction. The motion of this interacting electron and hole is correlated and the resulting e-h pair is called exciton [201].
If the conditions are given (e.g., low temperature) that the binding energy of the excitons is sufficiently larger than the thermal energy, the formation of excitons can be promoted in a PL experiment and their radiative annihilation produces PL emission. The aforementioned exciton state is called free-exciton to distinguish it from the bound-exciton, which is an exciton bound to a neutral impurity (D^0 or A^0) via an attractive van der Waals interaction. Bound excitons can also undergo radiative recombination, producing PL [58, 209, 210].
The energy of a photon emitted as a result of radiative recombination of an exciton can be written as follows:

$$\begin{aligned} \hbar\omega &= E_g - E_X \qquad (free - exciton) \\ \hbar\omega &= E_g - E_X - E_B \quad (bound - exciton) \end{aligned} \tag{3.36}$$

where E_X is the Coulomb energy of the exciton and E_B is the binding energy of the exciton to the impurity. Typical binding energy values of excitons in bulk semiconductors are of the order of $\sim$ 0.01 eV [211], which is well below the thermal energy at room temperature (RT) (0.026 eV), making radiative recombination of excitons very unlikely. For this reason, PL of free-excitons is usually observed at low temperature in high-purity and high-quality semiconductors [58]. When present, impurities are very efficient at trapping excitons and the emission of bound excitons is predominant in excitonic PL spectra. In certain cases, the excitons are also stable at RT. This is the case in two-dimensional samples of TMDs, where a remarkably large binding energy, an order of magnitude larger than that in bulk semiconductors, allows the observation of strong excitonic emission in RT PL experiments [47, 50, 144, 145, 212]. The reason for this huge binding energy is due to the strongly enhanced e-h Coulomb interaction, which is a consequence of the reduced dielectric screening in confined 2D crystals of TMDs [44, 45, 47, 213].

3.5.5 *Free-exciton PL in terms of exciton polariton emission*

To better understand the phenomenon of PL emission in semiconductors due to excitons, we need to introduce the concept of exciton-polariton (sometimes referred to as polariton for brevity), which we will discuss below.
An exciton can be considered as a two-particle system, its wave vector $\boldsymbol{K}$ can be assumed to be equal to $\boldsymbol{k_e} + \boldsymbol{k_h}$, where $\boldsymbol{k_e}$ and $\boldsymbol{k_h}$ are the wave vectors of the electron in CB and the hole in VB forming the e-h exciton pair. In this picture, the kinetic energy of the exciton can be expressed as the free particle expression $E_{ke} = \hbar^2 K^2/(2M)$, where M is the mass of the exciton $M = m_e + m_h$, with m_e and m_h, the effective masses of the electron and the hole, respectively [58]. The energy levels of an exciton can be represented by parabolas. When excited by light, an exciton can be thought of as the result of an optical absorption in which a photon is converted into an exciton. To satisfy conservation of energy and momentum, the conversion must occur at the intersection of the photon and exciton dispersion curves (see the dashed line in Figure 14).

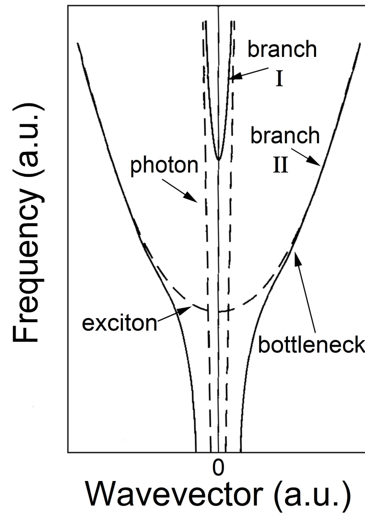

Figure 14. (solid curves) Exciton-polariton dispersion curves labeled as branch I and branch II and (dashed curves) dispersion curves of uncoupled photon and uncoupled exciton i.e. without considering their mutual interaction. Adapted from [58].

If we introduce an exciton-photon interaction, the exciton state must be more correctly interpreted as a combination of photon and exciton wave functions, and the resulting coupled state is known as exciton-polariton. An exciton-polariton can be viewed as a mixed mechanical-electromagnetic wave in the medium, where the mechanical component is a polarization wave associated with the electric dipole moments of

the excitons. In this picture, excitons radiate electromagnetic waves and, conversely, electromagnetic waves excite excitons. In an optical absorption process that leads to excitation of excitons, energy is converted from photons to excitons and vice versa, but energy is not necessarily lost in the medium, nor does optical absorption occur. Rather, absorption can occur because electron polaritons can undergo an inelastic scattering, e.g. with phonons.
In an PL experiment a photon field hits a sample, after inelastic scattering some optically excited exciton-polaritons can leave the sample by converting back to photons with a lower energy than the incoming photons, the exiting photon field forms the PL emission. The PL process can be explained with the help of Figure 14, exciton-polaritons (polaritons for brevity) can be optically excited into branch I, here they are called photon-like because of the predominant photon component of their wave functions. Their photon part has a very weak interaction with phonons. From branch I, the polaritons can be elastically scattered by defect into the branch II, here the polaritons have a predominant exciton component in their states and are called exciton-like. Unlike the photon component, the exciton component interacts very efficiently with phonons. The resulting relaxation process randomizes the energy and momentum distributions of the polaritons.
The conformation of the polariton dispersion curve shown in Figure 14, which has no energy minimum, does not suggest the occurrence of a peak in the energy distribution function of polaritons. Instead, however, as suggested by Toyozawa [214] and experimentally demonstrated by Askary and Yu [215], the polariton distribution has a peak, and it occurs in correspondence with the bottleneck of the branch II (see Figure 14). The PL spectrum results proportional to the product of the polariton distribution and the transmission coefficient of the polaritons at the exit [58]. Thus, with this approach it is possible to explain the shape and the energy position of the PL spectra in the case of exciton emission. In this work, the exciton emission was analysed to study the PL performance of nanosized samples of MoS_2.

3.6 FANO INTERFERENCE EFFECT IN RAMAN SCATTERING OF DOPED SI

This section is devoted to a basic description of Raman-specific Fano interference effects in Raman spectroscopy of highly doped semiconductors and in particular Si [23, 170]. Fano resonances were first described by Fano in his study of the absorption spectra of noble gases observed by Beutler [216, 217]. The nature of the unusual asymmetric sharp peaks in the electron energy loss spectrum of He was established by Fano via a theoretical treatment of the resonant interactions that occur in the excited gas between a discrete atomic eigenstate and a background of continuum eigenstates. In accordance with the superposition principle

of quantum mechanics, the asymmetry was attributed to quantum interference between the overlapping wavefunctions of the states. [170, 218, 219].
Asymmetry in Raman spectra of solid-state materials have been understood as Fano resonances in various studies on doped Si [23, 170, 171, 175, 220], Ge [221, 222], GaAs [221, 223], diamond [224, 225], and more recently in research on carbon nanotubes [226], graphene [227–230], WSe_2 [231], and in the layered topological insulator [232].
Cardona and coworkers were the first to adapt Fano theory to interpret striking spectroscopic effects in the Raman spectra of highly doped Si [23, 24, 175, 233]. In their work, it is observed how the one-phonon Raman spectral line changes as a function of both dopant concentration and excitation frequency. In highly doped Si, absorption of the exciting photons during a Raman scattering experiment can trigger, among other things, two processes, one leading to one-phonon Raman scattering and another involving interbands electronic transitions. In p-type (n-type) Si, these transitions consist of a one-electron excitation from filled to empty valence (conduction) bands [23, 170, 175, 220, 234]. The interbands electronic excitation can lead to inelastic scattering of electromagnetic radiation, a phenomenon known as electronic Raman scattering [235].

3.6.1 *p-type Si case*

In particular, in highly doped p-type Si, a high number of free holes is generated by the doping (the hole concentration varies approximately linearly with the dopant concentration [236]), and the Fermi level can be considered to be well below the valence band maximum, allowing inter-valence-band transitions [23]. As can be seen from the structure of the valence bands of Si (see Figure 15 (a) and (b)), electronic transitions from the light-hole valence band to the heavy-hole valence band with a continuum of electronic excitations can occur during the optical scattering process [170]. Because of the anisotropy of the valence bands (see Figure 15 (b)), the continuum of electronic excitation has energies that extend over a wide range, from a minimum to a maximum corresponding to the smallest and largest distance at $\boldsymbol{k} = \boldsymbol{k_F}$ between the light-hole and heavy-hole bands (with $\boldsymbol{k_F}$ the wavevector at Fermi energy μ). Since the minimum energy ω_m is smaller than the spin-orbit splitting of the valence bands in Si ($\sim 44\,meV$), and the maximum can be considered relatively high because of the flatness of the heavy-hole band in certain $\boldsymbol{k}$-directions, the continuum of energies overlaps with the discrete energy of about $65\,meV$ of the phonon of symmetry Γ'_{25} located at the Brillouin zone center involved in the one-phonon Raman scattering process [23, 68].
Due to the superposition principle of quantum mechanics, the coupling

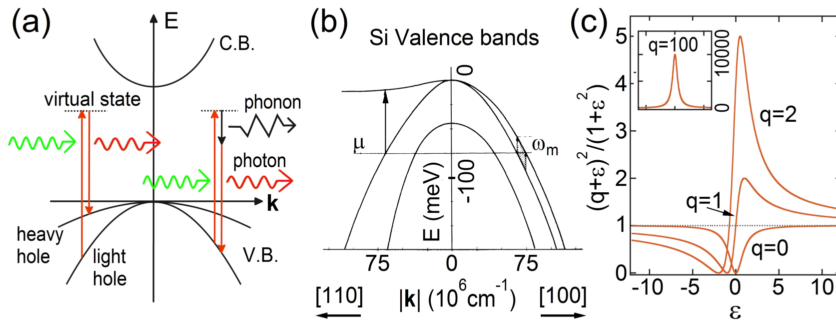

Figure 15. (a) Energy diagram of inter-valence-band transitions and optical phonon scattering in p-type Si for electronic and one-phonon Raman scattering. The vertical arrows mark the pure electronic transition between the light-hole and heavy-hole bands and the transition in one-phonon Raman scattering. (b) A detail of the valence bands in Si for two $\boldsymbol{k}$-directions in the BZ. Different inter-valence-band transitions from the Fermi level μ are shown by vertical arrows. The shaded region indicates the possible transitions for a given $\boldsymbol{k}$-direction. The smallest separation between the bands corresponds to the energy minimum of the electronic continuum. Adapted from [23]. (c) Plot of the Fano line shape (3.45) for various values of q. Adapted from [237].

via electron-phonon interaction between excited states with overlapping energies resulting from electronic Raman scattering and one-phonon Raman scattering leads to quantum interference, the effects of which are observable in the Raman spectrum as an asymmetric line shape of resonant emission (see Figure 15 (c)) [23, 170].

3.6.2 *n-type Si case*

Even in the case of highly doped n-type Si (e.g. with donor species like P, As, Sb), the high concentration of free electrons creates the conditions for the observation of interference phenomena as described by the Fano theory [23, 217, 218, 234].
In heavily doped n-type Si, the lowest conduction bands, i.e., the Δ_1 and Δ_2' bands along the <100> directions, can be sites of interband transitions ($\Delta_1 \rightarrow \Delta_2'$) by electronic Raman scattering, for example, after laser excitation in the visible [234]. In such a case, the electron excitations can interfere with the first-order one-phonon Raman excitation and produce a Fano-type asymmetric shape of the Raman Si line at 520 cm^{-1}. The energy of the electronic Raman interband transitions distributes in a continuum of values between a minimum $\hbar\omega_{min}$ and a maximum $\hbar\omega_{max}$ in dependence on the Fermi energy level, as shown in Figure 16.
If the doping is sufficiently high, the energy continuum contains the discrete energy of the one-phonon Raman transition and quantum interference between discrete and continuum excitations takes place

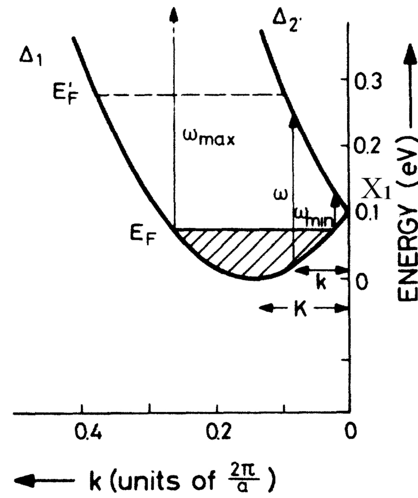

Figure 16. Schematic representation of the conduction bands in Si along the <100> direction near the edge of the Brillouin zone X_1. The bands are labelled Δ_1 and Δ_2'. $\hbar\omega$ is the energy difference between the two bands. For a given Fermi energy E_F, $\hbar\omega_{min}$, $\hbar\omega_{max}$ are the minimum and maximum transition energies associated with the electronic Raman scattering connecting Δ_1 and Δ_2'. E_F' indicates the Fermi level when it is above the high symmetry point X_1 at ~ 0.1 eV. Adapted from [220].

[234].

The conditions for Fano interference can be determined by simple reasoning. The bands Δ_1 and Δ_2' can be considered approximately parabolic at their minima, with the same concavity along the directions <100> and thus the same longitudinal effective mass m_l [220, 238–240]. Considering the Figure 16, the Δ_1 and Δ_2' bands can be thought of as longitudinally shifted from each other by 2K, where K denotes the minimum of Δ_1 measured from the edge of the BZ X_1 ($K = 2\pi/a \times 0.14$, with a the lattice constant [241]).

Given the above assumptions, simple geometrical considerations allow to express the energy differences between the bands Δ_1 and Δ_2' as follows [220]:

$$\hbar\omega = \frac{\hbar^2}{2m_l}[(K+k)^2 - (K-k)^2], \tag{3.37}$$

where k is indicated in Figure 16.

Considering a Fermi level E_F calculated from the minimum of the band Δ_1, and defining K_F from $E_F = \hbar^2 k_F^2/2m_l$, simple algebraic calculations lead to the determination of the minimum and maximum values of the transition energy corresponding to the electronic Raman scattering

[241]:

$$\hbar\omega_{min} = \mp\frac{\hbar^2 K^2}{m_l}(1 - \frac{k_F}{K}) \qquad \begin{cases} - & \text{if } k_F > K, \\ + & \text{if } k_F < K, \end{cases} \tag{3.38}$$

$$\hbar\omega_{max} = \frac{\hbar^2 K^2}{m_l}(1 + \frac{k_F}{K}). \tag{3.39}$$

Jouanne et al. [234] report that the energy continuum of Raman electronic excitations overlaps the discrete energy of the optical phonon of Si (65 eV) at a free electron concentration of at least 7×10^{19} cm^{-3}. Thus, a necessary condition for Fano interference to occur between active Raman excitations in n-type Si is that the dopant concentration be on the order of 10^{20} cm^{-3} and higher.

3.6.3 *General considerations*

Generally, a schematic representation of the Fano interaction between a continuum of excited states and a discrete excited state with overlapping energies can be seen in Figure 17.

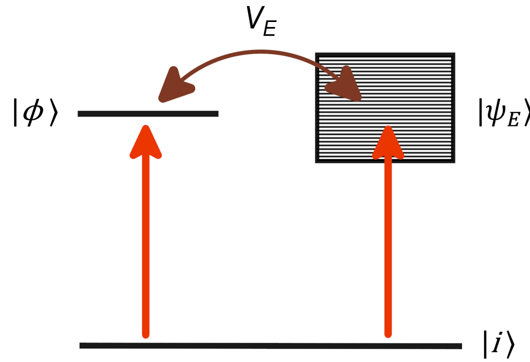

Figure 17. Schematic representation of a Fano resonance. If the system can be excited from an initial state $|i\rangle$ into a discrete state $|\phi\rangle$ or into a continuum of states $|\psi\rangle$ with two isoenergetic processes, and if the states are coupled by an interaction V_E, quantum interference takes place between the two paths, leading to Fano effects in absorption and emission spectroscopies. Adapted from [242].

According to Fano theory, if we consider a system in which a continuum of states $|\psi_E\rangle$ and a discrete state $|\phi\rangle$ with overlapping energy are available, the elements of the Hamiltonian matrix can be described as

follows [23, 218]:

$$\langle\phi|\,\hat{H}\,|\phi\rangle \;=\; E_\phi = \hbar\omega_0, \tag{3.40}$$

$$\langle\psi_E|\,\hat{H}\,|\phi\rangle \;=\; V_E, \tag{3.41}$$

$$\langle\psi_{E'}|\,\hat{H}\,|\psi_E\rangle \;=\; E\,\delta(E-E'). \tag{3.42}$$

Where $\hat{H}$ is the Hamiltonian, $E_\phi = \hbar\omega_0$ is the energy of the discrete state, V_E represents the coupling strength between the discrete and the continuum states and E is the energy associated with the continuum state $|\psi_E\rangle$ [14].
To give an example, the simplest quantum mechanical model that exhibits a Fano effect is the Fano-Anderson model of Hamiltonian [237]:

$$\hat{H} \;=\; E_\phi\hat{\phi}^+\hat{\phi} + \sum_E E\hat{b}_E^+\hat{b}_E + \sum_E V_E(\hat{\phi}\hat{b}_E^+ + \hat{\phi}^+\hat{b}_E), \tag{3.43}$$

where ϕ^+ (ϕ), b_E^+ (b_E) represent the operators of creation (annihilation) of the discrete state $|\phi\rangle$ and the continuous set of states $|\psi_E\rangle$, respectively [243].
The coupled system can be represented by an eigenvector $|\Psi_E\rangle$ given by a linear combination of the discrete eigenvector and the continuum of eigenvectors:

$$|\Psi_E\rangle \;=\; a_E\;|\phi\rangle + \int c_E\,|\psi_E\rangle\,dE, \tag{3.44}$$

with a_E, c_E functions of the energy. Given suitable transition operators $\hat{T}$, associated with an external perturbation, and an arbitrary initial state $|i\rangle$, the transition probabilities from $|i\rangle$ to the unperturbed continuum $|\psi_E\rangle$ and to the composite state $|\Psi_E\rangle$ can be defined as $|\langle\psi_E|\,\hat{T}\,|i\rangle|^2$ and $|\langle\Psi_E|\,\hat{T}\,|i\rangle|^2$, respectively.
Based on Fano theory, the ratio of the transition probability $|\langle\Psi_E|\,\hat{T}\,|i\rangle|^2$ to the probability $|\langle\psi_E|\,\hat{T}\,|i\rangle|^2$ is given by a single family of curves:

$$\frac{|\langle\Psi_E|\,\hat{T}\,|i\rangle|^2}{|\langle\psi_E|\,\hat{T}\,|i\rangle|^2} \;=\; \frac{(q+\varepsilon)^2}{1+\varepsilon^2}, \tag{3.45}$$

which also indicate the shape of the measured spectral lines. In (3.45) ε is

$$\varepsilon \;=\; \frac{\omega-\omega_0}{\Gamma_F}. \tag{3.46}$$

In the Raman spectrum of highly doped Si, ω_0 is the frequency of the central position of the one-phonon Raman peak, which is slightly shifted from the peak position in the absence of a continuum of states. We can set $\omega_0 = \omega_{intr} + \delta\omega$, where ω_{intr} is the frequency position of the one-phonon Raman peak of the intrinsic (undoped) material and $\delta\omega$ is the shift of the distorted signal due to the Fano interaction in the doped

material [26]. As a direct consequence of (3.45) and (3.46), ω_0 is simply related to the maximum and minimum points of the Fano curve:

$$\omega_0 = \omega_{max} - \Gamma_F / q, \tag{3.47}$$
$$\omega_0 = \omega_{min} + q\,\Gamma_F, \tag{3.48}$$

where ω_{max} (ω_{min}) is the frequency position of the maximum (minimum) of the Fano curve. Γ_F is the width of the distorted peak (more precisely the half width at half maximum of the Raman peak), again we can set $\Gamma_F = \Gamma_F^0 + \Gamma_L$, where Γ_L is the width in the absence of the Fano interaction as in undoped material, and Γ_F^0 is the additional contribution due to the electron-phonon interaction in highly doped material [14, 23, 28].
In [23] Γ_F and $\delta\omega$ are defined as:

$$\Gamma_F(\omega) = \frac{\pi}{\hbar} |V_E|^2, \tag{3.49}$$
$$\delta\omega(\omega) = \frac{1}{\pi} P \int d\omega' \frac{\Gamma_F(\omega')}{\omega - \omega'}, \tag{3.50}$$

where P denotes the principal value of the integral. Clearly, Γ_F and $\delta\omega$ depend on the coupling of the discrete excitation with the continuum (in (3.49) represented by the term V_E).
The parameter q in (3.45) can be written as [218]:

$$q = \frac{\langle\Phi|\,\hat{T}\,|i\rangle}{\pi \langle\phi|\,\hat{H}\,|\psi_E\rangle \langle\psi_E|\,\hat{T}\,|i\rangle} = \frac{\langle\Phi|\,\hat{T}\,|i\rangle}{\pi V_E^* \langle\psi_E|\,\hat{T}\,|i\rangle}, \tag{3.51}$$

where $|\Phi\rangle$ is the discrete state modified by its interaction with the continuum and can be written as follows [14, 218]:

$$|\Phi\rangle = |\phi\rangle + P \int V_{E'} \,|\psi_{E'}\rangle / (E - E')dE'. \tag{3.52}$$

Substituting (3.52) into (3.51), we get:

$$q = \frac{\langle\phi|\,\hat{T}\,|i\rangle + P\int V_{E'}^* \langle\psi_E'|\,\hat{T}\,|i\rangle / (E-E')\,dE'}{\pi V_E^* \langle\psi_E|\,\hat{T}\,|i\rangle}. \tag{3.53}$$

From this relation we can clearly see that q depends not only on the discrete-continuum coupling, but also on the relative excitation probabilities associated with the discrete and the continuum levels [237].
The parameter q determines the asymmetry of the Fano curves $(q + \varepsilon)^2/(1+\varepsilon^2)$ outlining the Raman line. The Fano curves become completely symmetric and Lorentzian in shape in the limit $|q| \to \infty$, while the asymmetry increases with decreasing value of |q|. When q is positive (as happens in p-type Si [23, 24]), the shape of the curve assumes an intensity gain on the high-energy side of the maximum (see Figure 15 (c)), when q is negative (as happens in n-type Si [220, 234]), the

gain is on the low-energy side. However, the sensitivity of the experimentally observable Fano effects at comparable doping concentrations is much higher for p-type Si than for n-type Si [220, 234, 244].
The Fano parameters q, Γ_F^0 and $\delta\omega$ can be expressed in terms of the microscopic properties of the material [24, 220]:

$$q = \Big(\frac{V_p T_p}{T_e} + \delta\omega\Big) / \Gamma_F^0, \tag{3.54}$$

$$\Gamma_F^0 = \pi V_p^2 D_d(\omega_{intr}), \tag{3.55}$$

$$\delta\omega = V_p^2 P \int D_d(\omega') \, (\frac{1}{\omega_{intr} - \omega'} - \frac{1}{-\omega_{intr} - \omega'}) \, d\omega'. \tag{3.56}$$

where V_p is an average of matrix elements for the electron-phonon interaction and T_p and T_e are the Raman matrix element connecting the ground and excited states of the phonon and electron in the continuum (T_e is also an average). The average spans the different excitable states of the continuum, taking into account the multiplicity of states for each energy when moving in k-space on a constant energy surface [23]. $D_d(\omega)$ is the combined density of states for the direct transition in the electronic continuum, P denotes the principal value of the integral.
$\delta\omega$ and Γ_F^0 represent the variation of the real and imaginary parts of the phonon self-energy due to the electron-phonon interaction [23] and are independent of the excitation frequency [175], but depend on the doping-induced free-carrier concentration [24].
As can be deduced from (3.54), the asymmetry parameter q depends on the other two parameters $\delta\omega$ and Γ_F^0 and thus on the concentration of free-carriers, moreover q depends on the excitation frequency via the ratio T_p/T_e [24]. In [24] studying boron doped Si (p-type Si), T_p and T_e are expressed as a function of the laser excitation frequency ω_L as:

$$T_p \sim P(\omega_L) \, \omega_L, \tag{3.57}$$

$$T_e \sim \Big(\frac{1}{\hbar\omega_L + E_g} - \frac{1}{\hbar\omega_L - E_g}\Big), \tag{3.58}$$

where $P(\omega_L)$ is the Raman tensor [220] and $E_g \simeq 3.4eV$ is the direct band gap in Si [245].
Again for p-type Si, in [23, 175] Cerdeira et al. determined the dependence of q on the excitation energy as:

$$q \propto (\omega_0' - \omega_L)^{-1}, \tag{3.59}$$

with $\hbar\omega_0' = 3.37 \, eV$ the energy of the zone center direct transition (E_0') in Si [245]. This dependence was derived from the resonant behavior of the ratio $T_p/T_e \propto (\omega_0' - \omega_L)^{-1}$ as ω_L approaches the value of ω_0', is thus strictly valid only for ω_L near the energy gap, but it has been shown to be valid also below ω_0' in the visible range [23, 175].
In this work, the relevance of Raman-specific Fano resonances has been

exploited to develop a fast, non-invasive and non-destructive method for doping monitoring of p-type Si. The concepts presented here will be further explored in the experimental study reported in chapter 5.

4 EXPERIMENTAL METHODOLOGY

The aim of this chapter is to provide an overview of the methodological approach used in this thesis to determine the useful parameters for the silicon and MoS_2 analysis techniques that will be developed in subsequent chapters. The three sections of the chapter describe the experimental setup, samples and methods used to acquire and study the Raman and PL spectra of Si and MoS_2.
In section 4.1 we start with a general explanation of the spectrometer setup with an illustration of the main parts of a Raman spectrometer. We then introduce the instruments used for the Raman and PL experiments in this work. We conclude the section with an overview of the other instruments and ancillary techniques used.
The second section 4.2 deals with the material and methods used for the doping characterization research of Si, which will be developed later in the section 5. We describe in turn the Si-based material samples used in the research, the geometrical configuration of the Raman spectroscopy experiments, and the optimal setting of the acquisition parameters for the best collection of Raman spectra. The section concludes with an illustration of the post-processing of the recorded spectra documenting the fitting method used to evaluate the Fano effect in the Raman spectra of doped Si, which is useful for the scope of this research.
The third section 4.3 deals with the preparation and characterization of MoS_2. The methodology explained in this section forms the basis for the experiments that will be developed later in section 6 to study the optoelectronic properties of 2D MoS_2. We will give a brief insight into the preparation and characterization of the samples to determine the number of layers. We will then explain the method used to analyse the Raman and PL spectra of single-layer MoS_2 samples, which is useful to obtain information about the optical and electrical properties of this material. We then report on the experimental setting of the acquisition parameters for optimal Raman and PL data acquisition, and describe the annealing procedures performed on MoS_2 samples to produce changes in the doping content in this material, which are useful for doping-dependent optoelectronic studies. This section concludes with the presentation of a statistical model of the population density of excitonic states in MoS_2, useful for understanding the excitonic PL emission and estimating the density of free electrons in the monolayer flakes of MoS_2.

4.1 EXPERIMENTAL SETUP

4.1.1 *Basic setup of a Raman and PL spectroscopy system*

Spectroscopies based on laser excitation are common characterization techniques for the study of crystals from bulk to two-dimensional phase. PL and Raman spectroscopy are examples of these techniques, which have benefited in recent decades from the technological development of lasers, detectors and, more recently, confocal microscopy, which allows improved spatial resolution down to the micrometer scale in all three dimensions. PL spectroscopy is performed with essentially the same experimental equipment used for Raman spectroscopy. Therefore, we will focus on the description of a Raman setup in the following.
Raman spectroscopy uses a second-order inelastic scattering process involving interactions between photons, electrons, and phonons, and has very low efficiency compared to first-order Rayleigh scattering, whose emission accounts for most of the scattered light in a Raman spectroscopy experiment. The Rayleigh signal is 4-6 orders of magnitude stronger than the Raman signal in most light scattering experiments on semiconductors [58], and typically only one photon out of 10^{12} of the incident photons is Raman-scattered [174]. For this reason, any component in the experimental setup capable of exciting the Raman effect and collecting the scattered radiation in Raman spectroscopy must be very effective. The main components of a Raman instrument are: a source of a collimated beam of monochromatic light, usually produced by a laser, an optical system such as a lens or microscope to focus the exciting beam on the sample and capture the scattered radiation, a filter, to eliminate the overwhelming Rayleigh emission and capture only the inelastic component of the scattered beam, a spectrometer to spatially separate the different spectral elements of the remaining scattered beam, and finally a detector stage to record and display the inelastic scattered radiation.
Figure 18 shows a schematic illustration of a general Raman setup. The same setup can be used to collect PL emission by changing the diffraction grating and conventional spectral frequency units accordingly. The incident light that effectively promotes Raman scattering processes is provided by a laser. Originally, C.V. Raman in his pioneering experiment in 1928 used monochromatic light obtained by filtering sunlight to obtain the radiation source [172, 246, 247] and before the advent of the laser researchers used discharge lamps, but spontaneous Raman radiation from opaque semiconductors became feasible only after the availability of continuous-wave (cw) lasers [58]. Typical examples of cw lasers are He-Ne gas laser with a wavelength of 632.8 nm, Ar^+ and Kr^+ gas ion lasers, whose most commonly used emission wavelengths are 647 nm, 564 nm, 514 nm, 488 nm and 458 nm. Another historically important laser is the Nd:YAG solid-state laser, whose wavelength of

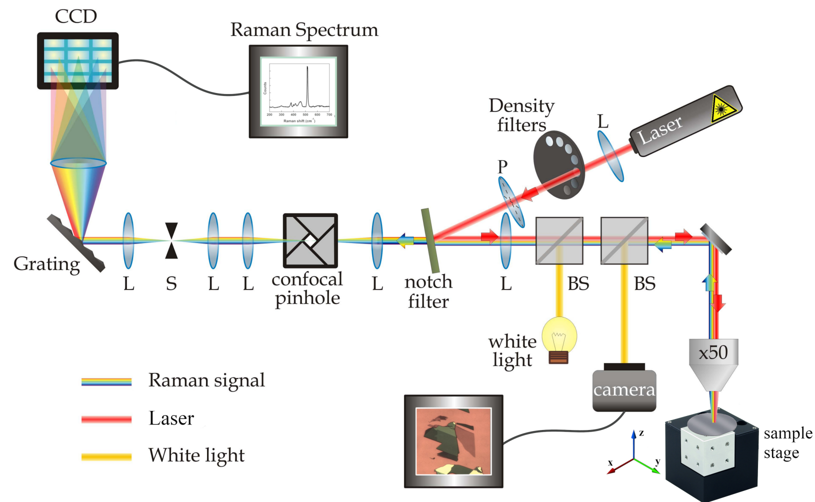

Figure 18. Schematic optical diagram of a micro-Raman spectrometer.

1064 nm can be frequency-doubled to produce laser light at 532 nm or higher harmonics at 355 nm, 266 nm, and so on. Today, it is also possible to resort to lasers whose wavelength can be continuously adjusted. An example are dye lasers ($1\mu m \geq \lambda \geq 450nm$) [58].
The power of the laser can be attenuated by interchangeable neutral density filters (ND). The ND filters allow precise adjustment of the laser power and reduce the intensity of all wavelengths equally. A ND filter can be identified by its optical density $D = -log_{10}I/I_0$, where D is the optical density, I_0 is the incident intensity, and I is the intensity after filtering. In this way, the fraction of power transmitted by the filter can be calculated by the fractional transmittance $T = I/I_0 = 10^{-D}$. For example, a filter with $D = 0.6$ ($T = 0.25$) releases 25% of the original laser power.
After filtering, the polarization of the beam is cleaned up using a polarizer (P) and then hits the notch filter, which at this stage acts as a reflecting mirror and directs the beam onto a microscope objective. Then the beam is focused on the specimen, which is on a motorized XYZ stage. Typically, the laser beam is focused on the sample with a high magnification objective, producing a laser spot about $1\mu m$ in diameter, which gives this technique of Raman spectroscopy its "micro" attribute. The lateral resolution, i.e., the smallest distance between two points that can be uniquely examined, can be defined as the diameter of the focused laser spot. If we consider the laser beam as a Gaussian beam just filling the focusing lens of the objective, we can define the minimum diameter of the beam at the focal point as $d_0 \simeq \lambda/\pi\theta$, where λ is the laser wavelength and θ is the divergence angle of the beam

identified with the numerical aperture (NA) of the objective [248]. For high NA objectives (i.e., 0.9 or more), as typically used in micro-Raman spectroscopy, a better approximation to d_0 is given by $d_0 \simeq 1.22\lambda/NA$ [248, 249]. Another important parameter characterizing a focused beam is the depth of focus $L = 2\,z_R$, where z_R is the so-called Rayleigh range $z_R = \pi d_0^2/\lambda$. L can be considered as the vertical resolution, which is generally of the order of micrometers when the material under investigation is transparent. For high NA objectives, L can be approximated by $L \simeq 4\lambda/NA^2$ [248, 249].
Generally, a color camera and a white light lamp are connected to the microscope so that the microscope view can be followed on a monitor. In this way, the microscope can be operated like a conventional optical microscope when the laser beam is blocked, and the specimen can be viewed after focusing.
In backscattering configuration, both the Raman and Rayleigh signals from the sample are collected by the same focusing microscope objective and redirected to the notch filter, which operates in transmission mode. In this case, the notch filter acts as a band-pass filter to remove the Rayleigh emission and prevent the stronger elastic Rayleigh signal from overlaying the weaker inelastic Raman signal. A notch filter has a sharp absorption peak at the laser wavelength and typically has an average transmission intensity of $\geq 90\%$ and a cutoff around $150\,cm^{-1}$ and transmits all other wavelengths as Stokes and anti-Stokes Raman signal and PL emission.
Then the backscattered light is focused on an adjustable pinhole (known as confocal pinhole), which blocks the light contribution that does not originate from the focal plane of the microscope [250]. It is important to note that only rays originating from the focal plane of the microscope objective, within the depth of focus in the case of a transparent specimen or within the depth of penetration in the case of an opaque sample, contribute to the detected signal.
After passing through the confocal pinhole, the light is focused on the entrance slit of the spectrometer and directed, collimated by optical elements, onto a diffraction grating that disperses the individual wavelength components at different angles, resulting in spatial separation of the wavelengths. A diffraction grating consists of a highly reflective material whose surface is etched by a series of very closely spaced grooves. Different types of gratings with different groove densities can be used (300 grooves/mm, 1800 grooves/mm and 2400 grooves/mm for our setups). The higher the groove density, the greater the dispersion. The angle of the grating can be changed (remotely by the computer) to select different frequency ranges of the spectrum to be measured.
The spectrometer projects the wavelength-dispersed light of the Raman signal onto the long axis of a charged coupled device (CCD) detector to record the spectrum by converting the photons into usable electronic signatures. A silicon-based CCD detector is suitable for UV, visible,

and near-infrared radiation. A CCD detector consists of a rectangular array of a large number (i.e., 1024×256) of individual light-sensitive, small-area elements called pixels, which allow multichannel detection, i.e., it can measure many different wavelengths at the same time. It works by the photoelectric process, that is, it responds to the photons illumination by releasing electrons. When a photon hits a pixel, it excites an electron from the valence band to the conduction band, from where it is stored in a capacitor. The charge stored on each pixel capacitor during a spectrum acquisition is proportional to the number of photons that have impinged on the pixel. The brighter the light and the longer the integration time, the more charge is stored. Each pixel along a longitudinal axis of the CCD detector corresponds to a small range of wavelengths, and the arrangement of pixels along the entire CCD axis allows the entire spectrum to be captured and registered. The first pixel detects wavelengths from the edge of the spectrum with lower wavenumber and the last pixel detects wavelengths from the edge of the spectrum with higher wavenumber. So the spectral resolution depends on the density of the pixels and the dispersion power of the grating (typically a few units cm^{-1}). The CCD detector must be cooled to minimize dark current in the pixels, which causes noise in the spectrum. Cooling is often provided by thermoelectric coolers that exploit the Peltier effect (down to -90 °C) or by cryogenic cooling with liquid nitrogen. Finally, a computer integrated in the instrument allows the observation and recording of the spectra, as well as the control of some mechanical parameters of the instrument and the programming of the detection in terms of spectral range, accumulation number and acquisition time.

4.1.2 *Raman and PL instruments*

The general operation of a device for performing Raman and PL experiments has just been described, now we report some technical details and specifications of the devices used in this thesis. We rely on two commercially produced devices, a *LabRAM* system from *Horiba Jobin Yvon* and an *InVia* system from *Renishaw*. Both systems are similar in basic structure and operating mechanism, but differ in design and equipment. We stress that prior to each set of measurement, the spectrometers were frequency calibrated and "health checks" were performed, using unstressed undoped CZ Silicon (face orientation (100)) by setting the first-order Raman peak wavenumber position at 520.3 ± 0.5; 520.5 ± 0.5; and 520.50 ± 0.75 cm^{-1} for the excitation lasers of 632.8, 532 and 355 nm respectively.

Horiba Jobin Yvon - LabRAM. This system is equipped with a He-Ne laser with parallel polarized monochromatic light of wavelength 632.8

nm (1.96 eV, red) and power 1 mW. Neutral density filters to attenuate the laser power are available with optical densities (and transmittances) of 0.3 (50%); 0.6 (25%); 1.0 (10%); 2.0 (1%). An Olimpus Bx40 optical microscope is integrated into the system with various objectives with magnification (and NA) of 10x (0.25); 20x (0.5); 50x (0.7); 100x (0.9). A notch filter Super Notch Plus with a suppression coefficient for the laser radiation > 10^6 is used. Spectral data are typically taken with the 100x objective, which gives a laser spot diameter of $\sim 1\,\mu m$. The measurement is performed with the sample at room temperature and in ambient air. Two interchangeable diffraction gratings are available mounted on the same shaft: a holographic grating with 1800 grooves/mm and a ruled grating with 300 grooves/mm. The system has a Peltier-cooled CCD detector with a size of 1024x256 pixels (pixel size 27 μm) cooled to -62 °C. The overall achievable spectral resolution is $\sim 1 cm^{-1}$ for Raman experiments (using 1800 grooves/mm grating) and 1 nm for PL experiments (using 300 grooves/mm grating).

Renishaw - InVia. This system is equipped with two laser sources of parallel polarized monochromatic light, a frequency-doubled Nd:YAG laser with a wavelength of 532 nm (2.33 eV, green) and a frequency-tripled Nd:YAG laser with a wavelength of 355 nm (3.49 eV, near-UV). Each laser has a different beam path between the laser and the objective position. After that, the beam paths are the same, but the objective, lens, and grating are adjusted for the particular wavelength used. The 532 nm laser operates with a confocal microscope with a 100x objective of 0.9 NA, which gives a laser spot diameter of $\sim 0.7\,\mu m$ and operates with a 1800 grooves/mm diffraction grating. The 355 nm laser uses a 40x magnification objective of 0.47 NA, resulting in a laser spot diameter of $\sim 1\,\mu m$ and operates with a 2400 grooves/mm diffraction grating. The system uses a CCD detector cooled to -65 °C with a Peltier-effect cooler. The overall spectral resolution achievable with the 532 nm laser is $\sim (1 \div 2)\, cm^{-1}$, while in the case of the 355 nm laser it is $\sim 2 cm^{-1}$. The laser power is 40 mW and 8 mW for the 532 nm and 355 nm lasers, respectively. Neutral density filters are available to attenuate the laser power.

4.1.3 *Additional instruments*

Optical microscope - Olympus BH2-UMA. This metallographic microscope is equipped with 5x, 20x, 50x, and 100x objectives and operates under broadband illumination by a 3200 K unfiltered halogen lamp. A JVC digital camera model TK-C1380 is integrated with the microscope and used for digital image acquisition. Here this device is used principally for the optical identification of 2D sample flakes of MoS_2 deposited onto atomically flat SiO_2/Si(100) substrate

Atomic force microscope (AFM) - Digital D5000 - Veeco. This AFM system operates in Tepping-mode [251] by using P doped n-type Si cantilever from Veeco (model RTESP with 100 KHz or 300 KHz nominal resonance frequency). Here is used principally for measurements of the high profile of the 2D flakes of MoS_2.

Heater systems for annealing processes. Nabertherm-P330 furnace and Hiedolph magnetic stirrer/heater are used for annealing processes in ambient air up to 400 °C. An ultra high vacuum (UHV) chamber borrowed from an X-ray photoelectron spectroscopy (XPS) setup is used for UHV annealing at 10^{-9} Torr up to 300 °C. These devices are used for annealing experiments on MoS_2 samples.

4.1.4 *Ancillary techniques*

To support the examination of Si wafer samples with respect to crystal structure state and doping configuration, we have relied on additional characterization techniques performed in external laboratories. Details on the working principle of these techniques can be found in [252].

Secondary ion mass spectrometry (SIMS). SIMS analyses were carried out in the Material Characterization Lab of the Centre for Materials and Microsystems - Fondazione Bruno Kesler - Trento (Italy). The analyses were performed using a Cameca SC -Ultra SIMS with a 1 keV ${O_2}^+$ primary ion beam at an angle of incidence of 68°. Sputter thickness measurements were performed with a mechanical profiler. The B and F secondary ion signals were converted to concentrations using reference materials calibrated with NIST samples. The SiO^+ signal was acquired to identify a surface oxide layer.

Spreading resistance profiling (SRP). SRP analyses were performed at Solecon Labs - Reno, Nevada (USA) using Si wafer samples with a bevel angle of 0.0045 rad (relative accuracy 3%) and measurement intervals of 2 μm step size providing $\sim 9\,nm$ depth resolution.

Transmission electron microscopy (TEM). TEM analyses were performed at Lfoundry - Physical and Failure Analysis Lab in Avezzano (Italy). Measurements were performed with a TECNAI G^2 TF30 STEM system. Samples for cross-sectional TEM acquisitions were cut from Si wafers and thinned to electron transparency by focused ion beam milling (FIB). Low and atomic resolution images were acquired under TEM bright field conditions using a high energy electron beam (300 keV). Diffraction patterns were recorded in diffraction mode.

4.2 SILICON ANALYSIS: MATERIALS AND METHODS

To characterize the dopant concentration in silicon as developed in chapter 5, we exploit the effect of Fano interference that appears in

the Raman spectrum of single-crystal Si samples (see section 3.6). We use the changes in the first-order Raman Si peak (520 cm^{-1}) to obtain information about the doping concentration in the material. We use different Si samples and methods illustrated in the following sections.

4.2.1 *Si samples*

Czochralski Si samples (CZ-Si). First, we use Si wafers prepared by the Czochralski method [253] with a homogeneous and constant dopant content throughout the volume of the material. These are monocrystalline Si(100) wafers with a diameter of 200 mm doped with boron at various concentrations measured with a relative uncertainty of 10% (in units cm^{-3} 6.0×10^{14}; 3.1×10^{15}; 3.0×10^{18}; 7.5×10^{18}; 1.8×10^{19}; 5.0×10^{19}.). The wafer with the lowest concentration can be considered like a reference sample for pure silicon, as suggested in [25]. These samples, whose crystalline and doping properties are very reliable, are used to find an accurate relation between the doping concentration and the features of the Raman Si peak, whose line shape depends on the doping via the Fano effect (see section 3.6). They are used in the section (5.2.1) to obtain a calibration of the spectral parameters for a quantitative analysis of the doping concentration in p-type Si with visible and near-UV Raman spectroscopy.

$BF_2{}^+$ implanted Si samples. Other samples used (see section 5.2.2) are p-type Si wafers obtained by ion implantation. Starting materials were p-type CZ-grown Si(100) wafers with a diameter of 200 mm and a B concentration of 1×10^{15} cm^{-3}. $BF_2{}^+$ ions with low kinetic energy (5 keV) were implanted onto the starting material at different doses, namely 5×10^{13} 5×10^{14} and 5×10^{15} At/cm^2. To activate the doping and restore the crystalline structure after implantation damage, the wafers were annealed using a laser thermal annealing process (LTA), which is known to lead to a box-shaped concentration profile [254, 255]. LTA was performed with an excimer laser using XeCl (wavelength 308 nm), in which the energy density of 2.15 J/cm^2 is irradiated onto the wafer surface in a single shot with a pulse duration of 160 ns (highest temperature of the annealed region of 1400 °C).
Implantation and annealing conditions were designed to achieve homogeneous doping from the surface to a depth of $\sim$ 100 nm. TEM and SIMS were considered to characterize the crystal recovery and doping profile of these samples (see Figure 28 in section 5.2.2).
Given the isoenergetic nature of the ion beam for each implantation dose, which results in an equivalent doping depth, the doping concentrations were estimated using the known doses via an optimized calibration by the SIMS doping profile of the sample implanted with the highest dose. Relying on the well-established LTA technique for crystal recovery and dopant activation [254, 255], and on the TEM im-

ages showing a highly ordered crystal pattern and a diffraction pattern typical of a single crystal (see Figure 28 in section 5.2.2), the doping concentration was estimated by assuming that the concentration of B atoms measured by SIMS corresponds to the concentration of charge carriers. The estimated doping concentrations are 3.5×10^{18}, 3.5×10^{19}, and 3.5×10^{20} cm^{-3} with a relative uncertainty of 15 %.
These samples provide an example of a modern nanoelectronic Si material with a very shallow doping configuration. Moreover, they are also useful for the question of the dimensioning experiment, where the different penetration depths of the laser excitation wavelengths into the material play an important role.

Si samples for doping profiling (beveled sample). Other Si samples were used to further develop the Raman-based doping characterization technique with the aim of determining the doping profile of the material with high spatial resolution (see section 5.2.3). We used realistic samples of the material of state-of-the-art electronic devices by analysing Si wafers with a doping configuration typical of the active regions of an n-channel field-effect transistor (FET) of a CMOS image sensor [256]. These samples are produced by B and BF_2^+ ion implantation and rapid thermal recovery (B and BF_2^+ doses up to 3×10^{15} At/cm^2, kinetic energies up to 15 keV (510 keV) for shallow (deep) doping configuration, rapid thermal processes with temperatures up to 1080 °C). As starting material we used Si(100) wafers, 200 mm diameter, composed of a superficial (4 μm thick) layer of p-type epitaxially grown Si at low B concentration of 7×10^{14} cm^{-3}. SIMS and SRP analysis were performed for the independent characterization of the doping concentration profile (see Figure 32 (a), (b) and (c) in section 5.2.3).
To probe the doping profiling technique (described in section 5.2.3), we used two beveled twin samples of the most heavily doped wafer from the sample set just mentioned. This wafer exhibits very high surface doping, starting with a concentration of 1.2×10^{20} cm^{-3} at the first nanometers depth and then steeply decreasing to a relatively low value within 200 nm depth (see Figure 32 (c)). The beveled surface is obtained by a beveling method used in the SRP technique, and the bevel angle (with respect to the basal plane direction of the wafer) is 0.0045 rad ($\pm$3%) [29].

4.2.2 *Si crystal orientation and scattering configuration*

Raman spectroscopy experiments were performed in backscattering configuration. The Si samples were positioned so that the [001]-crystal axis was parallel to the direction of the incident laser beam (z-axis of the laboratory). The polarization direction $\hat{\mathbf{e}}_\mathbf{i}$ of the incident light is set to match the [110] crystallographic direction of the Si lattice, while the scattered light is not under any control ($\hat{\mathbf{e}}_\mathbf{s}$ is free). Under this scattering

configuration, only the first-order one-phonon Raman scattering with the LO phonon is observed in crystalline Si [257, 258].

4.2.3 *Considerations on the spectral effects of laser power*

Since the technique developed in chapter 5 for monitoring the doping of Si is based on the measurement of the first-order Raman Si peak, it is important to make some methodological considerations about the effects on peak properties due to laser heating and free-hole pumping during excitation of spectra, which are directly related to laser power. The effects of laser heating on the shape and position of Raman spectral peaks are evident in nanometer-scale materials such as semiconductor nanowires and nanocrystals [259–262].

In Si nanostructures, typical peak changes upon laser heating are a frequency softening of the first-order Raman Si peak and an asymmetric broadening of the peak (generally toward the low-energy side of the peak) [259, 261, 262]. In [262], Raman spectra of Si nanowires show typical heating effects at laser powers above 0.5 mW (using a laser wavelength of 514 nm with a focal spot of $\sim 1\ \mu$m). In the range of $(0.5 \div 1.5)$ mW, the Raman Si peak exhibits a red-shift of about 0.5 cm^{-1} and the FWHM shows a broadening of about 0.6 cm^{-1} [262].

Indeed, nanoscale materials lead to asymmetric broadening of Raman peaks, and some studies attribute these changes to the effect of physical confinement of phonons in nanostructures [263–265] or to the effect of Fano interference [266–268] rather than to laser heating.

Adu et al. [260, 269] support the hypothesis of spectral modification as an effect of laser heating with the main evidence that the asymmetric broadening of Raman peaks decreases for semiconductor nanowires in thermal contact with a substrate compared to suspended nanowires. In the case of material in contact with the substrate, the substrate acts as a heat sink that intercepts the thermal energy emitted by the laser [260]. This also shows that the effects of laser heating are highly dependent on the ability of the laser probed material to dissipate the absorbed thermal energy.

The effects of laser heating can also be seen in Raman spectra of bulk Si samples, as shown in [270, 271]. In [270], the author reports a redshift of the first-order Raman Si peak as a function of incident laser power. The peak frequency softening has approximately a linear trend and totals 0.25 cm^{-1} in the power range $(\sim 1 \div 8)$ mW (using a laser with a wavelength of 458 nm and a focal spot of $\sim 1\mu$m. In [271], the authors show a redshift of about 1 cm^{-1} and a peak broadening of about 3.5 cm^{-1} for a variation of the laser power of about three orders of magnitude in the range $(0 \div 200)$ mW (using lasers with a wavelength of 532 nm and a focal spot of $\sim 1\mu$m).

In addition to laser heating effects, another possible manifestation in the Raman spectrum of Si directly related to the laser power could

be a Fano interference effect originating from the free holes excited by the laser itself [25]. Magidson et al. [25] first reported laser power-dependent Fano effects in undoped Si by showing that a Fano-type asymmetry of the Raman Si peak occurs when using lasers of 27 mW and 81 mW power, but not at 5 mW (using lasers with a wavelength of 514 nm and a focal spot of $\sim 1\mu$m).
In our analyses, the power of the lasers incident on the Si samples was kept sufficiently low ($\leq$5 mW) to avoid significant influence of light-induced free holes [25]. Conversely, sufficiently long integration time intervals of 3 to 10 seconds were used to maximise the signal-to-noise ratio. Laser heating effects cannot be excluded in our spectral data. This is especially true when using the laser with the wavelength of 355 nm, since the high absorption of Si at this wavelength implies thermal energy transfer into a volume of nanometric thickness (the penetration depth of 355 nm light in Si is $\sim$ 10 nm [272]). Nevertheless, due to the continuity of the probed volume with the innermost material, we can exclude a similarity with the case of a nanosized material.
Once the laser power is fixed, we can consider the effects of laser heating as systematic and constant spectral features that depend on the experimental setup. These effects do not affect the technique developed in chapter 5 for the characterization of doping in Si, which is based on the analysis of spectral changes in the Raman spectra of doped samples compared with (undoped) reference samples using experimental setups with controlled properties specified for each series of analyses.

4.2.4 *Fitting method for Raman analysis of Fano effect*

Fano function. As discussed in section 3.6, the shape of the Raman Si peak in undoped material can be well described by a Lorentzian distribution [273], while the same spectral signal in doped Si is better fitted by a Fano function [23, 24, 175, 233]. We propose a revised model of the Fano function, slightly different from the original expression: $A\,(q+\varepsilon)^2/(1+\varepsilon^2)$ where $\varepsilon = (\omega-\omega_0)/\Gamma_F$ and A is a scaling factor [24]. We use the expression:

$$F_{q,\Gamma_F}(\omega) = y_0 + m\omega + \frac{H}{q^2+1}\,\frac{\left[q+\left(\frac{\omega-\omega_0}{\Gamma_F}\right)\right]^2}{1+\left(\frac{\omega-\omega_0}{\Gamma_F}\right)^2}, \tag{4.1}$$

where y_0, m, H, q, ω_0, Γ_F are the adjustable parameters in the last square fit of the spectrum in the range $[470 \div 570]$ cm^{-1}, which covers well the first-order Raman Si peak. In Eq. 4.1 we included a linear background ($y_0 + m\omega$) with intercept y_0 and slope m. The Fano parameters ω_0 and Γ_F represent the frequency position and the half width at half maximum (HWHM) of the Fano line-shape, respectively (hence we often refer to $2\Gamma_F$ as the full width at half maximum (FWHM)). The pa-

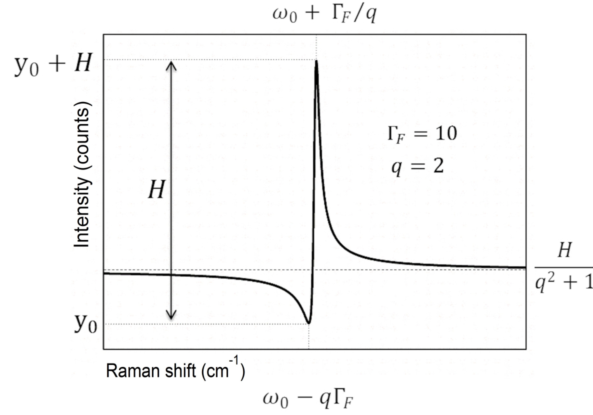

Figure 19. Schematic line-shape of a Fano function (Eq. 4.1) with $\Gamma_F = 10$ and $q = 2$.

rameter q is the asymmetry parameter and the parameter H represents the amplitude of the Fano function from the minimum to the maximum of the function profile, which are $(\omega_0 - q\Gamma_F)$ and $(\omega_0 + \Gamma_F/q)$, respectively. In Figure 19 is shown an example of a Fano line shape with $\Gamma_F = 10$ and $q = 2$, (the background slope m is set to 0 for simplicity). The novelty of this model function is the factor $(H/(q^2+1))$, where H and q are decoupled, allowing a direct measurement of the amplitude H, whereas in the previous representation of the Fano function the amplitude of the peak also depended on the value of q.
As explained in section 3.6, the central frequency position ω_0 can be viewed as the sum of two contributions ω_{intr} and $\delta\omega$ $(\omega_0 = \omega_{intr} + \delta\omega)$, ω_{intr} represents the central frequency position of the Raman Si peak of the intrinsic (*undoped*) Si crystal, and $\delta\omega$ is the frequency shift of the peak in the doped material with respect to the intrinsic value [26]. Like ω_0, the FWHM of the Fano peak can also be interpreted as the sum of two contributions, $(2\Gamma_F = 2\Gamma_L + 2\Gamma_F^0)$, where $2\Gamma_L$ represents the width of the intrinsic Si peak, which would have a Lorentzian shape, and $2\Gamma_F^0$ is the additional broadening of the peak that depends on the doping concentration. For an effective evaluation of the Raman Si peak features, we must also take into account the peak broadening caused by the measurement system itself. To account for this instrumental effect, we have chosen as a fitting function a convolution of the Fano function with a unit-area Gaussian function, as shown in the relation:

$$\mathcal{C}(\omega) = \int_{-\infty}^{+\infty} F_{q,\Gamma_F}(\omega')\, G_\sigma(\omega' - \omega) d\omega' = F_{q,\Gamma_F} * G_\sigma, \tag{4.2}$$

where $G_\sigma(\omega) = 1/\sqrt{2\pi\sigma^2}\, exp(-\omega^2/2\sigma^2)$ is a Gaussian centered in zero with standard deviation σ, ω is the frequency in cm^{-1} and ω' is the integration variable. The width of the Gaussian $(\propto \sigma)$ is determined

by the combination of several factors introduced by the experimental system, namely the quality of the laser beam through its coherence and bandwidth, the dispersion power of the diffraction grating, the size of the confocal pinhole and the spectrometer entrance slit, and finally the quality of the objective and other optical elements [274, 275]. The standard deviation σ of the Gaussian was determined for each experimental setup by a preliminary analysis in which its value was considered as an adjustable parameter of the fit. Subsequently, this value was fixed for all fitting experiments. In this way, the Fano parameters resulting from the fitting analysis are *deconvolved* data and can be considered independent of the particular recording system. This facilitates comparison with theory.

Fitting process and goodness of the fit. The fitting of the Raman spectra by the convolved Fano-Gaussian function was obtained by an adapted program developed for this purpose using the data analysis software Igor Pro [276]. The fitting process uses minimization of the statistical variable *Chi-square* (X^2) as determined in the least-squares method implemented in the Igor Pro program. Here, X^2 is defined as:

$$X^2 = \sum_{i=1}^{n} \frac{(y_i - \varphi(x_i, \vec{\theta}))^2}{\sigma_i^2}$$

where φ is the fitting function such that $\varphi(x_i, \vec{\theta})$ is the fitted value for the data point x_i, y_i is the original data for that point, $\vec{\theta} = (\theta_1, \theta_2, ..., \theta_r)$ describes the parameters of the fitting model, and σ_i is the standard error for the data y_i. The process of minimization is iterative, as the fitting tries different values for the unknown parameters, starting from initial guesses that are reasonably chosen, i.e., starting from values that are already given in the literature.
In our case, where the fitting function is not a straight line, the program uses a form of nonlinear least squares method based on the Levenberg-Marquardt algorithm [276, 277]. The fitting process returns the best values for the parameters along with the associated uncertainties resulting from the variance of the parameters from the trend of X^2 near the minimum (see the labels in Figure 20).
We used $\mathcal{C}(\omega)$ (eq. 4.2) as the fitting function and considered the spectral data in a limited interval around the Raman Si peak. The experimental data y_i represent the intensity counts of the Raman spectrum and as the standard error σ_i for each y_i we used the square root of the data itself, since y_i can be considered as a Poisson variable corresponding to a number of counts in one bin of an intensity histogram. To evaluate the goodness of fit, we used the χ^2 test with number of freedom degrees the number of data points minus the number of free fit parameters. As an example, we show in Figure 20 the fit of the Raman Si peak of a p-type Si sample, in the labels we give the obtained fit parameters and the

calculated value of the Chi-square ($X^2_{fit} = 22.9$). The number of degrees of freedom is $n - r = 33 - 6 = 27$. At a significance level of 5%, the tabulated critical value of χ^2 in the case of 27 degrees of freedom is 40.1. Thus, the calculated Chi-square is smaller than the tabulated value and we can accept the initial hypothesis that the data are described by the assumed fitting model.

The described method allows to obtain the fitting parameters $2\Gamma_F$ and ω_0 with uncertainties of 0.02 cm^{-1} (0.04 cm^{-1} for $2\Gamma^0_F$ and $\delta\omega$), the parameters H and q are determined with uncertainties of 0.3% and 2%, respectively. Assuming that the estimates of the adjustable parameters of the fit are considered as Gaussian random variables, their determinations with the uncertainties obtained by the square root of the variances give confidence intervals with a confidence level of 68%.

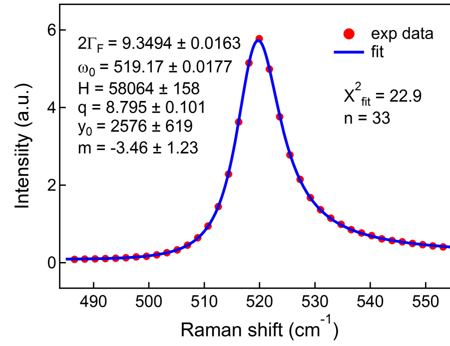

Figure 20. Schematic of a Raman Si peak fit with calculated Chi-square.

4.3 MoS_2 ANALYSIS: MATERIALS AND METHODS

In the following, we report samples and methods useful for research on MoS_2 reported in chapter 6. To obtain MoS_2 samples where the number of constituent layers is precisely known, we referred to our previous studies [75, 278].

4.3.1 *Samples of MoS_2 monolayer*

Few-layer MoS_2 flakes were mechanically exfoliated from bulk material SPI Supplies® Molybdenite in single crystal with a lateral dimension and thickness of $\sim (0.8 \times 0.8 \times 0.2)$ cm. We used the micromechanical exfoliation technique based on scotch-tape cleavage. To obtain the largest number of single- and few-layer MoS_2 flakes with the largest surface area, the number of iterations of scotch-tape cleavage was optimally adjusted from a minimum of three to a maximum of six [75]. The exfoliated flakes were deposited on atomically flat SiO_2/Si(100) wafer samples with a lateral size of ~ 1 cm. The thickness of the surface oxide layer was chosen to be 270 nm, which gives the optimal optical contrast for the detection of atomically thin TMDG flakes [279].

Before the MoS_2 flakes were transferred to the substrate with scotch-tape, the SiO_2/Si wafer samples were cleaned by three successive sonication cycles (10 min each) in acetone, isopropyl alcohol, and distilled water and dried under nitrogen flow. After the scotch-tape transfer, glue

residue was removed from the wafer samples in three successive baths at 40 °C for 10 min each in acetone, isopropyl alcohol, and distilled water. The samples were stored in plastic containers in air at normal temperature and pressure (NTP).
We then used optical microscopy and AFM studies to identify MoS_2 flakes with micrometric lateral dimensions and nanometric thickness. We used a method that synergistically employs optical microscopy, AFM, Raman spectroscopy, and PL spectroscopy to characterize the MoS_2 flakes and accurately determine the number of layers of the flakes. A preliminary screening of the flakes was performed using optical microscopy by analyzing the optical contrast between the flakes and the substrates [280, 281].
Further investigation of flake thickness was carried out using AFM to distinguish between flakes with few layers and thicker flakes, which were shown to have similar optical contrast [75]. The presence of a non-uniformly arranged water film under the MoS_2 flake at the interface with the substrate with a thickness of 1-2 nm does not allow an accurate measurement of the flake height by AFM for a reliable assessment of the number of layers composing each flake.
Therefore, we used a method based on resonant Raman spectroscopy (achievable with excitation at a wavelength of 632.8 nm [161, 163, 282]) and PL spectroscopy to effectively estimate the number of layers of MoS_2 flakes from 1 to 5. Quantitative analysis based on intensity comparison of resonant Raman spectra of MoS_2 flakes allows discrimination between flakes with different numbers of layers. The analysis of the PL signal detectable in the [750 ÷ 950] nm spectral region, originating from the indirect transition in the band gap of MoS_2 samples with few layers, but not in the monolayer MoS_2, which has a direct band gap, allowed the confirmation of the number of layers [75]. The absence of such a spectral PL feature also provided a fingerprint signature of the single-layer MoS_2 phase. The combined analysis of the Raman and PL spectra (via the intensity ratio of the two spectral types [75]) allowed further accurate layer numbering by eliminating the spectral effects due to the SiO_2/Si substrate that affect both the individual Raman and PL measurements [75].
Finally, monolayer MoS_2 flakes were unambiguously confirmed by non-resonant Raman experiments at an excitation wavelength of 532 nm (see Figure 9 (c) in section 2.2.3). All monolayer samples exhibited the typical distance of $\sim 18\,cm^{-1}$ (within experimental precision) between the first-order Raman peak E^1_{2g} and A_{1g} [46, 122, 162]

4.3.2 *Resonant Raman spectrum of MoS_2 monolayer*

In section 6.2.5 we report observations of changes in the resonant Raman spectra of monolayer MoS_2 flakes that occur as a consequence of an

annealing process. In Figure 44, we show the resonant Raman spectral emission of monolayer MoS_2 before and after annealing of the sample. Resonant conditions were achieved with excitation at a wavelength of 632.8 nm and using a spectrometer grating with 1800 grooves/mm. Under resonant conditions the second-order Raman scattering processes can be even more intense than the first-order Raman modes [58]. We observe the change in intensity of some peaks hidden in the complex spectral structure due to the envelope of the different Raman emissions produced by first and second order scattering processes. We have restricted our analysis to the $[360 \div 480]$ cm^{-1} spectral region where the most intense Raman features are observed [161, 163, 282]. We fitted each spectrum with a sum of Voigt line shapes [283] positioned in correspondence with spectral peaks due to specific Raman scattering interactions with phonons in the material. The energies of these phonons can be inferred from the spectral frequency position of the Raman peaks and can be compared with the energies of the high-symmetry points in the phonon dispersion curves in the first BZ of MoS_2 (see Figure 9 (b) in section 2.2.3). The identification of the overlapping peaks, as indicated in the labels in Figure 44 in section 6.2.5, was determined according to various studies in the literature [122, 161, 284, 285] and supported by energy comparisons using the phonon dispersion curves.
The background PL signal, present in the resonant Raman spectrum of single-layer MoS_2, was subtracted with a spline fit to obtain a better comparison of Raman spectral features.
All Raman spectra of the MoS_2 samples were normalized to the integrated intensity of the first-order Raman-Si peak (520 cm^{-1}) of the SiO_2/Si substrate acquired with the same acquisition setting and laser spot focusing of the MoS_2 Raman acquisition, unless otherwise stated. This was particularly useful for obtaining information from the intensity of the MoS_2 spectra taken before and after thermal annealing of the sample under study and used in the intensity ratio relation in the section 6.2.5. The normalization to the Si peak intensity is necessary to neutralize the fluctuation of the spectral intensity due to the inevitable variations of the recording conditions such as the focusing of the laser spot and the fluctuation in laser power.

4.3.3 *PL spectrum of MoS_2 monolayer*

Concerning the PL measurements, the PL spectra of 2D MoS_2 samples and of monolayer MoS_2 before and after annealing were recorded under identical experimental conditions at room temperature with excitation at a wavelength of 632.8 nm and using a 300 grooves/mm grating. The broad PL peak at $\sim$ 670 nm (1.84 eV), which is due to the superposition of two PL emissions produced by the radiative recombination of neutral and charged (trion) excitons in the monolayer MoS_2 [45, 47, 147, 286],

was fitted with two Lorentzian peaks slightly shifted in energy (see Figure 40 in section 6.2.2). The central energy positions of the exciton and trion peaks (labelled A^0 and A^-) were constrained during the fitting to fixed values derived from the theoretically calculated binding energies of the excitonic states and the value of the direct band gap in single-layer MoS_2, as reported in [3]. The binding energies of the neutral exciton and trion were taken to be 277 meV and 306 meV, respectively, and the direct band gap was taken to be 2.14 eV [109].
The thin spectral feature at $\sim$ 654 nm (1.89 eV) on the left shoulder of the PL peak of single-layer MoS_2 was attributed to the first-order Raman Si peak (520 cm^{-1}) of the SiO_2/Si substrate. In some cases, the second-order Raman band of Si in the range [920 $\div$ 1000] $cm^{-}1$ is also just visible in the PL spectrum of MoS_2 at the corresponding energy position.

4.3.4 *Setting for Raman measurements of MoS_2 samples*

To avoid damage to the MoS_2 flakes by the laser radiation, the laser power was set to 1 mW (or less for the power-dependent PL measurements using neutral density filters in section 6.2.4) for all Raman and PL experiments [287]. The acquisition time was set to 240 sec for Raman experiments and 10 sec for PL experiments, which is the best compromise with the spectral signal-to-noise ratio in both cases.

4.3.5 *Annealing procedures*

Annealing procedures were performed in air and in UHV. Each annealing process was performed on fresh exfoliated MoS_2 samples deposited on a SiO_2/Si wafer sample substrate. In air, samples were annealed using a Hiedolph magnetic stirrer/heater with the wafer sample positioned on the hot plate and the temperature controlled with a thermocouple thermometer. The annealing temperatures were set at 200, 250, 275, 300, and 400 °C, with each annealing lasting 40 min. In UHV annealing, the wafer sample was placed in the analysis chamber of an XPS instrument, then the pressure in the chamber was gradually decreased to 10^{-9} Torr in 20 min, then the temperature was increased from RT to 300 °C in 10 min. Other air annealing processes were performed using a Nabertherm P330 furnace, temperatures were selected between 200 and 300 °C at 12.5 °C intervals, and each annealing performed on freshly exfoliated MoS_2 samples lasted 1 hour. The annealing times were reasonably chosen based on previous studies [49, 288–291]

4.3.6 *Free electron density by three level model and mass-action law*

To calculate the density of free electrons (n_{el}) in the MoS_2 single layer by PL analysis, as reported in section 6.2.4, we used a three-level

model and a law of mass action based on the dynamical equilibrium between neutral excitons A⁰ , charged excitons (trions) A⁻ , and free electrons. The three-level model statistically describes the mechanism of PL emission in its A⁰ and A⁻ components. In Figure 21 we show an

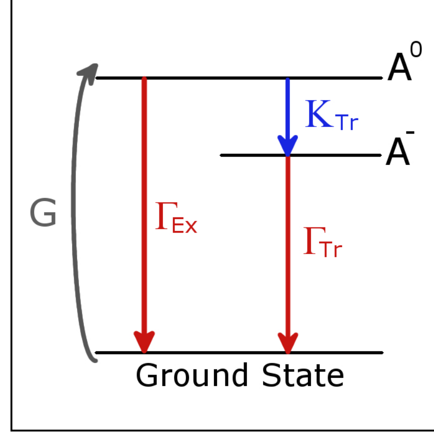

Figure 21. Energy level diagram of the three-level model for excitonic states in 2D MoS_2. The three levels are the **Ground State**, the neutral exciton state **A⁰** and the trion state **A⁻** .

energy level scheme of the three level model that includes a groud state a neutral exciton state and a charged exciton (trion) state. If we denote N_{A^0} and N_{A^-} as the density populations of excitons and trions, we can express the changes of N_{A^0} and N_{A^-} by the differential equations:

$$\begin{cases} \dfrac{dN_{A^0}}{dt} = G - (\Gamma_{Ex} + K_{Tr}) N_{A^0}, \\ \dfrac{dN_{A^-}}{dt} = K_{Tr} N_{A^0} - \Gamma_{Tr} N_{A^-}, \end{cases} \tag{4.3}$$

where G is the optical generation rate of excitons A⁰ , K_{Tr} is the formation rate of trions A⁻ , Γ_{Ex} is the total (radiative and non-radiative) decay rate of excitons A⁰ , and Γ_{Tr} is the total decay rate of trions A⁻ . During the PL experiment, in quasi-thermal equilibrium condition, we can consider $\frac{dN_{A^0}}{dt} = 0$ and $\frac{dN_{A^-}}{dt} = 0$, obtaining from Eqs. (4.3):

$$\begin{cases} N_{A^0} = \dfrac{G}{\Gamma_{Ex} + K_{Tr}}, \\ N_{A^-} = \dfrac{K_{Tr} N_{A^0}}{\Gamma_{Tr}} = \dfrac{K_{Tr} G}{\Gamma_{Tr} (\Gamma_{Ex} + K_{Tr})}. \end{cases} \tag{4.4}$$

The A⁰ and A⁻ components of the PL peak of monolayer MoS_2 (see Figure 40 in section 6.2.2) have intensities directly proportional to the population density N_{A^0} and N_{A^-}, respectively. Thus, if we denote I_{A^0} and I_{A^-} as the integrated intensities of the A⁰ and A⁻ components of

the PL peak, we can state:

$$\begin{cases} I_{A^0} = CN_{A^0}\gamma_{Ex}\,, \\ I_{A^-} = CN_{A^-}\gamma_{Tr}\,. \end{cases} \tag{4.5}$$

where γ_{Ex} and γ_{Tr} are the rates of radiative recombination of excitons and trions, respectively. C is a constant that depends on the efficiency of the experimental setup [292].
Using the above relations (4.5) we can calculate the intensity ratio I_A^- / I_{total} (where $I_{total} = I_A^0 + I_A^-$) as follows:

$$\frac{I_A^-}{I_{total}} = \frac{\frac{\gamma_{Tr}}{\gamma_{Ex}}\frac{N_{A^-}}{N_{A^0}}}{1 + \frac{\gamma_{Tr}}{\gamma_{Ex}}\frac{N_{A^-}}{N_{A^0}}}, \tag{4.6}$$

from which we simply obtain N_A^- / N_A^0 as:

$$\frac{N_A^-}{N_A^0} = \frac{\frac{I_A^-}{I_{total}}}{\frac{\gamma_{Tr}}{\gamma_{Ex}}\left(1 - \frac{I_A^-}{I_{total}}\right)}. \tag{4.7}$$

The ratio N_A^- / N_A^0 can be related to the density of free electrons (n_{el}) by the law of mass action in the form of the Saha equation [293, 294]:

$$\frac{N_{A^0} n_{el}}{N_{A^-}} = \frac{4 m_{A^0} m_e}{\pi \hbar^2 m_{A^-}} \cdot K_B T \cdot e^{-\frac{E_b}{K_B T}}\,, \tag{4.8}$$

where E_b is the trion binding energy (relative to the exciton binding energy, $\sim$ 29 meV in our calculation [3]), T is the temperature, K_B is the Boltzmann constant, $m_e = 0.35\, m_0$, $m_A{}^0 = 0.8\, m_0$, $m_A{}^- = 1.15\, m_0$ are the effective masses of the electron in the conduction band, the exciton and the trion, in units of the rest mass of the electron m_0 [106, 292].
From Eq. (4.8) we get:

$$\frac{N_A^-}{N_A^0} = \frac{n_{el}}{\frac{4 m_{A^0} m_e}{\pi \hbar^2 m_{A^-}} \cdot K_B T \cdot e^{-\frac{E_b}{K_B T}}}, \tag{4.9}$$

and using (4.9) in (4.7) we obtain after simple algebra:

$$n_{el} = \frac{\frac{I_A^-}{I_{total}}}{\frac{\gamma_{Tr}}{\gamma_{Ex}}\left(1 - \frac{I_A^-}{I_{total}}\right)} \left(\frac{4 m_{A^0} m_e}{\pi \hbar^2 m_{A^-}} \cdot K_B T \cdot e^{-\frac{E_b}{K_B T}}\right). \tag{4.10}$$

We now adopt the assumptions of Mouri et al. [292] that the values of γ_{Ex} and γ_{Tr} are essentially independent of the charge carrier density in the material, and set $\gamma_{Tr}/\gamma_{Ex} \simeq 0.15$ following the same authors [292].
Finally, using the above parameters, we obtain:

$$n_{el} = \frac{10^{14}\frac{I_A^-}{I_{total}}}{4\left(1 - \frac{I_A^-}{I_{total}}\right)} [cm^{-2}]. \tag{4.11}$$

We use this expression in section 6.2.4 to estimate the average electron density in the MoS_2 monolayer before and after annealing.

5 DOPING CHARACTERIZATION OF P-TYPE SI WAFERS VIA MULTI-WAVELENGTH MICRO-RAMAN SPECTROSCOPY

In semiconductor device manufacturing, process control and material characterization are essential due to the very high complexity of the entire process flow [210]. In particular, for the fabrication of advanced silicon-based integrated circuits, it is of utmost importance that the doping of the material introduced into the semiconductor substrate either by diffusion [295], ion implantation [296] or epitaxial growth [297] is carried out in concentrations and spatial arrangement that optimally match the design intentions. For this reason, it is important to rely on analytical methods to measure the doping state of the material, possibly after the various processes involved in the introduction and activation of the dopant and other high-temperature process steps that may inevitably affect the spatial configuration of the dopant [298–300].
In this chapter we study the reliability of a doping characterization technique. We exploit the Fano interference effect in highly doped p-type Si [22, 217, 218] through a multi-wavelength excitation Raman study [23, 24, 170].
Details on Fano interference theory can be found in section 3.6.
We use the change in the Raman spectrum of Si due to the Fano effect to characterize the doping state of p-type Si wafers commonly used for semiconductor device fabrication [14, 25–28, 244].
Our characterization includes dopant concentration in situations with constant dopant in the volume of the material, as well as in situations with shallow and ultrashallow dopant configurations with a strong concentration gradient that allows dopant profiling [15, 301, 302].
Ideally, the approach used in this chapter for the doping characterization of p-type Si could also be applied to n-type Si, although in this case the effectiveness of the characterization can be expected only for really high doping concentrations (on the order of 10^{20} cm^{-3} and higher), as can be deduced from various works in the literature in which the Fano effect has been detected in Raman spectra of heavily doped n-type Si [220, 234, 241] (see the discussion in section 3.6).
In section 5.1 we present the need for doping characterization in nanoelectronics, the state of the art of current solutions and our proposed approach based on Raman spectroscopy.
The details of the materials and methods used for the following experimental analyses are described in the Experimental Methodology chapter (see section 4.2).
Raman analyses on differently doped p-type Si samples are reported in section 5.2, where we illustrate our proposed doping characterization technique in section 5.2.1 with an application in section 5.2.2 and dop-

ing profiling in section 5.2.3.
Section 5.3 concludes the study reporting the principal results and achievements.
The results presented in this chapter was published in the journals, *Applied Surface Science 561 (2021) 149691* [1] and *Applied Surface Science 567 (2021) 150824* [2].

5.1 INTRODUCTION

State-of-the-art nanoelectronics inherently implies the fabrication of Silicon-based architectures with engineered doping level at the nanometer scale [33, 303]. Therefore, the integration of differentiated doped regions with high and medium doping concentration is required, in some cases with shallow and ultrashallow doping configuration, exhibiting a steep gradient of doping concentration decreasing from the highest value (of the order of 10^{20} cm^{-3}) near the surface to 5-6 orders of magnitude with increasing depth in the range of tens of nm [304]. Accurate measurement and characterization tools to determine the doping concentration, dopant activation, and dopant depth profile are therefore essential for proper design and require analytical methods with adequate spatial resolution in both lateral and depth directions [244, 305–312].
In this perspective, various methods are currently used to study the doping content of Si-based materials, which have different drawbacks. In some cases these techniques are destructive, such as propagation resistance profiling (SRP) [12, 313] and secondary ion mass spectrometry (SIMS) [13]. In other cases, these techniques have very low spatial resolution, such as electrochemical capacitance voltage (ECV) [10, 14, 19] and four-point-probe resistivity measurements [11].
Specifically for doping concentration profiling, SIMS and SRP are the current standard techniques. Using ion sputtering and mass spectroscopy in high vacuum equipment, SIMS provides an in-depth elemental dopant profile, whether or not the atoms of the dopant species are electrically active. SIMS potential sensitivity is 1 part-per-million (ppm) and achieves high lateral resolution (0.1-0.2 μm) and very high depth resolution (1 nm) [20, 21, 210, 313–315]. The SRP technique provides a profile of charge carrier concentration by measuring the spreading resistance between two ohmic metal-semiconductor contacts [12]. The SRP method is based on the study of the vertical distribution of carrier concentration using an angle lapped sample (bevel), where the depth dimension is stretched to a straight line along the downward direction of the wedge surface. SRP can probe a large concentration range (10^{12}-10^{21} cm^{-3}), but its spatial resolution is determined by the size of the electrical contact (about 1-4 μm), the spacing of the probes (not less than 20 μm), and the penetration of the probes into the beveled surface [16, 17, 210]. At standard probe loads of 10-15 g, penetration

of the probes into the material of about 10 nm has been measured, resulting in a local pressure of more than 10 GPa, which can distort the measurement [18]. Therefore, this technique has some shortcomings for accurate studies once the doping profile needs to be measured with nanometric accuracy.

Raman spectroscopy can be a possible alternative to the above techniques for doping characterization, which we aim to show with our studies. Indeed, Raman spectroscopy has been widely used to characterise heavily doped mono-crystalline Si [23–28] and its application has moved to the analysis of poly-crystalline Si [244, 301, 316–318], amorphous [319–321] Si and Si-based materials [257, 258, 322, 323]. Micro-Raman spectroscopy allows lateral resolution of about one micrometer, which is useful for analyzing small sample volumes, and the possibility to select the excitation wavelength, which changes the optical penetration depths, allows Raman experiments to probe both the bulk and surface of the analyzed material [275]. Considering the currently produced Si-based nanoelectronic devices, visible excitations are not suitable to probe their doping configuration at the nanoscale. For this reason, ultraviolet (UV) radiation is highly recommended compared to visible radiation, since Si absorbs strongly in the UV region, resulting in a shallower optical penetration depth of a few nanometers [272, 324], with the advantage that the optical setup normally used for visible micro-Raman experiments is also suitable for UV experiments [275]. In this respect, it should be emphasised that near-UV light is also advantageous for exploiting resonance-related effects due to its excitation energy close to the direct band gap of Si ($\sim$ 3.4 eV [245]), leading to an improved signal-to-noise ratio [325]. Furthermore, the high lateral (1 μm) and vertical (10 nm) resolutions achievable with near-UV excitation (355 nm wavelength) suggest that the implementation of a Raman technique to small-angle beveled samples (as in the SRP technique), could lead to potential use cases for doping profiling. Due to its specific technological appeal, near-UV Raman spectroscopy has been proposed for the study of complicated Si doped architectures and patterned wafers [174, 257, 325–327]. However, despite its potential benefits in nanoelectronics and the rich physics behind, so far, only few Raman studies have been performed on doped Si with near-UV radiation, and a comprehensive and validating Raman study using both visible and near-UV excitations and covering a wide range of doping concentrations has not yet been published in the literature for the very simple mono-crystalline Si system.

In addition, there are only few scattered studies dealing with Raman characterization by a small-angle beveling technique. [14, 328, 329]. These are mainly concerned with stress profiling of beveled undoped Si on relaxed SiGe substrate using visible and UV excitation [328, 329] or doping characterization at micrometric level using visible excitation of heavily doped beveled p-type regions on the backside of Si solar

cells [14]. The above visible excitation approaches are not suitable to effectively study beveled Si with shallow doping concentration at the nanoscale, which requires UV excitation.
In this perspective, we aimed to revisit the pioneering studies of Cardona's research group [23, 24, 175, 220, 233, 330] that date back to 70's and are considered milestones in this field of research, to update the methodological approach of doping concentration monitoring by Raman investigation to the state-of-the-art of nanoelectronic devices.
Indeed, Cardona and coworkers by monitoring the energy position, width, and intensity of the first-order Si Raman peak, have demonstrated the reliability of Raman analysis for controlling the doping concentration of p- and n-type doped mono-crystalline Si. They focused on a range of high doping concentrations (5×10^{18} - $4 \times 10^{20}\ cm^{-3}$) using only visible radiation [23, 24].
Their studies allowed the understanding of the Raman phenomenology of the first-order Si Raman peak with the doping concentration in the framework of the Fano interference model [22–24, 218]. Typically, the first-order Si Raman peak analysis within Fano model uses three main adjustable fitting parameters: the peak position, the full width at half maximum (FWHM) and the asymmetry parameter (q) [23, 170, 171]. In particular, according to the Fano theory [23], the first two primary parameters (peak position and FWHM) are expected to be independent of the excitation wavelength and dependent on the doping concentration. However, only Burke et al. [26] clearly reported this occurrence over a limited data range (7×10^{18}-$2.5 \times 10^{20}\ cm^{-3}$) together with other sparse evidence [27, 28]. The third parameter (q) quantifies the peculiar asymmetry of the Si peak upon doping and is expected to depend on both the excitation and doping concentrations. As in Cardona's model [24], q is not independent of peak position and FWHM, so that direct assignment of this parameter to physical "observables" is not straightforward. Indeed, researchers have so far focused only on the dependence of the parameter q on the doping concentration, obtaining scattered results that point out to a linear trend [14, 27, 28]. On the other hand, little attention has been paid to the dependence of the parameter q on the excitation wavelength, except for the first pioneering studies with visible radiation, which suggest a linear behavior [23, 175].
As for doping concentration studies, today's computational power enables accurate fitting with Fano and Gaussian convolved functions and complete control of the fitting processes with a detailed Chi-Square (χ^2) analysis. This rigorous fitting can increase the confidence error in the determination of the fitting parameters and consequently allows the extension of the approach to the study of low concentration regimes.
To fill this research gap, in this work we have extended Raman analysis of single-crystal Si using Fano effect interpretation to near-UV excitation and to a wide range of doping concentrations even at low concentrations (10^{14}-$10^{15}\ cm^{-3}$) to asses the portability of the Fano model analysis

proposed by Cardona's group to modern nanoelectronics and to determine the sensitivity of the technique to very low doping concentrations. In particular, we have performed a wavelength-dependent micro-Raman study under ambient conditions and at room temperature (RT) on p-type B-doped Czochralski (CZ) Si(100) wafers covering a wide range of doping concentrations from 6×10^{14} to 5×10^{19} cm^{-3} and using visible and near-UV laser excitations (632.8, 532, and 355 nm). The first-order Raman Si peak was fitted to a convolved Gaussian-Fano function using an improved fitting process that allows to accurately determine the variations in peak width and position. The entire Raman analysis is fully consistent for both visible and near-UV excitations and fully portable to near-UV radiation.
Furthermore, the portability of the analysis to state-of-the-art nanoelectronic devices is directly demonstrated using Si mono-crystalline Si wafers fabricated by BF_2^+ ion implantation and restored by laser thermal annealing (LTA).
As for the doping profiling analysis, we have tested the capability of UV micro-Raman spectroscopy as an alternative tool for doping profiling by using adjacent measurement points on beveled small-angle samples of ion-implanted and thermally recovered single-crystal p-type B-doped Si(100) wafers. Our study focuses on the broadening analysis of the first-order Si Raman peak for direct extrapolation of a doping concentration profile using a specific calibration curve derived from mono-crystalline CZ-Si wafers with well-established and homogeneous doping concentration. The results are also compared with other dopant profiling techniques, e.g. SRP and SIMS, taking into account that SRP measures the concentration of charge carriers and SIMS measures the totality of dopant atoms, which corresponds to an electrically active dopant concentration only if the crystal is perfectly recovered after the doping process.
Both the Raman and SRP methods require a beveling process, but are less expensive than SIMS. Compared to SRP, the Raman-based technique promises potentially better spatial resolution, which depends on the laser source and experimental setup used, and also does not require contact of the probe with the surface under investigation.

5.2 RESULTS AND DISCUSSION

5.2.1 *Raman analysis of Czochralski silicon wafers*

In this section, we report the results of Raman analysis within the Fano model of p-type B-doped CZ-Si samples and directly compare our results with relevant literature data. Figure 22 (panels (a), (b), and (c)) reports, superimposed, the Raman spectra taken at varying doping concentration using different excitation wavelengths (632.8, 532, and 355 nm). The spectra were normalized to the maximum peak intensity

of each recording. All raw Raman spectral data of the CZ-Si samples are shown in Figure 23 to provide directly discernible qualitative information about the change in spectral properties with the change in dopant concentration. From the upper panels of Figure 22 a general broadening of the first-order Raman Si peak for each excitation with increasing doping concentration is clearly visible. For visible excitation (632.8 and 532 nm) it is also noticeable an increasing asymmetry of the peak as a function of the B-doping concentration. However, in the case of UV (355 nm), broadening is observed but the spectra do not appear asymmetric.

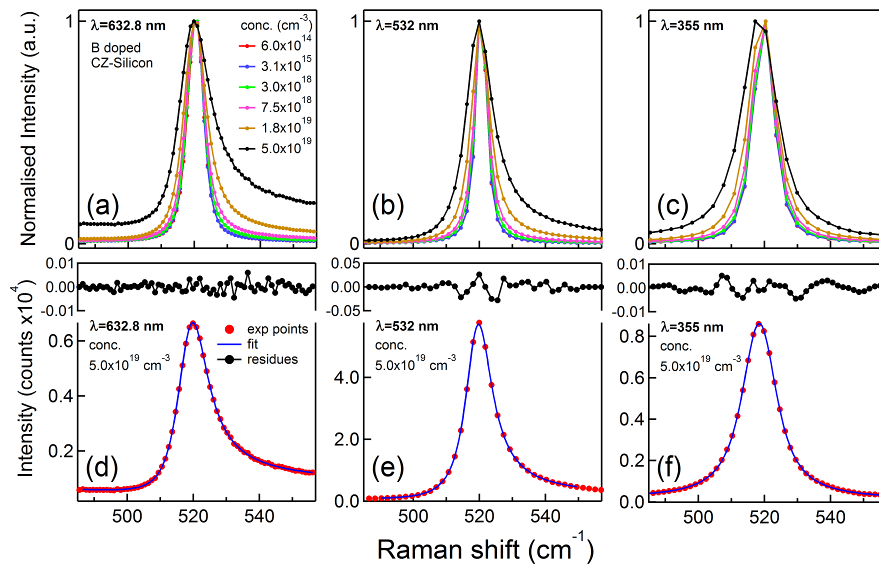

Figure 22. Superimposed normalized Raman spectra of CZ-Si samples at different B doping concentration acquired with 632.8 (a), 532 (b), and 355 (c) nm excitation wavelengths. The Raman spectra fitted to convolved Fano-Gaussian function (solid lines) of the highest doped CZ-Si sample are reported in (d,e,f) at different excitation wavelengths: 632.8 nm (d), 532 nm (e), and 355 nm (f). On the top of each panel are reported the fitting residuals to the experimental points. Taken from [1].

In the bottom panels (d), (e), and (f) of Figure 22 we show the Raman spectra fitted to the convolved Fano-Gaussian function of the highest doped CZ-Si sample (5×10^{19} cm^{-3} doping concentration) for each excitation wavelength. The residuals of the fitting process (shown in the upper part of panels (d), (e) and (f)) indicate that the convolved Fano-Gaussian function fits the experimental data very well for each laser excitation. The fitting method used (described in section 4.2.4) allows us to determine the width and spectral position of the Raman Si peak with an accuracy of 0.02 cm^{-1} (0.04 cm^{-1} for the doping-related peak broadening and peak shift).

Table 5.1 gives an overview of the Fano fitting parameters from the

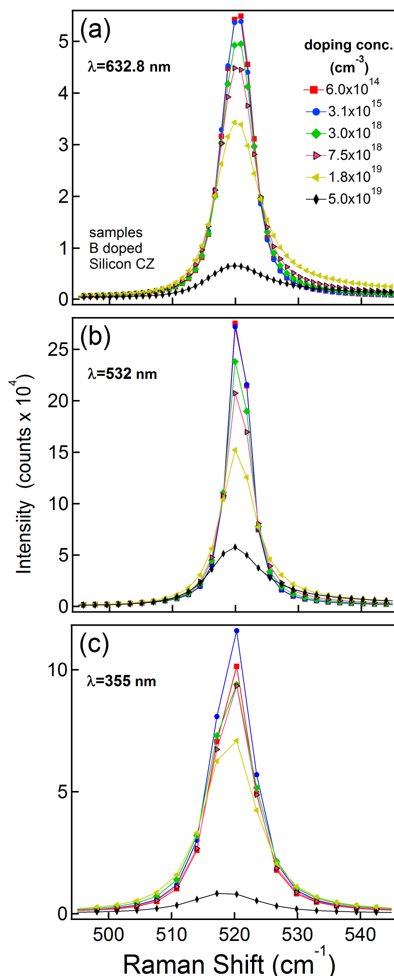

Figure 23. Raw data of Raman spectra of CZ-Si samples at different B doping concentration. The spectra were acquired with different excitation wavelengths: (a) 632.8 nm, (b) 532 nm, and (c) 355 nm. The doping concentrations are estimated from sheet resistance measurements. Taken from [1] (supporting information).

analysis of the spectra of Figure 22. The data from Table 5.1 are shown accordingly in Figure 24. The Fano parameter q for negligible spectral asymmetry ($q > 130$) is not given. Similarly, q is not given for all spectra recorded with near-UV excitations.

Concerning Figure 24, we first discuss the dependence of the peak broadening $2\Gamma_F^0$ on the doping concentration for each excitation wavelength in panel (a), which is the most suitable parameter for a direct evaluation of the doping concentration since it has the smallest relative fitting error. The data overlap perfectly at fixed doping concentration, and with our analysis accuracy, we state that the broadening of the Si peak is effectively independent of the excitation energy, for both visible and UV radiation, in line with what has been suggested previously in

Table 5.1. Summary table of Fano fitting parameters obtained by first-order Raman Si peak analysis at different excitation energies of CZ-Si samples doped at different boron concentrations. q values are given only for values < 130. Parameters $2\Gamma_F$ and ω_0 are given with uncertainties of 0.02 cm^{-1}, ($2\Gamma_F^0$ and $\delta\omega$ with uncertainties 0.04 cm^{-1}), H, q and H_{Norm} have uncertainties of 0.3%, 2% and 0.6%, respectively. Taken from [1].

doping	excitation	Silicon peak fitting parameters						
conc. (cm^{-3})	λ (nm)	q	$2\Gamma_F$ (cm^{-1})	$2\Gamma_F^0$ (cm^{-1})	ω_0 (cm^{-1})	$\delta\omega$ (cm^{-1})	H (counts)	H_{Norm}
6.0×10^{14}	633	-	3.16	0	520.29	0	84563	1
	532	-	2.83	0	520.56	0	371407	1
	355	-	4.47	0	519.70	0	146078	0.87
3.1×10^{15}	633	-	3.21	0.05	520.20	-0.09	82871	0.98
	532	-	2.83	0.00	520.58	0.02	369793	0.99
	355	-	4.51	0.04	519.71	0.01	166888	1
3.0×10^{18}	633	51	3.68	0.52	520.22	-0.07	70910	0.83
	532	109	3.46	0.63	520.47	-0.09	292098	0.78
	355	-	4.98	0.51	519.70	0.00	129226	0.77
7.5×10^{18}	633	26.6	4.45	1.29	520.03	-0.26	59018	0.69
	532	50	4.14	1.31	520.41	-0.15	239027	0.64
	355	-	5.76	1.29	519.56	-0.14	123667	0.74
1.8×10^{19}	633	11.1	6.34	3.18	519.68	-0.61	39753	0.47
	532	19.3	6.01	3.18	520.04	-0.52	159430	0.43
	355	-	7.37	2.90	519.24	-0.46	88035	0.52
5.0×10^{19}	633	5.2	9.75	6.59	518.70	-1.59	6569	0.07
	532	8.8	9.34	6.51	519.17	-1.39	58063	0.15
	355	-	10.80	6.33	518.42	-1.28	9398	0.06

the literature [23, 24, 26]. The inset in Figure 24 (a) focuses on the first three doping concentration values of the averaged trend and shows an increasing monotonic trend even in a relatively low doping concentration range ($10^{14} \div 10^{18}$) cm^{-3}. This occurrence is detectable only due to the high-precision Raman analysis and indicates that the Fano effect, which has been clearly demonstrated at high doping concentrations, is also present at low doping concentrations.
Considering the variation of the Si peak position with the doping concentration (see panel (b) in Figure 24), we detect a red-shift (softening) of the Raman mode quantified by $\delta\omega$. Similar to the case of $2\Gamma_F^0$, the $\delta\omega$ do not depend on the excitation energy at fixed doping concentration. Also in this case, the average decreasing monotonic trend of $\delta\omega$ is detected at low concentration (inset in panel (b) of Figure 24).
Another interesting parameter is the normalized amplitude (H_{Norm}) of the Si peak (panel (c) in Figure 24). This parameter shows a decreasing

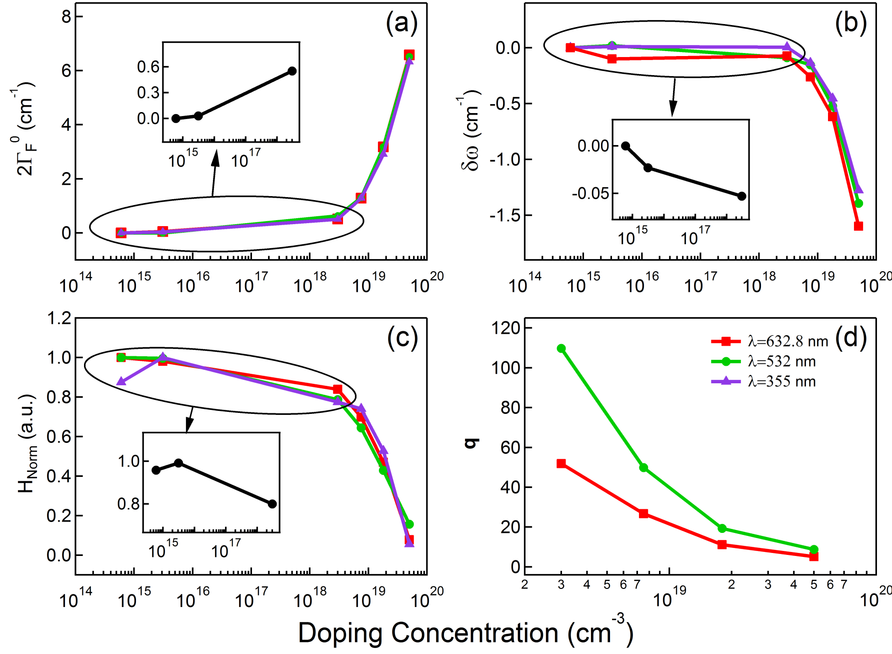

Figure 24. Dependence of Fano fitting parameters on B-doping concentration for the Raman spectra in Figure 22. Red squares, green circles, and violet triangles (see legend in panel (d)) correspond to fitting parameters derived from measurements with 632.8, 532, and 355 nm laser excitation, respectively. Panels (a), (b), and (c) refer to the peak broadening ($2\Gamma_F^0$), the shift in peak position relative to the intrinsic value ($\delta\omega$), and the normalized amplitude (H_{Norm}), respectively. The insets zoom in on the averaged trends at the lowest concentration values. Panel (d) refers to the asymmetry parameter q, which is restricted to relevant values (< 130) determined only with excitation wavelengths 632.8 and 532 nm. Taken from [1].

monotonic trend with the doping concentration, and again the trend does not depend on the excitation wavelength. This occurrence, which to our knowledge is not discussed in detail in the literature, is in any case consistent with the Fano theory, which predicts that the amplitude intensity decreases with the doping concentration for two main reasons: The Fano effect itself [22, 218] and the increase of the doping-induced free carrier density [258, 331], which causes a decrease of the Raman scattering amplitude [58, 275].

The last parameter of great interest is the asymmetry parameter (q) relevant only in the case of visible excitation (632.8 and 532 nm) and for high doping concentrations ($\geq 10^{18}$ cm^{-3}), where q values less than 130 are accounting for a reasonably detectable asymmetry of the spectra. This parameter quantifies (q^{-1} increases with asymmetry) the asymmetric line-shape of the first-order Raman Si peak, that manifest accordingly an increased scattered light intensity on the high-energy side of the peak. As known in Fano theory, q depends on the excitation

wavelength via the Raman scattering probability of the discrete and continuum electronic processes [23, 237] with the asymmetry increasing with excitation wavelength, starting from a nearly symmetric shape at near-UV excitation [23, 24, 26, 220]. Indeed, the Fano function becomes a fully symmetric Lorentzian in the limit $q \to \infty$. Panel (d) of Figure 24 shows the data of q as a function of the doping concentration, showing decreasing monotonic trends.
Our data from Figure 24 are plotted in Figure 25 against data available in the literature [23, 24] to allow direct comparison. Specifically, panels (a), (b), and (c) in Figure 25 refer to Cerdeira's data [23] (although the $2\Gamma_F^0$ values are not given in [23], we derived them from the experimental data in this paper). Panels (d), (e), and (f) in Figure 25 refer to Chandrasekhar's data [24], in this case we used the values from Table I of [24], where the values of the Raman Si peak parameters of *pure* silicon are also given, which we used to determine the values of $2\Gamma_F^0$ and $\delta\omega$.

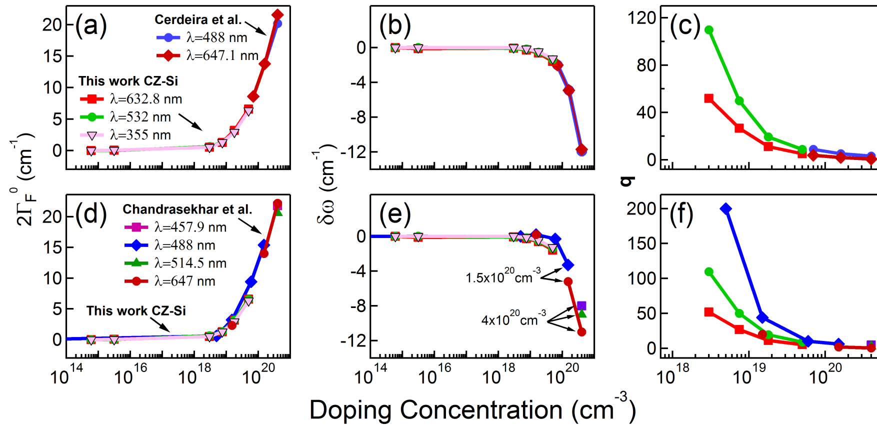

Figure 25. Fano fitting parameters as a function of doping concentration for the CZ-Si samples in this work are plotted along with data derived from Cerdeira et al. [23] (a,b, and c), and Chandrasekhar et al. [24] (d,e, and f). Taken from [1].

With respect to q, we restrict the comparison only to the relevant values, for which the asymmetry of the spectra is clearly visible.
From the comparisons in Figure 25 it appears that, in the region of shared dopant concentration, our results overlap very well with those published in the literature (see [24]). While previous experiments have focused on high dopant concentrations, we have deliberately chosen to investigate a dopant concentration range that also extends to a much lower B doping range. This direct comparison with literature data extends and strengthens the validity of the proposed Raman analysis even to a low concentration range, which so far has not been directly investigated.
Given the perfect superposition of $2\Gamma_F^0$ and $\delta\omega$, as clearly seen in Figure 24, it is convenient to rely on an average over the laser excitations

of these parameters. Therefore, to provide adequate evidence for the laser excitation-independent trends of the Fano fitting parameters, we report the values of $2\Gamma_F^0$ and $\delta\omega$ averaged over the laser excitations as a function of the doping concentration in panels (a) and (b) of Figure 26. Both are very well fitted by a linear model as a function of doping con-

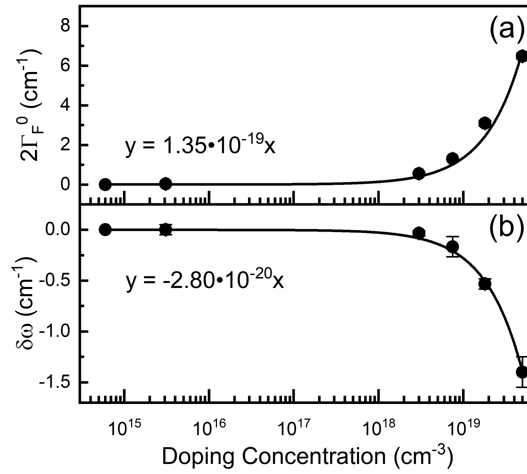

Figure 26. Mean values of $2\Gamma_F^0$ (a) and $\delta\omega$ (b) averaged over excitation wavelengths plotted as a function of doping concentration of CZ-Si samples. Both parameters are successfully fitted with a linear function. Taken from [1].

centration, which is in line with linear trends reported in the literature [27, 28]. Considering that we use both visible and near-UV excitations and a wide range of doping concentrations, these fitted lines can be used as a calibration curve for p-type mono-crystalline Si. Specifically, the linear slopes are 1.35×10^{-19} cm^2 and -2.80×10^{-20} cm^2 for $2\Gamma_F^0$ and $\delta\omega$. respectively.
We focus on the detailed analysis of the parameter q and its specific dependence on the excitation wavelength in Figure 27. q exhibits a double dependence on the doping concentration and the excitation frequency [23], namely, as can be clearly seen in panel (d) of Figure 24, q increases with the excitation frequency at fixed doping concentration and conversely it decreases with the doping concentration at fixed excitation. This is also consistent with the data reported in Figure 27 (a).

According to Cerdeira et al. [23], a linear dependence of the reciprocal of q on the excitation frequency stands in the limit of resonant condition with direct band gap transitions ($q^{-1} \propto \omega_0' - \omega_L$), where ω_0' is the frequency of the first critical point of the electronic bands of silicon ($E_0' = 3.37$ eV at the center of the Brillouin zone [245]) and ω_L is the frequency of the excitation light. However, this relation turns out to be valid in a wide range of frequencies even below the critical point in the visible spectrum [23].

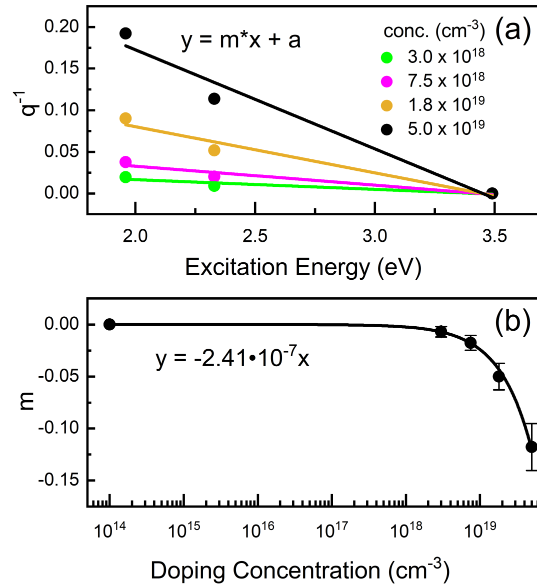

Figure 27. (a) Values of q^{-1} from Raman analysis of the most highly doped CZ-Si samples plotted as a function of laser excitation energy. (b) The slope values (m) of the trends in panel (a) are plotted as a function of doping concentration and linearly fitted; the solid line is a linear interpolation of the fitting model. Taken from [1].

In view of this model, we proposed a simple linear parametrization (y=m·x+a, where x is the excitation frequency) of the q^{-1} values at fixed doping concentration, with the aim of single out explicit its dependence on the excitation frequency. In panel (a) of Figure 27 we report the values of q^{-1} as a function of laser excitation energy for the relevant values of the doping concentration, where we set q^{-1} = 0 for UV laser excitation, since in this case no reasonably detectable asymmetry of the spectra is accounting. The slope values (m) are reported in panel (b) of Figure 27 showing a clear decrease with doping concentration (a value of m = 0 is added for 10^{14} cm^{-3} doping concentration simulating a pure CZ-Si sample). The slope values (m) are given in panel (b) of Figure 27 and show a clear decrease with doping concentration (a value of m = 0 is added for a doping concentration of 10^{14} cm^{-3} simulating a pure CZ-Si sample). The linear fit of the m values shows that the decrease of the slopes with doping concentration is ruled by the following linear law: $y = \beta \cdot x$, with $\beta = -2.41 \cdot 10^{-7}$ eV^{-1} cm^3.
The proportionality constant between the slopes m and the doping concentration is independent of both the doping concentration and the excitation energy. The theoretical Fano model as presented in Chandrasekhar et al. [24] states that $q = (V_p T_p / T_e + \delta\omega)/\Gamma_F^0$, where V_p is the average hole phonon matrix element and T_p/T_e is the ratio of Raman matrix elements of phonon and pure electronic scattering processes.

Considering that in this model for q only Γ_F^0 and $\delta\omega$ depend on the doping concentration and all the dependence on the excitation energy is in T_p/T_e, while V_p is assumed to be independent of both the excitation energy and the doping concentration [23, 24], we think that the constant β we obtained must be directly related to V_p. A detailed comparison between our result and related physical observables is beyond the scope of this study, but we expect that it will provide a basis for further investigation.
Remarkably, our multi-wavelength Raman analysis by verifying the wavelength independence of $2\Gamma_F^0$ and $\delta\omega$, the excellent agreement of our results with literature data, and the linear relationship between these parameters and the doping concentration, allows to state that the Raman analysis by the Fano effect is valid for monitoring the doping concentration from $\sim 10^{15}$ to $\sim 10^{19}$ cm^{-3} of p-type B-doped single-crystal Si, and that this analysis and experimental approach are fully portable to the near-UV excitation (355 nm, 3.49 eV), where the resonant Raman condition occurs.

5.2.2 *Raman analysis of implanted silicon wafers*

In this section, Raman analysis performed on p-type B-doped CZ-grown Si is extended to samples obtained by BF_2^+ ion implantation and laser thermal annealing for crystalline restoration (see section 4.2 for details). The aim of this study is to verify the full portability of Raman analysis with a convolved Fano-Gaussian model for monitoring the doping concentration of p-type doped monocrystalline Si with shallow doped layers of tens of nanometers thickness. In ion implantation doping, it must be taken into account that the process damages Si crystallinity and methods, such as LTA, are used to recrystallize Si [254, 255]. To verify the perfect crystalline reconstruction of the LTA samples, we performed ancillary TEM experiments.
We performed cross-sectional TEM analyses on all implanted samples considered in this work to verify the crystal structure, and SIMS analysis on the sample implanted with the highest dose for optimized calibration purposes to characterize the doping concentration after annealing (specifications are given in supporting information of [1] in table 1). Panel (a) of Figure 28 reports the high-resolution TEM (HRTEM) cross-sectional image of the sample with the highest implantation dose (5×10^{15} cm^{-2}) corresponding to an estimated doping concentration of 3.5×10^{19} cm^{-3} (determined with SIMS profile). In the TEM micrograph, some small dark areas are visible, indicating slight segregation of the B atoms [301], but in general the TEM analysis, combined with inspection of the diffraction pattern (inset of panel (a) of Figure 28), confirms that LTA has effectively recovered the Si crystallinity from the ion implantation process.
Panel (b) of Figure 28 shows the corresponding B and F depth con-

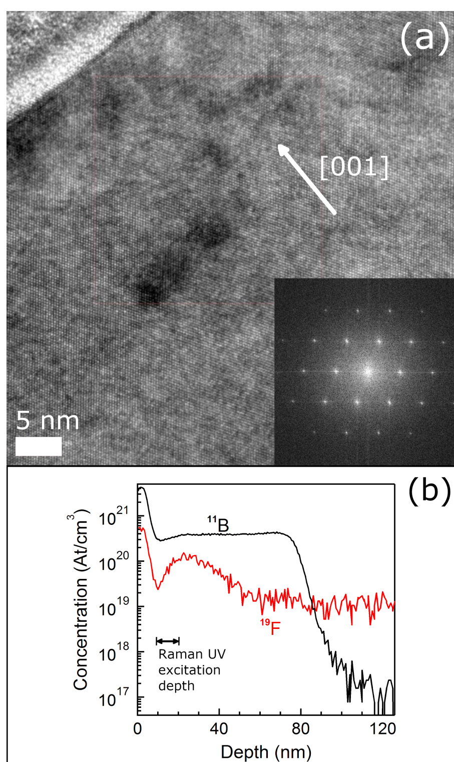

Figure 28. (a) HRTEM cross-sectional image of the BF_2^+-implanted & LTA silicon sample with the highest doping concentration (3.5x10^{19} cm^{-3}). The white arrow marks the [001]-axis direction and the inset shows the diffraction pattern. In (b), boron (B) and fluorine (F) SIMS depth profiles of the same sample of panel (a) are shown. Taken from [1].

centration profiles measured with SIMS. The peak in the concentration profile at the surface $\sim$ (0-5) nm, present in both the B and F profiles, is due to the segregation of ions on the top SiO_2 layer and in the Si/SiO_2 interface [299, 301, 332] (the SIMS concentration profile of SiO^+ ions is given in the supporting information of [1] in Figure 10). The B distribution, which determines Si doping, is almost constant up to a depth of 80 nm.

Raman spectra of the first-order Si peak were acquired with both visible (632.8 and 532 nm) and near-UV (355 nm) excitations. The variations of Fano width ($2\Gamma_F$) and peak position (ω_0) with doping concentration obtained by Raman spectra analysis are shown in Figure 29. Only in the case of near-UV excitation the Fano fitting parameters show a dependence on the doping concentration, while in the visible case they remain almost constant. This occurrence thus verifies that the visible Raman technique is not sensitive to doping concentration in shallow doping ($\sim$ 100 nm) even in the heavy doping regime due to its optical penetration depth ($\sim$ 1.27 μm for wavelength 532 nm and $\sim$ 3.05 μm for wavelength 632 nm in pure Si [272, 324]). On the contrary, the near-

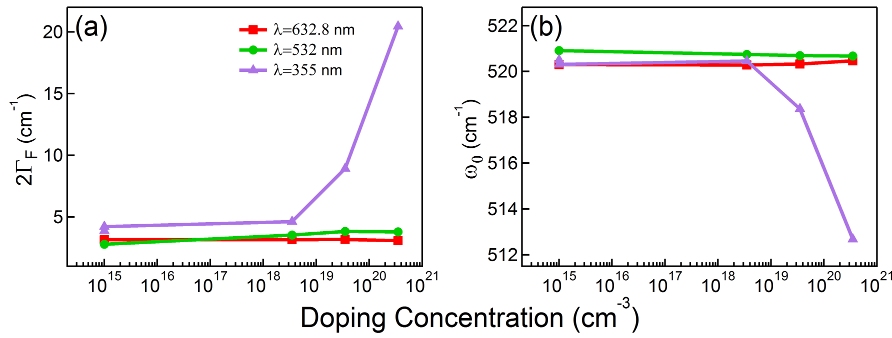

Figure 29. Dependence of the fitting parameters of the Raman spectra of BF_2^+-implanted & LTA silicon samples on the doping concentration, obtained with visible (632.8 and 532 nm) and near-UV (355 nm) excitations. (a) Raman Si peak Fano total width ($2\Gamma_F$), (b) Raman Si peak position (ω_0). Taken from [1] (supporting information).

UV radiation, which has a low optical penetration depth ($\sim$ 10 nm for wavelength 355 nm [272, 324]), is suitable for surface-sensitive probing of doped Si. For this reason, hereafter, we report only the relevant results of Raman analysis of BF_2^+-implanted & LTA Si acquired with near-UV excitation.

In particular, Figure 30 shows the raw Raman spectra in panel (a), the normalised spectra in panel (b), the fitted spectrum of the most heavily doped sample in panel (c), and the Fano fitting parameters ($2\Gamma_F^0$, $\delta\omega$, and H_{Norm}) plotted as a function of doping concentration in panels (d), (e), and (f). In panels (d), (e), and (f), the data are superimposed with those obtained from CZ-Si wafers. The inset in panel (d) highlights the increasing monotonic trend of $2\Gamma_F^0$ even at relatively low doping concentration (10^{15}-10^{18} cm^{-3}). The numerical values of the Fano fitting parameters are also given in Table 5.2.

The Raman spectra of BF_2^+-implanted <A Si show a very similar behavior to the CZ-Si spectra taken with the same near-UV excitation, showing a broadening and frequency-softening of the peak with doping concentration. Also in this case, the q parameter has values above the threshold of 130. Throughout the range of doping concentration considered, the $2\Gamma_F^0$ trends of the two data sets overlap perfectly, and the $\delta\omega$ and H_{Norm} trends are in good agreement.

Moreover, in Figure 31, we compare our Fano fitting parameter trends of both BF_2^+-implanted & LTA Si and CZ-Si with p-type B-doped single-crystalline Si data from Cardona's group studies [23, 24]. We observe a nice overlap and agreement of the $2\Gamma_F^0$ and $\delta\omega$ values. Thus, this comprehensive analysis and comparison demonstrate the full consistency of near-UV Raman analysis of BF_2^+-implanted & LTA-Si and show that monitoring the doping concentration of p-type single-crystalline Si with nanometer-scale doping depth by near-UV Raman analysis works

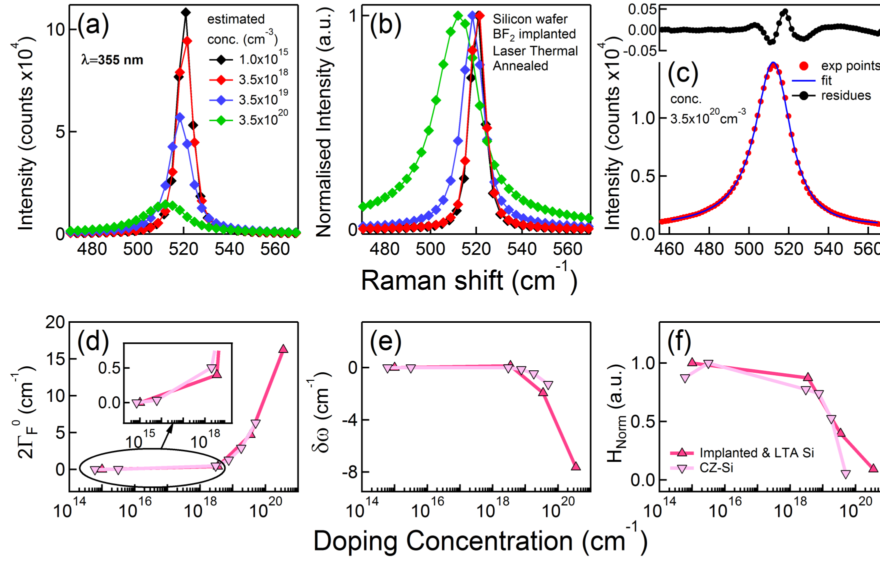

Figure 30. Near-UV Raman analysis of BF_2^+-implanted & LTA silicon samples at different doping concentration with excitation wavelength 355 nm. The raw spectra (a), the normalized spectra (b) and the spectrum of the most highly doped sample (3.5×10^{20} cm^{-3}) fitted to convolved Fano-Gaussian function (c) are shown. The parameters $2\Gamma_F^0$ (c), $\delta\omega$ (d), and H_{Norm} (e) are plotted as functions of doping concentration and superimposed to the data obtained from CZ-Si wafers. The inset in (d) zooms in on the $2\Gamma_F^0$ trend at lowest concentrations. Taken from [1].

perfectly and is sensitive even at relatively low doping concentrations.

5.2.3 *Raman analysis of beveled Si wafers*

Preliminary surface analysis. To effectively probe the doping distribution of ion-implanted Si wafers, which have heavy concentrated doping starting from the surface and drastically decreasing at shallow depths, the light source used for Raman analysis on the small-angle beveled surfaces must be carefully chosen. Indeed, the Raman signal must be an integrated signal at a few nanometers with respect to the typical surface implantation depths ($\sim$ 100 nm). Otherwise, the Raman signal would be integrated at depths greater than the surface implantation zone and, consequently, the Raman analysis on the bevel would not provide significant data.
Specifically, it is necessary to verify that the laser excitation used has the correct probing penetration depth of a few nanometers, which in the near-UV case is expected to be $\simeq$ 10 nm, corresponding to the optical penetration of light with a wavelength of 355 nm in pure Si [272, 324]. Moreover, a preliminary verification of the doping sensitivity of the proposed UV micro-Raman spectroscopy is needed to be then effectively applicable on beveled surfaces. Indeed, each Raman acquisition must

Table 5.2. Summary table of Fano fitting parameters obtained by Raman Si peak analysis with near-UV excitation (λ=355 nm) of BF_2^+-implanted & LTA silicon samples with different doping concentration. The uncertainty of $2\Gamma_F$ is 0.02 cm^{-1}, $2\Gamma_F^0$ and $\delta\omega$ are given with uncertainties of 0.04 cm^{-1}, H_{Norm} has uncertainty 0.6%. Taken from [1].

doping	Silicon peak fitting parameters			
conc. (cm^{-3})	$2\Gamma_F$ (cm^{-1})	$2\Gamma_F^0$ (cm^{-1})	$\delta\omega$ (cm^{-1})	H_{Norm}
1×10^{15}	4.22	0	0	1
3.5×10^{18}	4.62	0.40	0.15	0.87
3.5×10^{19}	8.92	4.70	-1.94	0.39
3.5×10^{20}	20.45	16.23	-7.63	0.09

be sufficiently sensitive to relatively small doping variations occurring at depths comparable to the acquisition scanning step size ($\simeq$ 5 nm) allowed by the micro-Raman setup on the small-angle bevel.
For these reasons, we first investigate the surface of three ion-implanted B-doped single-crystal Si(100) wafers with different implantation profiles and different doping concentration ranges characterized by independent SIMS and SRP (see panels (a), (b), and (c) in Figure 32) using near-UV Raman spectroscopy with Fano effect analysis. The Raman spectra obtained are shown in panels (d), (e), and (f) of Figure 32.
The first sample (Figure 32 (a)) has a uniform low doping concentration profile (3×10^{17} cm^{-3}) within the deep implantation zone. The other two (Figures 32 (b) and (c)) show different surface heavy doping concentrations (8×10^{19} and 1.2×10^{20} cm^{-3}, respectively) with rapid doping variations that drop rapidly to $\sim 10^{18}$ cm^{-3} within 100 nm. The surface doping concentrations are calculated by mediating the concentration values estimated by SIMS or SRP at the first 10 nm depth (highlighted with yellow areas in the upper panels of Figure 32), that is the same value of the expected near-UV probing depth. In the case of samples relative to Figure 32 (a) and (b) we could rely on SIMS profile while in the case of the most heavily doped sample (Figure 32 (c)), we relied on the SRP profile to calculate the effectively active doping concentration, since the two sharp peaks near the surface in the SIMS profile are clear indications of inactive dopant segregation of B atoms at a concentration above the solid solubility (2-3 $\times 10^{20}$ cm^{-3} for annealing temperature of 1000-1100 °C [333]) [15, 300, 305, 334, 335]. Indeed, the TEM cross-sectional image (see inset in Figure 34 (c)) shows non-uniform dark regions in the surface region to a depth of about 36 nm, which are due to the segregation of B atoms [301].
As can be seen from the Raman spectra in panels (d), (e), and (f) of

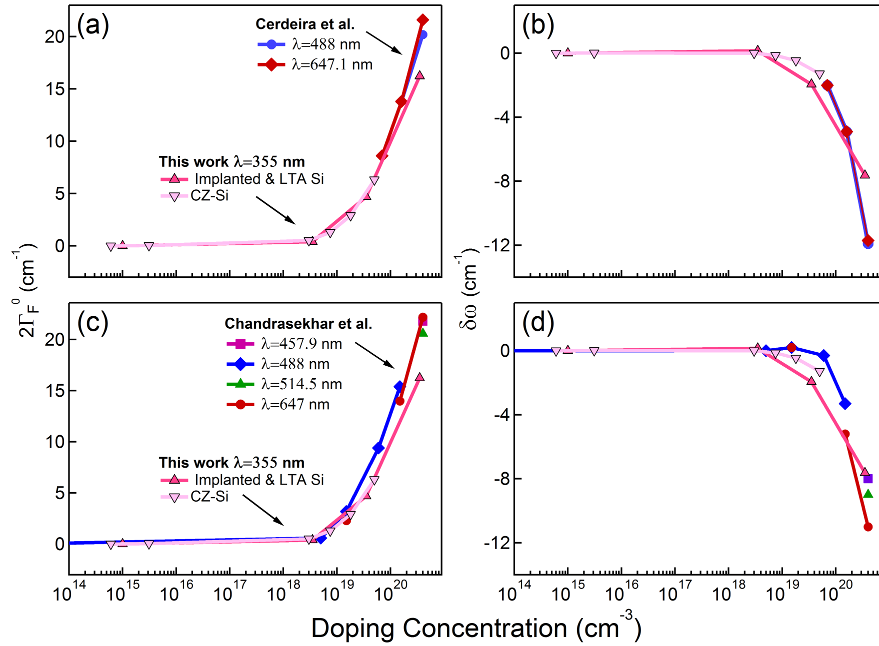

Figure 31. Fano fitting parameters as functions of the doping concentration of BF_2^+-implanted & LTA-Si samples are shown together with the data of this work CZ-Si wafers and those of Cerdeira et al. [23] (a,b) and Chandrasekhar et al. [24] (c,d). Taken from [1]

Figure 32, the Si peaks are symmetric at each doping concentration and show a general broadening with increasing doping concentration. The $2\Gamma_F^0$ values obtained by the Raman Fano analysis are plotted in Figure 33 as a function of the average surface doping concentration within the first 10 nm depth. In the same Figure 33, the red curve is the linear model that fits the Raman Si peak Fano broadening parameter as a function of the doping concentration obtained in the previous section (5.2.1) using multi-wavelength Raman analysis of B-doped CZ-Si samples (see Figure 26 (a)). Notably, within the experimental error, the $2\Gamma_F^0$ data evaluated from Figure 32 align well with this curve and confirms the self-consistency of the near-UV Raman analysis on single-crystal Si. The $2\Gamma_F^0$ parameter proves to be particularly sensitive to rapid doping changes.

Raman-based doping profiling. Having verified the reliability of the UV micro-Raman technique on the surface, in this section we move on to direct Raman measurements performed on the beveled surface with the aim of profiling the inner doping concentration. UV micro-Raman measurements were performed on two twin beveled surfaces obtained from the most heavily doped p-type Si wafer of Figure 32 (c) (see section 4.2 for details). This sample was properly chosen because it is the most suitable sample to test the limits of the Raman-based doping

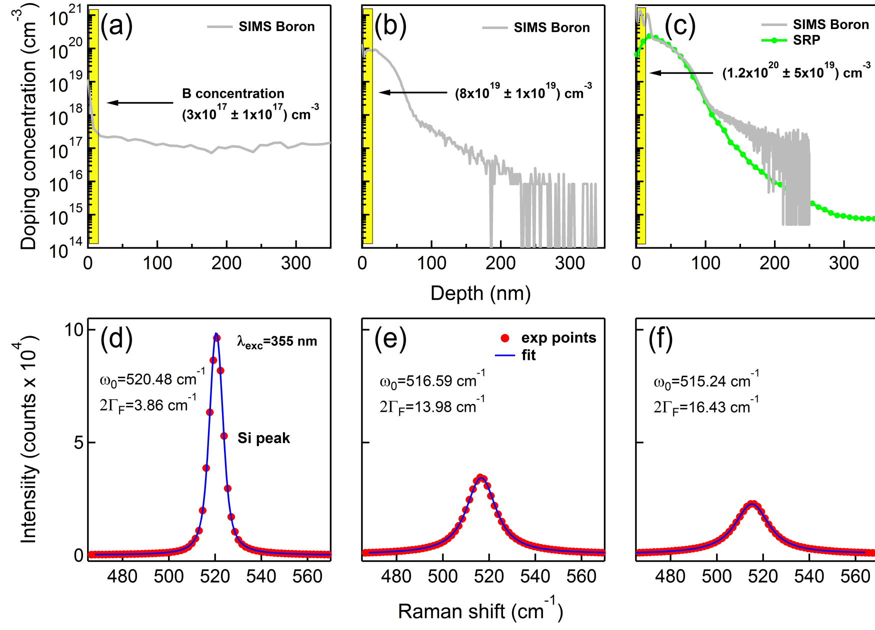

Figure 32. Boron SIMS profiles (upper panels) and corresponding Raman spectra obtained with near-UV (355 nm) excitation (bottom panels) of B-doped Si wafers with different surface doping concentrations: 3×10^{17} cm^{-3} (a,d), 8×10^{19} cm^{-3} (b,e), and 1.2×10^{20} cm^{-3} (c,f). The total Fano width ($2\Gamma_F$) and frequency position (ω_0) of the Raman Si peaks are reported in the corresponding panels. For the wafer relative to panel (c), the corresponding SRP profile is also reported. The yellow highlighted areas mark the optical penetration region of the UV laser excitation ($\simeq$ 10 nm) used to acquire the Raman spectra. Taken from [2]

profiling technique, since it exhibits strong, rapidly decreasing surface implantation and the wider doping concentration range.
Raman data were acquired with the optical microscope set perpendicular to the beveled surface along the maximum slope direction of the wafer wedge (see inset of Figure 34 (a) for an illustrative view of the measurement setup). The acquisition start point is set by the confocal optical microscope and subsequent data points are acquired by automated motorized x-y stage scanning with a step size of 1 μm between adjacent aligned measurement points. According to the relation $d = x\, sen(\theta)$, where d is the depth, x is the length along the wedge starting from the bevel edge, and θ is the bevel angle (0.0045 rad), a 1 μm longitudinal increment leads to a probing of the depth with a vertical increment of $\simeq$ 5 nm.
The Raman spectra recorded on the twin bevels were analyzed according to the Fano model and then merged to obtain a single data set for more convenient result presentation. Figure 34 (a) shows the $2\Gamma_F^0$ parameter determined along the bevel plotted as a function of the explored depth from the surface. We observe that up to a depth of 100 nm the Si peak narrows drastically following an almost linear trend. From

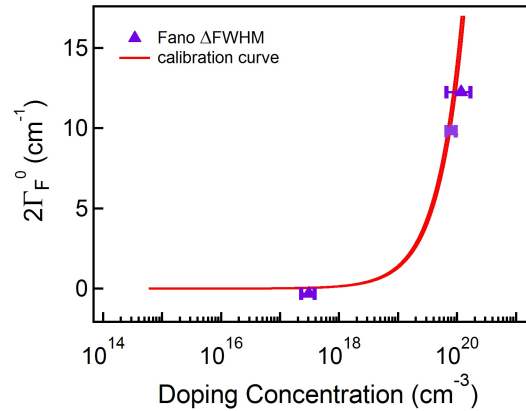

Figure 33. Fano broadening fitting parameter $2\Gamma_F^0$ (violet triangles) of the first-order Raman Stokes Si peak of B-doped Si wafers from Figure 32 plotted as a function of surface doping concentration (estimated by boron SIMS and SRP profiles). The red curve is the linear model that fits the Fano broadening parameter of B-doped CZ-Si (100) wafers as determined in the previous section (5.2.1). Taken from [2].

then on, the $2\Gamma_F^0$ values start to scatter around the zero plateau value loosing a specific trend.

After analyzing the Raman data and obtaining the $2\Gamma_F^0$ values associated with the depths, to obtain a direct doping concentration profile, we used the concentration dependence of the width as estimated in the previous section (see 5.2.1) using B-doped CZ-Si(100) wafers as a calibration curve. Accordingly, the $2\Gamma_F^0$ values of Figure 34 (a) are arranged on the calibration curve as shown in Figure 34 (b) to obtain a direct data set consisting of doping concentration and depth values. In this way, we generate a Raman-based doping concentration profile with the exclusive use of Raman data, without the need to independently characterize the doping concentration with other techniques.

The Raman-based doping profile is reported in Figure 34 (c) in direct comparison with the SIMS and SRP profiles. The profiles overlap nicely below the surface region where the Si has no B segregation and is well reconstructed from the ion implantation process (see cross-sectional TEM image in the inset of Figure 34 (c)). The Raman-based doping profile follows the same quantitative trend of both SIMS and SRP profiles. However, unlike SIMS and SRP, the Raman-based profile enters apparent saturation at a concentration of 10^{20} cm^{-3} underestimating concentrations above. Excellent agreement between the different doping profile methods exists up to the critical depth of 100 nm, where both the Raman-based doping profile and the B SIMS profile deviate from the SRP and lose their doping sensitivity in the 10^{17} cm^{-3} range. This occurrence indicates that the doping sensitivity limit of both Raman-based and SIMS techniques is 10^{18} cm^{-3} (10 ppm) for ion-implanted p-type

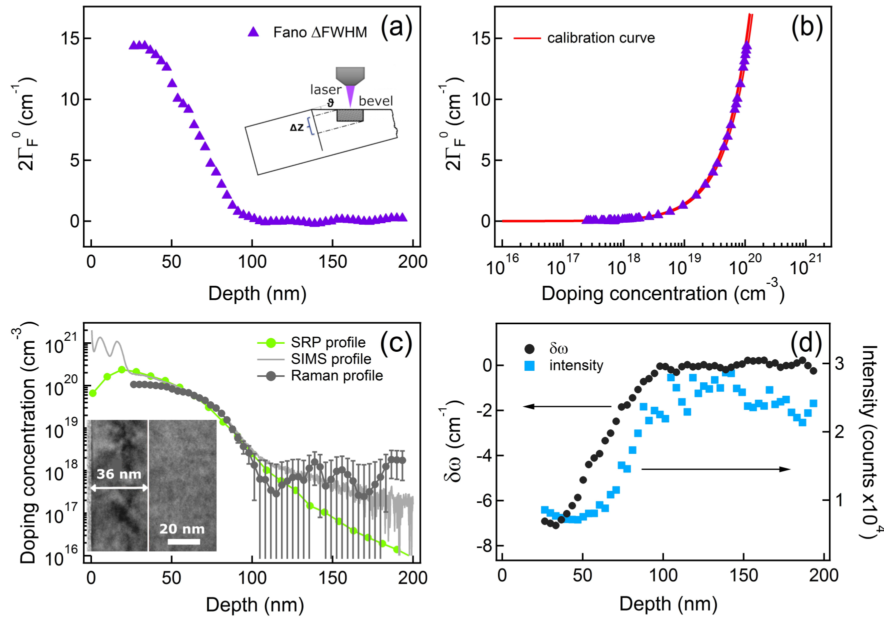

Figure 34. Doping profiling Raman analysis on the beveled surfaces of the p-type B-doped Si wafer of Figure 32 (c). (a) Fano broadening fitting parameters plotted as a function of depth from the Si surface. The inset shows an illustrative schematic of the UV Raman measurement setup on the bevel. (b) Fano broadening parameters (violet triangles) arranged on the calibration curve derived from B-doped Czochralski Si(100) wafers in section (5.2.1). (c) Raman-based doping concentration profile (dark gray) obtained by Czochralski calibration superimposed to boron SIMS (light gray) and SRP (green) profiles for direct comparison. The inset in (c) shows a TEM cross-sectional image of the dark region with boron segregation near the Si surface (left) and the lighter and well-reconstructed region on the inner part of the Si (right). (d) Frequency shift position (black dots) and peak intensity (light blue squares) data plotted as a function of depth from the Si surface. Taken from [2].

B-doped single-crystal Si, which is comparable to SIMS sensitivity of our work on the BF_2^+-implanted Si samples and other studies reported in the literature for B-doped Si [15, 301, 305, 336]. This sensitivity threshold, in our opinion, could also be due to the material itself, considering that it occurs at depths greater than 100 nm, where the doping may not be particularly uniform and the Si may not be well reconstructed.
Figure 34 (d) also reports the Raman Si peak frequency shift ($\delta\omega$) and intensity data providing others qualitative trends of the Raman parameters on the bevel. The same methodological approach of Raman-based doping profiling can be used by taking the Si peak position shift ($\delta\omega$) instead of the width broadening as the doping-sensitive Raman fitting parameter and exploiting the specific frequency shift calibration curve (see Figure 26 (b)). But in this case, the sensitivity to the doping and thus the accuracy of the method is lower due to the lower variability of

the frequency shift parameter compared to the peak broadening with the doping concentration.

5.3 CONCLUSIONS TO CHAPTER 5

In summary, we have performed a wavelength-dependent (using visible and near-UV excitations) room-temperature micro-Raman study to characterize the dopant content of B-doped CZ single-crystal Si(100) wafers covering a wide range of doping concentrations from 6×10^{14} to 5×10^{19} cm^{-3}. We applied the results of this study on BF_2^+ implanted and LTA Si wafers with surface doping depth ($\sim$ 100 nm), covering a wide doping concentration from $1.0x10^{15}$ to $3.5x10^{20}$ cm^{-3}. Subsequently, we have shown that near-UV micro-Raman spectroscopy implemented on a small-angle beveled sample is able to profile the doping concentration of p-type ion-implanted monocrystalline Si without further independent doping characterization.
The first-order Raman Si peak was fitted to a convolved Fano-Gaussian function, which allowed us to achieve a frequency accuracy of $\approx$ 0.02 cm^{-1}, well below the mesh density of the experimental spectra ($\approx$ 1 cm^{-1}). Thanks to the accuracy of the fitting, we have shown that the Fano fitting parameters such as $2\Gamma_F^0$, $\delta\omega$ and H_{Norm} are effectively wavelength independent, and in particular $2\Gamma_F^0$ and $\delta\omega$ follow a strictly linear dependence with the doping concentration. These results confirm and extend what has been reported in the literature about the trend of Fano fitting parameters with doping, obtained only with visible radiation and a limited range of doping concentration, to near-UV excitation and the low doping range [23, 27, 28, 236]. A wavelength-independent reduction of peak intensity with doping concentration was also observed, up to 90% of signal in heavily doped Si.
Raman analysis works finely with both visible and near-UV excitation and also at low doping, allowing potential ppm doping sensitivity of the Raman technique through our improved fitting procedure.
Considering the asymmetry parameter (q), we verified a decreasing linear dependence of q^{-1} with the excitation energy at fixed doping concentration. In particular, the slope values of the q^{-1} linear trends follow a strictly negative linear trend with the doping concentration and the derived β constant, which is both excitation and doping independent, is directly proportional to the hole-phonon average matrix element (V_p) involved in Fano interference [24].
Moreover, the experimental results were directly compared with relevant literature data [23, 24] to demonstrate that the proposed Raman analysis is perfectly consistent and complementary with literature.
Application of the technique to BF_2^+-implanted and LTA Si wafers with surface doping depth ($\sim$ 100 nm) showed that only near-UV radiation is suitable for doping monitoring for surface doped Si. The Fano fitting

parameters for near-UV excitation were found to line up very well with our CZ-Si and literature data [23, 24]. The results were correctly reproduced, demonstrating the full portability of our improved Raman analysis to state-of-the-art Si-based architectures for monitoring the doping concentration even at low doping regime. The noninvasive nature of Raman spectroscopy makes it a candidate for process monitoring and for potential application as an inline process characterization tool.

Finally, we implemented the Raman-based doping characterization technique on small-angle bevelled samples for doping concentration profiling, achieving high vertical and lateral resolutions of 10 nm and 1 μm, respectively, as well as a p-type doping sensitivity of 10^{18} cm^{-3} (10 ppm), and high dynamic doping sensitivity in the 10^{18} cm^{-3}-10^{20} cm^{-3} concentration range. Moreover, it has been shown to work finely down to a depth of 100 nm, effectively probing the typical shallow doping distribution used in Si-based nanoelectronics [33, 303, 305, 306, 308, 310, 312].

The proposed Raman-based technique proves to be an efficient and effective alternative to SIMS and SRP. In particular, compared to SIMS, the advantage is that the Raman-based method is sensitive only to the effectively active dopants. It requires the beveling process like SRP, but is better than SRP in terms of lateral resolution and for avoiding probe contact with the analyzed surface.

6 RAMAN AND PHOTOLUMINESCENCE ANALYSES OF SINGLE-LAYER MoS_2 VIA THERMALLY CONTROLLED SULPHUR VACANCY DOPING

Moore's law states that the number of transistors that can be packed into a given unit of an integrated circuit doubles approximately every 18 months, which is achieved by reducing the size of the active elements in the transistor [30, 31, 337, 338]. However, this cannot be sustained indefinitely due to the limitations imposed by material size and manufacturing process [338]. Studies on two-dimensional (2D) materials aim to continue this law and extend this limitation of miniaturization to the atomic level [33]. Moreover, 2D crystals with atomic thickness represent a perfect playground for the exploration of physics in low dimensions, with the prospect of realizing new types of devices based on completely new paradigms of information processing, as proposed in the so-called Beyond CMOS strategy [33]. As an exfoliable material that can be reduced to a 2D dimension, the MoS_2 crystal has aroused great interest for the study of electronic devices such as FETs, photodetectors, photodiodes, and so on [89, 95, 339–342]. The electronic properties of MoS_2 are strongly dependent on the thickness of the material. Its peculiar electronic semiconductor structure, which depends on the number of layers and undergoes an indirect-direct transition from bulk to monolayer phase, makes MoS_2 particularly interesting for optoelectronic applications [41–43]. The special excitonic properties of MoS_2 are exploited for the invention of novel excitonic devices based on the exciton as a new computational variable of state, as envisaged in the Beyond CMOS strategy [33, 38–40].

In the ultrathin state, the enhancement of quantum confinement and the reduction of dielectric screening lead to enhanced interactions between charged particles in the material and strong interaction with electric fields [44, 45]. For these reasons surface modifications that introduce doping become particularly effective, leading to new optoelectronic effects and opening the prospect of powerful optoelectronic devices [46–50].

Since the study of the electrical and optical properties of MoS_2 is crucial for potential applications, it is important to search for a simple, effective and reliable method to study them and control their changes caused by surface defects. For this reason, in this chapter we use Raman and PL spectroscopy to study the optoelectronic properties of single-layer MoS_2 and their changes after layer engineering by thermal annealing, where the doping state of the material is changed by a controlled creation of surface defects. The fundamental properties of excitons are also investigated by studying the phonon-exciton interaction.

In section 6.1, we introduce the need to characterise the doping level in

MoS_2 as a function of the sulphur vacancy defects that may arise from a post-exfoliation thinning treatment, such as thermal annealing, and propose our approach based on Raman and PL spectroscopy.
The details of the materials and methods used for the following experimental analyses are described in the Experimental Methodology chapter (see section 4.3).
Raman and PL analyses of few-layer and single-layer MoS_2 before and after annealing processes are reported in section 6.2.
Morphological evidence for the effects of annealing on the material and the resulting changes studied by AFM analysis are described in section 6.2.1.
Non-resonant Raman and PL studies of defect-induced changes in optical response are performed in section 6.2.2.
A rationale for the morphological and optical response changes is given in section 6.2.3.
The detailed evolution of distinct excitonic components in the PL emission is investigated in section 6.2.4 through power-dependent PL.
Resonant-Raman and correlated PL measurements of monolayer MoS_2 as a function of post-annealing effects are analysed in section 6.2.5.
Section 6.3 concludes the study and reports the main results and achievements.
The results presented in this chapter were published in the journals *2D Material 7 (2020) 025001* [3] and *Nanoscale 12 (2020) 18899-18907* [4].

6.1 INTRODUCTION

Single-layer MoS_2 is a semiconductor with direct band gap at the K point of the first Brillouin zone (of about 2.14 eV according to [109]) [94, 104, 128]. Due to a pronounced spin-orbit interaction, the valence bands are split into two spin bands with an energetic separation of ≈ 0.2 eV [47, 94] and the conduction band is split by a few tens of meV [343]. Due to the reduced dimensionality, the screening of the Coulomb interaction is strongly suppressed [45, 344], and the two direct optical transitions from the highest spin-split valence bands to the lowest conduction bands lead to the formation of strongly bound excitons (referred to as A and B in the literature [47, 94, 104]) with relatively high binding energies, which determine the optical response of the system up to room temperature (RT).
It is well established that the optical properties of single-layer MoS_2 can be modified by doping. This can be done in several ways, by substrate-induced doping [146, 147, 286], chemical doping [45, 292], laser irradiation [345–347], ion implantation [348–350], or by thermal annealing [49, 148, 290, 291, 351–354]. Indeed, the doping level of MoS_2 was found to depend on the formation of defects (sulphur vacancies) or partial oxidation after post-exfoliation thinning treatments used to control and engineer the number of layers of thin MoS_2 samples using

different experimental approaches [49, 148, 290, 355, 356].
The controlled exfoliation of few-layer MoS_2 was explored via laser annealing [346, 347, 357], Ar+ [358] or O_2 [359] plasma treatments, microwave plasma etching [360], palladium deposition and annealing [361], lithographic techniques such as focused ion beam [350] or local anodic oxidation [50, 362]. Even more interestingly, given the practical feasibility of the approach, the thinning of few-layer MoS_2 has been investigated by means of thermal annealing in oxidising [288, 289, 354, 363, 364], inert [353, 365], or reducing [291, 364] atmospheres.
Wu et al. [288] exposed exfoliated MoS_2 deposited on 90 nm SiO_2/Si(100) to annealing for 10 hours at 330 °C in air. They firstly demonstrated layer engineering by obtaining a monolayer flake from a bilayer. In addition, above 300 °C they showed the appearance of submicrometric triangular pits that formed on the flakes after 15 h. With this post processing treatment, they fabricated a FET with the thinned flake and showed the conversion of MoS_2 from n- to p-type semiconductor. Yamamoto et al. [363] have singled out the role of oxygen by performing a systematic study as a function of temperature from RT up to 350 °C in a controlled O_2-Ar atmosphere. They showed evidences that etching occurs on native defects of the MoS_2 basal plane in mechanically exfoliated flakes. They demonstrated that the layer etching initiates above 200 °C, while real oxidation starts above 300 °C. In their work, they ruled out a significant role of the substrate for the thinning process.
So far, the potential role of interfacial adsorbed water and contaminant molecules on the hydrophilic oxide surfaces (typically SiO_2) used for the optical identification of few-layer samples of TMDs, has been largely neglected. Only in the case of thick WSe_2, it was demonstrated, by means of secondary ion mass spectroscopy (SIMS), that after thermal annealing at 400 °C oxidation also occurs at the bottom surface [356]. This may be related to the water trapped between the exfoliated WSe_2 and the substrate. Under ambient conditions, at RT and with a relative humidity of 60 % the evolution of an ultra-thin film of water on the SiO_2/Si(100) wafer is always expected, and can be regarded as a universal occurrence.Its very presence is indirectly but undoubtedly evidenced by the demonstrated viability of atomic force microscopy (AFM) local anodic oxidation (LAO) experiments on the native oxide layer of SiO_2, since LAO is only possible due to the presence of a water meniscus between the AFM tip and the substrate [362].
Although the presence of water during annealing suggests its involvement in the generation of defects (sulphur vacancies) in MoS_2, the role of water in annealing-induced changes in the optical properties of the material has not yet been investigated.
Several papers report that PL intensity in MoS_2 increases after annealing processes [49, 131, 290, 351, 353]. It is also known that sulphur vacancies introduce donor levels into the MoS_2 band gap, leading to n-type doping [366, 367], while increases in PL yield are known to be

due to p-type doping [147, 148, 286, 292].
Therefore, understanding the mechanism of p-type doping with annealing, which produces the sulphur vacancies that should, in contrast, induce n-type doping, is not immediate and is probably due to absorption at the sulphur vacancies of more electronegative elements such as molecules of O_2, H_2O, and so on [49, 148].
The effects of the presence of defects on the PL spectra induced by annealing have been reported in several studies [148, 290, 351], but excitation laser power-dependent PL measurements that allow to study the evolution of the excitonic transitions in annealed single-layer MoS_2 in the temperature range of (200 ÷ 300) °C are, to our knowledge, missing in the literature. Moreover, a non-resonant Raman study specifically on the effects of annealing on MoS_2 has been recently performed [291], but resonant Raman studies providing a wealth of information on the first- and second-order phonon modes have not yet been reported for MoS_2 or for other 2D TMD systems as a function of post exfoliation thermal annealing in the temperature range of 200 ÷ 300 °C. Spatially resolved micro-Raman and PL techniques are pivotal and complementary for the investigation of doping related modifications in the optical response of the material. PL provides direct access to the optical response of the system and its excitonic spectrum [45, 47, 286, 368–370]. Resonant Raman spectroscopy not only enables the investigation of electron-phonon and exciton-phonon interactions, which are of obvious relevance to the fundamental and device physics of low-dimensional materials [46, 108, 122, 161, 163, 189, 371–375] but also the spatial symmetry of the A excitons [376, 377] which dominate the PL response of MoS_2.
In this work, by using optical microscopy (OM), tapping mode atomic force microscopy (AFM), power-dependent PL spectroscopy, Raman and resonant Raman spectroscopy, we address the study of the thermal treatment of mechanically exfoliated MoS_2 in the crucial annealing temperature range between 200 °C and 300 °C. We clearly demonstrate the presence and crucial role of an interfacial water film at the MoS_2/SiO_2 interface in the chemical doping of MoS_2 and the layer engineering of the 2D material up to the monolayer limit. A quantitative analysis of the PL spectra allows us to locally probe the variation of the sulphur vacancy concentration in monolayer MoS_2. We have studied in detail the evolution of the A excitons (i.e., the neutral exciton A^0 and the negatively charged exciton, also called trion A^-) as a function of annealing temperature showing that the PL spectral weight of the excitons can be modulated in this temperature range. We notice that the PL signal increases after annealing above 225 °C. The PL enhancement is tunable with the annealing temperature and shows a specific hyperbolic trend as a function of the PL intensity ratio of the A type excitons. We observe that the Raman signal also increases after annealing and is tunable with the annealing temperature, with the values of the signal increase matching those of the PL signal increase within the experimental error. We

show that the Raman spectral yield correlates one-to-one with the PL spectral yield, giving thus direct experimental evidence of the exciton-phonon coupling effect. We demonstrate that the A type excitons only couple with in-plane first-order and second-order Raman modes and strongly couple with the E^1_{2g} in-plane Raman mode, while they do not couple with the A_{1g} out-of-plane Raman mode. Therefore, in agreement with previous PL experimental evidence [377], with this cross correlated study we assign this occurrence to an in-plane spatial orientation of the A type excitons.

6.2 RESULTS AND DISCUSSION

6.2.1 *Morphological evidences of thermal annealing on 2D MoS_2*

In the following, we report experimental evidence of the effects of thermal annealing performed in both reducing (UHV) and oxidising (air) environments aimed at layer number engineering of few-layer MoS_2. The potential of this post-exfoliation procedure to tune the number of layers of TMDs has already been reported in several publications [288, 351, 365].
In Figure 35 we summarise the results of our quantitative AFM investigation of the morphological changes occurring in mechanically exfoliated MoS_2 upon annealing, both in air and in UHV, in the specific case of few-layer and monolayer flakes. Remarkably, we systematically observe that the morphology of MoS_2 flakes remains unchanged in shape and size for almost all samples when heated to 300 °C. However, in Figure 35 the stacking distance from the substrate is observed to systematically decrease upon annealing. From (a) to (b), after annealing in air, the flakes stick on average 0.6 nm closer to the substrate. On the other hand, once annealing occurs in UHV,the stacking distance dramatically decreases from 3.2 nm to 1.1 nm. Such an observation is systematic, and as discussed below, height variation estimates on the same samples are to be considered a consequence of a physical lowering of the flake-substrate distance.
To discuss this point against the literature, we stress that once adhesion of a 2D material exfoliated on a flat inert substrate is considered, then there is no fundamental justification for the 2D-substrate stacking distance to be equal or comparable to a homogeneous 2D/2D interlayer distance. The same presence of impurities typically increases the distance of the flake from the substrate, as was already stressed by Novoselov and co-workers [378], while others, such as Benameur et al. [279], speculated on the presence of an adsorbed uniform water film, approximately 1-2 nm thick, at the interface with the substrate. Typically, the stacking distance from the substrate of mechanically exfoliated 2D materials is in the range of 1 to 2 nm. In the work of Quereda et al. [379], for example, the authors report a stacking distance of 1.5

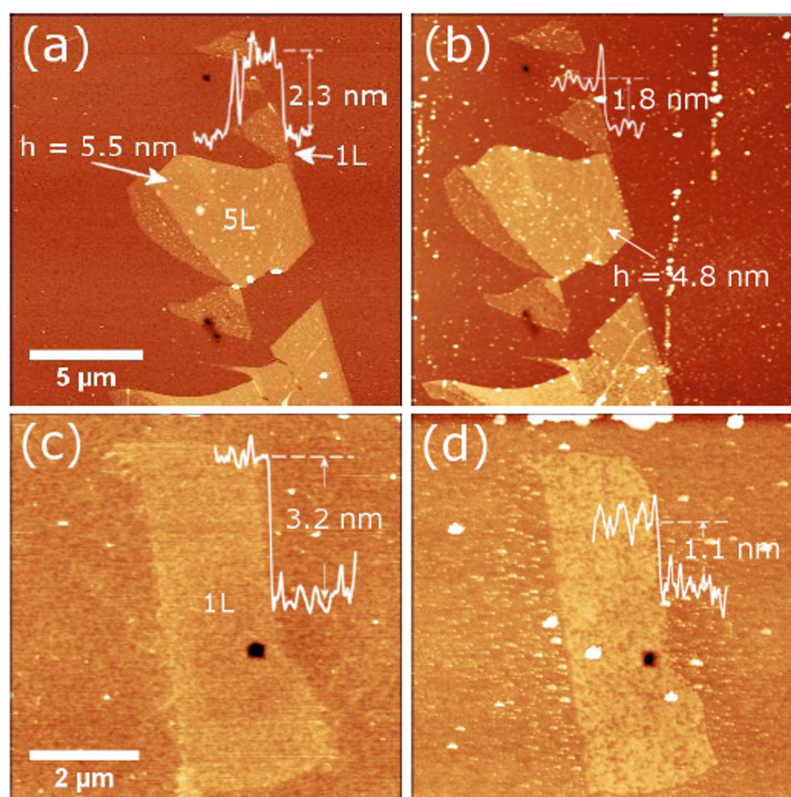

Figure 35. AFM images of mechanically exfoliated MoS_2 flakes on 270 nm SiO_2/Si(100) substrate: (a) and (c) show flakes before annealing, while (b) and (d) show the same flakes under different annealing conditions. (b) at 275 °C for 40 min in air and (d) at 300 °C for 40 min in UHV. The mean height profiles measured from the top of the MoS_2 flakes to the substrate are shown in the figures. Taken from [3].

nm from the SiO_2 substrate. Larger anomalous stacking heights ($\sim$ 2 nm) are not infrequently reported for MoS_2, such as for chemically exfoliated MoS_2 by Coleman's groups [380] and in a paper by Li et al. [381].

To further elaborate on this point, we also rule out the occurrence of instrumental artefacts. Since the AFM is a force detection tool, height anomalies might be introduced by a different elastic behaviour of the substrate with respect to the 2D flakes (see the work of Nemes-Incze et al. [382]). In particular, in tapping mode AFM, such anomalies can be explained with differences in tip-sample tip-substrate adhesion effects. However, tip-substrate adhesion effects can cause height offsets usually in Ångström level, which cannot be the reason that gives us 2-3 nm height values. Moreover, such effects cannot explain our observed variation of the stacking height from the substrate after the annealing. This occurrence has to be ascribed to the presence of a water film nano-confined at the interface between the SiO_2 and the first layer of

MoS_2. May we then note here that, although with no emphasis on layer number engineering, the presence of water at the interface between hydrophobic and hydrophilic substrates and mechanically exfoliated 2D materials has already been documented and summarised in many recent papers and is reviewed by Li et al. in [383] (and the references therein). Our analysis, on the one hand, provides several evidences for the existence of such a water film and, on the other hand, addresses its potential for the study of nano-confinement of water and its interaction with 2D systems.

To unequivocally demonstrate the presence of water at the interface of mechanically exfoliated MoS_2 with SiO_2, we performed dedicated additional experiments inspired by a work of Lee et al. [384]. In that work, the authors directly demonstrated, via time-dependent micro-Raman maps performed at time intervals of days, the effective intercalation via capillary forces of a nano-confined film of water in between a graphene/SiO_2 interface once the system is immersed in water for several days [384]. To this purpose, we retrieved from our sample archive a mechanically exfoliated sample of few-layer MoS_2 that exhibited a monolayer region (1L), as determined by layers-number identification [75]. Such sample (already reported in the Supporting Information (SI) of our previous study [75]) exhibited a stacking distance from the substrate of 3.3 nm after mechanical exfoliation. Considerably, its morphology was re-examined with AFM (see panel (a) of Figure 36) and we observed, after an ageing of 48 months in dry air, a new stacking distance from the substrate of 2.5 nm. The same sample was then immersed in deionized water for one hour, then, after a thorough rinse in dry nitrogen, its morphology was again examined by AFM, revealing a stacking distance of 4 nm (see Figure 36 (b)). The line profiles demonstrate that, after 1 hour water soaking, the substrate to 1L distance of MoS_2 has increased by about 1.5 nm (remarkably, the interlayer distance between adjacent MoS_2 planes is not changed after the immersion in water indicating no water intercalation in between them). This is a notable finding, as we demonstrate the same occurrence reported by Lee et al. [384], but for the first time on MoS_2 and on a time scale one order of magnitude smaller. We then directly demonstrated with AFM, that the distance to the substrate of exfoliated MoS_2 depends on the presence of a nano-confined film of water, that can be removed after annealing or ageing and can be then readily restored via capillary forces by immersing the samples in water.

The water film trapped between the substrate and the MoS_2 is expectedly highly reactive with the MoS_2 bottom layer, especially once the substrate temperature is increased above 250 °C, where the onset of the thermal desorption of sulphur from the MoS_2 basal plane occurs [385]. A striking example supporting such an argument can be found in Figure 37. Here we show two optical images of few-layer flakes of MoS_2 on SiO_2 before (a) and after (b) annealing in air at 400 °C for 40 min.

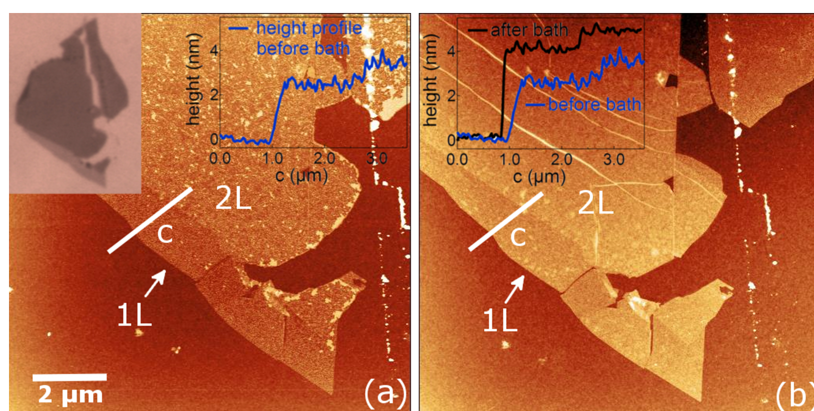

Figure 36. AFM images of a mechanically exfoliated flake of MoS_2 on SiO_2/Si(100) substrate: in (a) the flake after ageing for 48 months in dry air, while in (b) the same flake after a bath in deionized water for 1 hour. The mean height profiles measured along segment c before and after the bath are indicated in the figures. The inset in the top left corner of (a) shows an optical image of the flake. Taken from [3].

Such an annealing temperature in air is already reported as an upper limit before that rapid and complete thermal degradation of MoS_2 occurs [351]. In Figure 37, the image after thermal annealing demonstrates dramatic changes. As reported earlier [351], etching occurs at the flake edges. This can be clearly noticed as a shape shrinkage of the flakes in the bottom right corner of Figure 37 (b). For the triangular, few-layer flake in the middle of the image, the optical contrast is changed from that typical of eight layers to that of three layers [75]. This flake exhibits the appearance of few μm circular pits where the SiO_2 substrate underneath is exposed. Moreover, a monolayer flake, clearly detectable by optical contrast in panel (a) of the figure, at the left of the central triangular flake, is not present anymore on the annealed

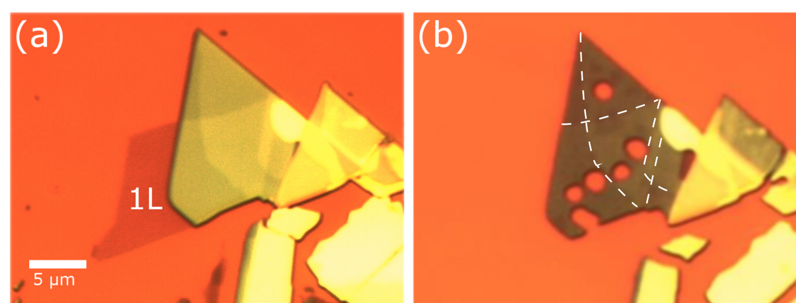

Figure 37. Optical microscope images (100x) of mechanically exfoliated few-layer MoS_2 flakes deposited on 270 nm SiO_2/Si(100) (a) before and (b) after annealing at 400 °C for 40 min in air. In panel (a), '1L' indicates a monolayer. The heat-induced degradation is clearly visible. Taken from [3].

sample. All these effects demonstrate with impressive visual evidence that partial sublimation of the MoS_2 layers has occurred. Moreover, they point toward the evidence of a bottom-up thermal thinning of the flakes. Indeed, a careful visual inspection of further details of the image reveals important aspects of such phenomenon. For example, the detailed texture of the contrast on all the top layers of the flakes remained unchanged after thermal annealing. This strongly points to the unlikely sublimation of the topmost layers of MoS_2.
Our model picture of thermal thinning from the substrate is impressively confirmed in cases when we clearly observe the disappearance of MoS_2 layers at the interface with the substrate. Illustrated in Figure 38, we show optical and AFM images of the same region of a sample containing monolayer (1L) and bilayer (2L) flakes before (panel (a) and (c)) and after (panel (b) and (d)) annealing in air at 275 °C for 40 min. The flake in Figure 38 was correspondingly investigated with Raman spectroscopy and also PL before and after the annealing (see the corresponding spectra in Figure 39 and Figure 40 (a)). The analysis

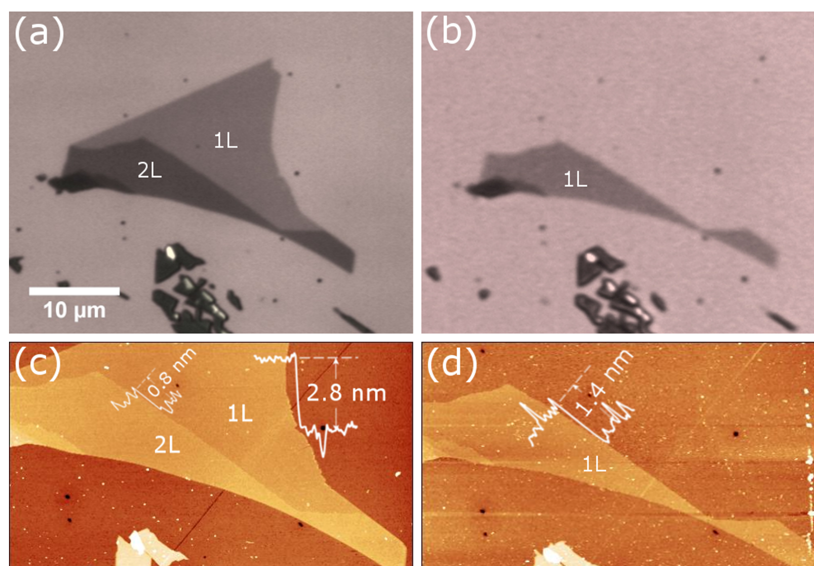

Figure 38. (a) Optical images of a mechanically exfoliated MoS_2 flake before and (b) after annealing in air (at T=275 °C for 40 min). In (c) and (d), the corresponding AFM images are shown. The mean AFM height profiles are inserted to indicate the thickness of the flakes. Taken from [3].

of Figure 38 evidently indicates the thinning of a bilayer into a monolayer, confirmed by non resonant Raman showing an E^1_{2g} -A_{1g} spectral distance of $\sim$ 18.5 cm^{-1} [46]. This is produced by the sublimation of the bottom layer. Again, also in this case, the phenomenon is accompanied by a 1.4 nm decrease in the distance between the flakes and the substrate (see AFM profiles of the 1L regions in Figure 38 (c) and (d)). This bottom-up layer thinning occurrence has not been clearly evi-

denced so far and is an experimental evidence in contrast to previous work, in which a removal of the upper layer by annealing was suggested [288, 351, 365]. The rationale that we propose to explain such an occurrence are discussed in the following sections along with the PL and Raman results. However, considering the increasing interest in layer thinning techniques to obtain single-layer TMDs starting from few-layer flakes, we believe that this very result (Figure 38) can be useful to develop a new mechanism of bottom-exfoliation of layered materials by annealing. To iterate this "thinning-from-the-bottom" procedure a layer of water could be added back. This can be done in principle using the same exfoliated samples on the same substrate and then adding a layer of water back as demonstrated in Figure 36. However, full immersion in the water bath inevitably leads to wetting of the upper surface of the 2D flake, which foreshadows a significant surface degradation during annealing. This methodology needs further investigation, which is beyond the scope of the present study. We also suggest alternative, cleaner strategies. For example, after annealing and sublimation of the bottom MoS_2 layer, one could pick up the remaining flake and stamp it onto another substrate using the clean transfer method first proposed in [386]. This would restore the water layer at the interface without wetting the MoS_2 surface, making the transferred sample ready to be annealed again.

6.2.2 *Non-resonant Raman and PL analyses before and after annealing*

Beside evident morphological changes, annealing processes induce changes in the optical and electrical response of nano-sized flakes of MoS_2 and other TMDs [49, 288, 290, 352, 355, 365].
To gain further insight into these aspects, we have performed Raman and PL spectroscopy studies on MoS_2 monolayers before and after annealing. First, to benchmark our findings against the state of the art in the literature, we measured the Raman spectra of 1L-MoS_2 in the non-resonant condition (achievable with the laser excitation wavelength 532 nm) [46, 122, 371].
In Figure 39, we compare the spectra of monolayer MoS_2 before and after annealing in air as well as in UHV at 275 °C and 300 °C, respectively. From Figure 39, the ratio of the integrated intensity of the peaks E^1_{2g} and A_{1g} for each spectrum is reported in Table 6.1. Within the experimental error, there is no significant variation of this ratio. A more detailed analysis shows that the FWHM of the A_{1g} peak changes slightly after annealing, as it decreases from 9 cm^{-1} to 6-7 cm^{-1}, while the FWHM of the E^1_{2g} peak remains unchanged. The A_{1g} peak also shows a blue shift of about 1-2 cm^{-1} after both the annealing processes. These observations are consistent with some experiments already reported in the literature, where a blue shift of the A_{1g} peak by 1 cm^{-1}

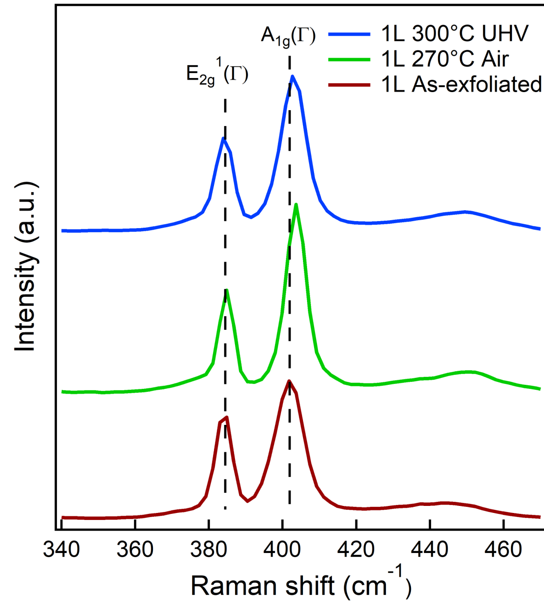

Figure 39. Non-resonant Raman spectra acquired at room temperature with excitation wavelength 532 nm (E=2.33 eV) plotted in the 340÷470 cm^{-1} region of monolayer (1L) MoS_2 on 270 nm SiO_2/Si(100) before (as-exfoliated) and after annealing in air and UHV at 275 °C and 300 °C for 40 min each. The dashed lines show the positions of the E^1_{2g} and A_{1g} peaks. The intensity of the Raman signal in the range 370÷420 cm^{-1} was normalized to unity. The spectra are shifted vertically for clarity. Taken from [3].

was observed after heating [49, 147, 288, 365, 387]. According to [49, 147, 387], the shift of the A_{1g} mode can be used to estimate the density of free electrons in the material. Specifically, the A_{1g} peak exhibits a blue shift in correspondence of a decrement of the density of free electrons. We argue below that the change in such a parameter can be more quantitatively estimated by PL, which ultimately explains our morphological findings.

As has been clearly demonstrated, the PL integrated intensity of MoS_2 is, by far more than non resonant Raman, strongly sensitive to the free electron density in the system [49, 212]. To comprehensively give a rationale to the above observations, we propose a systematic quantitative study of the effects of thermal annealing on the PL spectral intensity and line-shape of monolayer MoS_2.

In Figure 40 we report PL spectra acquired with excitation wavelength 632.8 nm (E=1.96 eV) and laser power 1 mW of monolayer MoS_2 before and after 40 min annealing process in air (a) and in UHV (b) at 275 °C and 300 °C, respectively. The spectra were acquired at RT under identical experimental conditions. In both cases we observe: *i)* a marked increase of the PL integrated intensity by a factor of 2.6 ± 0.1 and 2.7 ± 0.1, respectively (calculated in the range of $640 \div 800$ nm),

Table 6.1. The first row shows the ratio of the integrated intensities ($I_{E^1_{2g}}/I_{A_{1g}}$) of peaks E^1_{2g} and A_{1g} obtained from the non-resonant Raman spectra of single-layer MoS_2 flakes before annealing (as-exfoliated) and after annealing in air and in UHV at 275 °C and 300 °C, respectively. Peak frequency positions E^1_{2g}, A_{1g} and FWHM $\Gamma_{E^1_{2g}}$, $\Gamma_{A_{1g}}$ are also given in units cm^{-1}. Taken from [3].

	As-exfoliated	Annealed 275 °C in air	Annealed 300 °C in UHV
$I_{E^1_{2g}}/I_{A_{1g}}$	0.38±0.02	0.37±0.02	0.40±0.02
E^1_{2g}	384	385	384
A_{1g}	402	404	403
$\Gamma_{E^1_{2g}}$	4	5	5
$\Gamma_{A_{1g}}$	9	6	7

and *ii)* a blue shift (of 17 and 30 meV after annealing in air and in UHV, respectively) of the PL spectra compared to the non-annealed samples. As a matter of fact, no strong differences in PL intensity are observed between the spectra of the samples annealed in air and in UHV, provided the annealing temperature is similar.

We note that the PL spectral line-shape is invariably asymmetric. The spectrum can be nicely fitted only once the interplay of two Lorentzian components is taken into account. This is indeed consistent with the interplay of neutral and charged (trion) excitons whose radiative emissions are present in the PL spectrum of MoS_2, as generally agreed in the literature [45, 47, 147, 286, 292, 370].

The neutral (charged) exciton component is observed at higher (lower) energy. The analysis of PL spectra of single-layer MoS_2 even at RT, based on such a model, is widely accepted and well received in the scientific community (see, e.g., the crucial work by Mouri et al. [292]). To strengthen the reliability of our fit, in our model analysis we set the exciton and trion binding energies to $B_{A_0} = 277$ meV and $B_{A^-} = 29$ meV, where the trion binding energy is conventionally defined as the energy difference between the neutral and charged exciton energies. Calculations within the 2D effective mass approximation are given in the SI of our work [3] and are consistent with previous results in [45, 138–140, 145]. Given the electronic band gap of 2.14 eV [109], the fitting analysis that we propose is performed by constraining to the above binding energies the energy position of the neutral and charged excitons. Once such a constrained fitting analysis is performed, an intensity interplay of the two types of excitons can be clearly inferred in our

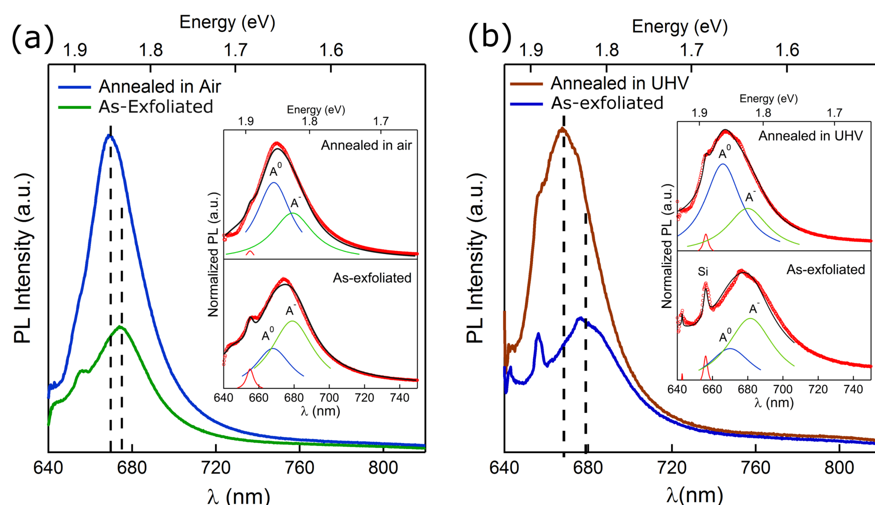

Figure 40. PL spectra acquired at room temperature with excitation wavelength 632.8 nm (E=1.96 eV) of monolayer MoS_2 before (as-exfoliated) and after annealing in air (a) at 275 °C for 40 min and in UHV (b) at 300 °C for 40 min. The insets show the same spectra after normalisation to unity: the spectra were fitted with two Lorentzian line shapes, A^0 for the exciton and A^- for the trion (at constrained binding energies of 277 and 29 meV, respectively). The fitting lines (experimental data) are shown in black (red). Taken from [3].

spectra before and after annealing.
The results of the quantitative fitting analysis of the PL spectra are reported in Table 6.2.
To further carefully monitor the annealing temperature dependence of the increase of the PL intensity, we conducted a systematic investigation in the ($RT \div 300$ °C) range, focusing on samples annealed in air. In Figure 41 we report, after normalisation to the PL value of as-exfoliated MoS_2, the variation of the PL spectral intensity as a function of the annealing temperature in air. Our trend is consistent, even in air, with the PL study by Nan et al. in [49], in which a monolayer of MoS_2 was subjected to thermal annealing in vacuum and showed a progressive increase in PL intensity as a function of annealing temperature after post annealing exposure to oxygen. In particular, in their work the authors demonstrate via spatially resolved measurements, that the increase in PL spectral intensity is clearly due to the creation of S vacancies by thermal annealing and their subsequent oxygen passivation. The very plausibility of the oxygen passivation has been theoretically addressed in [388], where Lu and co-authors, via DFT calculations, investigated different possible sulphur vacancy passivation schemes. In particular, they report of O_2 chemisorption at S vacancies, stating that it is energetically stable after overcoming an energy barrier at room temperature [388].
To directly benchmark this hypothesis, namely the increase of the PL

Table 6.2. Quantitative analysis of PL spectra reported in Figure 40 via a constrained fit in terms of neutral and charged excitons A^0 and A^-. Sample (a) (sample (b)) refers to the sample annealed in air (UHV) (40 min at 275 °C for (a) and 40 min at 300 °C for (b)). The peak positions of A^0 and A^- are given in eV. Taken from [3].

	As-exfoliated sample (a) | sample (b)	Annealed 275 °C in air sample (a)	Annealed 300 °C in UHV sample (b)
I_{A^0}/I_{A^-}	0.51 | 0.51	1.41	1.73
A^0	1.856 | 1.850	1.854	1.861
A^-	1.826 | 1.820	1.825	1.823

intensity with the formation of S vacancies, and its subsequent passivation in air, in the same Figure 41 on the right vertical axis we report a direct estimate of the percentage of sulphur vacancies determined as function of the annealing temperature for bulk MoS_2 with X-ray photoemission spectroscopy (XPS) experiments [385]. It is clearly visible from this graph the strict correlation between the onset of the formation of sulphur vacancies and the enhancement of the PL intensity as a function of the annealing temperature. It is important to stress that, from our previous studies, XPS clearly indicates that the formation of sulphur vacancies and its concentration as a function of annealing temperature is independent on the annealing environment (either UHV [385] or air [366]). Remarkably, both the PL response, and the S vacancy concentration, are left unchanged (with respect to RT) up to annealing at 200 °C.
Whether, a direct correlation of the increase of the PL intensity with the increase of the sulphur vacancies (and its subsequent counter passivation in air by oxygen) is clearly demonstrated, on phenomenological grounds, on the other hand, only a more fundamental analysis of the PL spectra can allow us to substantiate our findings on the basis of a simple model interpretation. We start with the observation that the changes in the PL response, have to be assigned to changes in the doping level of MoS_2. This system is an n-type semiconductor. The creation of an S vacancy inherently determine (as UHV studies demonstrate [385]) an increase of the n doping level in the system. Vice versa, a subsequent exposure of the S vacancies to oxygen determines (because of the oxygen electronegativity) a corresponding electron depletion (hole injection in the system). Within the investigated temperature range, we can safely state that system remains n doped, as directly evidenced in resistivity measurements in [366]. On the other hand, the onset of a

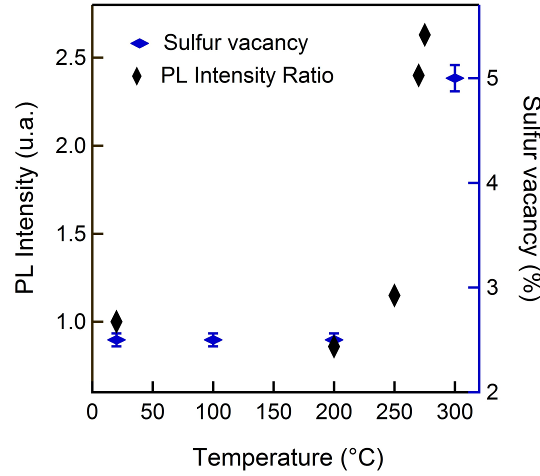

Figure 41. Left axis, normalised (to PL intensity before annealing) spectral PL integrated intensity as a function of annealing temperature (RT, 200 °C, 250 °C, 270 °C, 275 °C for 40 min) in air. Right axis (blue) percentage of sulphur vacancies determined for the surface of bulk MoS_2 by XPS as a function of annealing temperatures (RT, 100 °C, 200 °C, 300 °C) from ref. [385]. Taken from [3].

p-type behaviour, should manifest itself with the presence of a positive trion component in PL (which we do not observe) [144]. Now, if we call h_B, and x_s respectively the background hole concentration in the system and the surface percentage of S vacancies, then upon oxygen passivation in air, we can state that $h_B \propto x_s$. Calling n_B the background concentration of electrons in the system, then, as via the mass action law for semiconductors $n_B h_B = {n_i}^2$, (n_i being the carrier concentration for the intrinsic semiconductor) we can state $n_B(x_s) \propto 1/x_s$. Therefore, once the S vacancy concentration is changed from x_1 to x_2 we have $n_B(x_1)/n_B(x_2) = x_2/x_1$. Indeed this ratio is a measurable parameter from the fitting analysis of the PL spectra. One can more than plausibly state that, upon laser excitation, with decreasing the background conduction electrons the ratio of neutral/charged excitons increases. This has to be assigned to the fact that the population of electrons already available (background) in the system apart from the electron and hole pairs created by the laser excitation is decreased. In other words, the more (less) excess electrons are already present in the system the more (less) likely is the formation of trions, or, putting this argument in a trend:

$$n_{A^0}/n_{A^-} \approx 1/n_B. \tag{6.1}$$

Therefore, given two samples with two different doping levels $n_B(x_1)$ and $n_B(x_2)$, we can finally state, from the fitting analysis of two spectra, for a fixed pump of the laser, that:

$$\frac{n_{A^0}(x_2)/n_{A^-}(x_2)}{n_{A^0}(x_1)/n_{A^-}(x_1)} \approx x_2/x_1. \tag{6.2}$$

The relevant parameter, that we extract from our fit with constrained theoretically calculated binding energies for the two types of excitons, is then their intensity ratio as a function of the annealing temperature. Within the experimental error of the fit, that we estimate of the order of 15 %, the ratio measured at RT (for as exfoliated MoS_2 monolayers) is 0.5, while this ratio increases respectively to 1.4 and 1.7 for the annealed samples in air and UHV (see Table 6.2). This leads to an estimate of an increase of a factor 3 ± 0.4 of the concentration of the (passivated) sulphur vacancies upon annealing at 270-300 °C. We note also that this factor increase of the sulphur vacancy concentration is, within the error, the same increase experimentally observed in the PL intensity (see Figure 41 left axis). Despite the quite large uncertainty of such an estimate, on the other hand this is a local estimate having the same spatial resolution of the laser spot.
Summarising this part, we have demonstrated the strict phenomenological correlation of the increase of the PL intensity of monolayer MoS_2 with the increase of the sulphur vacancy concentration (up to 300 °C annealing either in UHV or in air). We have then correlated the variation of this latter parameter to the variation upon annealing of the neutral/charged exciton ratio.

6.2.3 *Bottom-up layer engineering and PL evidences: a rationale*

To understand our overall findings we have to thoroughly discuss the role and presence of sulphur vacancies in MoS_2. It is agreed that, for thermodynamic reasons [389], MoS_2 is inherently under stoichiometric and the formation of S vacancies makes the system thermodynamically stable. In a very recent work, the group of Tapaszo [390] has clearly showed that, in mechanically exfoliated MoS_2 single crystals (which is our case), that are generally believed to be high quality crystals, scanning tunneling microscopy (STM) directly evidences the presence of S vacancies with a surface concentration of $1\text{-}5 \times 10^{13}$ cm^{-2}. Given the surface sulphur concentration in pure MoS_2 of 1.16×10^{15} at/cm^2 [391], this sulphur vacancy concentration accounts for a presence of 1-5 percent of sulphur vacancies. This is in line with our indirect XPS observation for freshly cleaved bulk MoS_2 and we can plausibly argue that this value underestimates the vacancy concentration in the monolayer [385]. Remarkably, in a basal plane of mechanically exfoliated MoS_2 with a 1% (5%) concentration of sulphur vacancies, assuming that the vacancies are homogeneously distributed, the vacancy nearest neighbour distance is 3.3 (1.4) nm, whereas this value drops to 1.8 (0.8) nm if the vacancy concentration value is increase by a factor close to three as estimated from the PL analysis reported above. In other

words, once such values are put together with our PL estimate of the variation of the vacancy concentration, we can conclude that, under the more optimistic assumption of vacancy homogeneous distribution, upon annealing at around 300 °C, one can expect the MoS_2 basal plane to be literally "littered" by sulphur vacancies, that eventually might coalesce, due to their being very close one to another (down to the fifth coordination shell). This is in line with the sudden onset of degradation in air above 300 °C, ubiquitously reported in the literature [351].
Using the arguments illustrated above, let us now propose a rationale for the preferential sublimation of the MoS_2 bottom layer once a water film is present at the interface with the SiO_2 substrate. We have clearly demonstrated its presence, and the tunability of its thickness upon annealing. Evidently, once annealing in air, whether the top layers of a flake are exposed to a reactive gas mixture of oxygen and water vapour, on the other hand, only the bottom layer at the interface with the substrate is in contact with a high temperature water film. Remarkably, water pressure can even exceed ambient pressure, as reported in a recent molecular dynamics paper [392], where water droplets confined into graphene nano-blisters on a dielectric substrate are trapped in the blister by a local pressure of up to 7 MPa [392]. *S* vacancy sites are known to be active sites for H_2O exothermic dissociation into O and 2H atoms bound to Mo and S atoms, respectively [393]. Thus, upon thermal annealing and the creation of a sulphur vacancy (above 250 °C) its immediate oxidation due to water dissociation at the bottom MoS_2 layer is more than likely. A more efficient formation of Mo oxide is very likely there, although the occurrence of the same phenomenon at the top layer of the flake cannot be excluded. In other words, it is more than plausible that the highest reactive interface is the one at the bottom. The bottom interface plays then the role of a nano-reactor.
An interesting experimental finding is the observed decreased of the PL spectral yield at 200 °C. The rationale for such observation is the following. As demonstrated via XPS measurements of annealed MoS_2 in air [366] an annealing temperature of 200 °C is not enough to induce Sulphur desorption from the MoS_2 basal plane. The Sulphur vacancy concentration value remains unchanged with respect to the intrinsic concentration value of Sulphur vacancies. The PL response should therefore not change with respect to the RT response. Indeed, it is known from carbon nanotube studies that the SiO_2 substrate can reduce PL emission due to scattering processes with surface optical phonons [394, 395]. Therefore, due to the thinning of the interfacial water and impurity layer at the interface between the SiO_2 substrate and the MoS_2 monolayer, which reasonably occurs above 100 °C, a corresponding decrease in the PL spectral intensity is expected. A similar effect can be attributed to a decreased dielectric constant in the environment due to evaporation of the water base film, which, as reported in [45], decreases the quantum efficiency of the excitonic radiative recombinations.

6.2.4 *Power dependent PL analysis and electron density estimation*

In this section the evolution of excitonic transitions in MoS_2 in monolayer phase produced by annealing in the (200 ÷ 300) °C temperature range is discussed with power dependent PL measurements in the 0.01 ÷ 1.00 mW excitation laser power range. We studied in detail the evolution of A° and A⁻ excitons with the annealing temperature showing that the PL spectral weight of excitons can be modulated in this annealing temperature range.
We have analysed th e PL peak integrated intensity (hereafter spectral yield) as a function of excitation laser power (the raw PL spectra are shown in Figure 5 of the SI of our work [4]). Figure 42 shows the mean normalized PL spectral yields of as-exfoliated and annealed samples as functions of excitation laser power. We observe sub-linear behaviour of PL intensities that tends to high excitation saturation. Generally it is expected that PL intensity follows a power law $I \propto P^b$, where P is the excitation laser power and b is the exponent [396]. We performed the fit of the normalized (to the PL intensity obtained at 1.00 mW excitation laser power) PL spectral yield for each sample, before and after annealing, with a power law $I/I_0 = P^b$. Since we do not find trend indications of exponents (b) with annealing temperature (see Table 3 of the SI of [4]), we averaged the exponents over the annealing temperatures. We got mean fitted exponents b = 0.77 ± 0.01 (b = 0.76 ± 0.03) for as-exfoliated (annealed) samples.

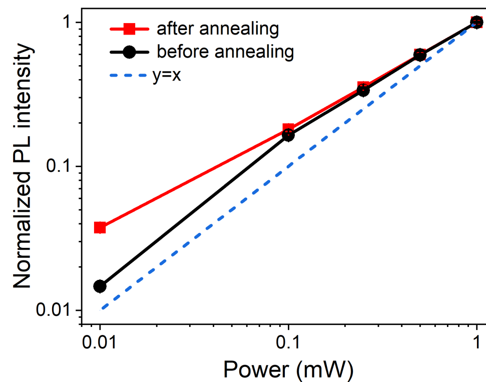

Figure 42. Log-log plot of normalized (to the mean PL intensity acquired at 1.00 mW excitation laser power) mean PL intensity yields as functions of excitation laser power measured before (black) and after (red) the annealing. Identity function (blue dashed line) is shown for comparison. Taken from [4].

In figure 43 we summarize the power dependent PL intensity analysis of total PL signal and fitted peaks (A^0 and A^-). The detailed analysis

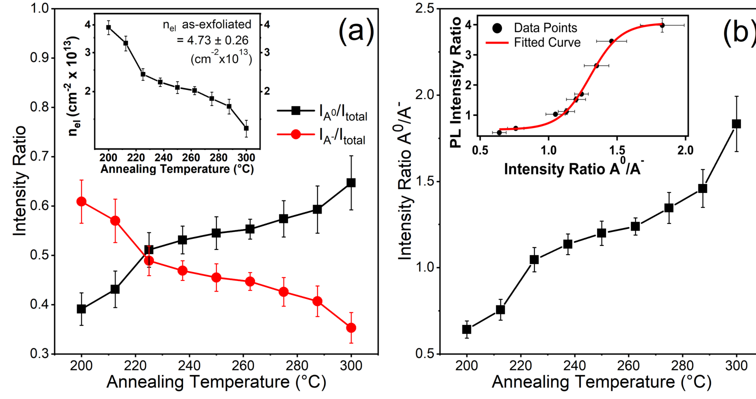

Figure 43. (a) Mean PL spectral weight of A^0 (black squares) and A^- (red dots) fitted peaks of annealed samples are plotted as functions of annealing temperature. The inset shows the log-linear plot of the mean electron density estimate of annealed samples as a function of annealing temperature. (b) The mean PL intensity ratio between A^0 and A^- fitted peaks of annealed samples are plotted as a function of annealing temperature. The inset shows the plot of the mean PL Intensity Ratio as a function of the mean PL intensity ratio between A^0 and A^- fitted peaks. The red line shows the hyperbolic tangent fitted curve for data points. Taken from [4].

of the excitons peak intensities (reported in the SI of [4]) does not show substantial variations with the excitation laser power. For this reason, we report in Figure 43 the results obtained by averaging on the laser powers. In panel (a) of Figure 43 the mean PL spectral weight of A^0 (defined as the intensity of the A^0 peak on the total PL signal intensity and labelled I_{A^0}/I_{total}) and the mean PL spectral weight of A^- (defined as the intensity of the A^- peak on the total PL signal intensity and labelled I_{A^-}/I_{total}) are plotted as functions of annealing temperature. PL spectral weight of the A^0 peak increases with annealing temperature, while PL spectral weight of the A^- peak decreases with annealing temperature. Moreover, the PL intensity is dominated by the A^- peak for the 200 °C annealed sample, while the PL intensity is dominated by the A^0 peak for the 300 °C annealed sample. The PL intensity of the A^0 and A^- peaks are comparable for the 225 °C annealed sample. It is noteworthy that the PL spectral weight of type A excitons (A^o and A^-) is tunable in this temperature range. This increase in the A^0 peak intensity is consistent with our previous findings (see Figure 40) and indicates the emergence of the neutral exciton contribution to the PL signal after p-type doping of MoS_2. In panel (b) of Figure 43 the mean PL intensity ratio between A^0 and A^- (defined as the intensity of the A^0 peak on the intensity of the A^- peak) is plotted as a function of annealing temperature.

For various post annealing temperatures, the total spectral yield of

PL response, after normalization to the corresponding spectral yield measured for the same as-exfoliated sample, is defined as PL Intensity Ratio (PLIR). As previously demonstrated the PLIR increase with annealing temperature. The PLIR value obtained at 1.00 mW excitation laser power of MoS_2 monolayer annealed at 300 °C for one hour is quantified as 4.03 ± 0.13. In the inset of panel (b) of Figure 43 the mean PLIR is plotted as a function of the mean PL intensity ratio of A^0 and A^- peaks. The best fitted curve indicates a close relationship between the PLIR and the PL intensity ratio of the A^0 and A^- peaks, and shows a specific hyperbolic tangent trend. This behaviour indicates that the PL signal increase is triggered when the PL spectral weight of A^0 becomes comparable to PL spectral weight of A^- that corresponds to a 225 °C annealing temperature. Then PLIR grows rapidly in the range that corresponds to annealing temperatures between 237.5 °C and 287.5 °C, where Sulphur desorption becomes considerable. However, when the PL spectral weight of A^0 is double compared the PL spectral weight of A^-, PLIR goes into saturation. This analysis suggests that annealing processes in air beyond 300 °C would not lead to any further significant PL signal increase because it is not possible to further increase the population of A^0 state due to sulphur desorption mechanism that goes into saturation.
In the inset of panel (a) of Figure 43 the mean electron density estimate of annealed samples is plotted as function of annealing temperature. The electron density was calculated by the mean PL spectral weight of the A^- peak using the 2D mass action law and a statistical three-level model as proposed by Mouri et al. [292] (see section 4.3.6). In this model the effective mass of electrons ($m_e = 0.35m_0$) and holes ($m_h = 0.45m_0$) have been chosen [106], where m_0 is the mass of a free electron. The effective masses of neutral exciton m_{A^0} and trion m_{A^-} can be calculated as 0.8 m_0 and 1.15 m_0 respectively [292]. Using these parameters, the electron density expression has form:

$$n_{el} = \frac{10^{14} \frac{I_{A^-}}{I_{total}}}{4(1 - \frac{I_{A^-}}{I_{total}})} [cm^{-2}]. \tag{6.3}$$

We estimate a mean electron density for as-exfoliated MoS_2 monolayer of 4.73 ± 0.26 ($cm^{-2} \times 10^{13}$) and electron density for annealed MoS_2 monolayers ranging from 3.90 ± 0.28 ($cm^{-2} \times 10^{13}$) for 200 °C annealed sample to 1.36 ± 0.12 ($cm^{-2} \times 10^{13}$) for 300 °C annealed sample. These values are comparable to that reported by Mouri et al. [292] of ~ 6 ($cm^{-2} \times 10^{13}$) for freshly mechanically exfoliated MoS_2 monolayers deposited on SiO_2/Si substrate, confirming that the thermal annealing process in air for one hour between 200 °C and 300 °C allows to slightly reduce and modulate the n-type MoS_2 doping due to sulphur desorption and consequent oxygen adsorption, without inducing heavy doping variation.

6.2.5 *Resonant Raman analysis*

In Figure 44 we show, on the same intensity scale, the RT resonant Raman spectra acquired at 1.00 mW excitation laser power of monolayer MoS_2 as-exfoliated (bottom panel) and annealed (top panel) at 275 °C in air for 40 min. The sample studied was the same single layer

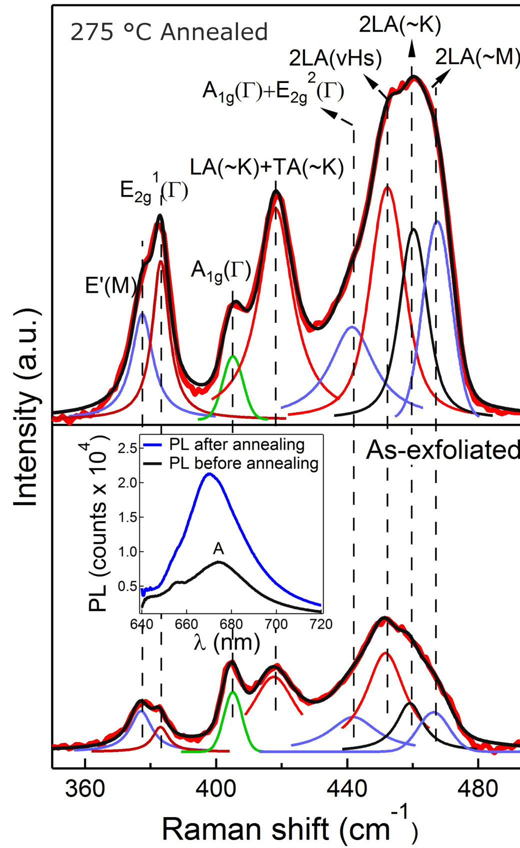

Figure 44. RT resonant Raman spectra acquired at 1.00 mW excitation laser power $\lambda = 632.8$ nm (E=1.96 eV) in the 360÷480 cm^{-1} range of single-layer MoS_2 on SiO_2/Si(100), as-exfoliated (bottom panel) and annealed (top panel) in air at 275 °C for 40 min. The spectra were fitted with Voigt line shapes (colored). The peaks positions were assigned and labeled according to the literature [122, 161, 284, 285]. The inset shows the corresponding PL spectra. Adapted from [4].

MoS_2 of the PL analysis of Figure 40 (a). The resonant Raman spectra were measured in the 360 ÷ 480 cm^{-1} range, where are observed the most intense spectral features of resonant Raman spectrum, related to first-order (E^1_{2g} and A_{1g}) and second-order Raman scattering modes. The spectrum related to the as-exfoliated monolayer (bottom panel) is in agreement with the ones reported in literature [161, 397] and with

our previous findings [75, 398]. The spectra are fitted with a sum of Voigt line-shapes associated at specific phonons (labeled in the top panel of Figure 44) at high-symmetry points within the Brillouin zone in line with the spectral identification proposed in literature[122, 161, 284, 285].

As evident from the Figure 44, the Raman signal has grown after annealing like the PL signal. In analogy to the quantitative analysis of the PL signal increase, the whole Raman integrated intensity (Raman spectral yield) is calculated in the $360 \div 480$ cm^{-1} range and the increase of the Raman spectral yield of MoS_2 monolayer annealed at 300 °C for one hour corresponds to a factor of 3.97 ± 0.31. This is, within the experimental error, the same increase correspondingly observed in the PL spectral yield. This correspondence is also verified at other annealing temperatures between 200 °C and 300 °C. On this regard we report in Figure 45, for various post annealing temperatures, the total spectral yield of the resonant Raman response, after normalization to the corresponding spectral yield measured for the as-exfoliated sample, defined as Raman Intensity Ratio (RIR). In the same Figure 45, for direct comparison, we report PLIR values obtained at 1.00 mW excitation laser power. We systematically observe RIR and PLIR values less than one,

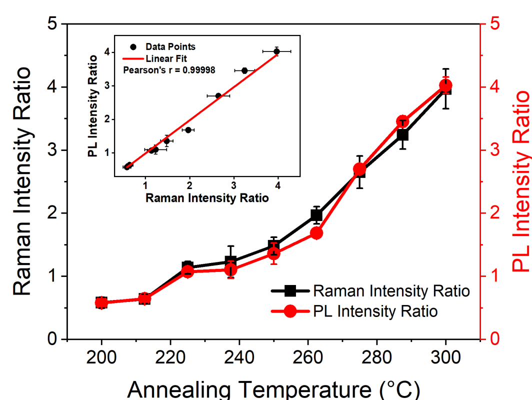

Figure 45. Left axis (black), normalized (to the Raman integrated intensity before annealing) Raman spectral yield (Raman Intensity Ratio) in the $360 \div 480$ cm^{-1} range plotted as a function of annealing temperature. Right axis (red), corresponding values of normalized (to the PL intensity before annealing) PL spectral yield (PL Intensity Ratio) in the $640 \div 800$ nm range. The inset shows the plot of the PL Intensity Ratio as a function of Raman Intensity Ratio. The red line shows that the one-to-one linear relationship between the data points is perfectly fulfilled with a calculated Pearson correlation coefficient $r \sim 1$. Taken from [4].

corresponding to decrease of Raman and PL intensities for the samples annealed at 200 °C and 212.5 °C. Contrarily, starting from 225 °C, both RIR and PLIR show growing trends up to 300 °C annealing temperature. It is also noteworthy that they show almost superimposing trend with annealing temperature. To further quantify this observation, we plot

PLIR as a function of RIR in the inset of Figure 45. The graph evidences a strict one-to-one linear correlation with a calculated Pearson r coefficient of 1. This close correlation means that the Raman signal increase is due to the same mechanism of the PL signal increase. Therefore, since PL is due to A type excitons, this correlation is a strong experimental evidence of the exciton-phonon coupling effect. Moreover these results provide demonstration that also the second order Raman modes, which involve two phonons, are coupled with A type excitons.
Finally a refined analysis of the first order E^1_{2g} and A_{1g} Raman modes is proposed in Figure 46. There, as a function of PLIR, we report, normalized to the spectral intensity for freshly exfoliated samples (before annealing), the relative intensity ratio of the E^1_{2g} and A_{1g} modes respectively. The E^1_{2g} peak intensity ratio exhibits appreciable increase of intensity with PLIR and the fitted curve shows an exponential trend with PLIR. Contrarily the A_{1g} peak intensity ratio does not exhibit appreciable increase of the A_{1g} intensity with PLIR remaining almost constant with PLIR. This occurrence is verified only for this specific spectral mode. To interpret these results we observe that the A_{1g} Raman

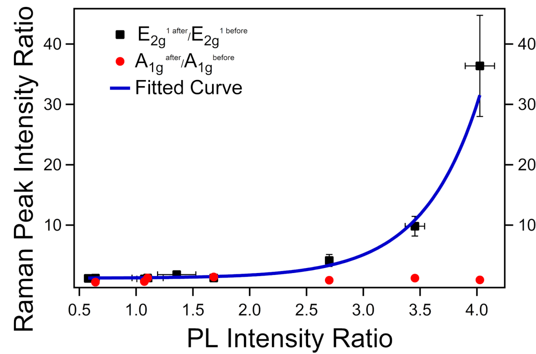

Figure 46. Intensity ratio of E^1_{2g} (black squares) and A_{1g} (red dots) Raman fitted peaks measured before and after the annealing plotted as functions of PL Intensity Ratio. The blue line shows the exponential fitted curve for E^1_{2g} Raman peak data points. Taken from [4].

mode is the only out-of-plane phonon mode. It is thus an experimental evidence that the A type excitons only couple with in-plane phonons. For obvious matrix element reasons that, via an exciton-phonon coupling Hamiltonian would lead to a reduced coupling in case of an in-plane phonon and an out-of-plane exciton, this strongly points to a in-plane symmetry of the A type excitons (both A^0 and A^-). This experimental result is in line with a reported study on MoS_2 PL by Schuller et al [377] but appear to contradict previous experimental [376] and theoretical reports [141] that point to an out-of-plane spatial symmetry of the A type excitons in single-layer MoS_2. To strengthen this point, it must be emphasized the fact that, in this work, without affecting

significantly the electronic, and accordingly the phonon structure of MoS_2 monolayer has not been changed. Indeed it has been varied just the population of A excitons, whereas, in the other resonant Raman works, the approach was to vary the excitation wavelength [376]. The fact that the electronic and phonon structures have not been altered significantly it is supported by the observation of no relevant spectral shifts and widening of Raman peaks (see Figure 44). Indeed, as directly demonstrated by Mignuzzi et al. [287], the energy position and width of the E^1_{2g} and A_{1g} modes only shift and increase upon very heavy doping via ion implantation with a surface concentration of defects close to $10^{14}/cm^2$, which is a value well above the sulphur vacancy concentration range that can be estimated in our case and that amounts to (1-5) $\times$ $10^{13}/cm^2$ [385]. Moreover in Figure 43 we have shown that the annealing did not cause heavy doping variations, because the electronic density estimates of the annealed samples are comparable with the mean electron density estimate of the as-exfoliated samples and with the value reported by Mouri et al. [292].
Furthermore, the choice of 1.96 eV laser excitation energy, which we used, should be the optimal choice for the coupling strength (as a function of laser wavelength) with the A_{1g} mode [376], but we still do not observe any exciton related enhancement of the out-of-plain A_{1g} Raman peak intensity (see Figure 44), which supports our point about the in-plain spatial symmetry of the A excitons.

6.3 CONCLUSIONS TO CHAPTER 6

In conclusion, thermal annealing effects on few-layer mechanically exfoliated MoS_2 have been studied by Raman and PL spectroscopies in the temperature range of 200-300 °C (which is reported to be crucial in the literature for doping and layer engineering) both in air and in UHV. The annealing in this temperature range varies the concentration of Sulphur vacancies and the corresponding PL spectral yield. Via AFM we demonstrate the presence of a 1-2 nm thick water film at the interface between the MoS_2 flakes and the SiO_2 (270 nm on Si(100)) used substrate. The film is thinned down with thermal annealing. In some cases upon annealing at 275 °C in air and above, contrarily to what reported in the literature, we show direct visual evidences of the sublimation of the bottom layer. This occurrence is explained with the aid of a quantitative interpretation of the PL spectra. In particular, in our model, we propose to use PL to locally probe the variations of the sulphur vacancy concentration. The PL spectra are fitted by means of a constrained analysis based on the interplay of neutral and charged (trion) excitons whose binding energies (277 meV and 29 meV respectively) have been calculated via two-dimensional model Hamiltonian. Using this constrained fitting analysis we derived directly the variation of sulphur vacancy concentration. In line with XPS in the literature, this

concentration does not increase upon annealing up to 200 °C. In the 200-300 °C range the PL intensity increases, and the estimated sulphur vacancy concentration increases of correspondingly a factor 3.0 ± 0.4. Being the sulphur vacancy concentration on freshly exfoliated monolayer MoS_2 in the 1-5 % concentration range, then this value raises, upon annealing, up to critical values close, or above 10%. With such thermally induced defect concentration values, given the presence of the water film at the interface of the bottom MoS_2 layer with the SiO_2 substrate, exothermic water dissociation at the vacancy sites is then the mechanism that most than likely leads to its sublimation. A layer engineering from the bottom of a 2D material is then demonstrated and rationalised.
The evolution of A^o and A^- excitons with the annealing temperature was studied by power dependent RT PL in the $0.01 \div 1.00$ mW power range demonstrating not substantial variation with the excitation laser power. The 200 °C annealed PL signal is dominated by the trion related peak, while the 300 °C annealed PL signal is dominated by the neutral exciton related peak, and the PL spectral weight of excitons are tunable in this temperature range.
We studied the RT resonant Raman (632.8 nm) response and the corresponding RT PL response, at 1.00 mW excitation laser power, of the same as-exfoliated and annealed MoS_2 monolayers. We calculated the annealing spectral yield of both resonant Raman and PL responses at the various annealing temperatures and correlated the two set of data upon normalization to the corresponding spectral yields measured on the as-exfoliated samples. The Raman intensity ratio and the PL intensity ratio exhibit one-to-one correlation providing a direct experimental evidence of the exciton-phonon coupling in 2D MoS_2. We demonstrated that the A type excitons only couple with in-plane first order and second order Raman modes and strongly couple with the E^1_{2g} in-plane Raman mode, while they do not couple with the A_{1g} out-of-plane Raman mode. This is an indication of the in-plane symmetry of the A type excitons in agreement with momentum resolved PL measurements [377]. In this way, the existence of a fundamental relationship between the morphology of two-dimensional materials and the orientation of excitons was demonstrated. Application of this technique to other cases of strongly oriented materials could lead to a better understanding of the processes of electron-hole generation and recombination in these materials [377].

Conclusions and Outlook

7

7.1 Conclusions

In this work, spectroscopic techniques have been developed to study some important aspects of two materials of great interest for present and future electronics, namely Si and MoS_2. The study of Si, which impacts the most widely used electronics technology in the world today, is more application-oriented, while the study of MoS_2 is mainly aimed at increasing the knowledge of fundamental aspects of this emerging research material.
With this aim, part of this work reports the investigation of a Raman spectroscopy-based technique for measuring the doping concentration in p-type crystalline Si. In addition to this study, another part of the thesis reports on a technique that uses Raman and PL spectroscopy together with annealing treatments to study the optical and electronic properties of MoS_2 as a function of defects in the material and associated changes in doping concentration. The common feature of the two studies is the use of spectroscopic analysis to investigate certain optical and electronic properties of the material as a function of the doping content of the material itself.
A characterization of the doping concentration in Si has been performed using a wavelength-dependent micro-Raman analysis to precisely measure the concentration of free holes in p-type Si in the wide range of $(10^{15} \div 10^{20})$ cm^{-3}. The first-order one-phonon Raman Stokes peak of Si is modified by the Fano effect associated with doping. An improved fitting method of the Si peak, which exploits a convolution of Fano and Gaussian functions, enabled the determination of the subsurface doping concentration in Si wafers with unprecedented accuracy. The experimental results were directly compared with relevant literature data that studied doped Si in the high concentration regime $> 5 \times 10^{18}$ cm^{-3}. This showed that the proposed analysis is consistent with previous studies and complementary for the intermediate concentration range $(10^{15} \div 10^{18})$ cm^{-3}. Specific Fano-fitting parameters of the first-order Raman Si line, such as the peak broadening $2\Gamma_F^0$ and the peak shift $\delta\omega$, were found to be independent of the excitation wavelength and their dependence on the doping concentration revealed linear trends. Using this particular dependence on doping concentration, it was possible to construct calibration curves useful for doping monitoring applications. Taking advantage of the different penetration depths of the different wavelengths of visible and near UV light in Si, the proposed technique can be used to probe the subsurface of Si wafers at different depths, allowing a clean characterization of the doping. Application of the analysis to Si samples with shallow doping configuration (100 nm) has shown that only near-UV radiation is suitable for monitoring the dop-

ing concentration at the nanoscale. Implementation of near-UV Raman analysis on small-angle beveled samples allows doping concentration profiling with a lateral resolution of $\sim 1\mu m$ and a vertical resolution of $\sim nm$, demonstrating that the technique is effective for the very shallow dopant distribution used in current Si-based devices. The non-invasive nature of spectroscopy measurements and the simple and fast character of Raman analysis performed on the surface of Si wafers make the proposed doping characterization technique a useful tool in foundries for product and process monitoring and as an in-line diagnostic tool. On the other hand, the doping profiling technique, which is destructive due to the use of beveled samples, can be an efficient alternative to the more onerous SIMS and SRP methods.
As for MoS_2, this thesis reports on a study of the Raman and PL spectra of mechanically exfoliated single- and few-layer MoS_2 samples deposited on SiO_2/Si substrate, analysing the changes in spectral responses due to annealing of the samples in the temperature range of (200 ÷ 300) °C. Optical microscopy and AFM analyses of samples annealed at temperatures up to 400 °C are also reported. Annealing processes in the range of (200 ÷ 300) °C produce defects such as sulphur vacancies on the basal (upper and lower) planes of the flakes, and accordingly PL, Raman and resonant-Raman analyzes on such materials show spectral changes compared to those obtained on freshly exfoliated samples. These changes in the spectra are attributed to a change in the concentration of free electrons in MoS_2. The change in the concentration of sulphur vacancies by annealing and their subsequent passivation, after the material has been exposed to the atmosphere, by physical and chemical adsorption of H_2O and O_2 molecules, leads to a change in the doping level by a kind of oxidation. In this way, an increase in the concentration of sulphur vacancies corresponds to a decrease in the concentration of free electrons in the material. Raman spectra obtained in the non-resonant condition (with 532 nm radiation) showed a small variation in the distance between the two first-order Raman peaks (E^1_{2g} and A_{1g}), which is interpreted in the literature as a consequence of a variation of the doping level in the material. PL spectra attributed to radiative recombination of A-type exciton states (A^0 and A^-) in MoS_2 showed an increase in integrated intensity after annealing, which is interpreted as a consequence of an increase in exciton populations caused by a decrease in the concentration of free electrons in the material. The PL spectral weight between the two components A^0 and A^- was found to be tunable by annealing in the temperature range (200 ÷ 300) °C, with the A^- component dominating at the lower temperatures and A^0 at the higher temperatures.
A mathematical model relating the increase in the PL spectrum, detailed into its two excitonic components A^0 and A^- , to the change in the concentration of free electrons in the material allowed us to estimate the concentration of vacancies generated by annealing processes. Simi-

larly, A^0 and A^- intensities were used in a statistical model (three-level model) to quantitatively evaluate the change in free electron density after annealing as a function of annealing temperature.
In addition to the analyses involving the optical and electronic properties of MoS_2, we also report a study using AFM and PL analyses showing the presence of a water film of nanometer thickness under the MoS_2 flakes at the interface between the samples and the SiO_2/Si substrate. This water film can be decreased by annealing and restored by water baths. We attribute an important role to the presence of water at the sample-substrate interface in the sublimation of the bottom layer of few-layer MoS_2 flakes, which was demonstrated after annealing at the highest temperatures. High pressure water nano-confined at the interface promotes the formation of thermally induced sulphur vacancies through the exothermic dissociation of H_2O molecules, and this is the mechanism that most plausibly contributes to the sublimation of the bottom layer of MoS_2. Estimation of the increase in sulphur vacancy concentration after annealing by PL analysis has allowed us to provide a quantitative explanation for the sublimation of the bottom layer of MoS_2, and an exfoliation technique from the bottom of the material by thermal treatments has been proposed.
A comparative analysis of the resonant-Raman integrated intensity yield and the PL intensity yield of correspondent annealed single-layer MoS_2 samples as a function of annealing temperature has shown that the type A excitons producing the PL emission are the real states participating in resonant-Raman scattering, and this is evidence for exciton-phonon coupling in 2D MoS_2. The detailed study of the annealing effects in the intensities of specific Raman modes in the resonant-Raman spectrum of MoS_2 allowed us to obtain indirect evidence for the spatial orientation of the excitonic wave functions within the 2D plane of single-layer MoS_2. The in-plane E^1_{2g} Raman phonon mode shows strong coupling with type A excitons, while the out-of-plane A_{1g} Raman mode does not. This indicates an in-plane spatial symmetry of the type A excitonic wave functions.

7.2 OUTLOOK

Micro-Raman spectroscopy has been shown to be capable of analysing the mechanical stress and the degree of crystallinity in submicron Si-based materials [174, 257, 316, 320, 399]. In such studies, changes in the Raman spectrum of Si due to stress or defects in crystallinity are used to characterise the presence of stress or amorphous zones in the material. In addition, Raman spectroscopy has also been used to study Si in the polycrystalline configuration (polysilicon) and has been shown to be sensitive to crystal grain size [317, 319, 400, 401].
Stress in Si leads to frequency shifts of the one-phonon Raman Si peak with respect to its position in the perfect crystal. In general, tensile

stress leads to a red-shift of the peak and, conversely, compressive stress leads to a blue-shift of the peak [173, 174, 220, 257]. The presence of amorphous regions in the material produces broad spectral bands to the left of the silicon peak (around 480 cm^{-1}) whose intensity is proportional to the relative volume of the amorphous material compared to the scattering volume in crystalline Si [319, 320]. The Si peak in the Raman spectrum of polysilicon may have shoulders in the left tail of the peak whose intensity and position depend approximately on the grain size of the polycrystal, and asymmetries in the shape of the peak may occur [319, 400, 401].

For these reasons, it is desirable to test the technique described herein for characterising doping in p-type Si also in Si-based materials in the presence of doping, stress, defects in the degree of crystallinity, or in polysilicon. The challenge is to distinguish quantitatively between the different effects in the Raman spectrum of Si, which depend on various factors such as doping concentration, stress, crystallinity, and so on. The integration of new characterization functionalities into the technique described herein could be used with the intention of monitoring the doping state along with other aspects such as amorphous regions or regions of poorly reconstructed crystal, or the doping state in materials such as polysilicon. In addition, such a technique could be used in failure analysis to look for stress regions in the material associated with microcracks in the thin structure of electronic devices.

It is also known in the literature that compressive stress in highly doped Si can affect the same intensity of the Fano effect in the Raman peak of Si [23, 24, 220, 299]. A further development of the presented work would be to perform further studies to investigate the correlation between the stress in the different crystallographic directions and the Fano interference. Also in dependence of the different geometrical configuration of the spectroscopic experiment. Another interesting research project is to evaluate the possibility of combining the doping monitoring technique with tip-enhanced Raman spectroscopy (TERS) to take advantage of the exceptional spatial resolution of TERS (on the order of $\sim$nm [402, 403]). In this way, we will improve the lateral resolution of our technique for applications in MOSFETs to study the distribution of doping in the lateral direction in the transition between the different active regions of the transistor, such as source and drain regions, source and drain extension, and conduction channel.

As for MoS_2, we have already discussed in Chapter 6.2.1 how our results can stimulate the development of a new method of "bottom-exfoliation" of layered materials by annealing. Another interesting development concerns the spatial symmetry properties of type A excitons in MoS_2. In this work, we reported a symmetry-dependent exciton-phonon coupling showing that type A excitons selectively interact with in-plane phonons. We considered this as evidence for the in-plane orientation of the excitonic wave functions. On this basis, a study of the spatial

symmetry of the orbitals associated with the exciton states (A^0 and A^-) is desirable, for example, starting from the symmetries of the states in the electronic band structure of MoS_2 at the point K of BZ, from which the type A excitonic states originate.

[1] Palleschi S, Mastrippolito D, Benassi P, Nardone M, and Ottaviano L (2021). Micro-Raman investigation of p-type B doped Si(1 0 0) revisited. In: *Applied Surface Science* **561**, p. 149691 (cit. on pp. 11, 89, 93–105).

[2] Mastrippolito D, Palleschi S, Tosti S, and Ottaviano L (2021). Doping profiling of beveled Si wafers via UV-micro Raman spectroscopy. In: *Applied Surface Science* **567**, p. 150824 (cit. on pp. 11, 89, 106–108).

[3] Palleschi S et al. (Jan. 2020). On the role of nano-confined water at the 2D/SiO_2 interface in layer number engineering of exfoliated MoS_2 via thermal annealing. In: *2D Materials* **7**.2, p. 025001 (cit. on pp. 11, 84, 86, 112, 116, 118, 119, 121–125).

[4] Mastrippolito D, Palleschi S, D'Olimpio G, Politano A, Nardone M, Benassi P, and Ottaviano L (2020). Exciton–phonon coupling and power dependent room temperature photoluminescence of sulphur vacancy doped MoS_2 via controlled thermal annealing. In: *Nanoscale* **12** (36), pp. 18899–18907 (cit. on pp. 11, 112, 128, 129, 131–133).

[5] Voinigescu S (2013). *High-frequency integrated circuits*. Cambridge University Press (cit. on p. 12).

[6] *Silicon vs Germanium Wafer Performance & Price Comparison* (2018). https://bit.ly/3DRvGzj (cit. on p. 12).

[7] *Semiconductor Market Size & Share | Industry Growth [2028]* (2021). https://www.fortunebusinessinsights.com/semiconductor-market-102365 (cit. on p. 13).

[8] *Worldwide Semiconductor Revenue Grew* 10.8% *in* 2020 (2021). URL: https://www.idc.com/getdoc.jsp?containerId=prUS47664821 (cit. on p. 13).

[9] *Semiconductor Market to Grow By* 17.3% *in* 2021 (2021). URL: https://www.idc.com/getdoc.jsp?containerId=prAP48247621 (cit. on p. 13).

[10] Peiner E, Schlachetzki A, and Krüger D (1995). Doping profile analysis in Si by electrochemical capacitance-voltage measurements. In: *Journal of the Electrochemical Society* **142**.2, p. 576 (cit. on pp. 13, 89).

[11] Smits F M (1958). Measurement of sheet resistivities with the four-point probe. In: *The Bell System Technical Journal* **37**.3, pp. 711–718 (cit. on pp. 13, 89).

[12] Mazur R G and Dickey D H (1966). A Spreading Resistance Technique for Resistivity Measurements on Silicon. In: *Journal of The Electrochemical Society* **113**.3, p. 255 (cit. on pp. 13, 89).

[13] Liebl H J and Herzog R F K (1963). Sputtering Ion Source for Solids. In: *Journal of Applied Physics* **34**.9, pp. 2893–2896 (cit. on pp. 13, 89).

[14] Becker M, Gosele U, Hofmann A, and Christiansen S (Nov. 2009). Highly p-doped regions in silicon solar cells quantitatively analyzed by small angle beveling and micro-Raman spectroscopy. In: *Journal of Applied Physics* **106**, pp. 074515–074515 (cit. on pp. 13, 14, 64, 65, 88–91).

[15] Severac F, Cristiano F, Bedel-Pereira E, Fazzini P F, Boucher J, Lerch W, and Hamm S (2010). Influence of boron-interstitials clusters on hole mobility degradation in high dose boron-implanted ultrashallow junctions. In: *Journal of Applied Physics* **107**.12, p. 123711 (cit. on pp. 13, 88, 104, 108).

[16] Vandervorst W, Clarysse T, and Eyben P (2002). Spreading resistance roadmap towards and beyond the 70 nm technology node. In: *Journal of Vacuum Science & Technology B: Microelectronics and Nanometer Structures Processing, Measurement, and Phenomena* **20**.1, pp. 451–458 (cit. on pp. 13, 89).

[17] Kuruc M, Hulényi L, and Kinder R (2008). Analysis and correction of carrier spilling effect for different Si structures. In: *Journal of Electrical Engineering* **59**.6, pp. 302–309 (cit. on pp. 13, 89).

[18] Snauwaert J, Hellemans L, Czech I, Clarysse T, Vandervorst W, and Pawlik M (1994). Towards a physical understanding of spreading resistance probe technique profiling. In: *Journal of Vacuum Science & Technology B: Microelectronics and Nanometer Structures Processing, Measurement, and Phenomena* **12**.1, pp. 304–311 (cit. on pp. 13, 90).

[19] Peiner E and Schlachetzki A (Feb. 1992). Anodic Dissolution during Electrochemical Carrier-Concentration Profiling of Silicon. In: *Journal of The Electrochemical Society* **139**.2, pp. 552–557 (cit. on pp. 13, 89).

[20] Budrevich A and Hunter J (1998). Metrology aspects of SIMS depth profiling for advanced ULSI processes. In: *AIP Conference Proceedings* **449**.1, pp. 169–181 (cit. on pp. 13, 89).

[21] Liu G L, Uchida H, Aikawa I, Kuroda S, and Hirashita N (1996). Accurate secondary ion mass spectrometry analysis of shallow doping profiles in Si based on the internal standard method. In: *Journal of Vacuum Science & Technology B: Microelectronics and Nanometer Structures Processing, Measurement, and Phenomena* **14**.1, pp. 324–328 (cit. on pp. 13, 89).

[22] Fano U and Cooper J W (Mar. 1965). Line Profiles in the Far-uv Absorption Spectra of the Rare Gases. In: *Phys. Rev.* **137** (5A), A1364–A1379 (cit. on pp. 14, 88, 91, 96).

[23] Cerdeira F, Fjeldly T A, and Cardona M (Nov. 1973a). Effect of Free Carriers on Zone-Center Vibrational Modes in Heavily Doped *p*-type Si. II. Optical Modes. In: *Phys. Rev. B* **8** (10),

pp. 4734–4745 (cit. on pp. 14, 21, 43, 59–61, 64–66, 78, 88, 90, 91, 95, 97, 98, 100, 102, 105, 109, 110, 139).
[24] Chandrasekhar M, Chandrasekhar H R, Grimsditch M, and Cardona M (Nov. 1980). Study of the localized vibrations of boron in heavily doped Si. In: *Phys. Rev. B* **22** (10), pp. 4825–4833 (cit. on pp. 14, 60, 65, 66, 78, 88, 90, 91, 95, 97, 99, 100, 102, 105, 109, 110, 139).
[25] Magidson V and Beserman R (Nov. 2002). Fano-type interference in the Raman spectrum of photoexcited Si. In: *Phys. Rev. B* **66** (19), p. 195206 (cit. on pp. 14, 75, 78, 88, 90).
[26] Burke B G, Chan J, Williams K A, Wu Z, Puretzky A A, and Geohegan D B (2010). Raman study of Fano interference in p-type doped silicon. In: *Journal of Raman Spectroscopy* **41**.12, pp. 1759–1764 (cit. on pp. 14, 65, 79, 88, 90, 91, 95, 97).
[27] Gundel P, Schubert M, Heinz F, Benick J, Zizak I, and Warta W (July 2010). Submicron resolution carrier lifetime analysis in silicon with Fano resonances. In: *physica status solidi (RRL) - Rapid Research Letters* **4**, pp. 160–162 (cit. on pp. 14, 88, 90, 91, 98, 109).
[28] Kunz T, Hessmann M T, Seren S, Meidel B, Terheiden B, and Brabec C J (2013). Dopant mapping in highly p-doped silicon by micro-Raman spectroscopy at various injection levels. In: *Journal of Applied Physics* **113**.2, p. 023514 (cit. on pp. 14, 65, 88, 90, 91, 98, 109).
[29] Dickey D H (2002). Developments in ultrashallow spreading resistance analysis. In: *Journal of Vacuum Science & Technology B: Microelectronics and Nanometer Structures Processing, Measurement, and Phenomena* **20**.1, pp. 467–470 (cit. on pp. 14, 76).
[30] Moore G (1998). Cramming More Components Onto Integrated Circuits. In: *Proceedings of the IEEE* **86**.1, pp. 82–85 (cit. on pp. 14, 111).
[31] Rogers J A and Huang Y (2009). A curvy, stretchy future for electronics. In: *Proceedings of the National Academy of Sciences* **106**.27, pp. 10875–10876 (cit. on pp. 14, 111).
[32] Krishnan S, Garimella S V, Chrysler G M, and Mahajan R V (2007). Towards a Thermal Moore's Law. In: *IEEE Transactions on Advanced Packaging* **30**.3, pp. 462–474 (cit. on p. 14).
[33] *International Roadmap for Devices and System (IRDS^{TM}) 2017 Edition* (2017). http://irds.ieee.org/ (cit. on pp. 14, 15, 89, 110, 111).
[34] Novoselov K S, Jiang D, Schedin F, Booth T J, Khotkevich V V, Morozov S V, and Geim A K (2005). Two-dimensional atomic crystals. In: *Proceedings of the National Academy of Sciences of the United States of America* **102**.30, pp. 10451–10453 (cit. on pp. 15, 23).

[35] Coleman J N et al. (2011). Two-Dimensional Nanosheets Produced by Liquid Exfoliation of Layered Materials. In: *Science* **331**.6017, pp. 568–571 (cit. on pp. 15, 23).
[36] Liu K.-K et al. (2012). Growth of Large-Area and Highly Crystalline MoS_2 Thin Layers on Insulating Substrates. In: *Nano Letters* **12**.3, pp. 1538–1544 (cit. on pp. 15, 23).
[37] Allen M J, Tung V C, and Kaner R B (2010). Honeycomb Carbon: A Review of Graphene. In: *Chemical Reviews* **110**.1. PMID: 19610631, pp. 132–145 (cit. on p. 15).
[38] Butov L (2017). Excitonic devices. In: *Superlattices and Microstructures* **108**. Indirect Excitons: Physics and Applications, pp. 2–26 (cit. on pp. 15, 111).
[39] Unuchek D, Ciarrocchi A, Avsar A, Watanabe K, Taniguchi T, and Kis A (2018). Room-temperature electrical control of exciton flux in a van der Waals heterostructure. In: *Nature* **560**.7718, pp. 340–344 (cit. on pp. 15, 111).
[40] Uddin S Z, Kim H, Lorenzon M, Yeh M, Lien D.-H, Barnard E S, Htoon H, Weber-Bargioni A, and Javey A (2020). Neutral Exciton Diffusion in Monolayer MoS_2. In: *ACS Nano* **14**.10, pp. 13433–13440 (cit. on pp. 15, 111).
[41] Lee J, Pak S, Lee Y.-W, Cho Y, Hong J, Giraud P, Shin H S, Morris S M, Sohn J I, Cha S, et al. (2017). Monolayer optical memory cells based on artificial trap-mediated charge storage and release. In: *Nature Communications* **8**.1, pp. 1–8 (cit. on pp. 15, 111).
[42] Lee J Y, Shin J.-H, Lee G.-H, and Lee C.-H (2016). Two-Dimensional Semiconductor Optoelectronics Based on van der Waals Heterostructures. In: *Nanomaterials* **6**.11 (cit. on pp. 15, 111).
[43] Tian H, Chin M L, Najmaei S, Guo Q, Xia F, Wang H, and Dubey M (2016). Optoelectronic devices based on two-dimensional transition metal dichalcogenides. In: *Nano Research* **9**.6, pp. 1543–1560 (cit. on pp. 15, 111).
[44] Hüser F, Olsen T, and Thygesen K S (Dec. 2013). How dielectric screening in two-dimensional crystals affects the convergence of excited-state calculations: Monolayer MoS_2. In: *Phys. Rev. B* **88** (24), p. 245309 (cit. on pp. 15, 57, 111).
[45] Lin Y, Ling X, Yu L, Huang S, Hsu A L, Lee Y.-H, Kong J, Dresselhaus M S, and Palacios T (2014). Dielectric Screening of Excitons and Trions in Single-Layer MoS_2. In: *Nano Letters* **14**.10, pp. 5569–5576 (cit. on pp. 15, 30, 31, 57, 83, 111, 112, 114, 122, 127).
[46] Lee C, Yan H, Brus L E, Heinz T F, Hone J, and Ryu S (2010). Anomalous Lattice Vibrations of Single- and Few-Layer MoS_2. In: *ACS Nano* **4**.5. PMID: 20392077, pp. 2695–2700 (cit. on pp. 15, 33, 34, 82, 111, 114, 119, 120).

[47] Mak K F, He K, Lee C, Lee G H, Hone J, Heinz T F, and Shan J (2013). Tightly bound trions in monolayer MoS_2. In: *Nature materials* **12**.3, pp. 207–211 (cit. on pp. 15, 28–31, 57, 83, 111, 112, 114, 122).

[48] Luo X, Zhao Y, Zhang J, Xiong Q, and Quek S Y (Aug. 2013). Anomalous frequency trends in MoS_2 thin films attributed to surface effects. In: *Phys. Rev. B* **88** (7), p. 075320 (cit. on pp. 15, 111).

[49] Nan H, Wang Z, Wang W, Liang Z, Lu Y, Chen Q, He D, Tan P, Miao F, Wang X, et al. (2014). Strong photoluminescence enhancement of MoS_2 through defect engineering and oxygen bonding. In: *ACS nano* **8**.6, pp. 5738–5745 (cit. on pp. 15, 31, 84, 111–114, 120, 121, 123).

[50] Fernandes T, C Gadelha A de, P M Barboza A, Paniago R, Campos L, Guimaraes P S, Assis P.-L de, and Neves B (Mar. 2018). Robust nanofabrication of monolayer MoS_2 islands with strong photoluminescence enhancement via local anodic oxidation. In: *2D Materials* **5**.2, p. 025018 (cit. on pp. 15, 57, 111, 113).

[51] Nishinaga T (2014). *Handbook of crystal growth: fundamentals (Second ed.)* Elsevier (cit. on p. 19).

[52] Ashcroft N W and Mermin N D (1976). *Solid State Physics*. Holt-Saunders (cit. on pp. 19, 35–39).

[53] Godwod K, Kowalczyk R, and Szmid Z (1974). Application of a precise double X-ray spectrometer for accurate lattice parameter determination. In: *physica status solidi (a)* **21**.1, pp. 227–234 (cit. on p. 19).

[54] Sverdlov V (2011). *Strain-induced effects in advanced MOSFETs*. Springer Science & Business media (cit. on p. 20).

[55] Sze S M, Li Y, and Ng K K (2007). *Physics of Semiconductor Devices. 3rd Edition*. John Wiley & Sons (cit. on pp. 20, 21).

[56] Chelikowsky J R and Cohen M L (July 1976). Nonlocal pseudopotential calculations for the electronic structure of eleven diamond and zinc-blende semiconductors. In: *Phys. Rev. B* **14** (2), pp. 556–582 (cit. on pp. 20, 21).

[57] Cohen M L and Chelikowsky J R (2012). *Electronic structure and optical properties of semiconductors*. Vol. 75. Springer Science & Business Media (cit. on p. 20).

[58] Peter Y and Cardona M (1996). *Fundamentals of Semiconductors: Physics and Materials Properties*. Springer Science & Business Media (cit. on pp. 20–22, 28, 43, 45, 47–50, 52–59, 69, 70, 83, 96).

[59] Enderlein R and Horing N J (1997). *Fundamentals of semiconductor physics and devices*. World Scientific (cit. on p. 20).

[60] Grosso G and Parravicini G (2000). *Solid State Physics* (cit. on p. 21).

[61] Patterson J D and Bailey B C (2007). *Solid-state physics: introduction to the theory*. Springer Science & Business Media (cit. on p. 21).

[62] Dolling G (1963). *in Inelastic Scattering of Neutrons in Solids and lquids.* International Atomic Energy Agency, Vienna, (cit. on pp. 21, 22).

[63] Warren J L, Yarnell J L, Dolling G, and Cowley R A (June 1967). Lattice Dynamics of Diamond. In: *Phys. Rev.* **158** (3), pp. 805–808 (cit. on p. 21).

[64] Nilsson G and Nelin G (Nov. 1972). Study of the Homology between Silicon and Germanium by Thermal-Neutron Spectrometry. In: *Phys. Rev. B* **6** (10), pp. 3777–3786 (cit. on p. 21).

[65] Johnson F A (Feb. 1959). Lattice Absorption Bands in Silicon. In: *Proceedings of the Physical Society* **73**.2, pp. 265–272 (cit. on p. 22).

[66] Johnson F A, Loudon R, and Cochran W (1964). Critical-point analysis of the phonon spectra of diamond, silicon and germanium. In: *Proceedings of the Royal Society of London. Series A. Mathematical and Physical Sciences* **281**.1385, pp. 274–290 (cit. on p. 22).

[67] Giannozzi P, Gironcoli S de, Pavone P, and Baroni S (Mar. 1991). Ab initio calculation of phonon dispersions in semiconductors. In: *Phys. Rev. B* **43** (9), pp. 7231–7242 (cit. on p. 22).

[68] Temple P A and Hathaway C E (Apr. 1973). Multiphonon Raman Spectrum of Silicon. In: *Phys. Rev. B* **7** (8), pp. 3685–3697 (cit. on pp. 22, 60).

[69] Castro Neto A H, Guinea F, Peres N M R, Novoselov K S, and Geim A K (Jan. 2009). The electronic properties of graphene. In: *Rev. Mod. Phys.* **81** (1), pp. 109–162 (cit. on p. 23).

[70] Zhang Y, Tan Y.-W, Stormer H L, and Kim P (2005). Experimental observation of the quantum Hall effect and Berry's phase in graphene. In: *nature* **438**.7065, pp. 201–204 (cit. on p. 23).

[71] Basu J, Basu J K, and Bhattacharyya T K (2010). The evolution of graphene-based electronic devices. In: *International Journal of Smart and Nano Materials* **1**.3, pp. 201–223 (cit. on p. 23).

[72] Han M Y, Özyilmaz B, Zhang Y, and Kim P (May 2007). Energy Band-Gap Engineering of Graphene Nanoribbons. In: *Phys. Rev. Lett.* **98** (20), p. 206805 (cit. on p. 23).

[73] Zeng Z, Yin Z, Huang X, Li H, He Q, Lu G, Boey F, and Zhang H (2011). Single-Layer Semiconducting Nanosheets: High-Yield Preparation and Device Fabrication. In: *Angewandte Chemie International Edition* **50**.47, pp. 11093–11097 (cit. on p. 23).

[74] Zhou K.-G, Mao N.-N, Wang H.-X, Peng Y, and Zhang H.-L (2011). A Mixed-Solvent Strategy for Efficient Exfoliation of Inorganic Graphene Analogues. In: *Angewandte Chemie International Edition* **50**.46, pp. 10839–10842 (cit. on p. 23).

[75] Ottaviano L et al. (Sept. 2017). Mechanical exfoliation and layer number identification of MoS_2 revisited. In: *2D Materials* **4**.4, p. 045013 (cit. on pp. 23, 81, 82, 117, 118, 132).

[76] Chang K and Chen W (June 2011). L-cysteine-assisted synthesis of layered MoS_2/graphene composites with excellent electrochemical performances for lithium ion batteries. In: *ACS nano* **5**.6, pp. 4720–4728 (cit. on p. 23).

[77] Zhou W, Yin Z, Du Y, Huang X, Zeng Z, Fan Z, Liu H, Wang J, and Zhang H (2013a). Synthesis of Few-Layer MoS_2 Nanosheet-Coated TiO_2 Nanobelt Heterostructures for Enhanced Photocatalytic Activities. In: *Small* **9**.1, pp. 140–147 (cit. on p. 23).

[78] Min Y, Moon G D, Kim B S, Lim B, Kim J.-S, Kang C Y, and Jeong U (2012). Quick, controlled synthesis of ultrathin Bi_2Se_3 nanodiscs and nanosheets. In: *Journal of the American Chemical Society* **134**.6, pp. 2872–2875 (cit. on p. 23).

[79] Liu H, Yuan H, Fukui N, Zhang L, Jia J, Iwasa Y, Chen M, Hashizume T, Sakurai T, and Xue Q (2010). Growth of topological insulator Bi_2Te_3 ultrathin films on Si (111) investigated by low-energy electron microscopy. In: *Crystal growth & design* **10**.10, pp. 4491–4493 (cit. on p. 23).

[80] Shi Y et al. (2012). van der Waals Epitaxy of MoS_2 Layers Using Graphene As Growth Templates. In: *Nano Letters* **12**.6, pp. 2784–2791 (cit. on p. 23).

[81] Wilson J and Yoffe A (1969). The transition metal dichalcogenides discussion and interpretation of the observed optical, electrical and structural properties. In: *Advances in Physics* **18**.73, pp. 193–335 (cit. on pp. 23, 24).

[82] Chhowalla M, Shin H S, Eda G, Li L.-J, Loh K P, and Zhang H (2013). The chemistry of two-dimensional layered transition metal dichalcogenide nanosheets. In: *Nature chemistry* **5**.4, pp. 263–275 (cit. on pp. 23, 25).

[83] Rasch J C E, Stemmler T, Müller B, Dudy L, and Manzke R (Dec. 2008). $1T-TiSe_2$: Semimetal or Semiconductor? In: *Phys. Rev. Lett.* **101** (23), p. 237602 (cit. on p. 23).

[84] Yoffe A D (1973). Layer Compounds. In: *Annual Review of Materials Science* **3**.1, pp. 147–170 (cit. on pp. 23, 24).

[85] — (1993). Low-dimensional systems: quantum size effects and electronic properties of semiconductor microcrystallites (zero-dimensional systems) and some quasi-two-dimensional systems. In: *Advances in Physics* **42**.2, pp. 173–262 (cit. on p. 23).

[86] Cohen S R, Rapoport L, Ponomarev E, Cohen H, Tsirlina T, Tenne R, and Lévy-Clément C (1998). The tribological behavior of type II textured MX2 (M = Mo, W; X = S, Se) films. In: *Thin Solid Films* **324**, pp. 190–197 (cit. on p. 23).

[87] Scharf T and Prasad S (2013). Solid lubricants: a review. In: *Journal of materials science* **48**.2, pp. 511–531 (cit. on p. 23).

[88] Voevodin A, Muratore C, and Aouadi S (2014). Hard coatings with high temperature adaptive lubrication and contact thermal management: review. In: *Surface and Coatings Technology* **257**. 25 years of TiAlN hard coatings in research and industry, pp. 247–265 (cit. on p. 23).

[89] Wang Q H, Kalantar-Zadeh K, Kis A, Coleman J N, and Strano M S (2012). Electronics and optoelectronics of two-dimensional transition metal dichalcogenides. In: *Nature nanotechnology* **7**.11, pp. 699–712 (cit. on pp. 24–26, 111).

[90] Frindt R (1966). Single crystals of MoS_2 several molecular layers thick. In: *Journal of Applied Physics* **37**.4, pp. 1928–1929 (cit. on p. 24).

[91] Popov I, Seifert G, and Tománek D (Apr. 2012). Designing electrical contacts to MoS_2 monolayers: a computational study. In: *Physical review letters* **108**.15, p. 156802 (cit. on p. 24).

[92] Yin Z, Li H, Li H, Jiang L, Shi Y, Sun Y, Lu G, Zhang Q, Chen X, and Zhang H (Jan. 2012). Single-layer MoS_2 phototransistors. In: *ACS nano* **6**.1, pp. 74–80 (cit. on pp. 24, 27).

[93] Li H, Yin Z, He Q, Li H, Huang X, Lu G, Fam D W H, Tok A I Y, Zhang Q, and Zhang H (Jan. 2012a). Fabrication of single- and multilayer MoS_2 film-based field-effect transistors for sensing NO at room temperature. In: *Small (Weinheim an der Bergstrasse, Germany)* **8**.1, pp. 63–67 (cit. on p. 24).

[94] Mak K F, Lee C, Hone J, Shan J, and Heinz T F (Sept. 2010). Atomically Thin MoS_2: A New Direct-Gap Semiconductor. In: *Phys. Rev. Lett.* **105** (13), p. 136805 (cit. on pp. 24, 25, 27, 28, 112).

[95] Radisavljevic B, Radenovic A, Brivio J, Giacometti V, and Kis A (Mar. 2011). Single-layer MoS_2 transistors. In: *Nature nanotechnology* **6**.3, pp. 147–150 (cit. on pp. 24, 27, 111).

[96] Wikipedia (2013). *Molibdenite — Wikipedia, L'enciclopedia libera*. [Online; in data 1-ottobre-2014] (cit. on p. 24).

[97] Chhowalla M and Amaratunga G A (2000). Thin films of fullerene-like MoS_2 nanoparticles with ultra-low friction and wear. In: *Nature* **407**.6801, pp. 164–167 (cit. on p. 24).

[98] Kim Y, Huang J.-L, and Lieber C M (1991). Characterization of nanometer scale wear and oxidation of transition metal dichalcogenide lubricants by atomic force microscopy. In: *Applied physics letters* **59**.26, pp. 3404–3406 (cit. on p. 24).

[99] Trakarnpruk W and Seentrakoon B (2007). Hydrodesulfurization activity of MoS_2 and bimetallic catalysts prepared by in situ decomposition of thiosalt. In: *Industrial & Engineering Chemistry Research* **46**.7, pp. 1874–1882 (cit. on p. 24).

[100] Chen J, Kuriyama N, Yuan H, Takeshita H T, and Sakai T (Nov. 2001). Electrochemical hydrogen storage in MoS_2 nanotubes. In: *Journal of the American Chemical Society* **123**.47, pp. 11813–11814 (cit. on p. 24).

[101] Soon J M and Loh K P (2007). Electrochemical double-layer capacitance of MoS_2 nanowall films. In: *Electrochemical and Solid-State Letters* **10**.11, A250–A254 (cit. on p. 24).

[102] Haering R, Stiles J, and Brandt K (Sept. 1980). *Lithium molybdenum disulphide battery cathode*. US Patent 4,224,390 (cit. on p. 25).

[103] Kam K K and Parkinson B A (1982). Detailed photocurrent spectroscopy of the semiconducting group VIB transition metal dichalcogenides. In: *The Journal of Physical Chemistry* **86**.4, pp. 463–467 (cit. on p. 25).

[104] Splendiani A, Sun L, Zhang Y, Li T, Kim J, Chim C.-Y, Galli G, and Wang F (2010). Emerging Photoluminescence in Monolayer MoS_2. In: *Nano Letters* **10**.4. PMID: 20229981, pp. 1271–1275 (cit. on pp. 25, 27–29, 112).

[105] Ramasubramaniam A (Sept. 2012). Large excitonic effects in monolayers of molybdenum and tungsten dichalcogenides. In: *Phys. Rev. B* **86** (11), p. 115409 (cit. on pp. 25, 28).

[106] Cheiwchanchamnangij T and Lambrecht W R L (May 2012). Quasiparticle band structure calculation of monolayer, bilayer, and bulk MoS_2. In: *Phys. Rev. B* **85** (20), p. 205302 (cit. on pp. 25, 27, 28, 86, 130).

[107] Klots A, Newaz A, Wang B, Prasai D, Krzyzanowska H, Lin J, Caudel D, Ghimire N, Yan J, Ivanov B, et al. (2014). Probing excitonic states in suspended two-dimensional semiconductors by photocurrent spectroscopy. In: *Scientific reports* **4**.1, pp. 1–7 (cit. on pp. 25, 28, 30).

[108] Lee J.-U, Park J, Son Y.-W, and Cheong H (2015). Anomalous excitonic resonance Raman effects in few-layered MoS_2. In: *Nanoscale* **7** (7), pp. 3229–3236 (cit. on pp. 25, 114).

[109] Kang J, Sahin H, and Peeters F M (2015). Mechanical properties of monolayer sulphides: a comparative study between MoS_2, HfS_2 and TiS_3. In: *Physical Chemistry Chemical Physics* **17**.41, pp. 27742–27749 (cit. on pp. 25, 84, 112, 122).

[110] Mattheiss L F (Oct. 1973). Band Structures of Transition Metal Dichalcogenide Layer Compounds. In: *Phys. Rev. B* **8** (8), pp. 3719–3740 (cit. on p. 25).

[111] Coehoorn R, Haas C, Dijkstra J, Flipse C J F, Groot R A de, and Wold A (Apr. 1987). Electronic structure of $MoSe_2$, MoS_2, and WSe_2. I. Band-structure calculations and photoelectron spectroscopy. In: *Phys. Rev. B* **35** (12), pp. 6195–6202 (cit. on p. 25).

[112] Coehoorn R, Haas C, and Groot R A de (Apr. 1987). Electronic structure of $MoSe_2$, MoS_2, and WSe_2. II. The nature of the optical band gaps. In: *Phys. Rev. B* **35** (12), pp. 6203–6206 (cit. on pp. 25, 28).

[113] Böker T, Severin R, Müller A, Janowitz C, Manzke R, Voß D, Krüger P, Mazur A, and Pollmann J (Nov. 2001). Band structure of MoS_2, $MoSe_2$, and $\alpha-MoTe_2$: Angle-resolved photoelectron

spectroscopy and ab initio calculations. In: *Phys. Rev. B* **64** (23), p. 235305 (cit. on p. 25).

[114] Björkman T, Gulans A, Krasheninnikov A V, and Nieminen R M (June 2012). van der Waals Bonding in Layered Compounds from Advanced Density-Functional First-Principles Calculations. In: *Phys. Rev. Lett.* **108** (23), p. 235502 (cit. on p. 25).

[115] Wells A (1975). *Structural Inorganic Chemistry*. 4th ed. London: Clarendon Press-Oxford and Oxford University Press (cit. on p. 25).

[116] Py M A and Haering R R (1983). Structural destabilization induced by lithium intercalation in MoS_2 and related compounds. In: *Canadian Journal of Physics* **61**.1, pp. 76–84 (cit. on p. 25).

[117] Wypych F and Schollhorn R (1992). 1T-MoS_2 a new metallic modification of molybdenum disulfide. In: *J. Chem. Soc., Chem. Commun.* (19), pp. 1386–1388 (cit. on p. 26).

[118] Eda G, Yamaguchi H, Voiry D, Fujita T, Chen M, and Chhowalla M (2011). Photoluminescence from Chemically Exfoliated MoS_2. In: *Nano Letters* **11**.12, pp. 5111–5116 (cit. on p. 26).

[119] Jiménez Sandoval S, Yang D, Frindt R F, and Irwin J C (Aug. 1991). Raman study and lattice dynamics of single molecular layers of MoS_2. In: *Phys. Rev. B* **44** (8), pp. 3955–3962 (cit. on pp. 26, 32).

[120] Wakabayashi N, Smith H G, and Nicklow R M (July 1975). Lattice dynamics of hexagonal MoS_2 studied by neutron scattering. In: *Phys. Rev. B* **12** (2), pp. 659–663 (cit. on p. 26).

[121] Wyckoff R (1964). *Crystal Structures*. New York: Wiley (cit. on p. 26).

[122] Molina-Sánchez A and Wirtz L (Oct. 2011). Phonons in single-layer and few-layer MoS_2 and WS_2. In: *Phys. Rev. B* **84** (15), p. 155413 (cit. on pp. 26, 27, 32, 34, 35, 82, 83, 114, 120, 131, 132).

[123] Traill R (1963). A rhombohedral polytype of molybdenite. In: *The Canadian Mineralogist* **7**.3, pp. 524–526 (cit. on p. 26).

[124] Dungey K E, Curtis M D, and Penner-Hahn J E (1998). Structural Characterization and Thermal Stability of MoS_2 Intercalation Compounds. In: *Chemistry of Materials* **10**.8, pp. 2152–2161 (cit. on p. 26).

[125] Eda G, Fujita T, Yamaguchi H, Voiry D, Chen M, and Chhowalla M (2012). Coherent Atomic and Electronic Heterostructures of Single-Layer MoS_2. In: *ACS Nano* **6**.8, pp. 7311–7317 (cit. on p. 26).

[126] Lebègue S and Eriksson O (Mar. 2009). Electronic structure of two-dimensional crystals from *ab initio* theory. In: *Phys. Rev. B* **79** (11), p. 115409 (cit. on p. 27).

[127] Kuc A, Zibouche N, and Heine T (June 2011). Influence of quantum confinement on the electronic structure of the transition

metal sulfide TS_2. In: *Phys. Rev. B* **83** (24), p. 245213 (cit. on pp. 27, 28).

[128] Ben Amara I, Ben Salem E, and Jaziri S (2016). Optoelectronic response and excitonic properties of monolayer MoS_2. In: *Journal of Applied Physics* **120**.5, p. 051707 (cit. on pp. 27, 112).

[129] Wu W, Wang L, Yu R, Liu Y, Wei S.-H, Hone J, and Wang Z L (2016). Piezophototronic Effect in Single-Atomic-Layer MoS_2 for Strain-Gated Flexible Optoelectronics. In: *Advanced Materials* **28**.38, pp. 8463–8468 (cit. on p. 27).

[130] Setyawan W and Curtarolo S (2010). High-throughput electronic band structure calculations: Challenges and tools. In: *Computational Materials Science* **49**.2, pp. 299–312 (cit. on p. 27).

[131] Tongay S, Zhou J, Ataca C, Lo K, Matthews T S, Li J, Grossman J C, and Wu J (2012). Thermally Driven Crossover from Indirect toward Direct Bandgap in 2D Semiconductors: $MoSe_2$ versus MoS_2. In: *Nano Letters* **12**.11. PMID: 23098085, pp. 5576–5580 (cit. on pp. 28, 113).

[132] Zhao W, Ribeiro R M, Toh M, Carvalho A, Kloc C, Neto A H C, and Eda G (2013). Origin of Indirect Optical Transitions in Few-Layer MoS_2, WS_2, and WSe_2. In: *Nano Letters* **13**.11, pp. 5627–5634 (cit. on p. 28).

[133] Alidoust N, Bian G, Xu S.-Y, Sankar R, Neupane M, Liu C, Belopolski I, Qu D.-X, Denlinger J D, Chou F.-C, et al. (2014). Observation of monolayer valence band spin-orbit effect and induced quantum well states in MoX_2. In: *Nature communications* **5**.1, pp. 1–9 (cit. on p. 28).

[134] Acrivos J V, Liang W Y, Wilson J A, and Yoffe A D (1971). Optical studies of metal-semiconductor transmutations produced by intercalation. In: *Journal of Physics C: Solid State Physics* **4**.1, p. L18 (cit. on p. 28).

[135] Zeng H, Liu G.-B, Dai J, Yan Y, Zhu B, He R, Xie L, Xu S, Chen X, Yao W, et al. (2013). Optical signature of symmetry variations and spin-valley coupling in atomically thin tungsten dichalcogenides. In: *Scientific reports* **3**.1, pp. 1–5 (cit. on p. 28).

[136] Chernikov A, Berkelbach T C, Hill H M, Rigosi A, Li Y, Aslan O B, Reichman D R, Hybertsen M S, and Heinz T F (Aug. 2014). Exciton Binding Energy and Nonhydrogenic Rydberg Series in Monolayer WS_2. In: *Phys. Rev. Lett.* **113** (7), p. 076802 (cit. on p. 28).

[137] Berghäuser G and Malic E (Mar. 2014). Analytical approach to excitonic properties of MoS_2. In: *Phys. Rev. B* **89** (12), p. 125309 (cit. on p. 30).

[138] Zhang C, Johnson A, Hsu C.-L, Li L.-J, and Shih C.-K (2014). Direct Imaging of Band Profile in Single Layer MoS2 on Graphite: Quasiparticle Energy Gap, Metallic Edge States, and Edge Band Bending. In: *Nano Letters* **14**.5, pp. 2443–2447 (cit. on pp. 30, 122).

[139] Chiu M.-H, Zhang C, Shiu H.-W, Chuu C.-P, Chen C.-H, Chang C.-Y, Chen C.-H, Chou M.-Y, Shih C.-K, and Li L (July 2015). Determination of band alignment in the single-layer MoS2/WSe2 heterojunction. In: *Nature Communications* **6**, p. 7666 (cit. on pp. 30, 122).

[140] Yu H, Cui X, Xu X, and Yao W (Jan. 2015). Valley excitons in two-dimensional semiconductors. In: *National Science Review* **2**.1, pp. 57–70 (cit. on pp. 30, 122).

[141] Qiu D Y, Jornada F H da, and Louie S G (Nov. 2013). Optical Spectrum of MoS_2: Many-Body Effects and Diversity of Exciton States. In: *Phys. Rev. Lett.* **111** (21), p. 216805 (cit. on pp. 30, 133).

[142] Kheng K, Cox R T, Aubigné M Y d', Bassani F, Saminadayar K, and Tatarenko S (Sept. 1993). Observation of negatively charged excitons X^- in semiconductor quantum wells. In: *Phys. Rev. Lett.* **71** (11), pp. 1752–1755 (cit. on p. 30).

[143] Bracker A S et al. (July 2005). Binding energies of positive and negative trions: From quantum wells to quantum dots. In: *Phys. Rev. B* **72** (3), p. 035332 (cit. on p. 30).

[144] Ross J S, Wu S, Yu H, Ghimire N J, Jones A M, Aivazian G, Yan J, Mandrus D G, Xiao D, Yao W, et al. (2013). Electrical control of neutral and charged excitons in a monolayer semiconductor. In: *Nature communications* **4**, p. 1474 (cit. on pp. 30, 31, 57, 125).

[145] Lui C H, Frenzel A J, Pilon D V, Lee Y.-H, Ling X, Akselrod G M, Kong J, and Gedik N (Oct. 2014). Trion-Induced Negative Photoconductivity in Monolayer MoS_2. In: *Phys. Rev. Lett.* **113** (16), p. 166801 (cit. on pp. 31, 57, 122).

[146] Li Y, Qi Z, Liu M, Wang Y, Cheng X, Zhang G, and Sheng L (2014a). Photoluminescence of monolayer MoS_2 on $LaAlO_3$ and $SrTiO_3$ substrates. In: *Nanoscale* **6** (24), pp. 15248–15254 (cit. on pp. 31, 112).

[147] Buscema M, Steele G A, Zant H S J van der, and Castellanos-Gomez A (2014). The effect of the substrate on the Raman and photoluminescence emission of single-layer MoS_2. In: *Nano Research* **7**.4, pp. 561–571 (cit. on pp. 31, 83, 112, 114, 121, 122).

[148] Tongay S, Zhou J, Ataca C, Liu J, Kang J S, Matthews T S, You L, Li J, Grossman J C, and Wu J (2013). Broad-range modulation of light emission in two-dimensional semiconductors by molecular physisorption gating. In: *Nano letters* **13**.6, pp. 2831–2836 (cit. on pp. 31, 112–114).

[149] Mak K F, He K, Shan J, and Heinz T F (2012). Control of valley polarization in monolayer MoS_2 by optical helicity. In: *Nature nanotechnology* **7**.8, pp. 494–498 (cit. on p. 31).

[150] Zeng H, Dai J, Yao W, Xiao D, and Cui X (Aug. 2012). Valley polarization in MoS_2 monolayers by optical pumping. In: *Nature nanotechnology* **7**.8, pp. 490–493 (cit. on p. 31).

[151] Xiao D, Liu G.-B, Feng W, Xu X, and Yao W (May 2012). Coupled Spin and Valley Physics in Monolayers of MoS_2 and Other Group-VI Dichalcogenides. In: *Phys. Rev. Lett.* **108** (19), p. 196802 (cit. on p. 31).

[152] Jiang T, Liu H, Huang D, Zhang S, Li Y, Gong X, Shen Y.-R, Liu W.-T, and Wu S (2014). Valley and band structure engineering of folded MoS_2 bilayers. In: *Nature nanotechnology* **9**.10, pp. 825–829 (cit. on p. 31).

[153] Cao T, Wang G, Han W, Ye H, Zhu C, Shi J, Niu Q, Tan P, Wang E, Liu B, et al. (2012). Valley-selective circular dichroism of monolayer molybdenum disulphide. In: *Nature communications* **3**.1, pp. 1–5 (cit. on p. 31).

[154] Jones A M, Yu H, Ghimire N J, Wu S, Aivazian G, Ross J S, Zhao B, Yan J, Mandrus D G, Xiao D, et al. (2013). Optical generation of excitonic valley coherence in monolayer WSe_2. In: *Nature nanotechnology* **8**.9, pp. 634–638 (cit. on p. 31).

[155] Tinkham M (2003). *Group theory and quantum mechanics*. Dover Publications (cit. on p. 31).

[156] Dresselhaus M S, Dresselhaus G, and Jorio A (2007). *Group theory: application to the physics of condensed matter*. Springer Science & Business Media (cit. on p. 31).

[157] Verble J L and Wieting T J (Aug. 1970). Lattice Mode Degeneracy in MoS_2 and Other Layer Compounds. In: *Phys. Rev. Lett.* **25** (6), pp. 362–365 (cit. on pp. 31, 32).

[158] Wieting T J and Verble J L (June 1971). Infrared and Raman Studies of Long-Wavelength Optical Phonons in Hexagonal MoS_2. In: *Phys. Rev. B* **3** (12), pp. 4286–4292 (cit. on pp. 31, 32).

[159] Ataca C, Topsakal M, Akturk E, and Ciraci S (2011). A comparative study of lattice dynamics of three-and two-dimensional MoS_2. In: *The Journal of Physical Chemistry C* **115**.33, pp. 16354–16361 (cit. on pp. 31, 34).

[160] Verble J, Wietling T, and Reed P (1972). Rigid-layer lattice vibrations and van der waals bonding in hexagonal MoS2. In: *Solid State Communications* **11**.8, pp. 941–944 (cit. on p. 31).

[161] Gołasa K, Grzeszczyk M, Bożek R, Leszczyński P, Wysmołek A, Potemski M, and Babiński A (2014). Resonant Raman scattering in MoS_2—From bulk to monolayer. In: *Solid State Communications* **197**, pp. 53–56 (cit. on pp. 32, 34, 52, 82, 83, 114, 131, 132).

[162] Li H, Zhang Q, Yap C C R, Tay B K, Edwin T H T, Olivier A, and Baillargeat D (2012b). From bulk to monolayer MoS_2: evolution of Raman scattering. In: *Advanced Functional Materials* **22**.7, pp. 1385–1390 (cit. on pp. 34, 82).

[163] Chakraborty B, Matte H S S R, Sood A K, and Rao C N R (2013). Layer-dependent resonant Raman scattering of a few layer MoS_2. In: *Journal of Raman Spectroscopy* **44**.1, pp. 92–96 (cit. on pp. 34, 82, 83, 114).

[164] Green M A (1990). Intrinsic concentration, effective densities of states, and effective mass in silicon. In: *Journal of Applied Physics* **67**.6, pp. 2944–2954 (cit. on p. 36).

[165] Huang K (1987). *Statistical Mechanics, 2nd edition*. John Wiley & Sons (cit. on p. 38).

[166] Colinge J.-P and Colinge C A (2005). *Physics of semiconductor devices*. Springer Science & Business Media (cit. on p. 41).

[167] Joyce W B and Dixon R W (1977). Analytic approximations for the Fermi energy of an ideal Fermi gas. In: *Applied Physics Letters* **31**.5, pp. 354–356 (cit. on p. 42).

[168] Devereaux T P and Hackl R (Jan. 2007). Inelastic light scattering from correlated electrons. In: *Rev. Mod. Phys.* **79** (1), pp. 175–233 (cit. on p. 43).

[169] Gouadec G and Colomban P (2007). Raman Spectroscopy of nanomaterials: How spectra relate to disorder, particle size and mechanical properties. In: *Progress in Crystal Growth and Characterization of Materials* **53**.1, pp. 1–56 (cit. on p. 43).

[170] Balkanski M, Jain K P, Beserman R, and Jouanne M (Nov. 1975). Theory of interference distortion of Raman scattering line shapes in semiconductors. In: *Phys. Rev. B* **12** (10), pp. 4328–4337 (cit. on pp. 43, 59–61, 88, 91).

[171] Bechstedt F and Peuker K (1975). Theory of interference between electronic and phonon Raman Scattering. In: *physica status solidi (b)* **72**.2, pp. 743–752 (cit. on pp. 43, 60, 91).

[172] Raman C V and Krishnan K S (1928a). A new type of secondary radiation. In: *Nature* **121**.3048, pp. 501–502 (cit. on pp. 43, 69).

[173] Anastassakis E, Pinczuk A, Burstein E, Pollak F, and Cardona M (1970). Effect of static uniaxial stress on the Raman spectrum of silicon. In: *Solid State Communications* **8**.2, pp. 133–138 (cit. on pp. 43, 139).

[174] Wolf I D (Feb. 1996). Micro-Raman spectroscopy to study local mechanical stress in silicon integrated circuits. In: *Semiconductor Science and Technology* **11**.2, pp. 139–154 (cit. on pp. 43, 69, 90, 138, 139).

[175] Cerdeira F, Fjeldly T A, and Cardona M (1973b). Interaction between electronic and vibronic Raman scattering in heavily doped silicon. In: *Solid State Communications* **13**.3, pp. 325–328 (cit. on pp. 43, 60, 66, 78, 91).

[176] Ferrari A C and Basko D M (2013). Raman spectroscopy as a versatile tool for studying the properties of graphene. In: *Nature nanotechnology* **8**.4, pp. 235–246 (cit. on p. 43).

[177] Fang M, Wang K, Lu H, Yang Y, and Nutt S (2009). Covalent polymer functionalization of graphene nanosheets and mechanical properties of composites. In: *J. Mater. Chem.* **19** (38), pp. 7098–7105 (cit. on p. 43).

[178] Maciel I O, Anderson N, Pimenta M A, Hartschuh A, Qian H, Terrones M, Terrones H, Campos-Delgado J, Rao A M, Novotny L, et al. (2008). Electron and phonon renormalization near charged defects in carbon nanotubes. In: *Nature materials* **7**.11, pp. 878–883 (cit. on p. 43).
[179] Cançado L G, Jorio A, Ferreira E H M, Stavale F, Achete C A, Capaz R B, Moutinho M V O, Lombardo A, Kulmala T S, and Ferrari A C (2011). Quantifying Defects in Graphene via Raman Spectroscopy at Different Excitation Energies. In: *Nano Letters* **11**.8, pp. 3190–3196 (cit. on p. 43).
[180] Lee C, Jeong B G, Yun S J, Lee Y H, Lee S M, and Jeong M S (2018). Unveiling Defect-Related Raman Mode of Monolayer WS_2 via Tip-Enhanced Resonance Raman Scattering. In: *ACS Nano* **12**.10, pp. 9982–9990 (cit. on p. 43).
[181] Parry W (1973). *The Many-Body Problem, Clarendon* (cit. on p. 48).
[182] Berestetskii V, Lifshitz E, and Pitaevskii L (1980). *Quantum electrodynamics, ed* (cit. on p. 48).
[183] Belitsky V I, Cardona M, Lang I G, and Pavlov S T (Dec. 1992). Spatial correlation of electrons and holes in multiphonon resonant Raman scattering in a high magnetic field. In: *Phys. Rev. B* **46** (24), pp. 15767–15788 (cit. on p. 48).
[184] Koningstein J A (1972). *Introduction to the Theory of the Raman Effect*. D. Reidel Publishing Company/Dordrecht-Holland (cit. on p. 50).
[185] Harris D C and Bertolucci M D (1989). *Symmetry and spectroscopy: an introduction to vibrational and electronic spectroscopy*. Courier Corporation (cit. on p. 50).
[186] Long D A (2002). The Raman effect: a unified treatment of the theory of Raman scattering by molecules. In: (cit. on p. 50).
[187] Weinstein B A and Cardona M (Sept. 1973). Resonant First- and Second-Order Raman Scattering in GaP. In: *Phys. Rev. B* **8** (6), pp. 2795–2809 (cit. on p. 51).
[188] Bendow B and Birman J L (Feb. 1970). Polariton Theory of Resonance Raman Scattering in Insulating Crystals. In: *Phys. Rev. B* **1** (4), pp. 1678–1686 (cit. on p. 51).
[189] Livneh T and Sterer E (May 2010). Resonant Raman scattering at exciton states tuned by pressure and temperature in $2H$-MoS_2. In: *Physical Review B* **81**.19, p. 195209 (cit. on pp. 52, 114).
[190] Scheuschner N, Ochedowski O, Schleberger M, and Maultzsch J (2012). Resonant Raman profiles and μ-photoluminescence of atomically thin layers of molybdenum disulfide. In: *physica status solidi (b)* **249**.12, pp. 2644–2647 (cit. on p. 52).
[191] Dresselhaus M, Dresselhaus G, Jorio A, Souza Filho A, and Saito R (2002). Raman spectroscopy on isolated single wall carbon nanotubes. In: *Carbon* **40**.12, pp. 2043–2061 (cit. on p. 52).

[192] Muck T, Wagner J W, Hansen L, Wagner V, Geurts J, and Ivanov S V (June 2004). Vibration dynamics and interfacial chemistry of the CdSe/BeTe interface. In: *Phys. Rev. B* **69** (24), p. 245314 (cit. on p. 52).

[193] Yoshikawa M, Inoue K, Nakagawa T, Ishida H, Hasuike N, and Harima H (2008). Characterization of ZnO nanoparticles by resonant Raman scattering and cathodoluminescence spectroscopies. In: *Applied Physics Letters* **92**.11, p. 113115 (cit. on p. 52).

[194] Jorio A, Dresselhaus M S, Saito R, and Dresselhaus G (2011). *Raman spectroscopy in graphene related systems*. John Wiley & Sons (cit. on p. 52).

[195] Costa S D, Righi A, Fantini C, Hao Y, Magnuson C, Colombo L, Ruoff R S, and Pimenta M A (2012). Resonant Raman spectroscopy of graphene grown on copper substrates. In: *Solid State Communications* **152**.15. Exploring Graphene, Recent Research Advances, pp. 1317–1320 (cit. on p. 52).

[196] Gordeev G, Jorio A, Kusch P, Vieira B G M, Flavel B, Krupke R, Barros E B, and Reich S (Dec. 2017). Resonant anti-Stokes Raman scattering in single-walled carbon nanotubes. In: *Phys. Rev. B* **96** (24), p. 245415 (cit. on p. 52).

[197] Miranda H P C, Reichardt S, Froehlicher G, Molina-Sánchez A, Berciaud S, and Wirtz L (2017). Quantum Interference Effects in Resonant Raman Spectroscopy of Single- and Triple-Layer MoTe2 from First-Principles. In: *Nano Letters* **17**.4. PMID: 28199122, pp. 2381–2388 (cit. on p. 52).

[198] Corro E del et al. (2016). Atypical Exciton–Phonon Interactions in WS2 and WSe2 Monolayers Revealed by Resonance Raman Spectroscopy. In: *Nano Letters* **16**.4. PMID: 26998817, pp. 2363–2368 (cit. on p. 52).

[199] Saleem M F, Zhang H, Deng Y, and Wang D (2017). Resonant Raman scattering in nanocrystalline thin CdS film. In: *Journal of Raman Spectroscopy* **48**.2, pp. 224–229 (cit. on p. 52).

[200] Camassel J, Chiang T, Shen Y, Voitchovsky J.-P, and Amer N (1976). Multiphonon resonant Raman scattering in GaSe. In: *Solid State Communications* **19**.6, pp. 483–485 (cit. on p. 52).

[201] Pelant I and Valenta J (2012). *Luminescence spectroscopy of semiconductors*. Oxford University Press (cit. on pp. 52, 57).

[202] Liqiang J, Yichun Q, Baiqi W, Shudan L, Baojiang J, Libin Y, Wei F, Honggang F, and Jiazhong S (2006). Review of photoluminescence performance of nano-sized semiconductor materials and its relationships with photocatalytic activity. In: *Solar Energy Materials and Solar Cells* **90**.12, pp. 1773–1787 (cit. on p. 52).

[203] Heitler W (1984). *The quantum theory of radiation*. Courier Corporation (cit. on p. 52).

[204] Einstein A (1916). *Emission and Absorption of Radiation in Quantum Theory (in German)*. Verhandlungen der Deutschen Physikalischen Gesellschaft, 18, pp.318–323, 1916 (cit. on p. 52).

[205] Einstein A (1917). *The quantum theory of radiation (in German)*. Phys. Z. 18, pp.121–128, 1916 (cit. on p. 52).

[206] Fox M (2001). *Optical Properties of Solids*. Oxford University Press, New York (cit. on p. 52).

[207] Robertson H S (1993). *Statistical thermophysics*. Prentice-Hall, Englewood Cliffs, NJ (United States) (cit. on p. 53).

[208] Pankove J (1971). *Optical Processes in Semiconductors (Dover, New York)* (cit. on p. 56).

[209] Bebb H B and Williams E (1972). *Semiconductors and Semimetals, vol. 8* (cit. on p. 57).

[210] Schroder D K (2015a). *Semiconductor material and device characterization*. John Wiley & Sons (cit. on pp. 57, 88, 89).

[211] Wooten F (1972). *Optical properties of solids*. Academic press, New York. (cit. on p. 57).

[212] Amani M et al. (2015). Near-unity photoluminescence quantum yield in MoS_2. In: *Science* **350**.6264, pp. 1065–1068 (cit. on pp. 57, 121).

[213] Komsa H.-P and Krasheninnikov A V (Dec. 2012). Effects of confinement and environment on the electronic structure and exciton binding energy of MoS_2 from first principles. In: *Phys. Rev. B* **86** (24), p. 241201 (cit. on p. 57).

[214] Toyozawa Y (Apr. 1959). On the Dynamical Behavior of an Exciton. In: *Progress of Theoretical Physics Supplement* **12**, pp. 111–140 (cit. on p. 59).

[215] Askary F and Yu P Y (1983). Polariton luminescence and additional boundary conditions: comparison between theory and experiment. In: *Solid State Communications* **47**.4, pp. 241–246 (cit. on p. 59).

[216] Beutler H (1935). Über Absorptionsserien von Argon, Krypton und Xenon zu Termen zwischen den beiden Ionisierungsgrenzen ${}^2P_3^{2/0}$ und ${}^2P_1^{2/0}$. In: *Zeitschrift für Physik* **93**.3, pp. 177–196 (cit. on p. 59).

[217] Fano U (1935). Sullo spettro di assorbimento dei gas nobili presso il limite dello spettro d'arco. In: *Il Nuovo Cimento (1924-1942)* **12**.3, pp. 154–161 (cit. on pp. 59, 61, 88).

[218] Fano U (Dec. 1961). Effects of Configuration Interaction on Intensities and Phase Shifts. In: *Phys. Rev.* **124** (6), pp. 1866–1878 (cit. on pp. 60, 61, 64, 65, 88, 91, 96).

[219] Miroshnichenko A E, Flach S, and Kivshar Y S (Aug. 2010). Fano resonances in nanoscale structures. In: *Rev. Mod. Phys.* **82** (3), pp. 2257–2298 (cit. on p. 60).

[220] Chandrasekhar M, Renucci J B, and Cardona M (Feb. 1978). Effects of interband excitations on Raman phonons in heavily doped $n-$Si. In: *Phys. Rev. B* **17** (4), pp. 1623–1633 (cit. on pp. 60, 62, 65, 66, 88, 91, 97, 139).

[221] Olego D and Cardona M (June 1981). Self-energy effects of the optical phonons of heavily doped $p-$GaAs and $p-$Ge. In: *Phys. Rev. B* **23** (12), pp. 6592–6602 (cit. on p. 60).

[222] Wagner J and Cardona M (Dec. 1985). Electronic Raman scattering in heavily doped p-type germanium. In: *Phys. Rev. B* **32** (12), pp. 8071–8077 (cit. on p. 60).

[223] Bell M J V, Ioriatti L, and Nunes L A O (June 1998). Fano interference in periodic GaAs doping multilayers. In: *Phys. Rev. B* **57** (24), R15104–R15107 (cit. on p. 60).

[224] Ager J W, Walukiewicz W, McCluskey M, Plano M A, and Landstrass M I (1995). Fano interference of the Raman phonon in heavily boron-doped diamond films grown by chemical vapor deposition. In: *Applied Physics Letters* **66**.5, pp. 616–618 (cit. on p. 60).

[225] Wang Y G, Lau S P, Tay B K, and Zhang X H (2002). Resonant Raman scattering studies of Fano-type interference in boron doped diamond. In: *Journal of Applied Physics* **92**.12, pp. 7253–7256 (cit. on p. 60).

[226] Rao A M, Eklund P, Bandow S, Thess A, and Smalley R E (1997). Evidence for charge transfer in doped carbon nanotube bundles from Raman scattering. In: *Nature* **388**.6639, pp. 257–259 (cit. on p. 60).

[227] Kuzmenko A B, Benfatto L, Cappelluti E, Crassee I, Marel D van der, Blake P, Novoselov K S, and Geim A K (Sept. 2009). Gate Tunable Infrared Phonon Anomalies in Bilayer Graphene. In: *Phys. Rev. Lett.* **103** (11), p. 116804 (cit. on p. 60).

[228] Tan P.-H et al. (2012). The Shear Mode of Multi-Layer Graphene. In: *Nat Mater. 2012* **11**, pp. 294–300 (cit. on p. 60).

[229] Yoon D, Jeong D, Lee H.-J, Saito R, Son Y.-W, Lee H C, and Cheong H (2013). Fano resonance in Raman scattering of graphene. In: *Carbon* **61**, pp. 373–378 (cit. on p. 60).

[230] Hasdeo E H, Nugraha A R T, Dresselhaus M S, and Saito R (Dec. 2014). Breit-Wigner-Fano line shapes in Raman spectra of graphene. In: *Phys. Rev. B* **90** (24), p. 245140 (cit. on p. 60).

[231] Tan Q.-H, Sun Y.-J, Liu X.-L, Zhao Y, Xiong Q, Tan P.-H, and Zhang J (July 2017). Observation of forbidden phonons, Fano resonance and dark excitons by resonance Raman scattering in few-layer WS_2. In: *2D Materials* **4**.3, p. 031007 (cit. on p. 60).

[232] Zhang J, Peng Z, Soni A, Zhao Y, Xiong Y, Peng B, Wang J, Dresselhaus M S, and Xiong Q (2011). Raman Spectroscopy of Few-Quintuple Layer Topological Insulator Bi2Se3 Nanoplatelets. In: *Nano Letters* **11**.6. PMID: 21604748, pp. 2407–2414 (cit. on p. 60).

[233] Cerdeira F, Fjeldly T A, and Cardona M (May 1974). Raman study of the interaction between localized vibrations and electronic excitations in boron-doped silicon. In: *Phys. Rev. B* **9** (10), pp. 4344–4350 (cit. on pp. 60, 78, 91).

[234] Jouanne M, Beserman R, Ipatova I, and Subashiev A (1975). Electron-phonon coupling in highly doped n type silicon. In: *Solid State Communications* **16**.8, pp. 1047–1049 (cit. on pp. 60–63, 65, 66, 88).

[235] Kanehisa M A, Wallis R F, and Balkanski M (June 1982). Interband electronic Raman scattering in *p*-silicon. In: *Phys. Rev. B* **25** (12), pp. 7619–7625 (cit. on p. 60).

[236] Beserman R and Bernstein T (1977). Raman scattering measurement of the free-carrier concentration and of the impurity location in boron-implanted silicon. In: *Journal of Applied Physics* **48**.4, pp. 1548–1550 (cit. on pp. 60, 109).

[237] Riffe D M (Aug. 2011). Classical Fano oscillator. In: *Phys. Rev. B* **84** (6), p. 064308 (cit. on pp. 61, 64, 65, 97).

[238] Melz P J (1971). Energy band structure of strained crystals: Pseudopotential calculations for Ge and Si with trial calculations for GaAs and CdTe. In: *Journal of Physics and Chemistry of Solids* **32**.1, pp. 209–221 (cit. on p. 62).

[239] Cardona M and Pollak F H (1966). Energy-band structure of germanium and silicon: The k· p method. In: *Physical Review* **142**.2, p. 530 (cit. on p. 62).

[240] Hensel J, Hasegawa H, and Nakayama M (1965). Cyclotron resonance in uniaxially stressed silicon. II. Nature of the covalent bond. In: *Physical Review* **138**.1A, A225 (cit. on p. 62).

[241] Contreras G, Sood A, Cardona M, and Compaan A (1984). Effect of free carriers on the Raman frequency of ultraheavily doped n-Si. In: *Solid State Communications*, pp. 303–305 (cit. on pp. 62, 63, 88).

[242] Becker M, Sarau G, and Christiansen S (2011). *Submicrometer-Scale Characterization of Solar Silicon by Raman Spectroscopy.* In Mechanical Stress on the Nanoscale. (eds M. Hanbücken, P. Müller and R.B. Wehrspohn) (cit. on p. 63).

[243] Mahan G (1981). Many-particle physics. In: (cit. on p. 64).

[244] Nickel N H, Lengsfeld P, and Sieber I (June 2000). Raman spectroscopy of heavily doped polycrystalline silicon thin films. In: *Phys. Rev. B* **61** (23), pp. 15558–15561 (cit. on pp. 66, 88–90).

[245] Renucci J B, Tyte R N, and Cardona M (May 1975). Resonant Raman scattering in silicon. In: *Phys. Rev. B* **11** (10), pp. 3885–3895 (cit. on pp. 66, 90, 98).

[246] Raman C V (1928). A change of wave-length in light scattering. In: *Nature* **121**.3051, pp. 619–619 (cit. on p. 69).

[247] Raman C and Krishnan K (1928b). A new class of spectra due to secondary radiation. Part I. In: (cit. on p. 69).

[248] Everall N J (2009). Confocal Raman Microscopy: Performance, Pitfalls, and Best Practice: Invited Lecture at the Symposium "50 Years of SAS: Looking to the Future with Vibrational Spectroscopy" at Pittcon 2008, New Orleans, Louisiana. In: *Applied Spectroscopy* **63**.9. PMID: 19796478, 245A–262A (cit. on p. 71).

[249] Adar F (1981). Developments in Raman microanalysis. In: *Microbeam Analysis, ed. RH Geiss, San Franciso Press, San Francisco*, p. 67 (cit. on p. 71).

[250] HORIBA (2013). *LabRAM User Manual*. English. HORIBA Jobin Yvon (cit. on p. 71).

[251] Sarioglu A F and Solgaard O (2011). «Time-resolved tapping-mode atomic force microscopy». In: *Scanning Probe Microscopy in Nanoscience and Nanotechnology* 2. Springer, pp. 3–37 (cit. on p. 74).

[252] Schroder D K (2015b). *Semiconductor material and device characterization*. John Wiley & Sons (cit. on p. 74).

[253] Nishinaga T (2015). *Handbook of crystal growth: fundamentals (2nd Edition)*. Elsevier (cit. on p. 75).

[254] Negru R, Huet K, Ceccato P, and Godard B (2012). «Modeling of pulsed Laser Thermal Annealing for junction formation optimization and process control». In: *Proc. COMSOL Conf.* (Cit. on pp. 75, 100).

[255] Hernandez M et al. (2003). Laser thermal processing for ultra shallow junction formation: numerical simulation and comparison with experiments. In: *Applied Surface Science* **208-209**. Physics and Chemistry of Advanced Laser Materials Processing, pp. 345–351 (cit. on pp. 75, 100).

[256] Ohta J (2017). *Smart CMOS Image Sensors and Applications*. CRC Press (cit. on p. 76).

[257] Ureña F, Olsen S H, and Raskin J.-P (2013). Raman measurements of uniaxial strain in silicon nanostructures. In: *Journal of Applied Physics* **114**.14, p. 144507 (cit. on pp. 77, 90, 138, 139).

[258] Rodichkina S, Nychyporuk T, Pavlikov A, Lysenko V, and Timoshenko V (2019). Raman diagnostics of free charge carriers in boron-doped silicon nanowires. In: *Journal of Raman Spectroscopy* **50**.11, pp. 1642–1648 (cit. on pp. 77, 90, 96).

[259] Piscanec S, Cantoro M, Ferrari A C, Zapien J A, Lifshitz Y, Lee S T, Hofmann S, and Robertson J (Dec. 2003). Raman spectroscopy of silicon nanowires. In: *Phys. Rev. B* **68** (24), p. 241312 (cit. on p. 77).

[260] Adu K W, Gutiérrez H R, Kim U J, and Eklund P C (Apr. 2006a). Inhomogeneous laser heating and phonon confinement in silicon nanowires: A micro-Raman scattering study. In: *Phys. Rev. B* **73** (15), p. 155333 (cit. on p. 77).

[261] Faraci G, Gibilisco S, and Pennisi A R (2009). Superheating of silicon nanocrystals observed by Raman spectroscopy. In: *Physics Letters A* **373**.41, pp. 3779–3782 (cit. on p. 77).

[262] Zardo I (Dec. 2010). *Growth and Raman spectroscopy studies of gold-free catalyzed semiconductor nanowires*. Ph.D. Thesis (cit. on p. 77).

[263] Richter H, Wang Z, and Ley L (1981). The one phonon Raman spectrum in microcrystalline silicon. In: *Solid State Communications* **39**.5, pp. 625–629 (cit. on p. 77).

[264] Campbell I and Fauchet P (1986). The effects of microcrystal size and shape on the one phonon Raman spectra of crystalline semiconductors. In: *Solid State Communications* **58**.10, pp. 739–741 (cit. on p. 77).

[265] Fauchet P M and Campbell I H (1988). Raman spectroscopy of low-dimensional semiconductors. In: *Critical Reviews in Solid State and Materials Sciences* **14**.sup1, s79–s101 (cit. on p. 77).

[266] Gupta R, Xiong Q, Adu C K, Kim U J, and Eklund P C (2003). Laser-Induced Fano Resonance Scattering in Silicon Nanowires. In: *Nano Letters* **3**.5, pp. 627–631 (cit. on p. 77).

[267] Kumar R, Shukla A, Mavi H, and Vankar V (2008). Size-dependent Fano interaction in the laser-etched silicon nanostructures. In: *Nanoscale Research Letters* **3**.3, pp. 105–108 (cit. on p. 77).

[268] Saxena S K, Borah R, Kumar V, Rai H M, Late R, Sathe V, Kumar A, Sagdeo P R, and Kumar R (2016). Raman spectroscopy for study of interplay between phonon confinement and Fano effect in silicon nanowires. In: *Journal of Raman Spectroscopy* **47**.3, pp. 283–288 (cit. on p. 77).

[269] Adu K W, Xiong Q, Gutierrez H, Chen G, and Eklund P (2006b). Raman scattering as a probe of phonon confinement and surface optical modes in semiconducting nanowires. In: *Applied Physics A* **85**.3, pp. 287–297 (cit. on p. 77).

[270] Wolf I D (1999). Stress measurements in Si microelectronics devices using Raman spectroscopy. In: *Journal of Raman Spectroscopy* **30**.10, pp. 877–883 (cit. on p. 77).

[271] Kouteva-Arguirova S, Arguirov T, Wolfframm D, and Reif J (2003). Influence of local heating on micro-Raman spectroscopy of silicon. In: *Journal of Applied Physics* **94**.8, pp. 4946–4949 (cit. on p. 77).

[272] Green M A (2008). Self-consistent optical parameters of intrinsic silicon at 300K including temperature coefficients. In: *Solar Energy Materials and Solar Cells* **92**.11, pp. 1305–1310 (cit. on pp. 78, 90, 101–103).

[273] Di Bartolo B (1968). *Optical interactions in solids*. John Wiley and Sons, Inc., (cit. on p. 78).

[274] Yoo W S, Harima H, and Yoshimoto M (2015). Polarized Raman Signals from Si Wafers: Dependence of In-Plane Incident Orien-

tation of Probing Light. In: *ECS Journal of Solid State Science and Technology* **4**.9, P356–P363 (cit. on p. 80).
[275] Nazari M and Holtz M W (2018). Near-ultraviolet Raman and micro-Raman analysis of electronic materials. In: *Applied Physics Reviews* **5**.4, p. 041303 (cit. on pp. 80, 90, 96).
[276] WaveMetrics (1988-2013). Software for technical graphing and data analysis, IGOR PRO Version: 6,3,2,3. In: *(Lake Oswego, OR, USA)* (cit. on p. 80).
[277] Mardquardt D (1963). An algorithm for least square estimation of parameters. In: *J. Soc. Ind. Appl. Math* **11**, pp. 431–441 (cit. on p. 80).
[278] Palleschi S (2016). «Esfoliazione Identificazione ed Effetti Termici di Post-Annealing di Strati Singoli di MoS_2». Master thesis. L'Aquila, Italy: University of L'Aquila (cit. on p. 81).
[279] Benameur M M, Radisavljevic B, Héron J S, Sahoo S, Berger H, and Kis A (2011). Visibility of dichalcogenide nanolayers. In: *Nanotechnology* **22**.12, p. 125706 (cit. on pp. 81, 115).
[280] Müller M R, Gumprich A, Ecik E, Kallis K T, Winkler F, Kardynal B, Petrov I, Kunze U, and Knoch J (2015). Visibility of two-dimensional layered materials on various substrates. In: *Journal of Applied Physics* **118**.14, p. 145305 (cit. on p. 82).
[281] Simsek E and Mukherjee B (2015). Visibility of atomically-thin layered materials buried in silicon dioxide. English. In: *Nanotechnology* **26**.45 (cit. on p. 82).
[282] Lee J U, Kim K, and Cheong H (2015). Resonant Raman and photoluminescence spectra of suspended molybdenum disulfide. In: *2D Materials* **2**.4, p. 044003 (cit. on pp. 82, 83).
[283] Posener D (1959). The shape of spectral lines: Tables of the Voigt profile. In: *Australian Journal of Physics* **12**.2, pp. 184–196 (cit. on p. 83).
[284] Pena-Alvarez M, Corro E del, Morales-García Á, Kavan L, Kalbac M, and Frank O (2015). Single Layer Molybdenum Disulfide under Direct Out-of-Plane Compression: Low-Stress Band-Gap Engineering. In: *Nano Letters* **15**.5, pp. 3139–3146 (cit. on pp. 83, 131, 132).
[285] Carvalho B R, Wang Y, Mignuzzi S, Roy D, Terrones M, Fantini C, Crespi V, Malard L, and Pimenta M (2017). Intervalley scattering by acoustic phonons in two-dimensional MoS_2 revealed by double-resonance Raman spectroscopy. In: *Nature Communications* **8**.14670, pp. 1–8 (cit. on pp. 83, 131, 132).
[286] Scheuschner N, Ochedowski O, Kaulitz A, Gillen R, Schleberger M, and Maultzsch J (2014). Photoluminescence of freestanding single- and few-layer MoS_2. In: *Physical Review B* **89**.12, p. 125406 (cit. on pp. 83, 112, 114, 122).
[287] Mignuzzi S, Pollard A J, Bonini N, Brennan B, Gilmore I S, Pimenta M A, Richards D, and Roy D (2015). Effect of disorder

on Raman scattering of single-layer MoS_2. In: *Physical Review B* **91**.19, p. 195411 (cit. on pp. 84, 134).
[288] Wu J, Li H, Yin Z, Li H, Liu J, Cao X, Zhang Q, and Zhang H (2013). Layer Thinning and Etching of Mechanically Exfoliated MoS_2 Nanosheets by Thermal Annealing in Air. In: *Small* **9**.19, pp. 3314–3319 (cit. on pp. 84, 113, 115, 120, 121).
[289] Zhou H et al. (Oct. 2013b). Thickness-dependent patterning of MoS_2 sheets with well-oriented triangular pits by heating in air. In: *Nano Research* **6**.10, pp. 703–711 (cit. on pp. 84, 113).
[290] Ryu Y, Park M K, and Ryu S (Oct. 2014). Thermal Modulation of Photoluminescence from Single-Layer MoS_2. In: *Bulletin of the Korean Chemical Society* **10**.10 (cit. on pp. 84, 112–114, 120).
[291] Kim H.-J, Kim D, Jung S, Bae M.-H, Yun Y J, Yi S N, Yu J.-S, Kim J.-H, and Ha D H (2018). Changes in the Raman spectra of monolayer MoS_2 upon thermal annealing. In: *Journal of Raman Spectroscopy* **49**.12, pp. 1938–1944 (cit. on pp. 84, 112–114).
[292] Mouri S, Miyauchi Y, and Matsuda K (2013). Tunable photoluminescence of monolayer MoS_2 via chemical doping. In: *Nano Letters* **13**.12, pp. 5944–5948 (cit. on pp. 86, 112, 114, 122, 130, 134).
[293] J. Berney M.T. Portella-Oberli B D.-P (2009). Theoretical derivation of the bi- and tri-molecular trion formation coefficients. In: (cit. on p. 86).
[294] Esser A, Runge E, Zimmermann R, and Langbein W (2000). Trions in GaAs Quantum Wells: Photoluminescence Lineshape Analysis. In: *physica status solidi (a)* **178**.1, pp. 489–494 (cit. on p. 86).
[295] Fahey P M, Griffin P B, and Plummer J D (Apr. 1989). Point defects and dopant diffusion in silicon. In: *Rev. Mod. Phys.* **61** (2), pp. 289–384 (cit. on p. 88).
[296] Collart E J H, Weemers K, Gravesteijn D J, and Berkum J G M van (1998). Characterization of low-energy (100 eV–10 keV) boron ion implantation. In: *Journal of Vacuum Science & Technology B: Microelectronics and Nanometer Structures Processing, Measurement, and Phenomena* **16**.1, pp. 280–285 (cit. on p. 88).
[297] Chrostowski M, Peyronnet R, Chen W, Vaissiere N, Alvarez J, Drahi E, and Cabarrocas P R i (2018). Low temperature epitaxial growth of boron-doped silicon thin films. In: *AIP Conference Proceedings* **1999**.1, p. 070001 (cit. on p. 88).
[298] Nishi Y and Doering R (2008). *Handbook of Semiconductor Manufacturing Technology, Second Edition*. CRC Press (cit. on p. 88).
[299] Cabuz C, Fukatsu K, Kurabayashi T, Minami K, and Esashi M (1995). Microphysical investigations on mechanical structures realized in p^+ silicon. In: *Journal of Microelectromechanical Systems* **4**.3, pp. 109–118 (cit. on pp. 88, 101, 139).

[300] Wong P and Simard-Normandin M (Apr. 1985). Characterization of Boron-Implanted Silicon at Various Depths from the Surface by Raman Scattering. In: *Journal of The Electrochemical Society* **132**.4, pp. 980–982 (cit. on pp. 88, 104).

[301] Yoshimoto M, Nishigaki H, Harima H, Isshiki T, Kang K, and Yoo W S (2006). Application of UV-Raman Spectroscopy for Characterization of the Physical Crystal Structure Following Flash Anneal of an Ultrashallow Implanted Layer. In: *Journal of The Electrochemical Society* **153**.7, G697 (cit. on pp. 88, 90, 100, 101, 104, 108).

[302] Petersen D H, Hansen O, Lin R, and Nielsen P F (2008). Micro-four-point probe Hall effect measurement method. In: *Journal of Applied Physics* **104**.1, p. 013710 (cit. on p. 88).

[303] «Chapter 14 - Electronics and Communication» (2018). In: *Fundamentals and Applications of Nano Silicon in Plasmonics and Fullerines*. Ed. by M Nayfeh. Micro and Nano Technologies. Elsevier, pp. 431–485 (cit. on pp. 89, 110).

[304] Criegern R von, Weitzel L, Zeininger H, and Lange-Gieseler R (1990). Optimization of the dynamic range of SIMS depth profiles by sample preparation. In: *Surface and Interface Analysis* **15**.7, pp. 415–421 (cit. on p. 89).

[305] Murrell A, Collart E, Foad M, De Cock G, Dowsett M, Elliner D, Wang T, and Cullis T (1998). «Characterisation of ultra-shallow junctions using advanced SIMS, SRP and HRTEM techniques». In: *1998 International Conference on Ion Implantation Technology. Proceedings (Cat. No.98EX144)*. Vol. 2, 688–691 vol.2 (cit. on pp. 89, 104, 108, 110).

[306] Deen M J and Pascal F (2006). Electrical characterization of semiconductor materials and devices. In: *Journal of Materials Science: Materials in Electronics* **17**.8, pp. 549–575 (cit. on pp. 89, 110).

[307] Hönicke P, Beckhoff B, Kolbe M, Giubertoni D, Berg J van den, and Pepponi G (2010). Depth profile characterization of ultra shallow junction implants. In: *Analytical and Bioanalytical Chemistry* **396**.8, pp. 2825–2832 (cit. on p. 89).

[308] Zhang L, Koike M, Ono M, Itai S, Matsuzawa K, Ono S, Saito W, Yamaguchi M, Hayase Y, and Hara K (2015). Comprehensive 2D-carrier profiling of low-doping region by high-sensitivity scanning spreading resistance microscopy (SSRM) for power device applications. In: *Microelectronics Reliability* **55**.9-10, pp. 1559–1563 (cit. on pp. 89, 110).

[309] Shanmugam V, Khanna A, Basu P K, Aberle A G, Mueller T, and Wong J (2016). Impact of the phosphorus emitter doping profile on metal contact recombination of silicon wafer solar cells. In: *Solar Energy Materials and Solar Cells* **147**, pp. 171–176 (cit. on p. 89).

[310] Kim J H, Kim S, and Park B.-G (2019). Double-gate TFET with vertical channel sandwiched by lightly doped Si. In: *IEEE Transactions on Electron Devices* **66**.4, pp. 1656–1661 (cit. on pp. 89, 110).

[311] Feldmann F, Schoen J, Niess J, Lerch W, and Hermle M (2019). Studying dopant diffusion from poly-Si passivating contacts. In: *Solar Energy Materials and Solar Cells* **200**, p. 109978 (cit. on p. 89).

[312] Kumar C S et al. (2021). Evaluation of secondary electron intensities for dopant profiling in ion implanted semiconductors: A correlative study combining SE, SIMS and ECV methods. In: *Semiconductor Science and Technology* **36**, p. 085003 (cit. on pp. 89, 110).

[313] Hu S M (1982). Between carrier distributions and dopant atomic distribution in beveled silicon substrates. In: *Journal of Applied Physics* **53**.3, pp. 1499–1510 (cit. on p. 89).

[314] Zinner E (1980). Depth profiling by secondary ion mass spectrometry. In: *Scanning* **3**.2, pp. 57–78 (cit. on p. 89).

[315] Wilson R G and Novak S W (1991). Systematics of secondary-ion-mass spectrometry relative sensitivity factors versus electron affinity and ionization potential for a variety of matrices determined from implanted standards of more than 70 elements. In: *Journal of Applied Physics* **69**.1, pp. 466–474 (cit. on p. 89).

[316] Nakashima S, Inoue Y, Miyauchi M, Mitsuishi A, Nishimura T, Fukumoto T, and Akasaka Y (1983). Raman microprobe study of recrystallization in ion-implanted and laser-annealed polycrystalline silicon. In: *Journal of Applied Physics* **54**.5, pp. 2611–2617 (cit. on pp. 90, 138).

[317] Nakano N, Marville L, and Reif R (1992). Raman scattering in polycrystalline silicon doped with boron. In: *Journal of Applied Physics* **72**.8, pp. 3641–3647 (cit. on pp. 90, 138).

[318] Yoo W S et al. (2014). «Grain size monitoring of 3D flash memory channel poly-Si using multiwavelength Raman spectroscopy». In: *2014 14th Annual Non-Volatile Memory Technology Symposium (NVMTS)*, pp. 1–4 (cit. on p. 90).

[319] Tallant D R, Headley T J, Medernach J W, and Geyling F (1993). Characterization of Polysilicon Films by Raman Spectroscopy and Transmission Electron Microscopy: a Comparative Study. In: *MRS Proceedings* **324**, p. 255 (cit. on pp. 90, 138, 139).

[320] Othonos A, Christofides C, Boussey-Said J, and Bisson M (1994). Raman spectroscopy and spreading resistance analysis of phosphorus implanted and annealed silicon. In: *Journal of Applied Physics* **75**.12, pp. 8032–8038 (cit. on pp. 90, 138, 139).

[321] Smit C, Swaaij R A C M M van, Donker H, Petit A M H N, Kessels W M M, and Sanden M C M van de (2003). Determining the material structure of microcrystalline silicon from Raman

spectra. In: *Journal of Applied Physics* **94**.5, pp. 3582–3588 (cit. on p. 90).

[322] Meng C.-Y, Chen J.-L, Lee S.-C, and Chia C.-T (June 2006). Doping effects on the Raman spectra of silicon nanowires. In: *Phys. Rev. B* **73** (24), p. 245309 (cit. on p. 90).

[323] Iatsunskyi I, Nowaczyk G, Jurga S, Fedorenko V, Pavlenko M, and Smyntyna V (2015). One and two-phonon Raman scattering from nanostructured silicon. In: *Optik* **126**.18, pp. 1650–1655 (cit. on p. 90).

[324] Aspnes D E and Studna A A (1983). Dielectric functions and optical parameters of Si, Ge, GaP, GaAs, GaSb, InP, InAs, and InSb from 1.5 to 6.0 eV. In: *Phys. Rev. B* **27** (2), pp. 985–1009 (cit. on pp. 90, 101–103).

[325] Ogura A, Kosemura D, Takei M, Uchida H, Hattori N, Yoshimaru M, Mayuzumi S, and Wakabayashi H (2009). Evaluation of local strain in Si using UV-Raman spectroscopy. In: *Materials Science and Engineering: B* **159-160**. EMRS 2008 Spring Conference Symposium K: Advanced Silicon Materials Research for Electronic and Photovoltaic Applications, pp. 206–211 (cit. on p. 90).

[326] Wilton A de, Simard-Normandin M, and Wong P (1986). «A Raman Study Of The Dopant Distribution In Submicron pn Junctions In B^+ Or BF_2^+ Ion Implanted Silicon». In: *Advanced Processing and Characterization of Semiconductors III*. Vol. 623. International Society for Optics and Photonics, pp. 26–35 (cit. on p. 90).

[327] Holtz M, Carty J C, and Duncan W M (1999). Ultraviolet Raman stress mapping in silicon. In: *Applied Physics Letters* **74**.14, pp. 2008–2010 (cit. on p. 90).

[328] Agaiby R M B, Olsen S H, Dobrosz P, Coulson H, Bull S J, and O'Neill A G (2008). Nanometer strain profiling through Si/SiGe quantum layers. In: *Journal of Applied Physics* **104**.1, p. 013507 (cit. on p. 90).

[329] Agaiby R M B, Becker M, Thapa S B, Urmoneit U, Berger A, Gawlik A, Sarau G, and Christiansen S H (2010). Stress and doping uniformity of laser crystallized amorphous silicon in thin film silicon solar cells. In: *Journal of Applied Physics* **107**.5, p. 054312 (cit. on p. 90).

[330] Chandrasekhar M, Cardona M, and Kane E O (Oct. 1977). Intraband Raman scattering by free carriers in heavily doped $n-$Si. In: *Phys. Rev. B* **16** (8), pp. 3579–3595 (cit. on p. 91).

[331] Schmid P E (May 1981). Optical absorption in heavily doped silicon. In: *Phys. Rev. B* **23** (10), pp. 5531–5536 (cit. on p. 96).

[332] Ridgway M C, Scanlon P J, and Whitton J (1987). Nuclear Reaction Analysis of Shallow B And BF_2 Implants in Si. In: *MRS Proceedings* **92**, p. 39 (cit. on p. 101).

[333] Plummer J D, Deal M D, and Griffin P B (2000). *Silicon VLSI technology: Fundamentals, practice, and modeling.* Upper Saddle River, NJ: Prentice Hall. (cit. on p. 104).

[334] Lee J J, Fulghum J E, McGuire G E, Ray M A, Osburn C M, and Linton R W (1990). Optimization of primary beam conditions for secondary ion mass spectrometry depth profiling of shallow junctions in silicon using the Perkin–Elmer 6300. In: *Journal of Vacuum Science & Technology A* **8**.3, pp. 2287–2294 (cit. on p. 104).

[335] Felch S, Brennan R, Corcoran S, and Webster G (1993). A comparison of three techniques for profiling ultra-shallow p^+-n junctions. In: *Nuclear Instruments and Methods in Physics Research Section B: Beam Interactions with Materials and Atoms* **74**.1, pp. 156–159 (cit. on p. 104).

[336] Yoo W S and Kang K (2005). Electrical activation of ultra-shallow B and BF2 implanted silicon by flash anneal. In: *Nuclear Instruments and Methods in Physics Research Section B: Beam Interactions with Materials and Atoms* **237**.1. Ion Implantation Technology, pp. 12–17 (cit. on p. 108).

[337] Moore G E (2006). Progress in digital integrated electronics [Technical literaiture, Copyright 1975 IEEE. Reprinted, with permission. Technical Digest. International Electron Devices Meeting, IEEE, 1975, pp. 11-13.] In: *IEEE Solid-State Circuits Society Newsletter* **11**.3, pp. 36–37 (cit. on p. 111).

[338] Lloyd S (2000). Ultimate physical limits to computation. In: *Nature* **406**.6799, pp. 1047–1054 (cit. on p. 111).

[339] Lembke D, Bertolazzi S, and Kis A (2015). Single-Layer MoS2 Electronics. In: *Accounts of Chemical Research* **48**.1, pp. 100–110 (cit. on p. 111).

[340] Frisenda R, Molina-Mendoza A J, Mueller T, Castellanos-Gomez A, and Zant H S J van der (2018). Atomically thin p–n junctions based on two-dimensional materials. In: *Chem. Soc. Rev.* **47** (9), pp. 3339–3358 (cit. on p. 111).

[341] Chuang S et al. (2014). MoS2 P-type Transistors and Diodes Enabled by High Work Function MoOx Contacts. In: *Nano Letters* **14**.3, pp. 1337–1342 (cit. on p. 111).

[342] Lopez-Sanchez O, Lembke D, Kayci M, Radenovic A, and Kis A (2013). Ultrasensitive photodetectors based on monolayer MoS 2. In: *Nature nanotechnology* **8**.7, pp. 497–501 (cit. on p. 111).

[343] Roldán R, Silva-Guillén J A, López-Sancho M P, Guinea F, Cappelluti E, and Ordejón P (2014). Electronic properties of single-layer and multilayer transition metal dichalcogenides MX2 (M= Mo, W and X= S, Se). In: *Annalen der Physik* **526**.9-10, pp. 347–357 (cit. on p. 112).

[344] Berkelbach T C, Hybertsen M S, and Reichman D R (July 2013). Theory of neutral and charged excitons in monolayer transition

metal dichalcogenides. In: *Phys. Rev. B* **88** (4), p. 045318 (cit. on p. 112).

[345] Castellanos-Gomez A, Barkelid M, Goossens A M, Calado V E, Zant H S J van der, and Steele G A (2012). Laser-Thinning of MoS_2: On Demand Generation of a Single-Layer Semiconductor. In: *Nano Letters* **12**.6, pp. 3187–3192 (cit. on p. 112).

[346] Gu E, Wang Q, Zhang Y, Cong C, Hu L, Tian P, Liu R, Zhang S.-L, and Qiu Z.-J (2017). A real-time Raman spectroscopy study of the dynamics of laser-thinning of MoS_2 flakes to monolayers. In: *AIP Advances* **7**.12, p. 125329 (cit. on pp. 112, 113).

[347] Alrasheed A, Gorham J M, Tran Khac B C, Alsaffar F, DelRio F W, Chung K.-H, and Amer M R (2018). Surface Properties of Laser-Treated Molybdenum Disulfide Nanosheets for Optoelectronic Applications. In: *ACS applied materials & interfaces* **10**.21, pp. 18104–18112 (cit. on pp. 112, 113).

[348] Kang N, Paudel H P, Leuenberger M N, Tetard L, and Khondaker S I (2014). Photoluminescence quenching in single-layer MoS_2 via oxygen plasma treatment. In: *The Journal of Physical Chemistry C* **118**.36, pp. 21258–21263 (cit. on p. 112).

[349] Islam M R, Kang N, Bhanu U, Paudel H P, Erementchouk M, Tetard L, Leuenberger M N, and Khondaker S I (2014). Tuning the electrical property via defect engineering of single layer MoS_2 by oxygen plasma. In: *Nanoscale* **6** (17), pp. 10033–10039 (cit. on p. 112).

[350] Wang D, Wang Y, Chen X, Zhu Y, Zhan K, Cheng H, and Wang X (2016). Layer-by-layer thinning of two-dimensional MoS_2 films by using a focused ion beam. In: *Nanoscale* **8** (7), pp. 4107–4112 (cit. on pp. 112, 113).

[351] Wang Q, Zhang Y, Cong C, Hu L, Tian P, Liu R, and Qiu Z J (2017). Layer thinning of MoS_2 flakes by thermal annealing in air. In: *IEEE 12th International Conference on ASIC (ASICON)*, pp. 580–583 (cit. on pp. 112–115, 118, 120, 127).

[352] Namgung S D, Yang S, Park K, Cho A.-J, Kim H, and Kwon J.-Y (Feb. 2015). Influence of post-annealing on the off current of MoS_2 field-effect transistors. In: *Nanoscale Research Letters* **10**.1, p. 62 (cit. on pp. 112, 120).

[353] Su L, Yu Y, Cao L, and Zhang Y (Mar. 2017). In Situ Monitoring of the Thermal-Annealing Effect in a Monolayer of MoS_2. In: *Physical Review Applied* **7** (3), p. 034009 (cit. on pp. 112, 113).

[354] Rao R, Islam A E, Campbell P M, Vogel E M, and Maruyama B (Mar. 2017). In situ thermal oxidation kinetics in few layer MoS_2. In: *2D Materials* **4**.2, p. 025058 (cit. on pp. 112, 113).

[355] Qiu H, Pan L, Yao Z, Li J, Shi Y, and Wang X (2012). Electrical characterization of back-gated bi-layer MoS_2 field-effect transistors and the effect of ambient on their performances. In: *Applied Physics Letters* **100**.12, p. 123104 (cit. on pp. 113, 120).

[356] Liu Y et al. (2015). Thermal Oxidation of WSe_2 Nanosheets Adhered on SiO_2/Si Substrates. In: *Nano Letters* **15**.8, pp. 4979–4984 (cit. on p. 113).
[357] Hu L, Shan X, Wu Y, Zhao J, and Lu X (2017). Laser Thinning and Patterning of MoS_2 with Layer-by-Layer Precision. In: *Scientific reports* **7**.1, p. 15538 (cit. on p. 113).
[358] Liu Y, Nan H, Wu X, Pan W, Wang W, Bai J, Zhao W, Sun L, Wang X, and Ni Z (2013). Layer-by-layer thinning of MoS_2 by plasma. In: *ACS nano* **7**.5, pp. 4202–4209 (cit. on p. 113).
[359] Zhu H, Qin X, Cheng L, Azcatl A, Kim J, and Wallace R M (2016). Remote Plasma Oxidation and Atomic Layer Etching of MoS_2. In: *ACS Applied Materials & Interfaces* **8**.29, pp. 19119–19126 (cit. on p. 113).
[360] Varghese A, Sharma C H, and Thalakulam M (2017). Topography preserved microwave plasma etching for top-down layer engineering in MoS_2 and other van der Waals materials. In: *Nanoscale* **9**.11, pp. 3818–3825 (cit. on p. 113).
[361] Deng Y, Chen M, Zhang J, Hu X, Zhao Y, Nshimiyimana J P, Chi X, Hou G, Chu W, and Sun L (2016). Thinning of n-layer MoS_2 by annealing a palladium film under vacuum. In: *RSC Adv.* **6** (56), pp. 50595–50598 (cit. on p. 113).
[362] Donarelli M, Perrozzi F, Bisti F, Paparella F, Feyer V, Ponzoni A, Gonchigsuren M, and Ottaviano L (2015a). Few layered MoS_2 lithography with an AFM tip: description of the technique and nanospectroscopy investigations. In: *Nanoscale* **7** (26), pp. 11453–11459 (cit. on p. 113).
[363] Yamamoto M, Einstein T L, Fuhrer M S, and Cullen W G (2013). Anisotropic Etching of Atomically Thin MoS_2. In: *The Journal of Physical Chemistry C* **117**.48, pp. 25643–25649 (cit. on p. 113).
[364] Wang X, Fan W, Fan Z, Dai W, Zhu K, Hong S, Sun Y, Wu J, and Liu K (2018). Substrate modified thermal stability of mono- and few-layer MoS_2. In: *Nanoscale* **10** (7), pp. 3540–3546 (cit. on p. 113).
[365] Lu X, Utama M I B, Zhang J, Zhao Y, and Xiong Q (2013). Layer-by-layer thinning of MoS_2 by thermal annealing. In: *Nanoscale* **5** (19), pp. 8904–8908 (cit. on pp. 113, 115, 120, 121).
[366] Donarelli M, Prezioso S, Perrozzi F, Bisti F, Nardone M, Giancaterini L, Cantalini C, and Ottaviano L (2015b). Response to NO_2 and other gases of resistive chemically exfoliated MoS_2-based gas sensors. In: *Sensors and Actuators B: Chemical* **207, Part A**, pp. 602–613 (cit. on pp. 113, 124, 127).
[367] Takahashi N and Shiojiri M (1993). Stacking faults in hexagonal and rhombohedral MoS2 crystals produced by mechanical operation in relation to lubrication. In: *Wear* **167**.2, pp. 163–171 (cit. on p. 113).

[368] Steinhoff A, Kim J.-H, Jahnke F, Rösner M, Kim D.-S, Lee C, Han G H, Jeong M S, Wehling T O, and Gies C (2015). Efficient Excitonic Photoluminescence in Direct and Indirect Band Gap Monolayer MoS_2. In: *Nano Letters* **15**.10, pp. 6841–6847 (cit. on p. 114).

[369] Sundaram R S, Engel M, Lombardo A, Krupke R, Ferrari A C, Avouris P, and Steiner M (2013). Electroluminescence in Single Layer MoS_2. In: *Nano Letters* **13**.4. PMID: 23514373, pp. 1416–1421 (cit. on p. 114).

[370] Li Y, Qi Z, Liu M, Wang Y, Cheng X, Zhang G, and Sheng L (2014b). Photoluminescence of monolayer MoS_2 on $LaAlO_3$ and $SrTiO_3$ substrates. In: *Nanoscale* **6** (24), pp. 15248–15254 (cit. on pp. 114, 122).

[371] Li H, Zhang Q, Yap C C R, Tay B K, Edwin T H T, Olivier A, and Baillargeat D (2012c). From Bulk to Monolayer MoS_2: Evolution of Raman Scattering. In: *Advanced Functional Materials* **22**.7, pp. 1385–1390 (cit. on pp. 114, 120).

[372] Gołasa K, Grzeszczyk M, Korona K, Bożek R, Binder J, Szczytko J, Wysmołek A, and Babiński A (2013). Optical Properties of Molybdenum Disulfide (MoS_2). In: *Acta Physica Polonica, A.* **124**.5 (cit. on p. 114).

[373] Shree S et al. (2018). Observation of exciton-phonon coupling in $MoSe_2$ monolayers. In: *Physical Review B* **98**.3, p. 035302 (cit. on p. 114).

[374] Raja A et al. (2018). Enhancement of Exciton-Phonon Scattering from Monolayer to Bilayer WS_2. In: *Nano Letters* **18**.10, pp. 6135–6143 (cit. on p. 114).

[375] Helmrich S et al. (2018). Exciton–phonon coupling in mono-and bilayer $MoTe_2$. In: *2D Materials* **5**.4, p. 045007 (cit. on p. 114).

[376] Carvalho B R, Malard L M, Alves J M, Fantini C, and Pimenta M A (2015). Symmetry-dependent exciton-phonon coupling in 2D and bulk MoS_2 observed by resonance Raman scattering. In: *Physical Review Letters* **114**.13, p. 136403 (cit. on pp. 114, 133, 134).

[377] Schuller J A, Karaveli S, Schiros T, He K, Yang S, Kymissis I, Shan J, and Zia R (2013). Orientation of luminescent excitons in layered nanomaterials. In: *Nature Nanotechnology* **8**.4, pp. 271–276 (cit. on pp. 114, 115, 133, 135).

[378] Novoselov K S, Geim A K, Morozov S V, Jiang D, Zhang Y, Dubonos S V, Grigorieva I V, and Firsov A A (2004). Electric Field Effect in Atomically Thin Carbon Films. In: *Science* **306**.5696, pp. 666–669 (cit. on p. 115).

[379] Quereda J, Castellanos-Gomez A, Agraït N, and Rubio-Bollinger G (2014). Single-layer MoS_2 roughness and sliding friction quenching by interaction with atomically flat substrates. In: *Applied Physics Letters* **105**.5, p. 053111 (cit. on p. 115).

[380] Backes C et al. (2014). Edge and confinement effects allow in situ measurement of size and thickness of liquid-exfoliated nanosheets. In: *Nature Communications* **5**.4576, pp. 1–10 (cit. on p. 116).
[381] Li S.-L, Miyazaki H, Song H, Kuramochi H, Nakaharai S, and Tsukagoshi K (2012d). Quantitative Raman Spectrum and Reliable Thickness Identification for Atomic Layers on Insulating Substrates. In: *ACS Nano* **6**.8, pp. 7381–7388 (cit. on p. 116).
[382] Nemes-Incze P, Osváth Z, Kamarás K, and Biró L (2008). Anomalies in thickness measurements of graphene and few layer graphite crystals by tapping mode atomic force microscopy. In: *Carbon* **46**.11, pp. 1435–1442 (cit. on p. 116).
[383] Li Q, Song J, Besenbacher F, and Dong M (2015). Two-Dimensional Material Confined Water. In: *Accounts of Chemical Research* **48**.1, pp. 119–127 (cit. on p. 117).
[384] Lee D, Ahn G, and Ryu S (2014). Two-Dimensional Water Diffusion at a Graphene–Silica Interface. In: *Journal of the American Chemical Society* **136**.18, pp. 6634–6642 (cit. on p. 117).
[385] Donarelli M, Bisti F, Perrozzi F, and Ottaviano L (2013). Tunable sulfur desorption in exfoliated MoS_2 by means of thermal annealing in ultra-high vacuum. In: *Chemical Physics Letters* **588**, pp. 198–202 (cit. on pp. 117, 124–126, 134).
[386] Castellanos-Gomez A, Buscema M, Molenaar R, Singh V, Janssen L, Zant H S J van der, and Steele G A (Apr. 2014). Deterministic transfer of two-dimensional materials by all-dry viscoelastic stamping. In: *2D Materials* **1**.1, p. 011002 (cit. on p. 120).
[387] Chakraborty B, Bera A, Muthu D V S, Bhowmick S, Waghmare U V, and Sood A K (Apr. 2012). Symmetry-dependent phonon renormalization in monolayer MoS_2 transistor. In: *Phys. Rev. B* **85** (16), p. 161403 (cit. on p. 121).
[388] Lu H, Kummel A, and Robertson J (2018). Passivating the sulfur vacancy in monolayer MoS_2. In: *APL Materials* **6**.6, p. 066104 (cit. on p. 123).
[389] Förster A, Gemming S, Seifert G, and Tománek D (2017). Chemical and Electronic Repair Mechanism of Defects in MoS_2 Monolayers. In: *ACS Nano* **11**.10, pp. 9989–9996 (cit. on p. 126).
[390] Vancsó P, Zsolt Magda G, Pető J, Noh J.-Y, Kim Y.-S, Hwang C, Biro L, and Tapaszto L (July 2016). The intrinsic defect structure of exfoliated MoS_2 single layers revealed by Scanning Tunneling Microscopy. In: *Scientific Reports* **6**, p. 29726 (cit. on p. 126).
[391] Schönfeld B, Huang J J, and Moss S C (Aug. 1983). Anisotropic mean-square displacements (MSD) in single-crystals of 2*H*- and 3*R*-MoS_2. In: *Acta Crystallographica Section B* **39**.4, pp. 404–407 (cit. on p. 126).
[392] Sanchez D A, Dai Z, Wang P, Cantu-Chavez A, Brennan C J, Huang R, and Lu N (2018). Mechanics of spontaneously formed

nanoblisters trapped by transferred 2D crystals. In: *Proceedings of the National Academy of Sciences* **115**.31, pp. 7884–7889 (cit. on p. 127).

[393] Ataca C and Ciraci S (May 2012). Dissociation of H_2O at the vacancies of single-layer MoS_2. In: *Phys. Rev. B* **85** (19), p. 195410 (cit. on p. 127).

[394] Lefebvre J, Homma Y, and Finnie P (May 2003). Bright Band Gap Photoluminescence from Unprocessed Single-Walled Carbon Nanotubes. In: *Phys. Rev. Lett.* **90** (21), p. 217401 (cit. on p. 127).

[395] Avouris P, Freitag M, and Perebeinos V (June 2008). Cabonnanotube photonics and optoelectronics. In: *Nature Photonics* **2**, pp. 341–350 (cit. on p. 127).

[396] Spindler C, Galvani T, Wirtz L, Rey G, and Siebentritt S (2019). Excitation-intensity dependence of shallow and deep-level photoluminescence transitions in semiconductors. In: *Journal of Applied Physics* **126**.17, p. 175703 (cit. on p. 128).

[397] Pimenta M A, Del Corro E, Carvalho B R, Fantini C, and Malard L M (2015). Comparative study of Raman spectroscopy in graphene and MoS_2-type transition metal dichalcogenides. In: *Accounts of Chemical Research* **48**.1, pp. 41–47 (cit. on p. 131).

[398] Munkhbayar G, Palleschi S, Perrozzi F, Nardone M, Davaasambuu J, and Ottaviano L (2018). A study of exfoliated molybdenum disulfide (MoS_2) based on Raman and photoluminescence spectroscopy. In: *Solid State Phenomena* **271**, pp. 40–46 (cit. on p. 132).

[399] Fukumoto M, Minami H, Hasuike N, Harima H, Yoshimoto M, and Yoo W S (Dec. 2019). Characterization of Annealing Effects in Ultra-Shallow Boron-Implanted Si Wafers using Raman Scattering. In: *ECS Transactions* **19**.1, pp. 127–133 (cit. on p. 138).

[400] Paillard V, Puech P, Laguna M A, Temple-Boyer P, Caussat B, Couderc J P, and Mauduit B de (1998). Resonant Raman scattering in polycrystalline silicon thin films. In: *Applied Physics Letters* **73**.12, pp. 1718–1720 (cit. on pp. 138, 139).

[401] Yoshikawa M, Murakami M, Matsuda K, Matsunobe T, Sugie S, Okada K, and Ishida H (2005). Characterization of Si nanopolycrystalline films at the nanometer level using resonant Raman scattering. In: *Journal of Applied Physics* **98**.6, p. 063531 (cit. on pp. 138, 139).

[402] Novotny L and Hecht B (2012). *Principles of nano-optics*. Cambridge university press (cit. on p. 139).

[403] Mahapatra S, Ning Y, Schultz J F, Li L, Zhang J.-L, and Jiang N (2019). Angstrom Scale Chemical Analysis of Metal Supported Trans- and Cis-Regioisomers by Ultrahigh Vacuum Tip-Enhanced Raman Mapping. In: *Nano Letters* **19**.5, pp. 3267–3272 (cit. on p. 139).

La borsa di dottorato è stata cofinanziata con risorse del
Programma Operativo Nazionale Ricerca e Innovazione 2014-2020 (CCI 2014IT16M2OP005)
Fondo Sociale Europeo, Azione I.1 “Dottorati Innovativi con caratterizzazione Industriale”

UNIONE EUROPEA
Fondo Sociale Europeo

Ministero dell'Università
e della Ricerca

PON
RICERCA
E INNOVAZIONE
2014 - 2020